Phonon Coupling and Electric-Field Switching of Excitons in Semiconductor Nanocrystals

DISSERTATION
for attainment of the degree
doctor rerum naturalium
(Dr. rer. nat.)

submitted by

Florian Funk
(born Johst)

Institute for Physical Chemistry,
University of Hamburg

Hamburg 2025

Eingereicht von:	Florian Funk (geb. Johst)
Matrikelnummer:	6788940
ORCiD	0000-0002-7594-8440
Gutachter der Dissertation:	PD. Dr. Tobias Kipp
	Prof. Dr. Gabriel Bester
Gutachter der Disputation:	PD. Dr. Tobias Kipp
	Prof. Dr. Dorota Koziej
	PD Dr. Christoph Wutz
Datum der Disputation:	26.09.2025
Datum der Druckfreigabe:	30.09.2025

Die vorliegende Dissertation wurde im Zeitraum von Oktober 2020 bis August 2025 am Institut für Physikalische Chemie der Universität Hamburg angefertigt.

Publications

Articles in Journals

- Rebmann, J.; Werners, H.; Johst, F.; Dohrmann, M.; Staechelin, Y. U.; Strelow, C.; Mews, A.; Kipp, T. *Chem. Mater.* **2023**, 35, 1238–1248.

- Johst, F.; Rebmann, J.; Werners, H.; Klemeyer, L.; Kopula Kesavan, J.; Koziej, D.; Strelow, C.; Bester, G.; Mews, A.; Kipp, T. *ACS Photonics* **2024**, 11, 3741–3749.

- Leippe, S. C.; Johst, F.; Hoffmann, B.; Krohn, S.; Papagrigoriou, K.; Asmis, K. R.; Mews, A.; Bastian, B. *J. Phys. Chem. C* **2024**, 128, 21472–21478.

Contributions to Conferences

- 07/2021, DPG Summer School Exciting Nanostructures; Poster: Effective Mass Based Exciton Calculations Using COMSOL Multiphysics

- 10/2022, GRK Nanohybrid conference; Poster: Spectroscopy of $\text{Zn}_{1-x}\text{Cd}_x\text{Se/CdS}$ dot-in-rod nanostructures

- 06/2023, DBG Bunsentagung; Poster: Spectroscopy of $\text{Zn}_{1-x}\text{Cd}_x\text{Se/CdS}$ dot-in-rod nanostructures

- 07/2023, NaNax10 2023; Poster: Spectroscopy of $\text{Zn}_{1-x}\text{Cd}_x\text{Se/CdS}$ dot-in-rod nanostructures

Contents

Publications I
List of Abbreviations IV
Abstract VI
Kurzfassung VIII

1. Introduction **1**

2. Theoretical Background **3**
2.1. Properties of Semiconductor Nanocrystals 3
  2.1.1. Electronic Structure 3
  2.1.2. Optical Properties of Nanocrystals 7
  2.1.3. Influence of Low Temperatures on Optical Properties 11
  2.1.4. Exciton–Phonon Coupling 15
  2.1.5. Influence of External Electric Fields on Optical Properties 21
2.2. Type-I and Type-II Dot-in-Rod Nanocrystals 24
2.3. Giant-Shell CdSe/CdS Quantum Dots 27

3. Experimental Methods **29**
3.1. Confocal Laser Scanning Microscopy 29
3.2. Atomic Force Microscopy 30
3.3. Calculation of Excitons in Nanocrystals 31
3.4. Optical and Electron-Beam Lithography 35

4. Experimental Details **37**
4.1. Chemicals 37
4.2. Optical Spectroscopy 37
  4.2.1. Confocal Microscope Setup 37
  4.2.2. Spectroscopy in External Electric Fields 39
  4.2.3. Sample Synthesis 39
  4.2.4. Sample Preparation 40
4.3. Production of Interdigitated Electrode Substrates 41
  4.3.1. Optical Lithography Procedure 41

    4.3.2. Device Preparation 42
    4.3.3. Atomic Force Microscopy Measurements 43
    4.3.4. E-beam Lithography 43
  4.4. Quantum Mechanical Calculations using COMSOL Multiphysics 43

5. Motivation and Goals 49

6. Results and Discussion 51
  6.1. Exciton–Phonon Coupling in ZnCdSe/CdS Dot-in-Rod Nanocrystals 51
    6.1.1. Ensemble Spectroscopy 51
    6.1.2. Simulation of Excitons in ZnCdSe dots 55
    6.1.3. Single-Particle Spectroscopy 56
    6.1.4. Calculation of Excitons and their Phonon Coupling 63
  6.2. Spectroscopy of Spherical CdSe/CdS Nanocrystals 80
    6.2.1. Exciton–Phonon Coupling in Spherical CdSe/CdS Nanocrystals 80
    6.2.2. CdSe/CdS Dots as Temperature Probes 83
  6.3. Spectroscopy of Dot-in-Rod Nanocrystals in Electric Fields 85
    6.3.1. Device Development for Spectroscopy in Electric Fields 85
    6.3.2. CdSe/CdS Dot-in-Rod NCs in external Electric Fields 90
    6.3.3. ZnCdSe/CdS Dot-in-Rod NCs in external Electric Field 110

7. Conclusion 115

8. Outlook 119

9. References 121

A. Appendix 135
  A.1. Supplementary Information 135
  A.2. Hazard and Safety 142
  A.3. Acknowledgement 145
  A.4. Eidesstattliche Erklärung 147

List of Abbreviations

AFM atomic force microscopy

APD avalanche photodiode

CCD charge-coupled device

DOP degree of polarization

DOS density of states

DR dot-in-rod nanocrystal

EXAFS extended X-ray absorption fine structure

FEM finite-element method

FWHM full width at half maximum

HOMO highest occupied molecular orbital

HR Huang–Rhys

HSAB hard and soft acids and bases

IDE interdigitated electrode

LUMO lowest unoccupied molecular orbital

LA longitudinal acoustic

LCAO linear combination of atomic orbitals

LO longitudinal optical

ML monolayer

NC nanocrystal

PDE partial differential equation

PL photoluminescence

PMMA poly(methylmethacrylat)

PVD physical vapor deposition

QCSE	quantum-confined Stark effect
QY	quantum yield
ROI	region of interest
SEM	scanning electron microscope
SILAR	successive ionic layer adsorption and reaction
SMU	source measure unit
TA	transversal acoustic
TCSPC	time-correlated single photon counting
TEM	transmission electron microscopy
TO	transversal optical
ZPL	zero-phonon line

Abstract

The optical and electronic properties of semiconductor nanocrystal (NC) are governed by the charge-carrier localization. One possibility to gain information about the charge-carrier localization is through exciton–phonon coupling. In semiconductors, exciton–phonon coupling plays a central role, as it limits the homogeneous emission line width and the coherence of emitted photons, as well as relaxation processes. Therefore, a profound understanding of exciton–phonon coupling is needed to improve the properties of NCs. However, experimental results and sophisticated calculations of exciton–phonon coupling show discrepancies. Hitherto, most research on exciton–phonon coupling was primarily focused on ensemble measurements, and single-particle spectroscopy data is lacking. Another important aspect in NCs is the presence of surface charges because they can strongly influence excitons, which limits the emission linewidth of NC and is presumed to affect exciton–phonon coupling.

In this work, single-particle photoluminescence (PL) spectroscopy at cryogenic temperatures was used to measure the optical properties of semiconductor heteronanocrystals with different charge-carrier localizations. It was investigated how the charge-carrier localization affects exciton–phonon coupling when the band alignment changes from type-II to type-I. For this purpose, $\mathrm{Zn}_{1-x}\mathrm{Cd}_x\mathrm{Se}/\mathrm{CdS}$ dot-in-rod nanocrystals (DRs) with different Cd fraction x and CdSe/CdS DRs were analyzed. Statistical single-particle spectroscopy revealed that the relative intensities of the first-order longitudinal optical phonons reflect the change in charge-carrier localization. A new model was developed to predict the strength of exciton–phonon coupling. This model derives the strength of exciton–phonon coupling from the difference of electron and hole localization, weighted by material and particle-dependent coupling constants. Quantum mechanical calculations of the exciton were carried out within the effective-mass approximation to support the data evaluation. It was revealed that the derived coupling constants share similarities with Fröhlich coupling constants, which are used in bulk. Moreover, the calculations allowed for the estimation of the partially unknown Cd fractions x. Accounting for surface charges in the calculations revealed that they strongly affect the exciton–phonon coupling. Furthermore, the results of this work strongly suggest that surface charges have a strong effect on exciton–phonon coupling. Single-particle spectroscopy of CdSe/CdS quantum dots showed that an increase in the shell thickness leads to a distinct increase in the exciton–phonon coupling. By applying external electric fields, the charge-carrier localization in DRs was manipulated during spectroscopy. Measurements of CdSe/CdS and ZnSe/CdS DRs revealed that the magnitude of exciton–phonon coupling can be controlled by these electric fields. Moreover, multiple new effects were found that are linked to surface charges. These effects include blue-shifts of the emission in CdSe/CdS DRs, the memory effect of

the previous electric field direction, directed spectral diffusion, and induced repeatable spectral jumps.

Kurzfassung

Die optischen und elektronischen Eigenschaften von Halbleiter-Nanokristallen NCs werden durch die Ladungsträgerlokalisation bestimmt. Hierbei stellt die Exziton-Phonon-Kopplung eine Möglichkeit dar, um Informationen über die Ladungsträgerlokalisation zu erhalten. In Halbleitern spielt Exziton–Phonon-Kopplung eine zentrale Rolle, da sie die homogene Linienbreite der Emission und die Kohärenz von emittierten Photonen, sowie Relaxationsprozesse limitiert. Daher ist ein tiefgreifendes Verständnis über die Exziton-Phonon-Kopplung notwendig, um diese Eigenschaften von NCs für Anwendungen zu verbessern. Ein Problem besteht darin, dass bisherige experimentelle Ergebnisse und theoretische Vorhersagen der Exziton–Phonon-Kopplung voneinander abweichen. Bisher war zudem der Großteil der Forschung von Exziton–Phonon-Kopplung primär auf Ensemblemessungen fokussiert. Daher mangelt es an Daten, die mittels Einzelteilchenspektroskopie gemessen wurden. Ein weiterer wichtiger Aspekt in Nanokristallen, welcher die Linienbreite der Emission und vermutlich die Exziton–Phonon-Kopplung beeinflusst, ist die Wechselwirkung von Exzitonen mit Oberflächenladungen.

In dieser Arbeit wurde Einzelteilchenspektroskopie bei kryogenen Temperaturen durchgeführt, um die optischen Eigenschaften von Halbleiter-NCs zu messen. Es wurde untersucht wie die Ladungsträgerlokalisation die Exziton–Phonon-Kopplung beeinflusst, wenn sich die Bandanordnung von Typ-II zu Typ-I ändert. Zu diesem Zweck wurden Kugel-in-Stab-Nanokristalle (DRs) aus $\mathrm{Zn}_{1-x}\mathrm{Cd}_x\mathrm{Se/CdS}$ mit verschiedenen Cd-Anteilen x untersucht. Hierbei wurde über statistische Einzelteilchenspektroskopie festgestellt, dass die relativen Intensitäten der longitudinalen optischen Phononen erster Ordnung die Änderungen der Ladungsträgerlokalisation widerspiegelten. Darüber hinaus wurde ein neues Modell entwickelt, um die Stärke der Exziton–Phonon-Kopplung vorherzusagen. Dieses Modell leitet die Stärke der Exziton–Phonon-Kopplung aus der Differenz der Lokalisation von Elektron und Loch her, die mit material- und teilchen-spezifischen Kopplungskonstanten gewichtet wurden. Zur Auswertung der experimentellen Daten wurden quantenmechanische Berechnungen des Exzitons durchgeführt, wobei die effektive-Masse-Näherung verwendet wurde. Dabei wurde aufgedeckt, dass diese Kopplungskonstanten Ähnlichkeiten mit Fröhlich-Konstanten aufweisen, welche im makroskopischen Fall genutzt werden. Zudem erlaubten die Berechnungen eine Einschätzung der zum Teil unbekannten Cd-Anteile x. Des Weiteren enthüllten die Ergebnisse dieser Arbeit, dass Oberflächenladungen die Exziton–Phonon-Kopplung stark beeinflussen. Weitere Einzelteilchenmessungen von CdSe/CdS Quantenpunkten zeigten, dass eine Zunahme der Schalendicke zu einem deutlichen Anstieg der Exziton–Phonon-Kopplung führt. Die Ladungsträgerlokalisation wurde ebenfalls durch externe elektrische Felder variiert. Hierbei enthüllten spektroskopische Untersuchungen von CdSe/CdS- und $\mathrm{Zn}_{1-x}\mathrm{Cd}_x\mathrm{Se/CdS}$-DRs, dass die Stärke der

Exziton–Phonon-Kopplung durch elektrischen Felder kontrolliert werden kann. Darüber hinaus wurden mehrere neue Effekte entdeckt, welche mit Oberflächenladungen zusammenhängen. Diese Effekte beinhalten die Blauverschiebung der Emission von CdSe/CdS-DRs, einen "Gedächtniseffekt" der CdSe/CdS-DRs aufgrund der vorherigen elektrischen Feldrichtung, eine gerichtete spektrale Diffusion und induzierte wiederholbare spektrale Sprünge.

1. Introduction

In the past decades, nanocrystals (NCs) have emerged as a new material type. NCs have spatial dimensions on the nanometer scale (1–100 nm), which is a billionth of a meter. What makes NCs unique is that their properties can be controlled through their size and shape, in contrast to macroscopic systems that keep their properties regardless of morphological changes. This effect is a consequence of quantum confinement, which, in the case of semiconductor NCs, increases the band gap energy with decreasing size.[1] Semiconductor NCs can be used in a variety of different applications. Due to their tunable band gap energy, they are interesting as light sources in light-emitting diodes[2–4] or as light harvesters in solar cells.[5] Their large surface-to-volume ratio also makes them ideal candidates for catalytic applications.[6]

All optical and electronic properties of semiconductor NCs are controlled by the charge-carrier localization. The charge-carrier localization can only be roughly estimated by measuring, for example, the excited-state lifetime or emission energy.[7,8] Another potential way to obtain information about charge-carrier localization is through the exciton–phonon coupling. In general, exciton–phonon coupling describes the interplay between electronic and vibrational states. Consequently, exciton–phonon coupling is a key aspect to consider as it takes part in electronic relaxation processes, as well as in electronic and thermal transport properties.[9–11] Following the nature of exciton–phonon coupling, it controls properties like the homogeneous emission linewidth and excited state lifetimes.[12,13] However, theoretical predictions and experimental results still deviate from each other, even when sophisticated modeling is employed.[14,15] This makes it clear that further research into exciton–phonon coupling is needed.

Various methods are used to investigate exciton–phonon coupling, like Raman spectroscopy[16–18], PL excitation spectroscopy[19], and fluorescence line-narrowing spectroscopy[20]. The drawback of, for example, Raman spectroscopy is that it yields results that are not fully representative of the exciton–phonon coupling occurring during PL. Ensemble measurements, in general, have the problem that they average out effects like the influence of surface charges. Therefore, a preferred method to investigate the exciton–phonon coupling in detail is the single-particle PL spectroscopy at cryogenic temperatures. These measurements allow to resolve temporal changes in exciton–phonon coupling in single NCs, as well as to directly probe the lowest exciton states. If the exciton–phonon coupling is more precisely measured and better understood, then more accurate information about the charge-carrier localization can be derived from it. Moreover, surface charges have been assumed to impact exciton–phonon coupling.[12,21–25] Similar to exciton–phonon coupling, surface charges also limit the emission linewidth and coherence of emitted photons. Consequently, it is important to understand the influence of surface charges.

Another interesting part of NCs is that the charge-carrier localization can be controlled by creating heterostructures. Heterostructured NCs have been synthesized in various shapes and compositions, and unique optical properties arise from the different exciton confinement in these structures.[26] An interesting example for these are dot-in-rod nanocrystals DRs, which are composed of a spherical core, also known as a quantum dot, that is embedded in a rod-shaped shell. What makes DRs special is that they emit polarized light[27,28], making them suitable candidates for light-emitting diodes[29] and lasers[30]. Their anisotropy has also sparked interest in using them for catalytic water splitting for hydrogen production, when combined with metal tips. More importantly for this work, the geometry of DRs promotes charge-carrier delocalization, which increases exciton–phonon coupling. Additionally, the charge-carrier localization in these structures can be manipulated by external electric fields, allowing them to be used as optical switches.[31]

In this work, the charge-carrier localization in $Zn_{1-x}Cd_xSe$/CdS DRs, CdSe/CdS DRs, and CdSe/CdS quantum dots is investigated by single-particle PL spectroscopy at cryogenic temperatures. For this purpose, the charge-carrier localization was varied on one hand by the composition and geometry of the NCs, and on the other hand by external electric fields. To support the evaluation of the exciton–phonon coupling, quantum mechanical calculations of the exciton within the effective-mass approximation were carried out.

2. Theoretical Background

2.1. Properties of Semiconductor Nanocrystals

2.1.1. Electronic Structure

In solid states, many atoms are present to form molecular orbitals. These molecular orbitals can be constructed by the linear combination of atomic orbitals (LCAO), resulting in bonding and antibonding states. If enough atoms are present, the molecular orbitals form continuous energy bands. Important for the properties of a material are the highest occupied and lowest unoccupied energy bands, similar to the highest occupied molecular orbital (HOMO) and lowest unoccupied molecular orbital (LUMO) of a molecule. The highest occupied band is called the valence band, and the lowest unoccupied band is called the conduction band. In the case of insulators and semiconductors, an energy gap is present between these two bands, as sketched in Figure 2.1a and b. The corresponding Fermi level E_F lies in the middle of the band gap. In metals, see Figure 2.1c, the band gap is absent, and E_F is located in the highest occupied band. As a consequence of the partially filled band, metals are electrically conducting at $T = 0$ K, while insulators and semiconductors are not. The band gap in semiconductors is sufficiently small compared to insulators that external energy in the form of heat or light can excite electrons from the valence to the conduction band without damaging the material, making them conducting.[32,33]

An electron can be excited from the valence to the conduction band by light or thermal energy. In this process, a positive charge is left behind in the valence band. This positive charge is called a hole and behaves like a particle. In the first approximation, the electron and hole can be described as free particles. The energy of the electron and hole is then given by the parabolic dispersion relation

$$E(\mathbf{k}) = \frac{\hbar^2 \mathbf{k}^2}{2m_\mathrm{e/h}}. \tag{2.1.1}$$

In this equation, $\hbar$ is the reduced Planck constant, $\mathbf{k}$ is the wave vector of the particle, and $m_\mathrm{e/h}$ is the mass of the electron or hole.[34]

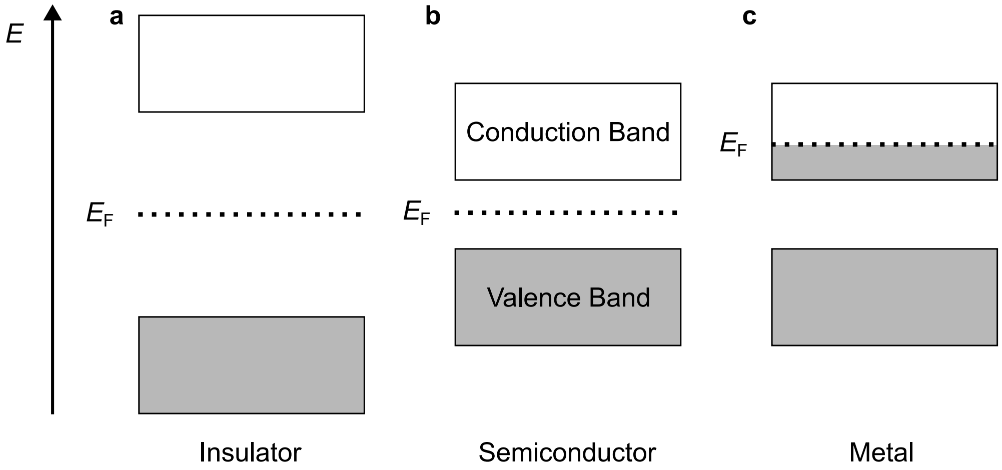

Figure 2.1.: Band schemes of (a) an insulator, (b) a semiconductor, and (c) a metal. The grey areas represent occupation of the bands with electrons, while the white areas in the bands are empty electronic states. The dotted lines indicate the Fermi levels. Adapted from Gross.[33]

Inside a semiconductor, the electrons and holes occupy molecular orbitals that can have an angular momentum. The interaction between the spin of the charge carrier and the angular momentum of the molecular orbitals is known as spin–orbit coupling and results in an energetic splitting of the energy bands. This work is centered around the II-VI semiconductors ZnSe, CdSe, and CdS. In these II-VI semiconductors, the valence band is built from p-orbitals and the conduction band from s-orbitals. If spin–orbit coupling is accounted for, the valence band splits into three bands, while the conduction band remains a single band. Figure 2.2 shows this four-band structure in the reciprocal space.[32,35] These energy bands show different curvatures. Evaluating and reordering the curvature of the dispersion relation from Equation 2.1.1 to

$$\frac{1}{m_{\mathrm{e/h,eff}}} = \frac{1}{\hbar^2}\frac{\mathrm{d}^2 E}{\mathrm{d}\mathbf{k}^2} \tag{2.1.2}$$

shows that it is related to a reciprocal mass. This mass is called the effective mass and can be used to describe the behavior of charge carriers in crystal lattices as quasi-free particles. The conduction band with the lowest curvature arises from the heavy hole, followed by the larger curvature of the light hole and split-off bands. The heavy hole band correspond to the total angular moment $J = 3/2$ with the projection $m_J = \pm 3/2$, the light hole band to $J = 3/2$ with $m_J = \pm 1/2$ and the split-off hole band to $J = 1/2$ with $m_J = \pm 1/2$.[35,36]

The electron and hole can form a bound state, via Coulomb interaction, known as an exciton. Excitons resemble hydrogen atoms (or more specifically positronium atoms) as both are two-particle systems that are bound by Coulomb interaction. A better understanding of the exciton can be gained by evaluating the so-called exciton-Bohr radius in

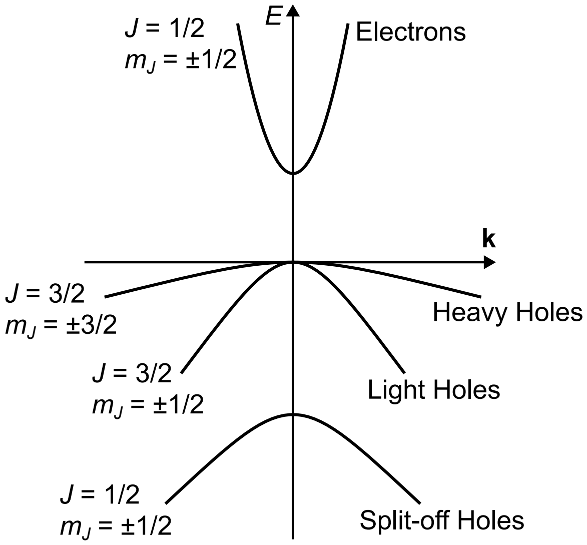

Figure 2.2.: Simplified band diagram of the conduction and valence bands of a II-VI semiconductor including the angular momentums of electron and hole J and their 1-D projections m_J. Adapted from literature.[35,36]

analogy to the Bohr radius. The masses of the electron and the hole within a semiconductor are more similar to each other compared to the ones of the proton and the electron of a hydrogen atom. Thus, for separating center-off-mass and relative motion, it is necessary to introduce a reduced mass

$$m_{\mathrm{red,eff}} = \frac{m_{\mathrm{e,eff}} m_{\mathrm{h,eff}}}{m_{\mathrm{e,eff}} + m_{\mathrm{h,eff}}} \tag{2.1.3}$$

for the exciton.[37] Additionally, the electron and hole charges are shielded inside the semiconductor by the crystal ions. Therefore, the relative dielectric constant of the semiconductor ϵ_{r} needs to be accounted for. The exciton–Bohr radius can then be expressed as

$$a_0 = \frac{4\pi\hbar^2 \epsilon_{\mathrm{r}} \epsilon_0}{e^2 m_{\mathrm{red,eff}}}, \tag{2.1.4}$$

where ϵ_0 is the dielectric constant of the vacuum and e is the elementary charge.[32,38] In NCs, the movement of the exciton is confined, and the exciton–Bohr radius is commonly used to categorize this confinement into three regimes.[39]

In the weak confinement $a_0 \ll R_{\mathrm{NC}}$, the Coulomb binding energy is larger than the confinement energy. As a consequence of the weak confinement, the center of mass of the exciton is affected by the confinement, while the radius of the exciton stays nearly the same. In the intermediate confinement regime, the radius of the NC lies in between the electron–Bohr radius a_0^{e} and the hole–Bohr radius a_0^{e}: $a_0^{\mathrm{e}} > R_{\mathrm{NC}} > a_0^{\mathrm{h}}$. In this case, the Coulomb and confinement energies are similar. Hence, only the electron states are effectively quantized. In the third regime, the strong confinement $a_0^{\mathrm{e/h}} \gg R_{\mathrm{NC}}$, the

Coulomb energy is lower than the confinement energy. Consequently, the states of both charge carriers are quantized.[37] For comparison, the exciton-bohr radii of the materials used in this work are: a_0(ZnSe) = 4.5 nm, a_0(CdSe) =5.4 nm, and a_0(CdS) = 2.7 nm.[39] In addition to the size of the NCs, their shape also influences the confinement effect. Figure 2.3 illustrates the different degrees of confinement and the corresponding density of states (DOS). The bulk case (3D material) is shown in Figure 2.3a, in which no confinement is present. As the degree of confinement increases, in Figure 2.3b–d, the DOS gets more discretized. Examples of nanostructures for these different dimensionalities are: nanoplatelets (2D), nanowires/nanorods (1D), and quantum dots (0D).[32,40]

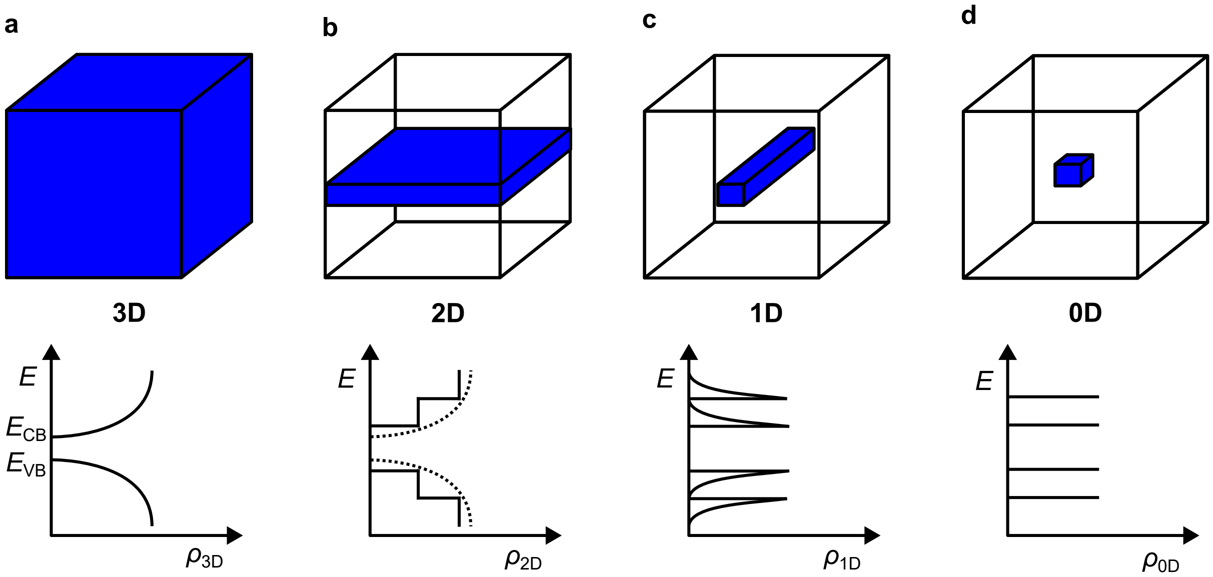

Figure 2.3.: Comparison of semiconductors of different dimensionality with their respective density of states ρ ranging from (a–d) 3D to 0D. Adapted from literature.[32,40]

For a complete description of the localization and energies of the exciton states in a NC, the corresponding Schrödinger equation has to be solved. The time-independent Schrödinger equation of an exciton within the effective-mass approximation is

$$\left(-\frac{\hbar^2}{2m_{\mathrm{e,eff}}}\nabla_{\mathrm{e}}^2-\frac{\hbar^2}{2m_{\mathrm{h,eff}}}\nabla_{\mathrm{h}}^2-\frac{e^2}{4\pi\epsilon_{\mathrm{r}}\epsilon_0|\mathbf{r}_{\mathrm{e}}-\mathbf{r}_{\mathrm{h}}|}\right)\Psi=E\Psi, \qquad (2.1.5)$$

in which $\mathbf{r}_{\mathrm{e}}$ and $\mathbf{r}_{\mathrm{h}}$ are the electron and hole coordinates , Ψ the exciton wave function and E the energy of the exciton. The first two terms in the brackets are the operators for the kinetic energy of the electron and hole, respectively, while the third term is the operator for the Coulomb binding energy of the electron and hole.[37]

Solving the Schrödinger equation for complex systems requires a lot of computational resources, making approximations, numerical calculations, and, nowadays, also machine learning essential. Even with approximations, the computation time typically scales with the number of electrons in the system to the power of 3–7.[41]

In 1986, Louis Brus formulated a simpler approach by constructing a semi-empirical relationship of the exciton energy E_{NC} and the radius R_{NC} of a spherical NC:

$$E_{\mathrm{NC}} \simeq E_{\mathrm{g}} + \frac{\hbar^2 \pi^2}{2R_{\mathrm{NC}}^2}\left(\frac{1}{m_{\mathrm{e,eff}}} + \frac{1}{m_{\mathrm{h,eff}}}\right) - \frac{1.8e^2}{4\pi\epsilon_0\epsilon_{\mathrm{r}}R_{\mathrm{NC}}}. \tag{2.1.6}$$

In this equation, E_{g} is the bulk band gap of the semiconductor, and 1.8 is a factor to account for the average distance between the electron and the hole in a spherical geometry. From this equation, it becomes apparent that the confinement energy in spherical NCs scales with $1/R_{\mathrm{NC}}^2$, while the Coulomb energy scales with $1/R_{\mathrm{NC}}$.[42]

2.1.2. Optical Properties of Nanocrystals

Blinking

One of the primary interests in NCs lies in their optical properties. Figure 2.4 shows the PL intensity of an individual NC over time. The PL intensity fluctuates over time and turns on and off. This phenomenon was first observed for individual NCs in 1996 and is called blinking.[43] A consequence of the blinking is that the amount of excitons that are generated in a NC is smaller than the number of photons that are emitted. This ratio is also known as the quantum yield.[32] The commonly used model for the explanation of blinking is illustrated in Figure 2.5. Starting point of the model is an uncharged NC in an excited state, in which an exciton is present (Figure 2.5a). If the exciton recombines, a photon is emitted. Hence, the NC is in an emissive state called the on-state. The neutral NC can get charged locally if either the electron or the hole gets captured into a so-called trap state. Multiple pathways for the trapping of a charge carrier are possible, and the two of them are depicted in Figure 2.5b and c. In the first pathway (Figure 2.5b)

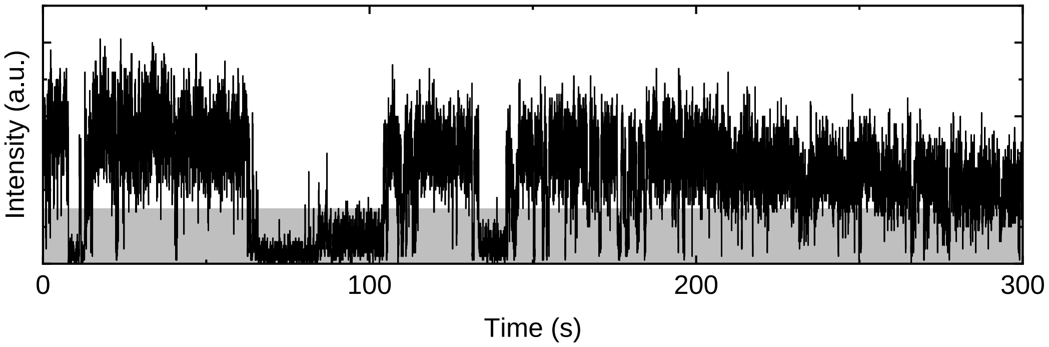

Figure 2.4.: Time trace of the PL measured from a single NC with an integration time of 20 ms. The off states are shaded in grey.

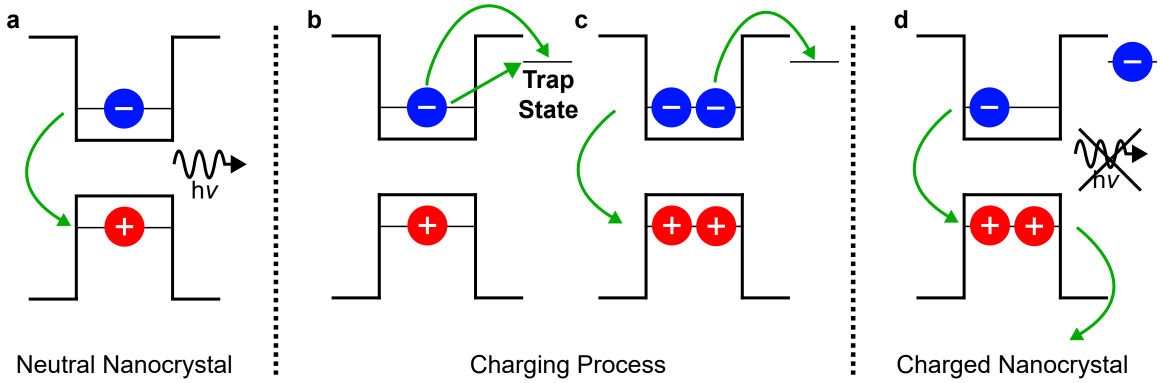

Figure 2.5.: Schematic overview of the steps leading to the blinking process starting from (a) a neutral NC that emits light. After charging due to (b) direct tunneling or (c) thermo-ejection the NC becomes (d) charged. In this charged state the dominant recombination process is the non-radiative Auger recombination, thus no more light is emitted. Adapted from Efros.[44]

only one exciton is present. Here, one of the charge carriers could tunnel directly into a trap state or could get thermally ejected into a trap state. Another possibility is Auger auto-ionization, shown in Figure 2.5c, that can take place when a biexciton is formed. In this case, the recombination of one exciton transfers the energy onto one charge carrier of the other exciton, thereby supplying sufficient energy for ejecting the charge carrier into a trap state. In Figure 2.5d, the NC is in a charged state, also called off-state. This is a consequence of the now possible Auger recombination, in which the recombination energy of the exciton is transferred to the third charge carrier in the form of kinetic energy. This process significantly reduces PL as it is an order of magnitude faster and usually takes place on a time scale of 10–100 ps.[44] The off-states of NCs can span a wide range of time scales from 100 µs to multiple hours.[44,45] In order to accommodate for the different time scales, different modifications have been proposed for the aforementioned model that include, for example, the introduction of multiple different trap sites[46] or fluctuating energy barriers[47].[48]

In order to fully understand the blinking process, the nature of trap states has to be understood. Trap states are energy states that originate from vacancies in the crystal lattice, impurity atoms, unsaturated bonds on the NC surface, ligands, or the surrounding environment.[44,49–51] For example, Veamatahau et al. have used PL spectroscopy and X-ray photoelectron spectroscopy to show that sulfur vacancies on the surface of CdS quantum dots act as deep trap states for electrons.[52] Another important factor for the optical properties of NC is their interaction with air. Mueller et al. found that for CdSe/ZnS NCs, oxygen can neutralize charged NCs as an oxidation agent by taking up a single electron, leading to an average PL increase by a factor of 2. If water is also present, it broadens the LUMOs of the oxygen, thereby facilitating the oxidation process. This, in turn, means that the PL emission intensity of NCs in vacuum is decreased, which is the case for all low-temperature measurements.[53]

Depending on the nature of the trap states, two different blinking types have been identified by Galland et al. by investigation of single CdSe/CdS NCs inside a three-electrode electrochemical cell. They named the blinking due to charging and discharging, as described before in Figure 2.5, as A-type blinking. In A-type blinking, the PL intensity increases and decreases together with the fluorescence lifetime. Furthermore, in A-type blinking, the NC is either in a highly emissive on-state or a non-emissive off-state, and no medium-intensity grey-states occur. The second blinking type they found was B-type blinking, which originates from the charge fluctuation of electron trap states that capture hot electrons before their relaxation. As a result, in B-type blinking, the PL intensity changes more continuously and in smaller steps, enabling also emissive grey-states, as opposed to A-type blinking. Additionally, the fluorescence lifetime changes are much smaller in B-type blinking.[54] Further investigations by Yuan et al. revealed that multiple blinking types can occur in the same NC.[55]

Decay Dynamics

A better understanding of the exciton relaxation pathways can be gained by time-resolved measurements. For this, decay curves of the PL can be measured by performing time-correlated single photon counting (TCSPC). In TCSPC, the semiconductor is excited with pulsed laser light, and the delay time between each laser pulse generation and detection of a single emitted photon is recorded. The decay curve can then be constructed as a histogram.[39]

When only a single recombination pathway for the exciton exists, the temporal decay of its population N can be described by a single exponential function

$$N(t) = N(0)\mathrm{e}^{-t/\tau_{\mathrm{fl}}}, \tag{2.1.7}$$

with the initial population N_0 and fluorescence lifetime τ_{fl}. The population in this case refers to the ensemble of the repeatedly probed excited state of a single NC. In NCs, multiple recombination pathways of different excited states are often present, and in these cases, multi-exponential functions

$$N(t) = \sum_i N(0)\mathrm{e}^{-t/\tau_{\mathrm{fl},i}} \tag{2.1.8}$$

are used.[32,34] For an easier comparison of different systems the intensity-averaged lifetime

$$\tau_{\mathrm{ave}} = \frac{\sum_i N_i \tau_{\mathrm{fl},i}^2}{\sum_i N_i \tau_{\mathrm{fl},i}} \tag{2.1.9}$$

can be derived.[56]

As described above, both radiative and non-radiative recombination pathways exist, thus the fluorescence lifetime τ_{fl} that is measured in experiments includes both the radiative decay rate k_{rad} and non-radiative decay rate k_{nrad}

$$\tau_{\mathrm{fl}} = \frac{1}{k_{\mathrm{fl}}} = \frac{1}{k_{\mathrm{rad}}} + \frac{1}{k_{\mathrm{nrad}}}. \tag{2.1.10}$$

The radiative and non-radiative decay rates are connected to the quantum yield (QY) by following relation:

$$\mathrm{QY} = \frac{k_{\mathrm{rad}}}{k_{\mathrm{rad}} + k_{\mathrm{nrad}}}. \tag{2.1.11}$$

This means that the presence of non-radiative decay pathways in addition to radiative ones, decreases the fluorescence lifetime and the QY.[44]

The radiative lifetime of the exciton depends on the overlap of the electron and hole wave functions. This overlap, in turn, is determined by the shape and composition of the semiconductor NCs. In particular, the degree of overlap in heterostructured semiconductor NCs can be controlled by choosing different materials that form different band alignments. The most common types of band alignment are shown in Figure 2.6. In the case of a type-I band alignment (Figure 2.6a), both the electron and hole have their lowest potential energy in the same material. Hence, the electron and hole wave functions have a large overlap, and the exciton has a short lifetime. This band alignment can be used in a core/shell NC to isolate the exciton from trap states on the surface. A quasi-type-II band alignment (Figure 2.6b) is present when the offset in one of the energy bands is relatively small. As a result of this small energy barrier difference, one of the charge carriers has the potential to delocalize (in this case, the electron) while the other charge carrier cannot move as freely. Thus, the wave function overlap is lower than in the type-I case. In the type-II band alignment case (Figure 2.6c), the electron and hole have their lowest potential energy in different materials, thus their wave function overlap is small, and this results in a long lifetime.[32,36] This makes the type-II band alignment particularly interesting for catalytic applications, in which the exciton recombination is undesirable.[57,58]

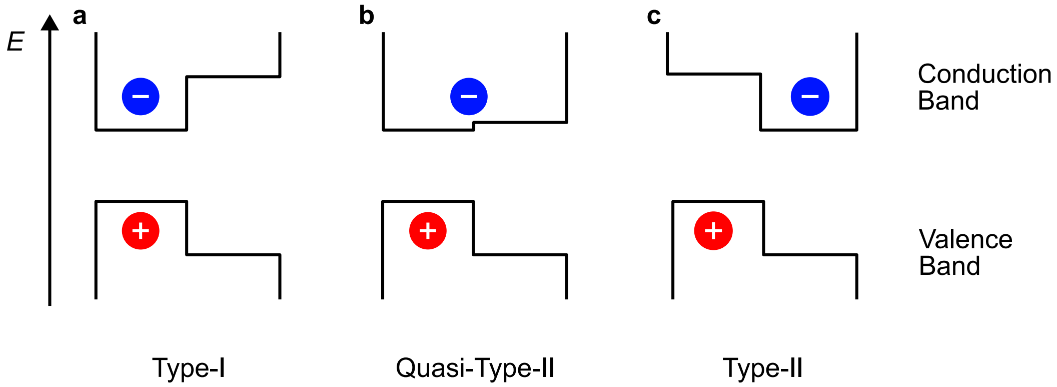

Figure 2.6.: Different band alignments of semiconductor heterostructures with illustrations of the electron and hole localizations. Adapted from literature.[32]

2.1.3. Influence of Low Temperatures on Optical Properties

Emission Energy, Linewidth and Lifetime

In semiconductors, the band gap energy E_g usually shifts to lower energies with increasing temperature T. This is a consequence of two combined effects: the thermal expansion of the crystal lattice on one hand, and the changes of the distribution of lattice vibrations on the other hand.[33] At low temperatures, the band gap changes quadratically and linearly at higher temperatures. This behavior is commonly described with the empirical Varshni relation

$$E_\mathrm{g} = E_0 - \frac{\alpha_\mathrm{T} T^2}{T + \beta_\mathrm{T}}. \tag{2.1.12}$$

In this equation, E_0 is the band gap energy at $T = 0$ K, α_T a fitting parameter, and β_T a second fit parameter related to the Debye temperature.[37,59] Deviations of the Varshni relation in NCs have been reported by Liu et al. for CdSe/CdS/ZnS quantum dots. They attributed the anomalous red shift at low temperatures to the temperature-dependent population of the exciton fine structure levels and the temperature-dependent exciton–phonon coupling.[60] (Both the exciton–phonon coupling and exciton fine structure will be explained later on.)

A temperature increase of the NCs is furthermore accompanied by an increased full width at half maximum (FWHM) Γ of the PL intensity spectrum that is commonly described by the expression

$$\Gamma(T) = \Gamma_\mathrm{inh} + \sigma T + \Gamma_\mathrm{LO}(\mathrm{e}^{E_\mathrm{LO}/k_\mathrm{B}T} - 1)^{-1}. \tag{2.1.13}$$

In this equation, Γ_inh is the inhomogeneous FWHM of the NCs, σ is the exciton–acoustic-phonon coupling coefficient, Γ_LO is the exciton–longitudinal-optical-phonon coupling coefficient, E_LO is the energy of the longitudinal-optical-phonon, and k_B is the Boltzmann constant.[61–63] Al Salman et al. found that for CdSe nanorods the FWHM Γ can also be well described with the equation for exciton scattering by ionized impurities:

$$\Gamma(T) = \Gamma_{\text{inh}} + \sigma T + (e^{E_{\text{LO}}/k_{\text{b}}T} - 1)^{-1} + \Gamma_{\text{ion}} e^{-E_{\text{A}}/k_{\text{B}}T}. \tag{2.1.14}$$

In this equation, E_{A} is presumed to be the energy of surface charge formation, and Γ_{ion} represents the linewidth due to ion-impurity scattering.[63–65] However, Wen et al. found that this additional term is not suitable for their spectroscopy data on CdSe/CdS DRs.[65]

A further optical property that is also temperature dependent is the fluorescence lifetime, which can be explained by taking a look at the energy levels of excitons. In addition to spin–orbit coupling, the exciton energy levels depend on the NC shape, crystal lattice, and exchange interaction of electron and hole. The exchange interaction is proportional to the wave function overlap of the electron and hole, which is increased in NCs compared to the bulk crystals.[67–69] An overview of the band-edge states in spherical CdSe NCs is illustrated in Figure 2.7 for the wurtzite and zinc blende crystal structures. The band-edge states from the LUMOs and HOMOs form the single particle states of the electron e_0 and hole h_0 / h_1, respectively. Due to the lower symmetry of the wurtzite crystal structure, the single particle hole states split up, which is also referred to as crystal-field splitting. The e-h states can be constructed from the single particle states with a product ansatz. This leads to two 4-fold degenerate states in the wurtzite crystal lattice and a single 8-fold degenerate state in the zinc blende crystal lattice. The so-called exciton fine structure emerges as the electron-hole exchange interaction further splits the e-h states. Within the fine structure, the corresponding states are named based on their total angular momentum J, and whether their relative energy position is upper (U) or lower (L).[66] The exciton states are categorized based on whether the exciton recombination from the respective state is optically allowed or forbidden by selection rules, which is indicated in

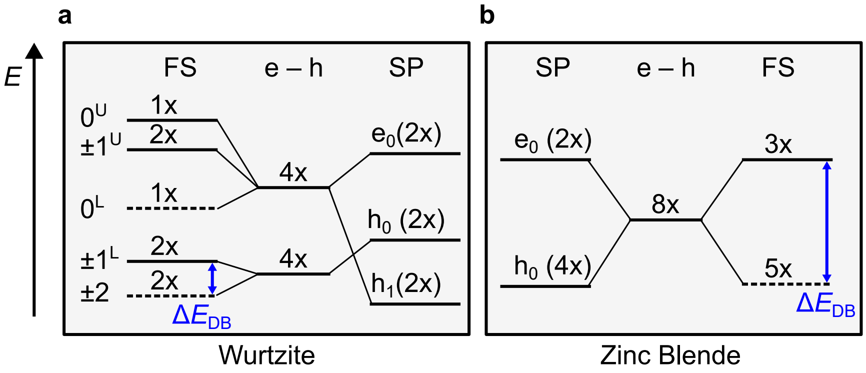

Figure 2.7.: Schematic depiction of the fine-structure (FS), and single particle states (SP) in (a) a wurtzite and (b) zinc blende crystal lattice. The solid lines indicate the bright states and dashed lines the dark states. The scheme was adapted from Bui et al.[66]

Figure 2.7 by solid lines for the allowed and dashed lines for the forbidden transitions. If the transition of the state is allowed, it is called a bright state, and vice versa. If the transition is forbidden, the state is called a dark state. The most important selection rule is that the transition must be dipole-allowed $\Delta J = \pm 1$.[39,66,70] Bui et al. have shown that for an accurate description of the exciton fine structure, atomistic calculations are needed, instead of simpler calculations within the effective-mass approximation. For example, they used atomic effective pseudopotentials together with screened configuration interaction in their work.[66]

Focussing now on the emissive properties of the NC, the situation is as follows: after its formation, the exciton is usually in a higher energy state and first relaxes to a band-edge state, before its recombination can take place. This intraband relaxation takes place on the picosecond scale, which is much faster than the radiative interband relaxation. Hence, the lowest exciton states in the fine structure are particularly important.[69] The temperature or magnetic-field-dependent emission properties are usually modeled with a three-state model as shown in Figure 2.8.[13,67,70,71] These three states are the semiconductor ground state $|G\rangle$ (no exciton), the lowest excitonic bright state $|A\rangle$ and lowest excitonic dark state $|F\rangle$, with the respective recombination rates of the bright state k_A and dark state k_F. The non-radiative transition from the bright to the dark state is facilitated by the zero-temperature spin-flip rate γ_0. This process is reversible because of thermal mixing via acoustic- phonon coupling defined by the relaxation rate γ_th. Additionally, this thermal relaxation rate is related to the zero-temperature spin-flip rate $\gamma_\mathrm{th} = \gamma_0 N_\mathrm{B}$, over the Bose-Einstein phonon number $N_\mathrm{B} = 1/[\exp(\Delta E_\mathrm{DB}/k_\mathrm{B}T) - 1]$. A further important variable is the energy difference between the dark and bright states, called the dark-bright splitting energy ΔE_DB, which is also highlighted in blue in Figure 2.7. The dark-bright splitting energy originates from the exciton fine structure and thus depends on the crystal structure and shape of the NCs, as explained above.[13,70]

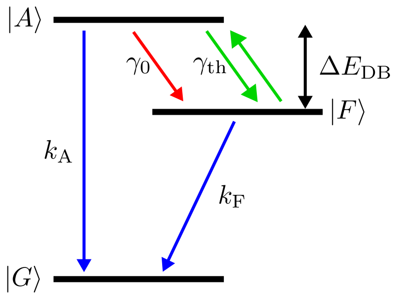

Figure 2.8.: Three-state model for the decay dynamics of the exciton. Shown are the zero exciton ground state $|G>$, the lowest exciton bright state $|A>$ and dark state $|F>$, the relaxation rate of the bright and dark states k_A / k_F, the zero-temperature spin-flip rate γ_0 and thermalization rate γ_th. Adapted from Labeau et al.[70]

In order to describe the experimentally observed decay behavior all transition rates and the dark-bright splitting energy have to be combined. Thereby, the temperature-dependent radiative decay rate of the short and long component can be derived[13,72]

$$k_{\mathrm{S,L}} = \frac{1}{2}\left\{k_{\mathrm{A}} + k_{\mathrm{F}} + \gamma_0 \coth\left(\frac{\Delta E_{\mathrm{DB}}}{2k_{\mathrm{B}}T}\right) \pm \sqrt{(k_{\mathrm{A}} - k_{\mathrm{F}} + \gamma_0)^2 + \gamma_0^2 \sinh^{-2}\left(\frac{\Delta E_{\mathrm{DB}}}{2k_{\mathrm{B}}T}\right)}\right\}. \tag{2.1.15}$$

Here, k_{S} is the decay rate of the short component and k_{L} of the long component, which are related to the "+" and "−" sign before the root, respectively. In time-resolved PL spectroscopy measurements, the dark state acts as a slow and the bright state as a fast recombination channel. At low temperatures, when the thermal mixing rate is slow, the emission follows a biexponential decay with the respective short and long components from Equation 2.1.15. As a result, the average fluorescence lifetime increases compared to room temperature. While at higher temperatures, the repopulation from the dark to the bright state is high, and the decay appears as "monoexponential". This change from bi- to monoexponential decay, for example, is visible for CdSe/ZnS NCs (r = 4 nm) at around 7 K.[13,69,72]

Spectral Diffusion

In 1996, Blanton et al.[73] and Empedocles et al.[74] independently discovered spectral diffusion for single NCs at low temperatures for the first time. Spectral diffusion describes the temporal change of the emission energy. At room temperature, the spectral diffusion first and foremost broadens the emission linewidth. As spectral diffusion only takes place at the <100 meV scale, its investigation needs to be carried out at single NCs at low temperature and with short integration times.[74] Figure 2.9 shows an example for spectral diffusion of the PL from a single DR at $T \approx 10$ K. In this 2D color plot, each vertical line corresponds to a spectrum. Two types of changes in the emission energy can be seen: on one hand, distinct jumps and on the other hand, a slower, more continuous energy shifting.

It is assumed that spectral diffusion is a result of the Stark effect from local charges. These charges could arise from photoionization or trapping of charge carriers in the surrounding.[74] Empedocles et al. found that the magnitude of spectral diffusion depends on excitation power. Furthermore, they observed that the emission linewidth increases the further the excitation energy is away from the band gap. They attributed the linewidth broadening to excess energy because the variation of the excitation energy and integration time had the same effect on the linewidth. As a mechanism, they proposed that phonon emission during the exciton-relaxation process couples to the local environment,

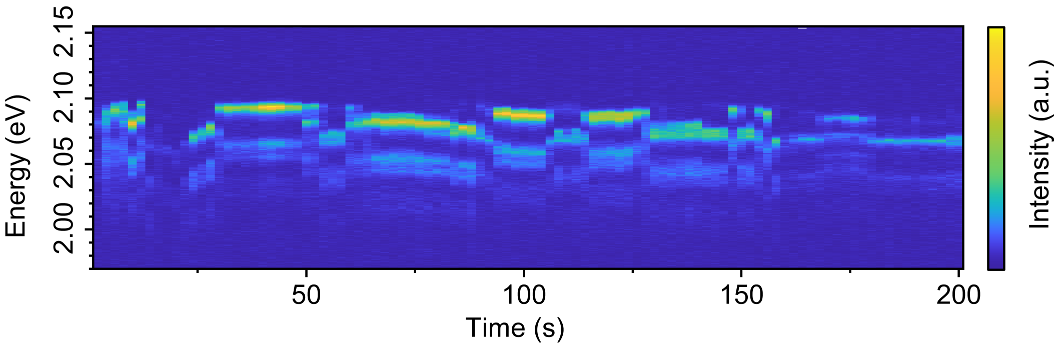

Figure 2.9.: Spectral time trace of the PL measured from a single NC at $T \approx 10$ K with an integration time of 2 s per spectrum.

thereby facilitating the movement of trapped charge carriers.[75] In support of the connection of spectral diffusion to photoionization, Neuhauser et al. found that sometimes spectral jumps are preceded by a blinking event.[76] It should also be noted that the charges responsible for spectral diffusion are commonly described as surface charges.[77–79] The nature of these surface charges is still not fully understood. For example, Lohmann et al. proposed that attachment and detachment of ligands forms surface charges.[79]. Vozznyy proposed, based on ab initio calculations, that the mobility of the ligands might play an important role in the movement of the surface charges.[80]

A deeper understanding of spectral diffusion is necessary, since it could play a key role in the degradation of the optical properties of NCs, in addition to broadening the emission linewidth.[74,81] A better understanding can be obtained by combining experimental results with theoretical modeling. In the modeling of surface charges, it has been proven suitable to approximate the surface charges as point charges that are placed on the NC surface.[77,79,82]

2.1.4. Exciton–Phonon Coupling

Mechanisms of Exciton–Phonon Coupling

Similar to electronic states, vibrational states are also quantized. The corresponding quantum of the vibration energy is known as a phonon. Within the harmonic approximation, their energy

$$E = \hbar\omega(v + \frac{1}{2}) \tag{2.1.16}$$

depends on the energy state $v = 0, 1, ...$, and their fundamental frequency ω.[33,35,38] Hitherto, for electronic transitions, the vibrational states were neglected, but during an electronic transition, the vibrational state can also change. The corresponding interaction of excitons and phonons is called exciton–phonon coupling. Exciton–phonon coupling can occur both in the absorption and emission process of a photon. The emission process is illustrated in Figure 2.10. After excitation of a semiconductor and formation of an exciton, the exciton relaxes to the lowest vibronic state within the excited electronic state. The bond order is reduced in this excited electronic state. Hence, the equilibrium distance is increased to larger values along the vibrational coordinate Q. The time scale of the electron transition is much faster compared to the movement of the atom cores, and because of this, the transitions can be approximated with vertical lines, also known as the Franck-Condon principle. If no exciton–phonon coupling occurs, all energy is emitted as a photon ($0' \rightarrow 0$), the resulting PL peak is called the zero-phonon line. Instead, if exciton–phonon coupling takes place ($0' \rightarrow 1$ & $0' \rightarrow 2$) the photon energy is reduced by the respective energy of the phonon, resulting in the so-called phonon replica. The energy steps of the phonon replica of different orders can then be approximated by Equation 2.1.16.[38,83,84] The magnitude of exciton–phonon coupling is commonly described using the Huang–Rhys (HR) factor

$$S = \Delta^2/2, \tag{2.1.17}$$

which depends on the displacement Δ of the energy minima in the potential energies between the ground and excited electronic states. In experiments, the HR factor can be

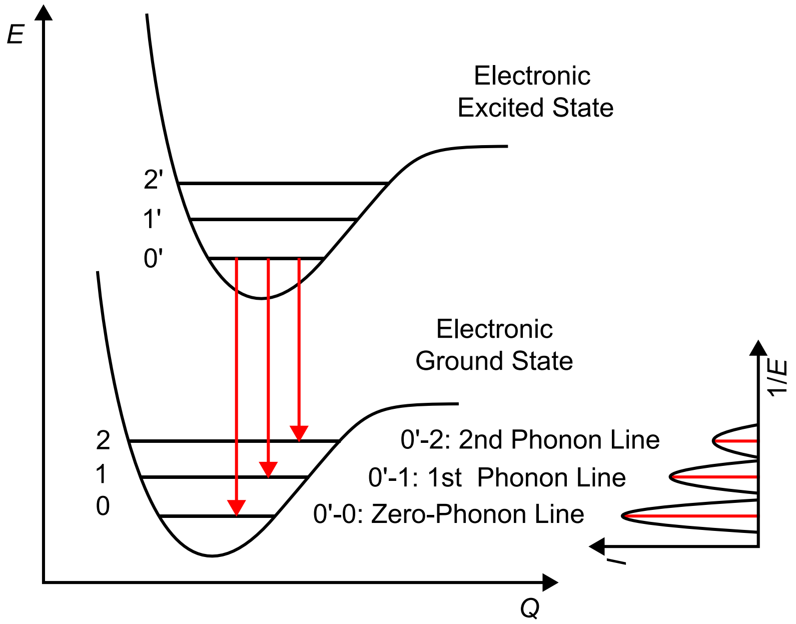

Figure 2.10.: Schematic depiction of exciton–phonon coupling. The curves represent the potential energies along the vibrational coordinate Q, while the horizontal lines are the respective vibrational states. The vertical red arrows indicate the emission of photons, following the Franck-Condon principle. These transitions correspond to the peaks in the PL spectrum on the bottom right. Adapted from literature.[38,83]

derived from the intensity progression of the phonon replica. In first approximation, the intensities I within a spectrum can be defined as a sum of Dirac delta δ functions

$$I(\hbar\omega) \propto \sum_{n=0}^{\infty} |\langle n, Q_0'|0, Q_0|\rangle|^2 \delta(\hbar\omega - \hbar\omega_0 - n\hbar\Omega). \tag{2.1.18}$$

In this equation, Q_0' and Q_0 are the equilibrium coordinates of the vibration in the electronic excited and ground state, respectively, ω_0 and Ω are the frequencies of the zero-phonon line and excited state, respectively. A Dirac delta function equals one at a single point only and zero everywhere else. The intensities of the peaks depend on the respective overlap integrals $|\langle n, Q_0'|0, Q_0|\rangle|^2$, also called Franck-Condon factors. They are connected to the HR factor S as follows:[19,83]

$$|\langle n, Q_0'|0, Q_0|\rangle|^2 = e^{-\mathrm{S}} \frac{S^n}{n!}. \tag{2.1.19}$$

In PL spectroscopy and fluorescence line narrowing, the HR factor is derived from the intensity ratio of the first-order phonon line to the zero-phonon line (ZPL),[85,86], whereas in Raman spectroscopy the intensity ratio of the second-order to the first-order phonon is used.[87]

In general, phonon modes can be grouped into four different types that are illustrated in Figure 2.11. In the case that the neighboring atoms move out of phase, the mode is called optical (Figure 2.11a,b). If the atoms also oscillate parallel to the direction of the wave propagation, the phonon mode is a longitudinal optical (LO) mode, whereas for orthogonal oscillation, it is a transversal optical (TO) mode. When neighboring atoms oscillate in phase, the phonon modes are called acoustic (Figure 2.11c,d). Accordingly, if the atoms then also oscillate parallel or orthogonal to the direction of the wave propagation, the modes are longitudinal acoustic (LA) or transversal acoustic (TA) phonon modes, respectively.[33]

In principle, exciton–phonon coupling can arise from three different mechanisms.[11] The first possible mechanism is Fröhlich interaction, which originates from the Coulomb interaction between the charge-carrier density of the exciton and the polarization of the crystal lattice. Hence, it is primarily important in polar semiconductors. The polarization of the crystal lattice is, in turn, determined by an optical phonon.[39,86,88]

A suitable starting point for the physical description of the charge-carrier–lattice interaction is a single charge carrier, e.g. an electron, within a polar crystal lattice, as illustrated in Figure 2.12. In this crystal lattice, the cations get pulled towards the electron, while the anions get pushed away. The deflection of the cation and anion sub-lattices are out-of-phase, thereby the Fröhlich interaction favors optical phonon modes.[11,37,39] To-

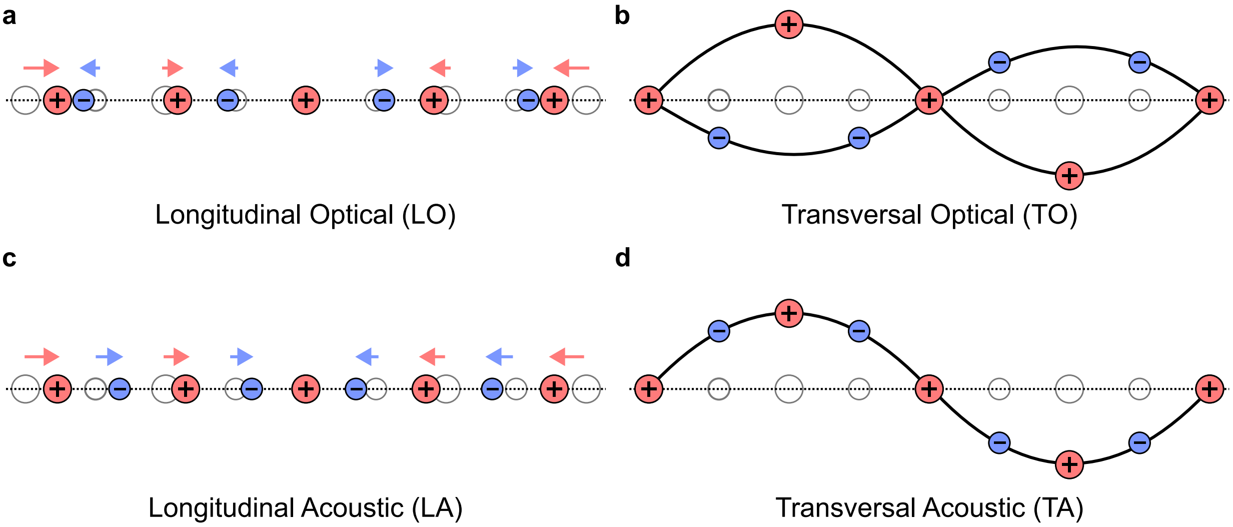
a
b
c
d
Longitudinal Optical (LO)
Transversal Optical (TO)
Longitudinal Acoustic (LA)
Transversal Acoustic (TA)

Figure 2.11.: Overview of the four different phonon types (a–d). Each blue and red circle represents an anion and cation, respectively. The grey circles indicate the atom positions in the absence of the phonon, while the arrows indicate the magnitude and direction of the movement. Adapted from Gross and Kittel.[33,35]

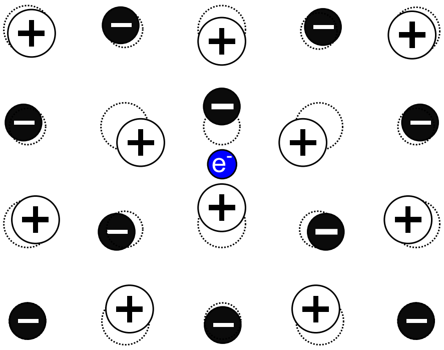

Figure 2.12.: Schematic illustration of a polaron formed by an electron in an ionic crystal. Adapted from literature.[35,89]

gether, the charge carrier and its polarization cloud are called a polaron.[37] Polarons can be categorized into small (Holstein) and large (Fröhlich) polarons. The former are localized on single ions, while the latter are larger than the lattice parameter and represent a continuum.[35,89] The strength of the long-range phonon coupling is commonly evaluated with the dimensionless Fröhlich coupling constant α, also known as polaron coupling constant:

$$\alpha_{\mathrm{e,h}} = \frac{e^2}{8\pi\epsilon_0\hbar\omega_{\mathrm{LO}}r_{\mathrm{p}}^{\mathrm{e/h}}}\left(\frac{1}{\epsilon_\infty} - \frac{1}{\epsilon_{\mathrm{s}}}\right). \tag{2.1.20}$$

In this equation ω_{LO} is the frequency of the LO phonon mode, ϵ_∞ and ϵ_0 are the high- and low frequency dielectric constants, and $r_{\mathrm{p}}^{\mathrm{e/h}}$ is the weak-coupling polaron radius of the electron or hole

$$r_{\mathrm{p}}^{\mathrm{e/h}} = \sqrt{\frac{\hbar}{2m_{\mathrm{e/h}}\omega_{\mathrm{LO}}}}. \tag{2.1.21}$$

This polaron radius describes how far the charge carrier diffuses during an atomic vibration, and is typically between 1–1.5 nm. In Equation 2.1.20 the first term describes the potential energy of the polaron, and the difference in the high-frequency (ϵ_∞) and static dielectric constant (ϵ_{s}) accounts for the ionic polarization.[37,39,89,90]

The second mechanism for exciton–phonon coupling is deformation-potential interaction. This interaction originates from the mutual interplay of the deformation of the crystal lattice and the energy bands. Crystal-lattice deformation has two related pathways to arise. The first pathway involves changes in bond order that in turn vary the bond lengths and angles. The second pathway is the reversed case of the first pathway, as the deformation originates from a phonon deforming the crystal lattice, thereby changing and shifting the energy bands. deformation-potential interaction is present in all semiconductors with a similar intensity, but is particularly important for non-polar crystals, since Fröhlich coupling is absent in them. Thus, it is primarily responsible for coupling to acoustic phonons.[11,39,91–93]

Another, third mechanism that facilitates exciton–phonon coupling is piezoelectric interaction, which is analogous to the piezoelectric effect, in which the mechanical deformation of a crystal lattice creates a macroscopic polarization. This piezoelectric effect can occur in all crystals that do not possess an inversion symmetry. Furthermore, the piezoelectric interaction is primarily relevant for acoustic phonon modes and is stronger than the deformation-potential interaction.[11,39]

Calculation of Exciton–Phonon Coupling

A seminal work on the calculation of exciton–phonon coupling in NCs was carried out by Nomura and Kobayashi. They were one of the first to calculate exciton–phonon coupling. According to their work, the Huang–Rhys factor can be expressed as

$$S = \frac{f_0^2}{(2\pi)^3 E_{\mathrm{LO}}^2} \int \frac{1}{|\mathbf{k}|^2} |\mathcal{F}(|\Psi_{\mathrm{e}}|^2 - |\Psi_{\mathrm{h}}|^2)|^2 \mathrm{d}^3\mathbf{k}. \tag{2.1.22}$$

Here, Ψ_{e} and Ψ_{h} are the electron and hole wave functions, $\mathcal{F}$ denotes the Fourier transform, and

$$f_0 = \sqrt{2\pi e^2 E_{\mathrm{LO}} \left(\frac{1}{\epsilon_\infty} - \frac{1}{\epsilon_{\mathrm{s}}}\right)} \tag{2.1.23}$$

is the Fröhlich constant. From Equation 2.1.22, one can see that the Huang–Rhys factor and thus the coupling intensity is proportional to the squared absolute difference of the electron and hole wave functions.[21,94,95]

Accurate atomistic calculations of excitons and their phonon coupling are a computationally resource-intensive task. These calculations are still actively developed in recent years. For example, by using unconstrained and constrained density functional theory together with pseudopotentials, Han and Bester reproduced the phonon replica of CdSe dots ($r = 1.16$ nm) to a high degree.[96] Reproduction of phonon replicas in heterostructures is still challenging, as shown by Lin et al. in their recent work. They performed atomistic calculations with pseudopotentials for CdSe dots ($r = 1.5$ nm) coated with 3 monolayers (MLs) CdS and modeled the intensity of the CdSe phonon accurately, but the CdS phonon peak was missing, although it was measured in experiments.[15]

A less accurate, but less resource-intensive approach has been reported by Lin et al. They calculated the exciton within the effective-mass approximation and derived the electric field of the exciton. This electric field was then introduced into force field calculations to obtain the phonon-coupling modes and intensities.[93,97]

Studies of Exciton–Phonon Coupling in Nanocrystals

In NCs, the charge carriers are confined into a small space. Thus, they overlap more with each other. Based on Equation 2.1.22, a weak exciton–LO-phonon coupling would be expected. Alivisatos et al. for example, measured a 20 times weaker coupling strength compared to the bulk case.[98] Direct comparisons between experiments and calculations have shown that the experimental coupling is much stronger than predicted. This observation could be related to the fact that the coupling intensities in NCs strongly vary with the methods used for their investigation.[14] One example of this is that Krauss et al. have reported an experimental coupling intensity of four orders of magnitude larger than predicted in the case of PbS NCs ($r = 1.5$ nm).[22] One possible explanation for these discrepancies could be that point defects and trapped charge carriers affect the coupling and thereby alter the intrinsic coupling.[12,21,22,99] In order to directly measure the intrinsic coupling, Krauss et al. applied spectroscopy on the femtosecond scale, which allowed the investigation of NCs prior to charge trapping.[99] These experiments confirmed very low coupling intensities with $S = 0.01$[23], compared to Raman spectroscopy with values of $S = 0.7$.[99] Cui et al. have reinforced the role of charge carrier trapping. By varying the shell material and thickness, and thus the probability of trapping, the linewidth broadening, originating from exciton–phonon coupling, was reduced.[12]

Regarding the size dependence of the coupling intensity, Nomura et al. predicted, based on their calculations, that the HR factor for spherical CdSe NCs has a minimum around

$r = 7$ nm, and increases towards smaller and larger radii.[21] The increase for smaller radii is in agreement with newer calculations by Han and Bester[100] and experimental reports.[67,95] However, a negligible size dependence is sometimes reported for experimental measurements.[97,101] These variations in the size dependence could, for example, originate from the influence of surface charges. The confinement in NCs also impacts the energy of LO phonon modes, and results in small red shifts on a scale below 1 meV.[102–104] This red shift is a consequence of the negative LO-phonon dispersion relation away from $\mathbf{k} = 0$.[105]

In order to investigate the state dependence of the exciton–phonon coupling Sagar et al. performed pump-probe spectroscopy of CdSe quantum dots. They found that the coupling of optical phonons strongly depends on the respective exciton state and that the strength of exciton–phonon decreases as the corresponding exciton state becomes more energetic.[23] Biadala et al. found that the lowest dark state ($J = \pm 2$) in spherical wurtzite CdSe/ZnS dots exhibit a stronger exciton–phonon coupling than the next higher lying bright state ($J = \pm 1^{\mathrm{L}}$).[13] Gronenveld et al. have argued that the stronger exciton–phonon coupling lies in the fact that the phonon coupling relaxes the selection rules for the dark-state via symmetry breaking.[19]

Exciton–phonon coupling also plays a role in the relaxation process of hot excitons from higher to lower states. Since the energy steps within the relaxation do not match the phonon energies, the relaxation would have logically been limited by the phonon coupling, known as the phonon bottleneck. Contrasting this, a phonon bottleneck has not been observed experimentally under normal circumstances, as the relaxation takes place in a sub-picosecond timeframe.[106] The repopulation between the dark and bright state is also governed by phonon coupling. For example, a weak phonon coupling leads to a slow repopulation of the bright state at low temperatures. This slow repopulation creates a phonon bottleneck for the exciton recombination, because the exciton lifetime in the dark state is much longer than in the bright state. In case of spherical CdSe/ZnS NCs, Biadala et al. have shown that at low temperatures, an acoustic phonon bottleneck is likely present, because the zero-temperature spin-flip rate γ_0 was only 0.87 ns^{-1}.[13] Likewise, Achtstein et al. found that in CdSe nanoplatelets, an LO phonon bottleneck is present between the s- and p-state exciton states, because the density of states of LO phonons needed for the transition is reduced due to the strong transversal confinement.[107]

2.1.5. Influence of External Electric Fields on Optical Properties

Quantum-Confined Stark Effect

For the application of semiconductor NCs in optoelectronic devices, it is highly interesting to control their properties externally, e.g., turning them on and off. This can be realized by subjecting NCs to an external electric field. In the presence of the electric field, the energy bands get tilted, and hence the exciton gets separated. As a consequence, the absorption and emission energies are lowered. In the case of atomic physics, this effect is known as the Stark effect. Consequently, for NCs it is called quantum-confined Stark effect (QCSE). In addition to the energy shift, the absorption peaks are broadened.[37,83] Figure 2.13 shows the cross section of a calculated exciton in a DR along the rod axis without an electric field and with a parallel field of $F = 476$ kV/cm. This electric field is strong enough to move the electron out of the core and thereby dissociate the exciton. A reduced overlap in the presence of the electric field also means that the average fluorescence lifetime is increased.

The energy shift of the exciton due to the presence of the electric field F can be described by the Stark effect equation

$$\Delta E = \mu F + \frac{1}{2}\alpha F^2, \tag{2.1.24}$$

where μ and α are the projections of the excited-state dipole moment and polarizability in the direction of the external electric field.[108,109] In order to observe a pronounced QCSE, strong electric fields on a scale of 100–500 kV/cm are needed, which are most commonly realized between interdigitated electrodes (IDEs) with gaps in the <20 µm range and applied voltages of several hundred volts.[108,110–112] In 1984, Miller et al.[113] were the first that observed the QCSE in nanostructures, by investigating $\text{Al}_x\text{Ga}_{1-x}\text{As}$ quantum wells.[113] The first measurements of the QCSE in colloidal (CdSe) NCs were carried out by Empedocles et al. in 1997. By application of electric fields of up to 350 kV/cm, they observed energy shifts up to 75 meV and a linewidth broadening up to two orders of magnitude. Furthermore, they found that the excited-state dipole moment parallel to

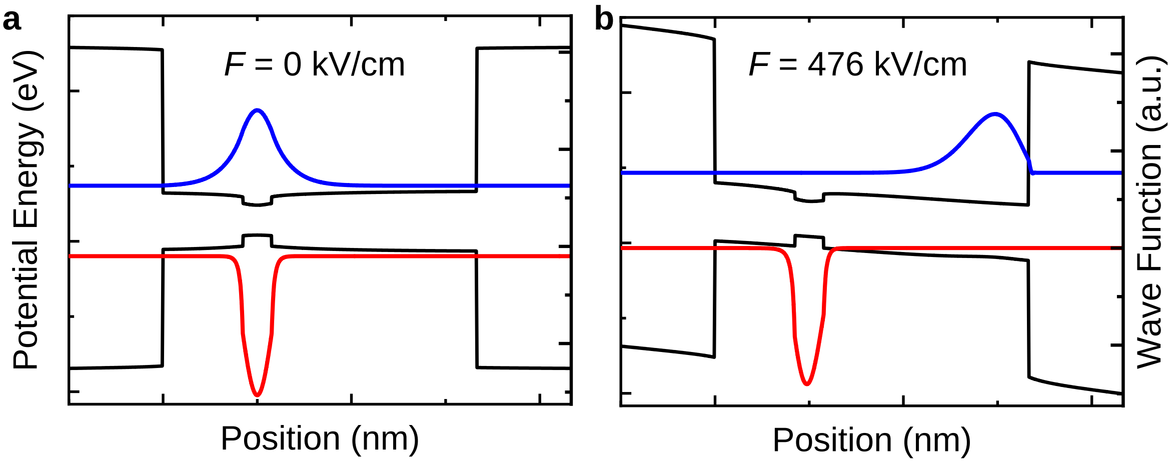

Figure 2.13.: Calculated energy potentials and electron/hole wave functions in a CdSe/CdS DR NCs (a) without and (b) with an external electric field, along the rod axis. The core diameter was 2.3 nm, the rod length 30 nm, and the rod diameter 5.0 nm.

the electric field varied in time for single NC, and was also not uniform among different NCs. This variation was explained by additional local electric fields of 100 kV/cm that were attributed to surface charges, formed by photoionization. They also found that the polarizability scales with the NC volume, and with it the excited state dipole moment, following expectations.[108] Rothenberg et al. have shown that the emission of CdSe quantum rods with a length of 35 nm can be turned on and off by external electric fields. The reason for this observation is that the anisotropy of the system offers enough volume for the electron and hole to be strongly separated in the direction of the electric field, compared to small dots. Moreover, they have shown that the applied electric fields of 350–400 kV/cm can be used to reversibly switch between neutral and charged exciton states, as the electric field assists charge carriers to move in and out of trap states. The energy shift between these two states was between 10–24 meV.[110]

Müller et al. performed measurements on CdSe/CdS DRs, with core radii of 2 nm, at a temperature of 5 K. They observed QCSE energy shifts up to 45 meV for $F = 375$ kV/cm and found that the QCSE increases with the aspect ratio of the DRs.[31] The QCSE has been investigated in several different NC geometries and compositions. Comparison of the QCSE data of different compositions confirmed that type-II DRs have the strongest response towards electric fields.[111,114]

Application of the Quantum-Confined Stark Effect

One of the possible applications for the QCSE is in color switchable light-emitting diodes. For example, Wang et al. presented electroluminescence LEDs based on ZnS/CdS tetrapods, which allow for a color change from red to blue.[115] Ossia et al. have demonstrated a different approach based on two differently sized CdSe dots, each of which is embedded into a CdS shell and fused, so that each nanoparticle includes one of each differently sized CdSe NC. The color-switch range that they achieved was up to 50 nm.[116]

Furthermore, QCSE in NCs is also of great interest for voltage sensing in biological systems.[112,114,117–120] For example, the electric field strengths along the plasma membranes in neurons are around 400 kV/cm, which is high enough for a good response of the QCSE in NCs. Moreover, the synthetically accessible asymmetric geometries of NCs like DRs are ideal for the application in biological membranes.[121] Park et al. have shown that tailored peptides can be used as ligands to promote the insertion and correct orientation into lipid membranes. In particular, they inserted CdSe/CdS DRs into HEK293 cells, which natively exhibit voltage oscillations (known as self-spiking), and successfully monitored their voltage oscillations in the modulation of the PL intensity.[122] Additionally, Ludwing et al. were able to successfully measure the QCSE of type-II ZnSe/CdS DRs in living neuron cells.[123]

To optimize the applications mentioned above, the QCSE has to be understood in detail. The QCSE also interacts with other effects in NCs. Only recently, Huang et al. have measured the QCSE of the phonon energy for the first time.[124] Conradt et al. have shown that external electric fields increase spectral diffusion.[125]

2.2. Type-I and Type-II Dot-in-Rod Nanocrystals

Synthesis and Properties

Shell growth onto NCs was originally developed for type-I band alignments, which isolate the exciton from trap states localized on the NC surface and its surrounding.[126] Aside from symmetric shells in NC syntheses, anisotropic shells are accessible, which enable unique optical properties. One example of these systems are CdSe/CdS DRs that were first synthesized by Talapin et al. in 2003. Their synthesis is based on the seeded hot-injection of spherical CdSe NCs on which an anisotropic wurtzite CdS shell is grown. The anisotropic growth is a result of two aspects. First, the lattice mismatch is largest along the c axis [001], thus favoring the growth over the [100] direction. Second, the Cd^{2+} ions on the $(00\bar{1})$ have three dangling bonds compared to only one for the other facets, making the $(00\bar{1})$ facet more reactive. The growth along the c axis is additionally enhanced by using an excess sulfur precursor and ligands that promote the anisotropic shell growth for this direction, like hexadecylamine, by preferential binding.[27] Due to the faster growth along the $[00\bar{1}]$ direction, the CdSe core is usually found between 1/3 to 1/4 of the rod length.[127] The simulated valence band offset between CdSe and CdS is reported between 0.42 eV[128] and −0.64 eV[129,130], while the values for the conduction band offset of −0.25 eV[131], 0.27 eV[126,132], 0.32 eV[133], and 0.33 eV[134] have been predicted. For experimental descriptions, band alignment values in the range of 0.1–0.3 are most commonly applied, which means that the band alignment lies in the borderline range between a type-I and quasi-type-II.[7,27,135–137] For example, Steiner et al. derived a conduction band offset of 0.3 eV from their scanning tunneling microscopy measurements.[138] By measuring transient emission spectroscopy, Stitt et al. observed that CdSe/CdS DRs exhibit type-I behavior for CdSe cores with diameters larger than 2.8 nm, and quasi type-II behavior for cores smaller than 2.8 nm.[139] Eshet et al. also reaffirmed this dependence on the core size by atomistic calculations. The band energies can also shift as a result of lattice strain between the core and shell material.[140] Lohmann et al. simulated this strain effect and found that it only shifts the conduction band offset ~50 meV.[141] As a consequence of the electron delocalization into the CdSe shell, the average lifetime changes with the rod length. For comparison, the average lifetime of short DRs (l = 15 nm) is ~20 ns and for long DRs (l = 100 nm) ~100 ns, in the case of a core diameter of 3.6 nm, rod width of ~5 nm, and excitation with laser light at 440 nm.[142]

By embedding ZnSe dots instead of CdSe dots into a CdS rod, a type-II band alignment can be obtained for the DRs, as Dorfs et al. first reported. The intrinsic separation of electron and hole due to the type-II band alignment reduces the overlap and thereby prolongs the lifetime. For example, in short ZnSe/CdS DRs, the lifetime is around 105 ns long, which is much higher compared to similar-sized CdSe/CdS DRs with a lifetime of 13 ns. As a result of the band alignment and Coulomb interaction, the lowest exciton states are localized at the ZnSe/CdS interface, and the primary emission pathway belongs to the spatially indirect transition of the exciton.[143]

Cation Exchange

Cation exchange is a reaction in which the cations of a crystal lattice are exchanged. The anion lattice is more stable and is usually conserved during cation exchange.[144] Although it is not uncommon that defects form during cation exchange.[145,146] Cation exchange in NCs is more rapid than in the bulk case, because of the much higher surface to volume ratio and faster diffusion, due to a lowered reaction barrier. Furthermore, the pathway of cation exchange allows to reach material compositions for NCs that are otherwise not accessible via the hot-injection or other methods.[147] Cation exchange is controlled by the thermodynamic stability of the reactants and products, on one hand, and the overall kinetics, on the other. The thermodynamic part includes the dissociation of the old cation–anion bond, the desolvation of the new cation, the association of the new cation with the anion, and the solvation of the old cation. Activation barriers of each reaction step, the reaction temperature, and the concentrations of the reactants govern the kinetics of the reaction. Overall, the cation exchange reaction is usually driven by using high excess concentrations of the new cations, temperature, and favorable solvation of the old cation. The latter can be predicted by the hard and soft acids and bases (HSAB) principle[148] for Lewis acids and bases, which states that bindings are forming preferentially between the reaction partners of similar *hardness*. Here, *hardness* is related to the polarizability of the reactants. In this case, the lower the polarizability of the Lewis acid or base, the higher is their corresponding hardness. In other words, small ions with high charges are considered as hard, whereas large ions with lower charges are considered soft.[147,149]

The most important cation exchange for this work is the exchange of Zn^{2+} to Cd^{2+} in ZnSe NCs, which Gronenveld et al. have investigated in great detail. ZnSe and CdSe are fully miscible. Thus, the exchange proceeds through the formation of $\mathrm{Zn}_{1-x}\mathrm{Cd}x\mathrm{Se}$. The cation exchange reaction can be written as

$$x\mathrm{Cd(Oleate)}_{2(\mathrm{sol})} + [\mathrm{ZnSe}_{\mathrm{NC}}] \longrightarrow x\mathrm{Zn(Oleate)}_{2(\mathrm{sol})} + [(\mathrm{Zn}_{1-x}\mathrm{Cd}_x)\mathrm{Se}]_{\mathrm{NC}}. \tag{2.2.1}$$

In this example, both the Zn^{2+} and Cd^{2+} are solved in oleate. They found that this reaction is primarily driven by the stronger bond energy of Cd–Se of 310 kJ/mol[150], compared to Zn–Se with Zn–Se 136 kJ/mol[150] In their model, the cation exchange primarily takes place at the NC surface, followed by a slow solid-state diffusion of the Cd^{2+} ions inwards and Zn^{2+} ions outwards. This diffusion process is facilitated by Frenkel pairs. Frenkel pairs are defects in which an ion moves from a regular lattice position into an interstitial position, leaving behind a vacancy. The concentration of Frenkel pairs increases with temperature, thereby controlling the final product of the cation exchange process. Groeneveld et al. observed that ZnSe/CdS core/shell particles are developed at 150 °C, gradient Zn_{1-x}CdxSe alloys emerge between 200–240 °C, and homogeneous alloys are formed above 240 °C.[151]

Emission Polarization

One key aspect that makes the DRs interesting for applications is that they emit light linearly polarized along the rod axis.[27] The degree of polarization (DOP) is commonly defined as

$$\mathrm{DOP} = \frac{I_{\parallel} - I_{\perp}}{I_{\parallel} + I_{\perp}}, \tag{2.2.2}$$

where $I_{\parallel}$ and $I_{\perp}$ are the parallel and orthogonal intensity components, respectively. In case of single CdSe/CdS DRs, the DOP can reach up to 0.75[27]. There are two contributions to the origin of polarized emission in DRs. The first is the dielectric screening of the anisotropic particle shape, favoring electric fields parallel to the c-axis, which alone would lead to a monotonic increase of the DOP with the aspect ratio. This contradicts experimental results that have shown a non-monotonic increase.[152–154] The second contribution is the polarization of the different band-edge exciton states. By performing calculations within the effective-mass approximation, Vezolli et al.[153] and Planelles et al.[154] have shown how the ordering and splitting energies of the band-edge exciton states change with the shape. They concluded that the DOP increases with the core size, core aspect ratio, and rod length, while it decreases with the rod diameter.[153,154] Zhang et al. conducted experiments where they measured the DOP of single DRs that were covered with n-doped indium tin oxide NCs. This allowed them to investigate the influence of surface charges and show that the distribution of the DOPs increases in the presence of surface charges, because the band-edge fine structure is changed.[155]

Application of Dot-in-Rod Nanocrystals

The type-II band alignment in ZnSe/CdS DR is beneficial for catalytic applications, like water splitting, where the excited electrons are used for the hydrogen evolution reaction. These catalytic application usually involves a metal NC as a cocatalyst that can be grown selectively on the $(00\bar{1})$ facets of the DRs.[57,58] As discussed in Chapter 2.1.5, their strong response to the QCSE makes them also interesting for optical switches and biosensors.[121,156]

CdSe/CdS DRs in combinations with metal cocatalysts have also successfully been used for hydrogen production by multiple groups.[157–160] Further applications of CdSe/CdS DRs are as gain media in lasers[161–164], or as light sources in light-emitting diodes.[29] Moreover, Biadala et al. proposed that the properties of CdSe/CdS DRs are particularly interesting for the generation of polarized entangled photon pairs.[68]

2.3. Giant-Shell CdSe/CdS Quantum Dots

Growing thick shells of CdS onto CdSe NCs can greatly increase the QY close to unity, because the probability of the electron or hole getting trapped on the surface is reduced, as they preferentially are localized in the CdSe core region.[165] In case of 15–19 MLs, these particles are called giant-shell quantum dots.[166] In order to grow these particles, the conventional hot injection method cannot be used directly. Instead, they are commonly synthesized by the successive ionic layer adsorption and reaction (SILAR) method[167], in which the different ion layers are added one by one. Alternatively, the hot injection method can be combined with a successive drop-wise addition of the precursors over a long time period to synthesize giant-shell quantum dots.[168] If an alloyed layer of $\mathrm{CdSe}_x\mathrm{S}_{1-x}$ is introduced between CdSe core and CdS shell, the Auger combination can be reduced, which further improves the QY.[169,170] Alloyed CdSe/CdS quantum dots have a low optical gain threshold threshold, which makes them suitable as gain media in lasers.[171] The reduction of Auger recombination had previously been proposed based on theoretical calculations by Cragg and Efros.[172]

3. Experimental Methods

3.1. Confocal Laser Scanning Microscopy

The spatial resolution in optical microscopy is determined by the fundamental diffraction limit of light. In an ideal situation, the diffraction pattern from a single point light source created by a lens and circular aperture takes the shape of an Airy pattern. The Airy pattern is composed of a spherical center, known as the Airy disc, followed by a pattern of rings. In optical microscopy, the Rayleigh criterion is the common description for the resolution. It states that the resolution is equal to the distance of the intensity maxima from two point light sources when the maximum of one lies within the first minimum of the other. In conventional wide-field microscopy the sample is illuminated in its entirety and recorded as a whole. In this case, the lateral resolution R_{lateral} is equal to the Abbe limit

$$R_{\mathrm{lateral}} = \frac{0.61\lambda}{\mathrm{NA}}, \tag{3.1.1}$$

where λ is the wavelength of the detected light, and NA the numerical aperture of the objective lens. The numerical aperture is a measure of how much light is captured by the objective and is given by

$$\mathrm{NA} = n_{\mathrm{r}} \sin(\alpha_{1/2}), \tag{3.1.2}$$

where n_{r} is the refractive index of the surrounding medium and $\alpha_{1/2}$ is half of the opening angle.[173]

A high spatial resolution and low signal-to-noise ratio are needed for the measurements of single NCs. For these reasons, confocal laser scanning microscopy is commonly applied. Figure 3.1 shows the principle of a confocal microscope. Initially, the laser light is guided onto a beamsplitter, then reflected towards the objective lens and focused onto the sample. Subsequently, the fluorescence and scattered laser light then pass through the objective lens and the beamsplitter. The laser light is filtered out by a longpass filter, and the fluorescence light is focused onto the detector with the pinhole lens. The pinhole blocks all light that does not come from the focus spot on the sample. Often, the detector itself acts as a pinhole, which, for example, is the case when an avalanche photodiode is used that has an active detector area size on the µm scale. A 2D image is generated by

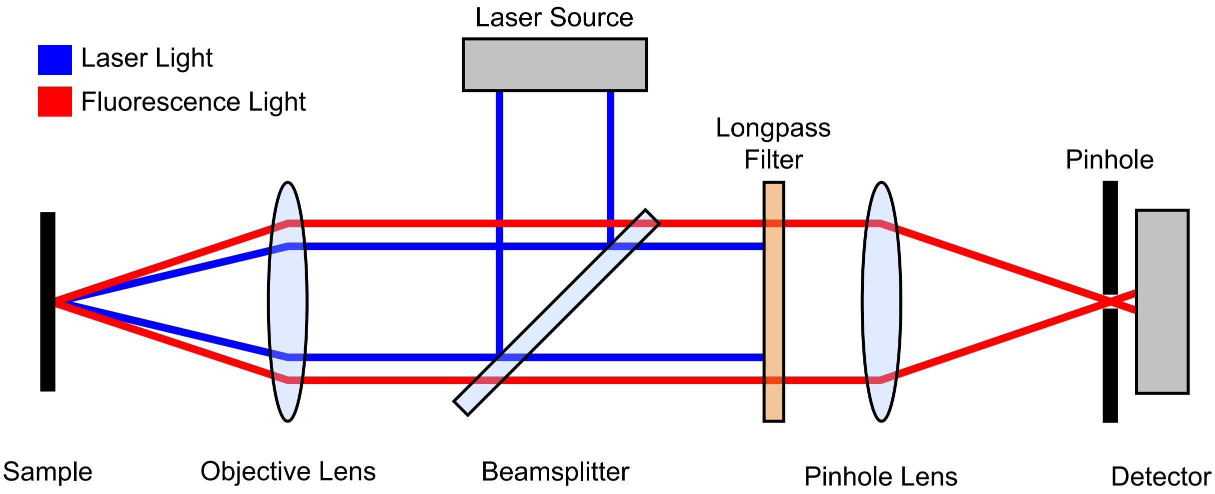

Figure 3.1.: Schematic of a confocal microscopy setup. The laser light is focused on the sample surface where a fluorophor is located. The fluorophor emits light, which is then detected behind a pinhole, which blocks any light from light sources out of focus. Adapter from literature.[174]

either moving the sample with a piezo-scanner or the laser light with a mirror scanner. By selective excitation and measurement only from the focus spot, both the spatial resolution and signal-to-noise ratio are improved. The lateral resolution that can be achieved using confocal microscopy is[175]

$$R_{\text{lateral,conf}} = \frac{0.4\lambda}{\text{NA}}. \tag{3.1.3}$$

3.2. Atomic Force Microscopy

Atomic force microscopy (AFM) enables precise topology measurements on the nanometer scale. It is based on the measurement of the force between a tip and a sample in close proximity. This interaction is often approximated by the Lennard-Jones potential U_{LJ}, which is conceived for the interaction of two neutral atoms as

$$U_{\text{LJ}} = 4U_0 \left[\left(\frac{R_{\text{a}}}{r} \right)^{12} - \left(\frac{R_{\text{a}}}{r} \right)^{6} \right], \tag{3.2.1}$$

which depends on the depth of the potential well U_0, the position where the potential reaches zero R_{a}, and the distance between the two atoms r. The first term describes the repulsive interaction, and the second term describes the attractive van der Waals interaction. Consequently, the resulting force can be calculated from the first derivative $F = -\frac{\partial U_{\text{LJ}}}{\partial r}$.[176]

Figure 3.2 illustrates the setup of an atomic force microscope. The tip is localized on a cantilever that functions as a spring. These tips are created by etching of the cantilever material, which is typically produced from silicon or silicon nitride. By applying Hooke's

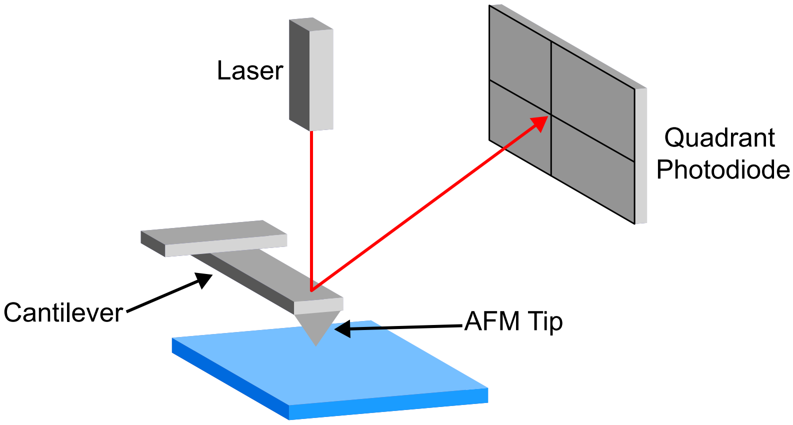

Figure 3.2.: Schematic depiction of an atomic force microscope that uses deflection of laser light from the back of the cantilever for the detection of its deformation. Adapted from literature.[177]

law, the tip-sample force can be approximated to the deflection of the cantilever. In this example, the deflection is measured by a laser beam directed at the back side of the cantilever, reflected from there, and then detected by a quadrant photodiode. In order to measure 2D scans, either the sample or the cantilever is moved line by line over the sample. For these 2D scans, the lateral resolution is limited by the tip sizes and lies typically in the range of 5–10 nm. For the vertical direction a resolution of < 1 nm is possible, enabling even atomic resolution in some situations.[177] The available operation modes in AFM are the contact, intermittent contact and non-contact mode. In the contact mode, the tip is in direct contact with the sample, resulting in heavy wear of the sample and tip. For the intermittent and non-contact mode, the cantilever oscillates up and down. In case of the intermittent mode, the oscillation amplitude is large and the tip touches the sample periodically, thereby reducing the wear. The lowest wear is offered by the non-contact mode at the expense of a lower sensitivity.[176]

3.3. Calculation of Excitons in Nanocrystals

The Finite Element Method

The Schrödinger and Poisson equations that have to be solved for the calculations of excitons in NCs are partial differential equations (PDEs) that in the majority of cases cannot be solved analytically, because of their complexity. Thus, these equations are solved numerically by using the finite-element method (FEM), which can be applied to any kind of PDE. The FEM has its origin in the field of engineering, where it is used for calculations on complex geometries. The FEM is based on the discretization of continuous functions by a finite number of elements N distributed as nodes in a mesh. In the FEM, the approximated function

$$u = \sum_{i=0}^{N} c_i \chi_i \tag{3.3.1}$$

is constructed as a linear combination of coefficients c_i and so-called shape functions χ_i, which are polynomial functions. The most important property of the shape functions is that their value is exactly one at a single node point, while being zero at all other node points. In Equation 3.3.1, there are $N + 1$ unknowns, which means that $N + 1$ PDEs are needed so that the system is not underdetermined. In order to create a linear system of equations with $N + 1$ equations, a set of $N + 1$ test functions is introduced. The resulting linear system of equations that has to be solved then takes the form

$$\mathbf{A}\mathbf{u} = \mathbf{f}, \tag{3.3.2}$$

where $\mathbf{A}$ is the operator matrix, $\mathbf{u}$ the unknown vector that is solved for and $\mathbf{f}$ is a known vector.

FEM calculations are always optimized by distributing the mesh elements not homogeneously in space but inhomogeneously, based on prior physical knowledge about the system. For example, in the case of a NC in vacuum, the mesh density far away from the NC can be reduced as the wave function is close to zero. Thus, an accurate approximation in this region can be achieved with fewer mesh points. In 3D, the mesh points are most commonly arranged by tetrahedra.[178,179]

Self-Consistent Coulomb Interaction

The Coulomb binding energy of an exciton can be calculated by iteratively solving the Schrödinger and Poisson equations in an alternating way, as Panfil et al. described in their reports.[82,129,180] For the Schrödinger equations, the effective-mass approximation was always used. In order to find a physically plausible and unique solution, boundary conditions have to be accounted for. For both, the the Schrödinger and Poisson equations, the Dirichlet boundary condition was applied to set the wave functions and electric potentials to zero 15 nm away from the NC surface. Furthermore, the Ben-Daniel-Duke boundary condition[81,129,181]

$$\Psi_j = \Psi_{j+1} \tag{3.3.3a}$$

$$\frac{1}{m_j}\nabla\Psi_j = \frac{1}{m_{j+1}}\nabla\Psi_{j+1} \tag{3.3.3b}$$

has to be considered to ensure the continuity of the solution. In this equation, m_j / m_{j+1} are the effective masses and Ψ_j / Ψ_{j+1} the wave functions of two adjacent domains. In order to account for the Ben-Daniel-Duke boundary condition, the Neumann boundary condition

$$-\mathbf{n}\left(-\frac{\hbar^2}{2m_{\mathrm{e,eff}}}\nabla\Psi\right) = 0, \tag{3.3.4}$$

was applied to all inner boundaries. Here, $\mathbf{n}$ is the normal vector on the boundary of two domains.

The results of the different calculation steps are visualized in Figure 3.3 using the example of a CdSe NC ($r = 3$ nm) in vacuum. In the first step of the iterative calculation the single-particle Schrödinger equations of electron and hole

$$\left(-\frac{\hbar^2}{2m_{\mathrm{e/h,eff}}}\nabla^2 + V_{\mathrm{cb/vb}}\right)\Psi_{\mathrm{e/h}} = E_{\mathrm{e/h}}\Psi_{\mathrm{e/h}}, \tag{3.3.5}$$

were solved, respectively. For the potential energy landscapes the corresponding bulk values of the conduction and valence band $V_{\mathrm{cb/vb}}$ were used. Thereby, the initial wave functions $\Psi_{\mathrm{e/h}}$ and energies $E_{\mathrm{e/h}}$ of electron and hole were obtained, respectively. In the second step, the corresponding probability densities of the electron and hole $|\Psi_{\mathrm{h}}|^2$ (Figure 3.3a) were then used to derive the electric potentials $\phi_{\mathrm{e/h}}$ (Figure 3.3b) by using the Poisson equation

$$-\nabla(\epsilon_0\epsilon_{\mathrm{r}}\nabla\phi_{\mathrm{e/h}}) = q_{\mathrm{e/h}}|\Psi_{\mathrm{e/h}}|^2, \tag{3.3.6}$$

with the respective charge of electron and hole $q_{\mathrm{e/h}}$. As a consequence of the dielectric mismatch of the NC and its surrounding, the self-polarization of each charge carrier has to be taken into account. Following the approach by Park et al.[111], the potentials of the self-polarizations $\phi_{\mathrm{e/h,sp}}$ (Figure 3.3c) were approximated by the difference of the electric potentials of the charge carrier in an inhomogeneous and homogeneous dielectric environment

$$\phi_{\mathrm{e/h,sp}} = \phi_{\mathrm{e/h}} - \phi_{\mathrm{e/h,homo}}. \tag{3.3.7}$$

The homogeneous dielectric potential $\phi_{\mathrm{e/h,homo}}$ was calculated using Poisson's equation:

$$-\nabla(\epsilon_0\epsilon_{\mathrm{r,homo}}\nabla\phi_{\mathrm{e/h,homo}}) = q_{\mathrm{e/h}}|\Psi_{\mathrm{e/h}}|^2, \tag{3.3.8}$$

where $\epsilon_{\mathrm{r,homo}}$ is the dielectric constant of the NC core. In case of the homogeneous environment no self-polarization is present, while it is present in the inhomogeneous case. Thus, after calculating the difference only the potential of the self-polarization remains.

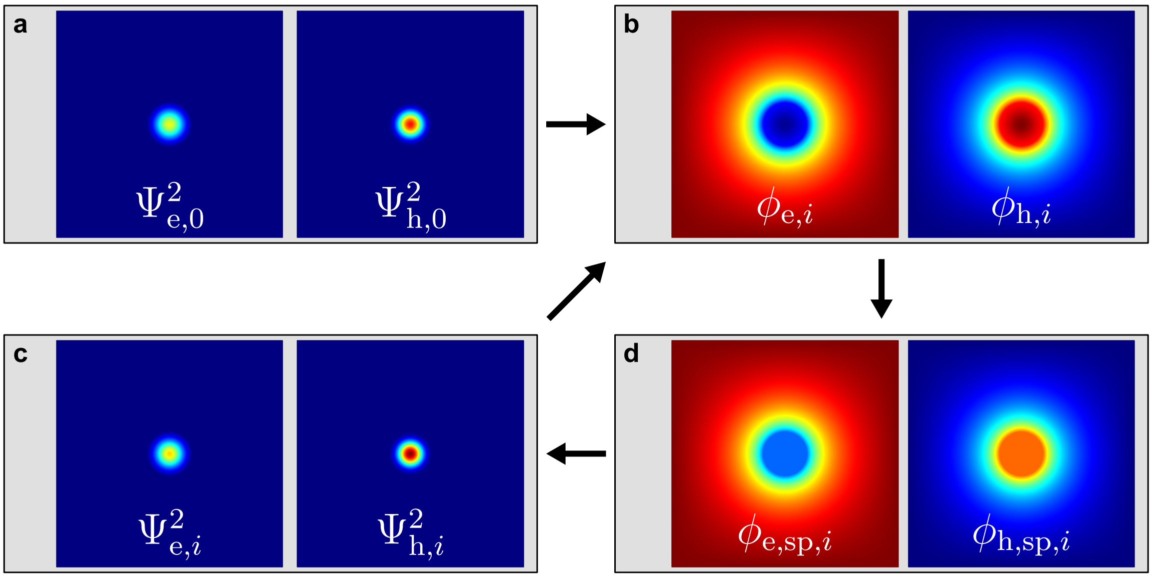

Figure 3.3.: Cross-sections of the probability densities and electric potentials of the electron and hole during different steps of the iterative Schrödinger-Poisson calculations of a CdSe NC ($r = 3$ nm) in vacuum.

These self-potentials and the electric potentials of the opposite charge carrier were then introduced into the Hamiltonian and the Schrödinger equations of the electron

$$\left(-\frac{\hbar^2}{2m_{\mathrm{e/h,eff}}}\nabla^2 + V_{\mathrm{cb/vb}} + q_{\mathrm{h/e}}\phi_{\mathrm{h/e}} + q_{\mathrm{e/h}}\phi_{\mathrm{e/h,sp}}\right)\Psi_{\mathrm{e/h},\phi_{\mathrm{h/e}},\phi_{\mathrm{e/h,sp}}} = E_{\mathrm{e/h},\phi_{\mathrm{h/e}},\phi_{\mathrm{e/h,sp}}}\Psi_{\mathrm{e/h},\phi_{\mathrm{h/e}},\phi_{\mathrm{e/h,sp}}}. \quad (3.3.9)$$

Once these equations are solved, they yield the wave functions $\Psi_{\mathrm{e/h},\phi_{\mathrm{h/e}},\phi_{\mathrm{e/h,sp}}}$ (Figure 3.3d) and eigenvalues $E_{\mathrm{e/h},\phi_{\mathrm{h/e}},\phi_{\mathrm{e/h,sp}}}$. The Schrödinger and Poisson equations were then solved in turns until the energies of the eigenvalues converged. In order to avoid the inclusion of the Coulomb interaction twice, the Coulomb interaction of the electron and hole were averaged. The total energy of the exciton can then be described as

$$E_{\mathrm{exc}} = E_{\mathrm{e},\phi_{\mathrm{e,sp}}} + E_{\mathrm{h},\phi_{\mathrm{h,sp}}} - \frac{E_{\mathrm{e},\phi_{\mathrm{e,sp}}} - E_{\mathrm{e},\phi_{\mathrm{h}},\phi_{\mathrm{e,sp}}} + (E_{\mathrm{h},\phi_{\mathrm{h,sp}}} - E_{\mathrm{h},\phi_{\mathrm{e}},\phi_{\mathrm{h,sp}}})}{2}, \quad (3.3.10)$$

where $E_{\mathrm{e},\phi_{\mathrm{e,sp}}}$ and $E_{\mathrm{h},\phi_{\mathrm{h,sp}}}$ are the eigenvalues of the electron and hole, including their self-polarization. Additionally, $E_{\mathrm{e},\phi_{\mathrm{h}},\phi_{\mathrm{e,sp}}}$ and $E_{\mathrm{h},\phi_{\mathrm{e}},\phi_{\mathrm{h,sp}}}$ are the eigenvalues that include both the self-polarization and Coulomb interaction.

For any calculations that included surface charges, point charges were added to the surface of the NCs. Furthermore, for the calculations of external electric fields, the Poisson equation was solved with adjusted Dirichlet boundary conditions according to the electric field. The corresponding potentials were then included in the Hamiltonians.

Calculation Parameters for Alloys

Most properties of alloys can be interpolated linearly based on the properties of the binary materials, following Vegard's law. The band gap energy is an exception from this and can be better described by quadratic interpolation. For a ternary alloy $\mathrm{A}_x\mathrm{B}_{1-x}\mathrm{C}$, the band gap energy can be calculated as

$$E_{\mathrm{ABC}}(x) = xE_{\mathrm{AC}} + (1-x)E_{\mathrm{BC}} + x(1-x)C_{\mathrm{AB}}, \tag{3.3.11}$$

where E_{AC} and E_{AC} are the band gap energies of the binary materials, and C_{AB} is the bowing parameter for this specific alloy. In a similar way, the band gap energy of a quaternary alloy $\mathrm{A}_x\mathrm{B}_{1-x}\mathrm{C}_y\mathrm{D}_{1-y}$ can be constructed from the ternary band gaps via

$$E_{\mathrm{ABCD}}(x,y) = \frac{x(1-x)[yE_{\mathrm{ABC}}(x) + (1-y)E_{\mathrm{ABD}}(x)] + y(1-y)[xE_{\mathrm{ACD}}(y) + (1-x)E_{\mathrm{BCD}}(y)]}{x(1-x) + y(1-y)}, \tag{3.3.12}$$

where E_{ABC}, E_{ABD}, E_{ACD} and E_{BCD} are the band gaps of the ternary alloys.[182]

3.4. Optical and Electron-Beam Lithography

Strong electric fields are required for the investigation of the QCSE, for which microstructured electrodes are needed. In this work, the IDEs were prepared by photolithography, also known as optical lithography. The process steps for photolithography are illustrated in Figure 3.4. At first, the Si/SiO$_2$ wafers are coated with a photoresist via spin-coating, which creates homogeneous films with adjustable thickness on a micrometer scale. In this work, a double-layer lift-off process is used. Therefore, in a first step, the substrate is coated with a lift-off resist followed by the regular photoresist. Each resist is soft-backed on a hot-plate in order to remove residual solvent, which improves the adhesion, reduces dark erosion during development, and prevents mixing of the different photoresist layers. Photoresists can be grouped into positive and negative resists. In this work, positive resists are used. These positive resists increase their solubility through illumination, while the negative resists reduce their solubility. Positive photoresists are commonly based on novolaks (a polymer made from phenol and formaldehyde) combined with diazonaphthoquinone-sulfonates as a photoactive compound. When this photoresist is exposed to UV light, diazonaphthoquinone-sulfonate splits off elemental nitrogen and forms a ketene. Then, the ketene reacts with water to form a carboxylic acid. This leads to an increase in the solubility by three to four orders of magnitude compared to pure novolak. The water in the photoresist originates from ambient air and thus depends on

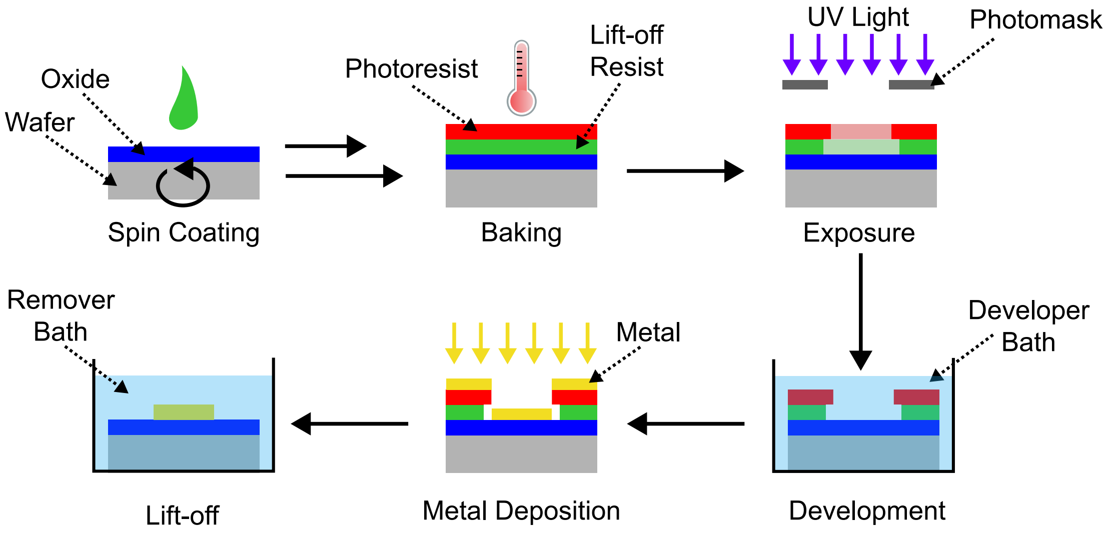

Figure 3.4.: Overview of the processing steps in photolithography based on the lift-off technique. In this case, positive photoresists are depicted, which have an increased solubility after the exposure to UV light.

the humidity and time between the baking and exposure steps. In the third step, the photoresists are exposed to UV light in the wavelength range of 320–440 nm, depending on the side chains of the specific photoactive compound. For this purpose, the substrate is either illuminated globally behind a physical photomask to create the desired illumination pattern. Alternatively, a maskless microwriter can be used to write the pattern directly onto the substrate step by step, eliminating the need for a physical photomask. After the exposure, the lithography pattern is developed by immersion of the substrate in an aqueous alkaline solution, which, in the case of a positive photoresist, dissolves the exposed pattern. Due to the higher development rate of the lift-off resist, a so-called undercut is formed, which eases the later lift-off. Following this, a metal film is deposited by physical vapor deposition. In order to evaporate the metals, they are heated in tungsten boats in the vacuum of 10^{-7}–10^{-8} mbar. In the last step, the lift-off, the substrate is immersed in an organic solvent like N-Methyl-2-pyrrolidon, or alternatively in an alkaline solution, thereby dissolving any unexposed resist.[183]

In addition to photolithography, electron-beam lithography was performed for the investigation of poly(methylmethacrylat) (PMMA) films that were used as a matrix for the deposition of DRs between the IDEs. The resolution that is possible in electron-beam lithography is below 10 nm.[184] Analogous to photolithography, the processing steps include the following: first, the photoresist is spin-coated and soft-baked. Then it is exposed and finally developed. In this case, PMMA directly acts as the "photoactive" compound.

4. Experimental Details

4.1. Chemicals

Acetone (≥ 99.5 %, Th. Geyer / 99.8 %, VWR Chemicals /≥ 99.8 %, Fisher Scientific), AR 600-56 developer (Allresist), *n*-hexane (99.7 % / 99 %, VWR Chemicals), LOR-5A Lift-Off Resist (Kayaku Advanced Materials), MICROPOSIT MF-319 developer (DuPont), MICROPOSIT Remover 1165 (DuPont), MICROPOSIT S1805 positive photo resist (DuPont), Poly(methyl methacrylate) (MW = 35 k, Fisher Scientific), 2-Propanol (99.7 %, VWR Chemicals), toluene (>99.5 %, VWR Chemicals / 99.85 %, Acros Organics). All chemicals were used without further purification.

4.2. Optical Spectroscopy

4.2.1. Confocal Microscope Setup

All optical spectroscopy measurements were carried out on a home-built confocal laser scanning microscope setup. Figure 4.1 shows a schematic overview of this setup. For the majority of measurements, a 446 nm PiL044Xm laser diode (Advanced Laser Diode Systems) in combination with an EIG2000DX (Advanced Laser Diode Systems) laser driver was used. For the excitation of the CdSe cores in Chapter 6.3, a 510 nm LDH-P-C-510 (Picoquant) laser diode with a PDL 800-D (Picoquant) laser driver was used. In both cases, the beam profile of the laser diodes was spatially filtered by focusing the light onto a pinhole with a diameter of 20 µm. The 446 nm laser was filtered by using a 450 nm short-pass filter, and the 510 nm laser was filtered with a 514 nm short-pass filter. If needed, the polarization of the laser light was rotated with a $\lambda/2$-waveplate. The laser intensity was fine-tuned with neutral density filters. The laser light is then guided through an 8:92 (reflection:transmission) beamsplitter, and the transmitted laser light reaches a Model 1918-C (Newport) power meter for online detection. The reflected part of the laser light then passes a galvanometer mirror scanner that, in combination with the installed telecentric lens system, enables the 2D scanning of the sample surface. For both measurements in and outside of the cryostat, the laser light was focused onto

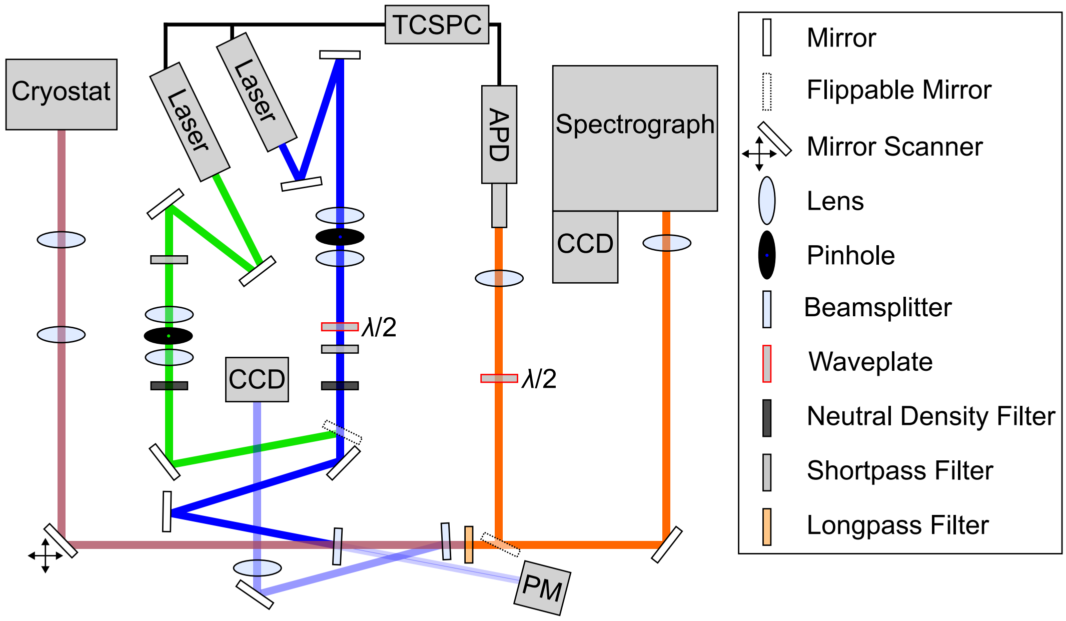

Figure 4.1.: Schematic depiction of the confocal laser scanning microscope. The laser light is color coded in blue (446 nm) and green (510 nm), while the PL light from the sample is shown in orange. The abbreviation PM stands for powermeter, and the abbreviation TCSPC stands for time-correlated single photon counting.

the sample with an LMPLFLN 100x microscope objective (Olympus), which has an NA of 0.8. The ensemble spectroscopy data shown in Chapter 6.1.1 was measured by using a lens ($f = 100$ mm) instead of the microscope objective. A customized attoDRY 700 (Attocube) closed-cycle He-cryostat allows to cool the samples down to $T \approx 10$ K. The scattered laser light and the PL light coming from the sample surface pass through the microscope objective and the first beam splitter, before reaching the second beam splitter (25:75). The light reflected by the beamsplitter is directed onto a CCD chip, which is used to evaluate the laser beam profile and check if the sample is in the focus of the objective. Depending on the laser source either a 488 nm or 532 nm long-pass filter is used to remove the laser light from the transmitted light. The remaining PL light then arrives at a mirror that either directs the light towards an PDM Series free space avalanche photodiode (APD) (Micro Photon Devices, 50 µm active sensing area, timing c) or, when flipped, lets the light pass towards the Acton SP-2-500i spectrograph (Princeton Instruments). Inside the spectrograph either a 300 grooves/mm (blaze = 500 nm) or a 150 grooves/mm (blaze = 800 nm) grating was used for single particle measurements, while for ensemble measurements, a 50 grooves/mm (blaze = 600 nm) grating was used. The spectrally separated light was then measured with a PIXIS 400B (Princeton Instruments) charge-coupled device (CCD). The APD and laser diodes (only one at a time) were connected to a PicoHarp300 (PicoQuant) TCSPC device, enabling the measurement of decay curves. Additionally, the setup included a Goldbox II (ADwin) real-time computer that was used to control the movement of the mirror scanner, as well as send trigger signals to multiple devices.

4.2.2. Spectroscopy in External Electric Fields

The cryostat provides electrical connections from the outside to the sample stage. In order to generate high voltages up to 200 V, which are needed for strong electric fields, a Series 2400 (Keithley) source measure unit was installed. For the hardware-software communication, the RS232 interface of the source measure unit (SMU) was addressed via MATLAB. The synchronization of all devices was implemented via MATLAB.

For the measurement of spectral time traces, with electric field sweeps, the MATLAB interface of the spectrograph software Lightfield was addressed. This way, the command starting the spectrum acquisition could be directly given following the RS232 command for the voltage change.

The PicoHarp300 (PicoQuant) was used to measure not only decay curves but time-tagged time-resolved data. To synchronize this data with the electric field sweep, a trigger signal was sent from the Goldbox II (ADwin) to the PicoHarp300 system for each voltage change of the SMU. The command for the trigger signal of the Goldbox II (ADwin) was also initiated via MATLAB.

For the measurement of the NC orientation, a $\lambda/2$-waveplate, mounted in a PRM1-Z8 motorized rotator (Thorlabs), was used in combination with a Wollaston prism positioned before the spectrograph. The motorized rotator was powered by a Kinesis Cube KDC101 (Thorlabs). Due to the low photostability of the NCs, this measurement was kept as short as possible. Thus, to save time, a spectra series was started in parallel to the continuous movement of the motorized $\lambda/2$-waveplate. If instead the angle of the $\lambda/2$-waveplate had been changed in set intervals for the spectra series, the measurement time would have been doubled.

4.2.3. Sample Synthesis

Dot-in-Rod Nanocrystals Analyzed in Chapter 6.1

The three $Zn_{1-x}Cd_xSe/CdS$ DR samples (DR-1–3) were synthesized by Jannik Rebmann[185] based syntheses approaches by Cozzoli et al.[186] and Dorfs et al.[143]. All three samples were synthesized from the same batch of ZnSe NCs. The degree of Cd within the $Zn_{1-x}Cd_xSe$ core was adjusted for each of the three samples by in situ cation exchange. This was achieved by the separate hot injections of the ZnSe NCs dispersion and S-precursor solution into a Cd-precursor solution at 320 °C. In the case of the DR-1 synthesis, both the ZnSe NCs and S-precursor were injected together ($\Delta t = 0$ s). For the other two samples

DR-2 and DR-3, the injection of the S-precursor was delayed in relation to the injection of the ZnSe NCs dispersion by $\Delta t = 10$ s and $\Delta t = 60$ s, respectively.

The CdSe/CdS NCs of sample DR-4 were synthesized by Jannik Rebmann according to the synthesis approach by Carbone et al.[127] Instead of CdSe NCs with an initial wurtzite crystal structure, CdSe NCs that initially had a zinc blende crystal structure were used for sample DR-4. These zinc blende CdSe NCs were synthesized based on the approach of Huang et al.[187]

CdSe/CdS Giant-Shell Dots Analyzed in Chapter 6.2

The CdSe/CdS giant-shell dots were synthesized by Sonja Zeller following the procedure reported by Chen et al.[167]

Dot-in-Rod Nanocrystals Analyzed in Chapter 6.3

The DRs that were investigated in external electric fields, were synthesized by Mareike Dittmar. The synthesis protocol of Carbone et al.[127] was used for the CdSe/CdS DRs, while the synthesis protocols by Cozolli et al.[186] and Dorfs et al.[143] were applied for the synthesis of the ZnSe/CdS DRs.

4.2.4. Sample Preparation

The ensemble and single particle spectra of Chapter 6.1 and Chapter 6.2 were measured on Si wafer pieces with a 300 nm thermal SiO_2 (Si-Tech, 500–550 µm thickness, <100>, N/As, 0.001–0.005 Ωcm). In order to avoid short circuits, a Si wafers with a thicker thermal oxide of 2000 nm (MicroChemicals, prime grade, 500–550 µm thickness, <100>,P/B, 1–10 Ωcm) were used for all electrically contacted samples in Chapter 6.3. (For more details, see Chapter 4.3) The wafers were first partially scribed with a diamond scriber, and then cleaved into 5x5 mm pieces. Afterwards, they were cleaned in an ultrasonic bath successively with acetone, 2-propanol, and deionized water, each time for 20–30 min and then dried under nitrogen flow.

The samples were diluted using either n-hexane (Chapter 6.1 and 6.2) or toluene (Chapter 6.3, more information in Chapter 4.3.2). For single particle measurement, dilution series were prepared, in order to find suitable concentrations in which the NCs are well separated and show homogenous PL intensities. The typical orders of magnitude of the dilutions were 1:100 for ensembles and $1{:}10^5$ for single particles. Following the dilution, the samples were homogenized using a vortex mixer for 30–60 s and then exposed to ultrasonics for 5–30 s. Aliquots from the samples of 10 µL were then dropped onto the samples and spin-coated at 5000 rpm for 15 s.

4.3. Production of Interdigitated Electrode Substrates

4.3.1. Optical Lithography Procedure

As a first step for the optical lithography, the above mentioned wafers were cleaved into 2.2x2x2 cm pieces, so that from each wafer piece multiple smaller devices can be obtained later on. In order to improve the reproducibility of the resist coating, the wafer pieces were first dehydrated on a hotplate at 200 °C for 5 min. Afterwards, the LOR-5A lift-off resist (Kayaku Advanced Materials) was spin-coated on the wafer pieces at 3000 rpm for 60 s, followed by a prebake at 180 °C for 5 min. After that, the positive resist MICROPOSIT S1805 (DuPont) was spin-coated on the wafer pieces at 4000 rpm for 60 s. Subsequently, a softbake was carried out at 120 °C for 1 min.

The electrode structures were then written on the substrates using a MicroWriter ML3 (Durham Magneto Optics). For this step, the digital lithography mask was designed in the software KLayout. The lithography was carried out with an excitation wavelength of 385 nm and an illumination dose of 50 mJ/cm^2. Additionally, the options for offset and rotation adjustment were activated, and the auto focus was turned on. Different settings were used for each part of the photo mask:

- Electrode pads and characters: normal quality / 1 µm resolution.
- Markers for orientation: normal quality / 0.6 µm resolution.
- IDEs: super quality / 0.6 µm resolution.

After the exposition, the substrate was immersed and gently swivelled in the developer MICROPOSIT MF-319 (DuPont) for 95–120 s. The development was stopped by immersion in deionized water and dried under nitrogen. By using a light microscope, the development time was controlled to verify that a sufficient undercut has formed.

In the next step, the substrates were cleaned in a PDC-002 (Harrick Plasma) plasma cleaner for 30 s at low power (~7.2 W), to ensure better adhesion for the metal deposition. The physical vapor deposition (PVD) was carried out in a Classic 250 (Pfeiffer) high vacuum coating system. Ti and Au were loaded into tungsten boats, and the vacuum was lowered to 10^{-7} mbar. The PVD was started with a 10 nm Ti layer, followed by a 50 nm Au layer.

For the lift-off process, the substrates were immersed and slowly stirred in MICROPOSIT Remover 1165 (DuPont) for 2–3 h. Following this, the substrates were successively cleaned in an ultrasonic bath each time for 30 s using acetone, 2-propanol, and deionized water, and then dried under nitrogen flow.

4.3.2. Device Preparation

The lithographically produced substrates were partially scribed with a diamond scriber and cleaved into 4x4 mm pieces. Any dust particles were then blown away with nitrogen. Instead of spin coating the NCs from pure solvent a PMMA solution was used, in order to fixate the NCs in a PMMA matrix between the IDEs. For this purpose, 1.25 wt% PMMA (average molecular weight = 35,000) was dissolved in toluene overnight, while stirring. Then, the solution was filtered by Rotilabo PTFE syringe filters (Carl Roth) with a pore diameter of 0.45 µm. In the next step, the NC stock solution was diluted with the PMMA-toluene solution and spin coated onto a substrate at 4000 rpm for 60 s. The same procedure was also used for experiments on the variation of the PMMA film height using different concentrations of 1.00 and 1.50 wt%, without any NCs. In preparation for wire bonding, the Au contact pads of the substrate were freed from the PMMA matrix by using cotton swabs soaked in acetone. Following this, the substrate was glued on a chip carrier using an electrically conductive adhesive based on silver. A schematic illustration of the chip carrier is shown in Figure 4.2. The chip carrier (Beta LAYOUT) was designed by Jan Flügge. This printed circuit board has a thickness of 1.6 mm and a hole with a diameter of 5.5 mm. Into the hole, a circular copper plate was embedded to improve the heat conductivity to the samples that are glued onto it.

The IDEs were bonded to the chip carrier with gold wires (d = 50 µm) at 100 °C by using an HB05 (TPT) wire bonder. For the first and second bonds the following settings were used: ball bonding, 40/200 ultrasonic power, 200/200 time, 25/30 force, tail 400 µm, and 20 µm feed.

After the bonding process, the electrical stability was tested with a Semiconductor Characterization System 4200-SCS (Keithley) by measuring I-V-curves in the range of 0–200 V, a compliance of 1 mA, and a measurement range of 1 mA. Figure 4.3 shows the electrical current measured through the chip carrier with a contacted sample (Figure 4.3a) and without (Figure 4.3b).

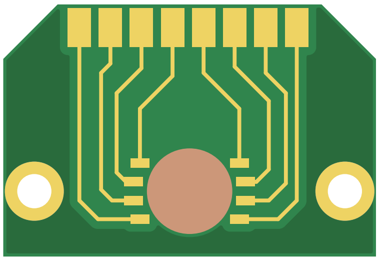

Figure 4.2.: Chip carrier for contacting the samples electrically. Designed by Jan Flügge.

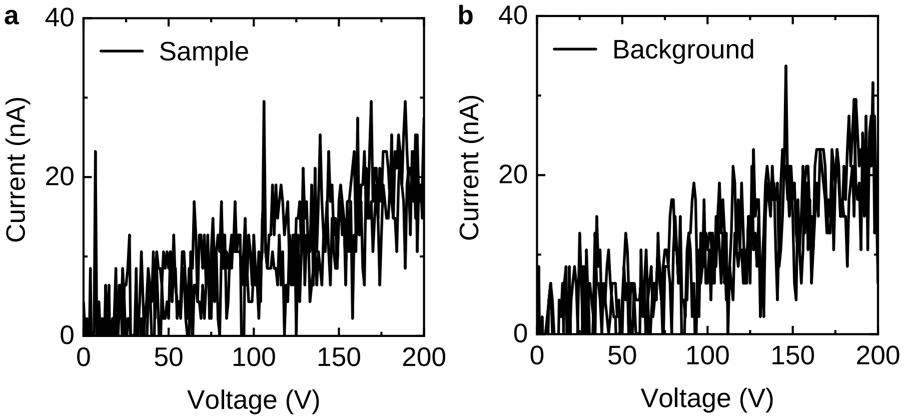

Figure 4.3.: Comparison of I-V-curves measured from the chip carrier (a) with and (b) without a bonded sample.

4.3.3. Atomic Force Microscopy Measurements

The AFM measurements were carried out on a Nanowizard II (JPK) in intermittent contact mode using PPP-NCHR silicone tips (Nanosensors). Then, the raw data was processed in the software Gwyddion. Within Gwyddion, row alignment, horizontal scar correction, and data leveling were applied.

4.3.4. E-beam Lithography

Before starting the lithography, the substrates with their PMMA films were baked on a hotplate at 120 °C for 120 s. For illumination, a Quanta 3D FEG (FEI) scanning electron microscope (SEM) was used. During the lithography step, the electron beam was always moved in a straight line towards the desired spot between the IDEs, in order to allow for later assignment of unwanted exposition. For the lithography writing, the selected position was imaged at 10 kV with a scan time of 20 µs. Afterwards, the substrates were immersed in the AR600-56 (Allresist) developer and gently swivelled. Finally, the development was stopped by immersion into 2-propanol.

4.4. Quantum Mechanical Calculations using COMSOL Multiphysics

The quantum mechanical and electrostatic equations were solved numerically using the software Comsol Multiphysics 5.4. For larger parameter sweeps the default Java heap size was allocation was increased to 5 gigabyte.

Meshing

Figure 4.4a shows the generated mesh for the averaged DR geometry, while Figure 4.4b and Figure 4.4c show magnifications of the DR and its core, respectively. Multiple domains were built in order to optimize the calculation time. The resolution was set to *extra fine* for every domain except the outer box, which was set to *extra coarse*. For example, the mesh in Figure 4.4a consists of 123804 tetrahedra, 7220 triangles, 619 edge elements, and 43 vertex elements.

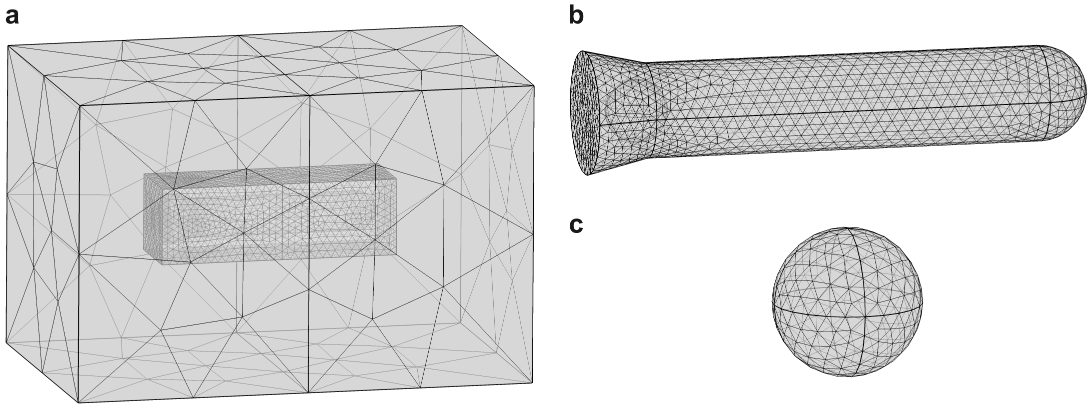

Figure 4.4.: Mesh generated in Comsol for (a) the full calculation space, (b) the DR and (c) its core.

Schrödinger–Poisson Calculation Sequence

In the framework of the FEM all physical equations were approximated with quadratic shape functions. For the self-consistent calculation of the Schrödinger–Poisson equations, three different calculation sequences have been used. Figure 4.5 shows the first two calculation sequences that are identical apart from the implementation of the self-polarization. The Schrödinger and Poisson equations were calculated iteratively (I) the electron and (II) the hole, until the eigenvalues converge after i iterations. The Coulomb interaction was calculated from the wave function of the counter-particle that included the self-polarization and Coulomb interaction. After the convergence (III), the eigenvalues were calculated again with the self-polarization of the latest iteration and the absence of the Coulomb interaction. These eigenvalues were then used to evaluate the energy of the exciton in a way that includes the Coulomb interaction only once.

For anisotropic heterostructures, the convergence of sequence 1 was improved by calculating the self-polarization as a superposition of the two previous iterations.

Figure 4.6 shows calculation sequence 3, which further improved the calculation convergence. Instead of solving the Poisson equations based on the Schrödinger equations

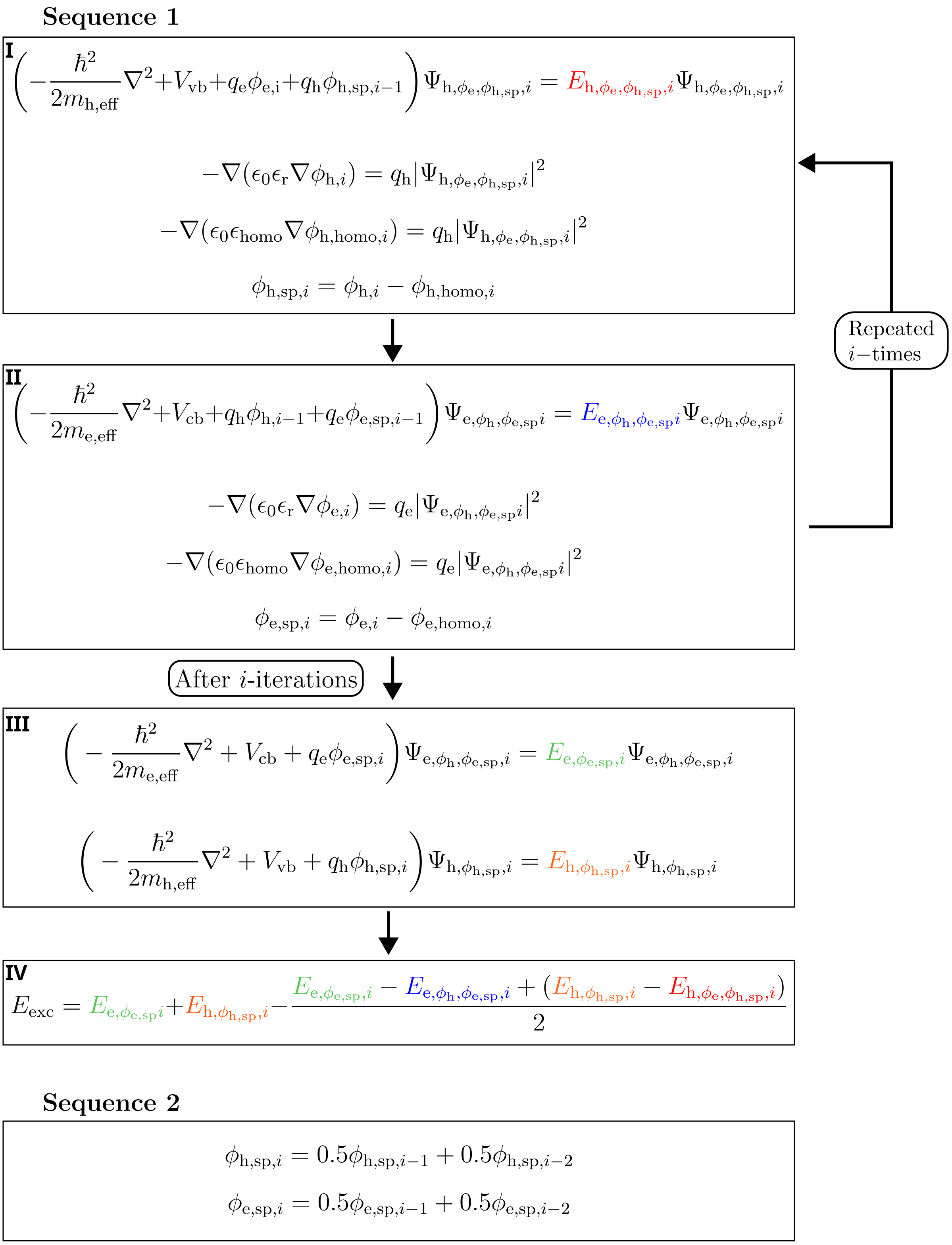

$$\left(-\frac{\hbar^2}{2m_{\mathrm{h,eff}}}\nabla^2+V_{\mathrm{vb}}+q_{\mathrm{e}}\phi_{\mathrm{e,i}}+q_{\mathrm{h}}\phi_{\mathrm{h,sp},i-1}\right)\Psi_{\mathrm{h},\phi_{\mathrm{e}},\phi_{\mathrm{h,sp}},i}=E_{\mathrm{h},\phi_{\mathrm{e}},\phi_{\mathrm{h,sp}},i}\Psi_{\mathrm{h},\phi_{\mathrm{e}},\phi_{\mathrm{h,sp}},i}$$

$$-\nabla(\epsilon_0\epsilon_{\mathrm{r}}\nabla\phi_{\mathrm{h},i})=q_{\mathrm{h}}|\Psi_{\mathrm{h},\phi_{\mathrm{e}},\phi_{\mathrm{h,sp}},i}|^2$$

$$-\nabla(\epsilon_0\epsilon_{\mathrm{homo}}\nabla\phi_{\mathrm{h,homo},i})=q_{\mathrm{h}}|\Psi_{\mathrm{h},\phi_{\mathrm{e}},\phi_{\mathrm{h,sp}},i}|^2$$

$$\phi_{\mathrm{h,sp},i}=\phi_{\mathrm{h},i}-\phi_{\mathrm{h,homo},i}$$

$$\left(-\frac{\hbar^2}{2m_{\mathrm{e,eff}}}\nabla^2+V_{\mathrm{cb}}+q_{\mathrm{h}}\phi_{\mathrm{h},i-1}+q_{\mathrm{e}}\phi_{\mathrm{e,sp},i-1}\right)\Psi_{\mathrm{e},\phi_{\mathrm{h}},\phi_{\mathrm{e,sp}}i}=E_{\mathrm{e},\phi_{\mathrm{h}},\phi_{\mathrm{e,sp}}i}\Psi_{\mathrm{e},\phi_{\mathrm{h}},\phi_{\mathrm{e,sp}}i}$$

$$-\nabla(\epsilon_0\epsilon_{\mathrm{r}}\nabla\phi_{\mathrm{e},i})=q_{\mathrm{e}}|\Psi_{\mathrm{e},\phi_{\mathrm{h}},\phi_{\mathrm{e,sp}}i}|^2$$

$$-\nabla(\epsilon_0\epsilon_{\mathrm{homo}}\nabla\phi_{\mathrm{e,homo},i})=q_{\mathrm{e}}|\Psi_{\mathrm{e},\phi_{\mathrm{h}},\phi_{\mathrm{e,sp}}i}|^2$$

$$\phi_{\mathrm{e,sp},i}=\phi_{\mathrm{e},i}-\phi_{\mathrm{e,homo},i}$$

$$\left(-\frac{\hbar^2}{2m_{\mathrm{e,eff}}}\nabla^2+V_{\mathrm{cb}}+q_{\mathrm{e}}\phi_{\mathrm{e,sp},i}\right)\Psi_{\mathrm{e},\phi_{\mathrm{h}},\phi_{\mathrm{e,sp}},i}=E_{\mathrm{e},\phi_{\mathrm{e,sp}},i}\Psi_{\mathrm{e},\phi_{\mathrm{h}},\phi_{\mathrm{e,sp}},i}$$

$$\left(-\frac{\hbar^2}{2m_{\mathrm{h,eff}}}\nabla^2+V_{\mathrm{vb}}+q_{\mathrm{h}}\phi_{\mathrm{h,sp},i}\right)\Psi_{\mathrm{h},\phi_{\mathrm{h,sp}},i}=E_{\mathrm{h},\phi_{\mathrm{h,sp}},i}\Psi_{\mathrm{h},\phi_{\mathrm{h,sp}},i}$$

$$E_{\mathrm{exc}}=E_{\mathrm{e},\phi_{\mathrm{e,sp}}i}+E_{\mathrm{h},\phi_{\mathrm{h,sp}},i}-\frac{E_{\mathrm{e},\phi_{\mathrm{e,sp}},i}-E_{\mathrm{e},\phi_{\mathrm{h}},\phi_{\mathrm{e,sp}},i}+(E_{\mathrm{h},\phi_{\mathrm{h,sp}},i}-E_{\mathrm{h},\phi_{\mathrm{e}},\phi_{\mathrm{h,sp}},i})}{2}$$

$$\phi_{\mathrm{h,sp},i}=0.5\phi_{\mathrm{h,sp},i-1}+0.5\phi_{\mathrm{h,sp},i-2}$$

$$\phi_{\mathrm{e,sp},i}=0.5\phi_{\mathrm{e,sp},i-1}+0.5\phi_{\mathrm{e,sp},i-2}$$

Figure 4.5.: Schrödinger-Poisson calculation sequences 1 and its modification for sequence 2.

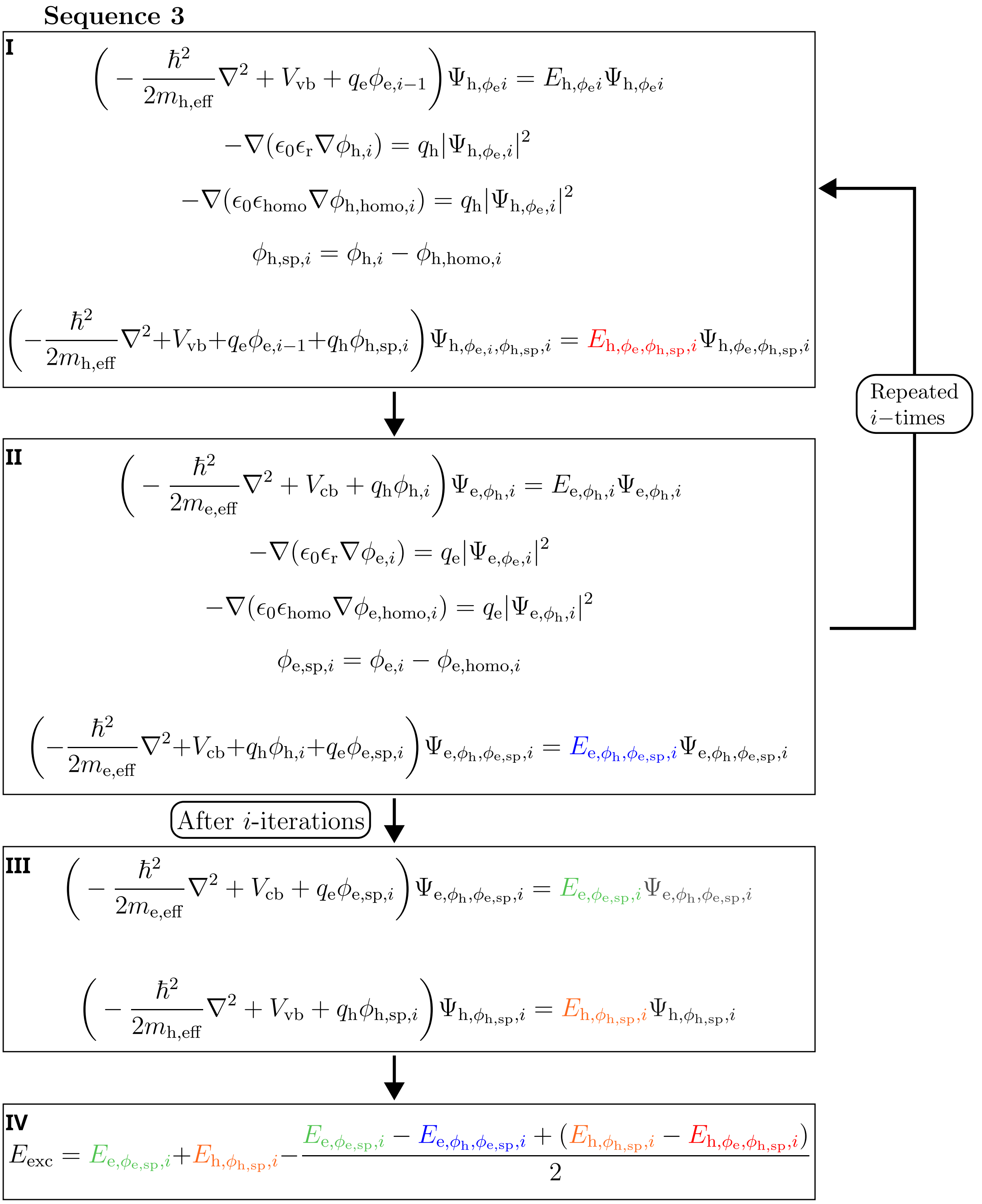

$$\left(-\frac{\hbar^2}{2m_{\mathrm{h,eff}}}\nabla^2 + V_{\mathrm{vb}} + q_{\mathrm{e}}\phi_{\mathrm{e},i-1}\right)\Psi_{\mathrm{h},\phi_{\mathrm{e}}i} = E_{\mathrm{h},\phi_{\mathrm{e}}i}\Psi_{\mathrm{h},\phi_{\mathrm{e}}i}$$

$$-\nabla(\epsilon_0\epsilon_{\mathrm{r}}\nabla\phi_{\mathrm{h},i}) = q_{\mathrm{h}}|\Psi_{\mathrm{h},\phi_{\mathrm{e}},i}|^2$$

$$-\nabla(\epsilon_0\epsilon_{\mathrm{homo}}\nabla\phi_{\mathrm{h,homo},i}) = q_{\mathrm{h}}|\Psi_{\mathrm{h},\phi_{\mathrm{e}},i}|^2$$

$$\phi_{\mathrm{h,sp},i} = \phi_{\mathrm{h},i} - \phi_{\mathrm{h,homo},i}$$

$$\left(-\frac{\hbar^2}{2m_{\mathrm{h,eff}}}\nabla^2+V_{\mathrm{vb}}+q_{\mathrm{e}}\phi_{\mathrm{e},i-1}+q_{\mathrm{h}}\phi_{\mathrm{h,sp},i}\right)\Psi_{\mathrm{h},\phi_{\mathrm{e},i},\phi_{\mathrm{h,sp}},i} = E_{\mathrm{h},\phi_{\mathrm{e}},\phi_{\mathrm{h,sp}},i}\Psi_{\mathrm{h},\phi_{\mathrm{e}},\phi_{\mathrm{h,sp}},i}$$

$$\left(-\frac{\hbar^2}{2m_{\mathrm{e,eff}}}\nabla^2 + V_{\mathrm{cb}} + q_{\mathrm{h}}\phi_{\mathrm{h},i}\right)\Psi_{\mathrm{e},\phi_{\mathrm{h}},i} = E_{\mathrm{e},\phi_{\mathrm{h}},i}\Psi_{\mathrm{e},\phi_{\mathrm{h}},i}$$

$$-\nabla(\epsilon_0\epsilon_{\mathrm{r}}\nabla\phi_{\mathrm{e},i}) = q_{\mathrm{e}}|\Psi_{\mathrm{e},\phi_{\mathrm{e}},i}|^2$$

$$-\nabla(\epsilon_0\epsilon_{\mathrm{homo}}\nabla\phi_{\mathrm{e,homo},i}) = q_{\mathrm{e}}|\Psi_{\mathrm{e},\phi_{\mathrm{h}},i}|^2$$

$$\phi_{\mathrm{e,sp},i} = \phi_{\mathrm{e},i} - \phi_{\mathrm{e,homo},i}$$

$$\left(-\frac{\hbar^2}{2m_{\mathrm{e,eff}}}\nabla^2+V_{\mathrm{cb}}+q_{\mathrm{h}}\phi_{\mathrm{h},i}+q_{\mathrm{e}}\phi_{\mathrm{e,sp},i}\right)\Psi_{\mathrm{e},\phi_{\mathrm{h}},\phi_{\mathrm{e,sp}},i} = E_{\mathrm{e},\phi_{\mathrm{h}},\phi_{\mathrm{e,sp}},i}\Psi_{\mathrm{e},\phi_{\mathrm{h}},\phi_{\mathrm{e,sp}},i}$$

$$\left(-\frac{\hbar^2}{2m_{\mathrm{e,eff}}}\nabla^2 + V_{\mathrm{cb}} + q_{\mathrm{e}}\phi_{\mathrm{e,sp},i}\right)\Psi_{\mathrm{e},\phi_{\mathrm{h}},\phi_{\mathrm{e,sp}},i} = E_{\mathrm{e},\phi_{\mathrm{e,sp}},i}\Psi_{\mathrm{e},\phi_{\mathrm{h}},\phi_{\mathrm{e,sp}},i}$$

$$\left(-\frac{\hbar^2}{2m_{\mathrm{h,eff}}}\nabla^2 + V_{\mathrm{vb}} + q_{\mathrm{h}}\phi_{\mathrm{h,sp},i}\right)\Psi_{\mathrm{h},\phi_{\mathrm{h,sp}},i} = E_{\mathrm{h},\phi_{\mathrm{h,sp}},i}\Psi_{\mathrm{h},\phi_{\mathrm{h,sp}},i}$$

$$E_{\mathrm{exc}} = E_{\mathrm{e},\phi_{\mathrm{e,sp}},i}+E_{\mathrm{h},\phi_{\mathrm{h,sp}},i}-\frac{E_{\mathrm{e},\phi_{\mathrm{e,sp}},i} - E_{\mathrm{e},\phi_{\mathrm{h}},\phi_{\mathrm{e,sp}},i} + (E_{\mathrm{h},\phi_{\mathrm{h,sp}},i} - E_{\mathrm{h},\phi_{\mathrm{e}},\phi_{\mathrm{h,sp}},i})}{2}$$

Figure 4.6.: Schrödinger-Poisson calculation sequence 3 that was used for anisotropic heterostructures.

that include both the self-polarization and Coulomb interaction, the self-polarization was neglected for these intermediate steps.

Parameters

The calculation parameters that were used are summarized in Table 4.1. In case of the alloys, the effective masses and dielectric constants were always interpolated linearly with the Cd fraction. For calculations of homostructures, the band gap was calculated quadratically under consideration of the bowing parameter $b = 0.387$ eV[182] from $Zn_{1-x}Cd_xSe$. While in the case of heterostructures, the valence band offset was interpolated linearly, and the conduction band offset was calculated from the sum of the valence band offset and quadratically interpolated band gap energy.

Table 4.1.: Calculation parameters for the effective masses $m_{\mathrm{e/h,eff}}$, dielectric constants $\epsilon_{0/\infty}$, band gaps E_{g} at 10 K, potential of the electron V_{e}, potential of the hole V_{h}. Direction-dependent properties are defined orthogonal $\perp$ and parallel $\parallel$ with respect to the crystallographic c-axis.

	CdS$\perp/\parallel$	ZnSe	CdSe	Vacuum	Ref.
$m_{\mathrm{e,eff}}(m_{\mathrm{e}})$	0.150 / 0.152	0.137	0.119	1.00	188
$m_{\mathrm{h,eff}}(m_{\mathrm{e}})$	0.40 / 1.82	0.52	0.33	1.00	188
$\epsilon_{\mathrm{s}}(\epsilon_0)$	10.2 / 9.0	8.9	9.6	1.0	188
$\epsilon_{\infty}(\epsilon_0)$	5.4 / 5.3	5.9	6.2	1.0	188
E_{g}(eV)	2.45	2.81	1.77	-	188
V_{e}(eV)	0.26	0.97	0.00	-	128
V_{h}(eV)	-0.42	-0.07	0.00	-	128

The bulk Fröhlich coupling constants that are listed in Table 4.2 were calculated according to Equation 2.1.20, using the bulk phonon energies CdSe = 26 meV, ZnSe = 31 meV, and CdS = 38 meV.[130]

Table 4.2.: Fröhlich coupling constants of electron α_{e} and hole α_{h} calculated with Equation 2.1.20.

	CdS	ZnSe	CdSe
α_{e}	0.62	0.48	0.45
α_{h}	1.49	0.86	0.75

5. Motivation and Goals

Measuring exciton–phonon coupling by single-particle spectroscopy is challenging, due to the low PL intensity of the phonon replica, as well as temporal fluctuations of the emission energy and photodarkening. As a consequence, no statistical data on exciton–phonon coupling exists for single-particle spectroscopy of heteronanocrystals. Since experimental results and theoretical calculations still deviate from each other, more experimental data is needed.[14,15] Therefore, single-particle PL spectroscopy is used in this work to improve the understanding of exciton–phonon coupling. Newly developed $Zn_{1-x}Cd_xSe/CdS$ DRs open up the possibility to vary the band alignment by controlling the Cd fraction x, and with it the charge-carrier localization and exciton–phonon coupling. The advantage of this sample system is that it allows to keep the geometry and synthesis conditions constant, which is important because geometrical changes or surface passivation can also affect exciton–phonon coupling. The determination of the Cd fraction x in these structures is difficult, due to the small volume fraction of the core of only a few percent. Therefore, evaluation of exciton–phonon coupling could be used to evaluate the charge-carrier localization and with it the Cd fraction x. The benefit of the DR structure is that it promotes the delocalization of the charge carriers, thereby increasing exciton–phonon coupling.

Atomistic calculations of exciton–phonon coupling are demanding. Because of this, it is desirable to develop a simplified model that can be used to estimate exciton–phonon coupling. For this purpose, quantum mechanical calculations within the effective-mass approximation are used to model the NCs.

DRs are of interest for various applications ranging from catalysis, light-emitting diodes, optical switches, to electric field sensors. In order to use DRs as optical switches or electric field sensors, their response to electric fields has to be understood. Consequently, single-particle PL spectroscopy at cryogenic temperatures is performed of DRs under the influence of externally controlled electric fields. These measurements will be used to characterize how optical properties, such as exciton–phonon coupling and spectral diffusion respond to external electric fields.

6. Results and Discussion

In the first section of this work, the correlation between charge-carrier localization and exciton–phonon coupling in individual NCs is investigated. For $Zn_{1-x}Cd_xSe/CdS$ DRs with different Cd fractions x, results from ensemble spectroscopy and single-particle spectroscopy are presented. The Cd fraction x of the first sample (DR-1) is predicted by quantum mechanical calculations within the effective-mass approximation. Afterwards, calculations of the electron and hole localizations are combined with a newly developed model for the prediction of exciton–phonon coupling. With these calculations different influences are evaluated, like the sample geometry, or the influence of surface charges. In the second section, the exciton–phonon coupling is again measured by single-particle spectroscopy, this time of spherical CdSe/CdS and $CdSe/CdSe_yS_{1-y}/CdS$ NCs. Furthermore, the temperature dependence of CdSe/CdS was analyzed, allowing them to be used as temperature probes. For the third section, the single-particle spectroscopy was combined with strong external electric fields, that allow to manipulate the charge-carrier localization during the measurement. Both, CdSe/CdS and $Zn_{1-x}Cd_xSe/CdS$ DRs were analyzed under influence of the electric fields.

6.1. Exciton–Phonon Coupling in ZnCdSe/CdS Dot-in-Rod Nanocrystals

6.1.1. Ensemble Spectroscopy

In order to investigate the correlation between exciton–phonon coupling and charge-carrier localization, either the geometry or the material composition of the NCs has to be varied. The best comparison between different samples can be achieved by keeping the geometry of the NCs constant while only changing the material composition so that other influences, like the size of the surface area or distance between the exciton and NC surface, remain unchanged between the samples.

A continuous change in the material composition can be achieved by cation exchange. Hence, $Zn_{1-x}Cd_xSe/CdS$ DRs were chosen as a novel model system. Here, the charge-carrier localization can be controlled by adjusting the Cd fraction in the core x, which in turn changes the band alignment continuously from type-II (ZnSe/CdS) to type-I (CdSe/CdS). Furthermore, DRs exhibit stronger exciton–phonon coupling than spherical NCs due to the stronger polarization of the exciton and reduced overlap. A set of four $Zn_{1-x}Cd_xSe$/CdS DRs samples, DR-1–4, with increasing Cd fraction x was provided by Jannik Rebmann. The first three samples, DR-1–4, were synthesized from the same batch of spherical ZnSe NCs with an average diameter of $d = 3.16$ nm. The cation exchange from Zn^{2+} to Cd^{2+} was carried out via in situ cation exchange prior to the anisotropic CdS shell growth. For sample DR-1, the ZnSe NCs were injected simultaneously with the S-precursor into a solution of the Cd-precursor at 320 °C, while for DR-2 and DR-3, the injection of the S-precursor was delayed by 10 s and 60 s, respectively. As a reference sample for a Cd fraction of $x = 1$, CdSe/CdS DRs were synthesized from CdSe NCs with a diameter of $d = 3.18$ nm, leading to sample DR-4. To increase the similarity of sample DR-4 and the other samples, CdSe NCs with an initial zinc blende crystal structure were used, which is uncommon for the synthesis of DRs. Although it should be noted that the synthesis conditions here promote a phase transformation from zinc blende to wurtzite.[187] (For further details on the synthesis, see Chapter 4.2.3.)

The band potentials and probability densities of the electron and hole that are possible in the $Zn_{1-x}Cd_xSe$/CdS DRs with an increasing Cd fraction x were calculated within the effective-mass approximation and are shown in Figure 6.1a–c as cross sections along the DR axis. As a consequence of the band alignment and Coulomb interaction, the exciton is primarily localized inside and around the $Zn_{1-x}Cd_xSe$ core. An increase of the Cd fraction x primarily reduces the conduction band offset, while the valence band offset is affected to a smaller degree. Therefore, the hole keeps its localization in the core while the electron steadily increases its localization in the core, resulting in a growing electron–hole wave function overlap. Additionally, the band gap energy and, with it, the exciton energy are decreasing. In Figure 6.1d, a representative transmission electron microscopy (TEM) image of sample DR-1 is shown. Here, it can be seen that the DRs do not have a symmetric rod shape but have a thickened side. This thickened side is already known to form around the position of the ZnSe core in ZnSe/CdS DRs.[143,189] The thickened side is also visible in the TEM data of the other samples DR-2–3, and also in DR-4, where it is unusual and likely arises due to the use of CdSe cores with an initial zinc blende phase. In the quantum mechanical calculations, the rod shape was adjusted by using a truncated cone, as illustrated in Figure 6.1e. The average geometries, together with their standard deviations of sample DR-1–4, are listed in Table A.1 (see Appendix A.1). The geometries of all four samples are similar to one another and also overlap in their standard deviations, as needed for the following investigation.

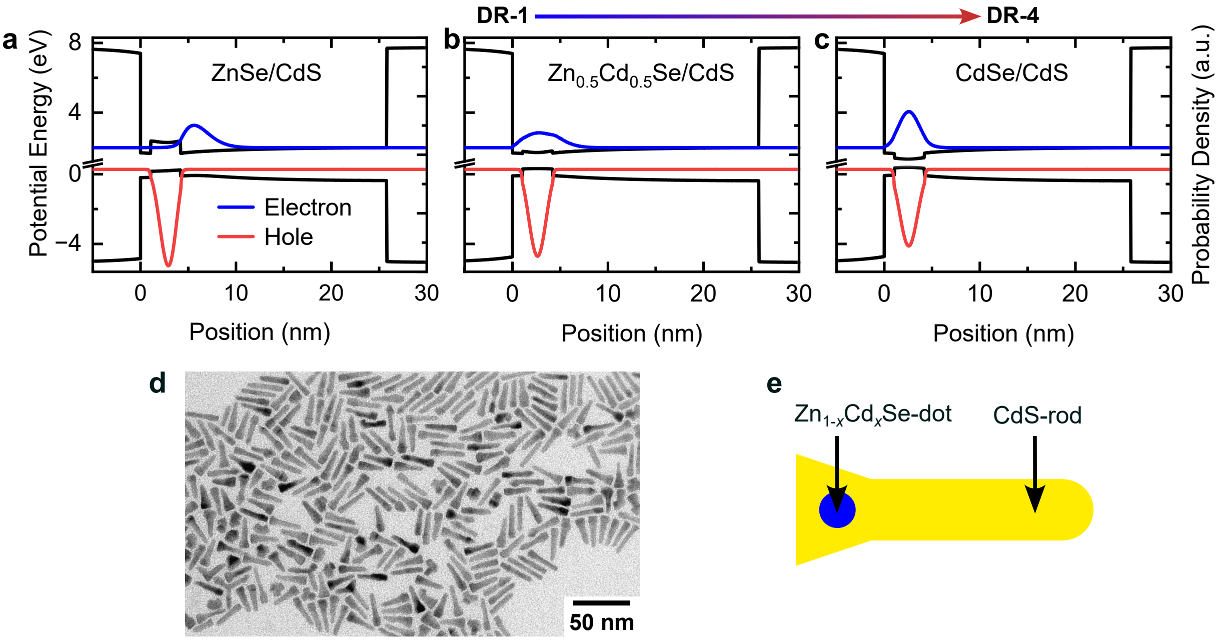

Figure 6.1.: (a–c) Cross sections of the calculated electron (blue) and hole (red) probability densities and their respective band potentials (black), including their Coulomb interaction, along the DR axis. (d) TEM image of the $Zn_{1-x}Cd_xSe/CdS$ DRs of sample DR-1. (e) 2D Sketch of the DR shape used in the quantum mechanical calculations. Adapted from Johst et al.[185]

Ensemble PL spectra of the samples were measured in vacuum at $T = 295$ K and $T = 10$ K[a], which are depicted in Figure 6.2a and b, respectively. In addition to the main PL peak, a second broader peak with lower energy and intensity arises around 1.75 eV at $T = 10$ K. The intensity of this side peak shows no clear trend within the sample series. The center wavelengths of the main PL peaks are listed in Table 6.1. In both temperature cases, the emission energy red-shifts within the sample series by about 100 meV, which is in agreement with an increasing Cd fraction x and lowered band gap energy. The position and FWHM of the secondary peak suggest that the peak originates from recombination of trapped charge carriers.[65,190] Figures 6.2c and d show the corresponding PL decay curves of the samples at $T = 295$ K and $T = 10$ K. It can be seen that the fluorescence lifetime decreases in the samples series, which is to be expected for an increasing electron–hole wave function overlap, as the band alignment changes from type-II to type-I with an increasing Cd fraction x. The curves were fitted using biexponential functions, and the fit results are compiled in Table 6.1.

In general, both the short and long components of the fluorescence lifetimes are decreasing along the sample series. The only small deviation of this trend lies between the short component of sample DR-3 and DR-4 at $T = 295$ K. If the temperature cases are

---

[a] The cryostat temperature of $T = 10$ K is an approximation of the exact sample temperature, which was obtained by the separate measurement of a temperature probe soldered on the sample holder.

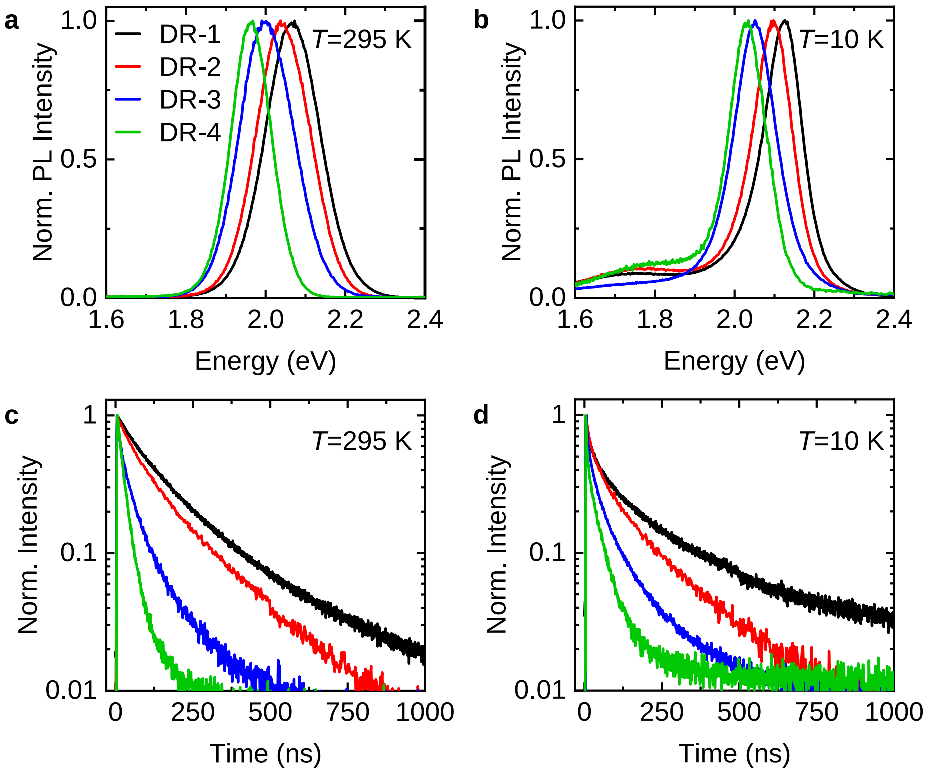

Figure 6.2.: (a,b) Ensemble PL spectra, and (c,d) ensemble PL decay curves of $Zn_{1-x}Cd_xSe/CdS$ DRs both measured in vacuum at T = 295 K and T = 10 K, respectively. Adapted from Johst et al.[185]

Table 6.1.: Fitting results of the spectral and time-resolved ensemble measurements at T = 295 K and T = 10 K: center of the photoluminescence energy E_{PL}, weight and lifetime of the short A_1 / τ_1 and long component A_2 / τ_2 and the intensity-averaged lifetime $\tau_{average}$.

Temperature	Sample	Core	E_{PL} (eV)	A_1	τ_1 (ns)	A_2	τ_2 (ns)	$\tau_{average}$(ns)
295 K	DR-1	ZnCdSe	2.060	0.41	68	0.58	210	184
	DR-2	ZnCdSe	2.036	0.44	53	0.51	184	158
	DR-3	ZnCdSe	1.998	0.51	14	0.41	76	65
	DR-4	CdSe	1.962	0.83	18	0.14	56	31
10 K	DR-1	ZnCdSe	2.120	0.50	18	0.42	198	172
	DR-2	ZnCdSe	2.094	0.48	14	0.40	140	126
	DR-3	ZnCdSe	2.051	0.53	8	0.35	77	67
	DR-4	CdSe	2.031	0.59	2	0.32	37	34

compared to each other, it is apparent that the average fluorescence lifetime at $T = 10$ K is shorter for DR-1 and DR-2, while it is slightly longer for DR-3 and DR-4.

In the commonly used three-state model[13,67,70,71], one might expect the fluorescence lifetime to increase with decreasing temperature. This is only the case for sample DR-3 and DR-4, and not for samples DR-1 and DR-2, which might be due to the fact that the complex underlying exciton-fine structure, in the case of alloying, cannot be approximated by the application of the simple three-state model. The deviation of the decreasing short component of the fluorescence lifetime between DR-3 and DR-4 could arise, for example, from a slight variation in the measured ensembles or likewise differences in the exciton-fine structure.

6.1.2. Simulation of Excitons in ZnCdSe dots

If the ZnSe NCs and S-precursor are injected simultaneously in the synthesis of the CdS shell in sample DR-1, an in situ cation exchange can occur. It is, therefore, essential to find the corresponding Cd fraction x of the unaltered synthesis. For the determination of the Cd fraction x quantum mechanical calculations, within the effective-mass approximation, of excitons in a spherical $\mathrm{Zn}_{1-x}\mathrm{Cd}_x\mathrm{Se}$ NC ($d = 3.16$ nm) were carried out. Figure 6.3a shows the calculated change of the exciton energy with increasing Cd fraction x for a homogeneous alloy and core/shell structure. In both cases, the homogeneous alloy and the core/shell formation, the exciton energy decreases nonlinearly. The horizontal lines indicate the temporal change of the emission energy of a cation exchange series[191], which was synthesized with the same conditions as the DRs but without the S-precursor.

In the synthesis of the CdS shell, the shell formation starts around 30–60 s and thereby inhibits the cation exchange. If the cation exchange would produce a core/shell structure, a much higher Cd fraction of $x = 0.8$ would be present in the core after the shell growth, compared to the formation of a homogeneous alloy, where x would be around 0.5. It has been reported that in $\mathrm{Zn}_{1-x}\mathrm{Cd}_x\mathrm{Se}$ NC, a homogeneous alloy forms above 240 °C.[151,192] The in situ cation exchange for sample DR-1-3 takes place at 320 °C. Thus, a homogeneous alloy should be assumed. The Cd fraction $x = 0.5$ is also consistent with inductively coupled plasma mass spectrometry.[191] Figure 6.3b shows the squared electron-hole overlap integral for different Cd fractions x. While the overlap increases steadily in the case of a homogeneous alloy, the overlap in the case of a core/shell structure would decrease first before increasing again. In spectroscopy measurements, the lifetime continuously increases in the first 120 s[191], which also suggests that a homogeneous alloy is present.

The spectroscopy data in Figure 6.2 point towards an increase of the Cd fraction x facilitated by the delayed injection of the S-precursor during the synthesis. As an additional confirmation of the increase in the Cd fraction of the core, Lars Klemeyer and Jagadesh

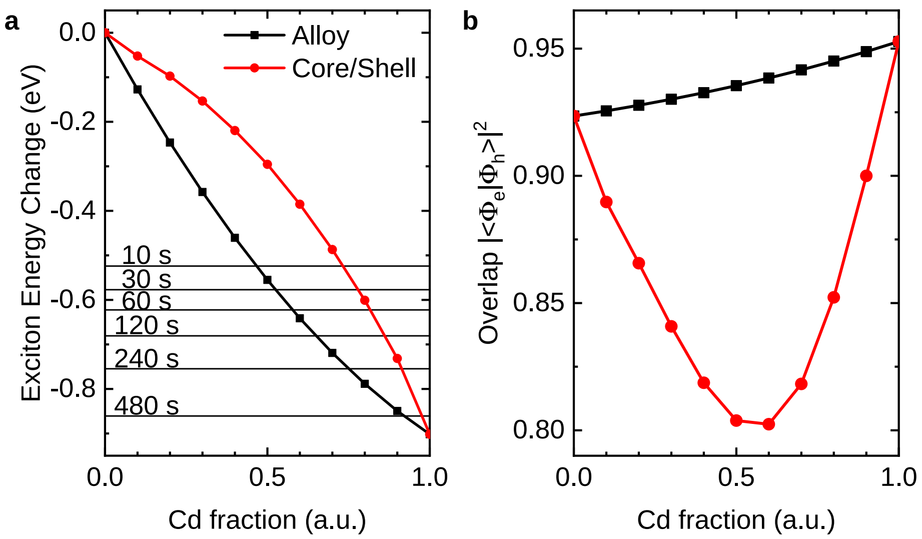

Figure 6.3.: Comparison of the calculated (a) exciton energy shift and (b) squared electron–hole wave function overlap of $Zn_{1-x}Cd_xSe$, with a diameter of $d = 3.16$ nm for different Cd fractions x. The horizontal lines indicate the experimental emission energies[191] during cation exchange at different reaction times. These experimental values were obtained from cation exchange of $Zn_{1-x}Cd_xSe$ NCs using the same conditions as for the DR synthesis, but without the addition of the S-precursor. Adapted from Rebmann et al.[191]

Jagadesh Kopula Kesavan from the Koziej group performed extended X-ray absorption fine structure (EXAFS) spectroscopy on $Zn_{1-x}Cd_xSe$/CdS DRs, which were synthesized using the same conditions with a slightly smaller ZnSe NCs diameter of 2.86 nm. They found Cd fractions of $x = 0.63$, 0.73, and 0.77 for the respective delay times of $\Delta t = 0$ s, $\Delta t = 10$ s, $\Delta t = 60$ s.[185] As a consequence of the smaller diameter and larger specific surface area, the cation exchange values determined by EXAFS spectroscopy represent upper boundaries for DR-1–3. The predicted Cd fractions of the EXAFS spectroscopy are also consistent with the evaluated Cd fraction of 0.5 for sample DR-1.

6.1.3. Single-Particle Spectroscopy

In this work, the exciton–phonon coupling is measured by PL spectroscopy of individual NCs. This method allows for direct analysis of the lowest exciton state, which is localized in the region of the $Zn_{1-x}Cd_xSe$/CdS interface (see Figure 6.1a–c). Other methods, like Raman spectroscopy, would be less suitable because the core volume makes up only around 3.4 % of the total DR volume. Hence, the signals of the CdS shell would overshadow the signals of the core area. Furthermore, the measurement of individual NCs allows for statistical investigation of the DRs and their exciton–phonon coupling behavior.

Resolving exciton–phonon coupling in PL spectroscopy requires a sufficiently small FWHM. The measurement of individual NCs reduces the FWHM of the PL by avoiding the inhomogeneous broadening present in the ensemble. The FWHM is further decreased by cooling the samples to $T = 10$ K, which reduces spectral diffusion and coupling to acoustic phonons.[81] Furthermore, the spectra were recorded with short integration times of only a few seconds, which further reduces the contribution of spectral diffusion. Figure 6.4 depicts a comparison of the temporal evolution of the PL of one individual DR from each of the four samples DR-1-4 at $T = 10$ K. Multiple peaks are visible in the single spectra; the peak with the largest energy and highest intensity is the ZPL. The red-shifted peaks are phonon replicas that originate from exciton–phonon coupling. The phonon replicas are repeated for higher orders, with decreasing intensities. The ZPL, together with the phonon replica, undergoes simultaneous spectral jumps of around 10–20 meV and jittering on a scale <7 meV, known as spectral diffusion. Spectral diffusion originates from the formation and movement of surface charges.[74,193,194] This simultaneous change of the ZPL and phonon replicas indicates the presence of individual DRs. The emission intensity exhibits grey states, as well as concrete off states, for example, between 82–92 s in panel c. The grey states originate from B-type blinking, while the off states are a result of A-type-blinking.[54] By tendency, the spectral diffusion becomes less pronounced with an increase of the Cd fraction x. This is a result of the increasing localization of the electron in the core for the transition from a type-II to a type-I band alignment. However, there are

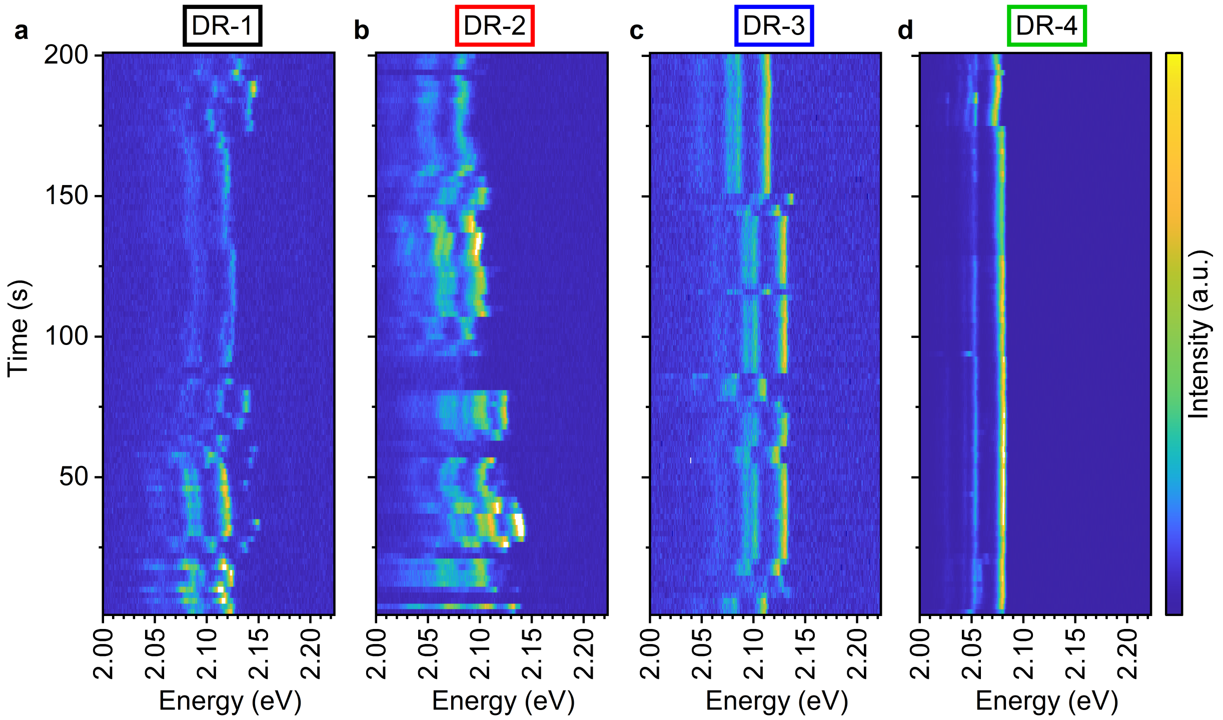

Figure 6.4.: Examples of spectral time traces, one from each of the four samples, measured from individual $Zn_{1-x}Cd_xSe/CdS$ DRs at $T = 10$ K with integration times of 2 s per spectrum.

exceptions to this trend, and spectral time traces with less strong spectral diffusion can be found in samples with a high Cd fraction x and vice versa.

Collecting statistical data from individual DRs is a difficult task because of the low PL intensity and pronounced photodarkening, which results in the fact that the PL of the DRs usually turns off after around 200 s. In order to increase the signal-to-noise ratio, spectra series with short integration times were measured from the individual DRs and then averaged. An example of this process is illustrated in Figure 6.5. From a spectral time trace like that shown in Figure 6.5a, a single ZPL energy was chosen. All spectra from the time trace that share a similar ZPL energy of $\Delta E \approx 2$ meV (equals $\lambda = 1$ nm) were then averaged. In this case the chosen ZPL energy was $E_{\mathrm{ZPL}} = 2.168$ eV. The ZPL energy was chosen based on the signal-to-noise ratio and on how well the phonon lines are separated. For this example, the averaged spectrum is shown in Figure 6.5b. The peak with the highest intensity is the ZPL, which is slightly broadened towards the lower energy side due to coupling to acoustic phonons. Red-shifted from the ZPL by around 28 meV and 38 meV, respectively, two first-order LO-phonon replicas are visible. Around

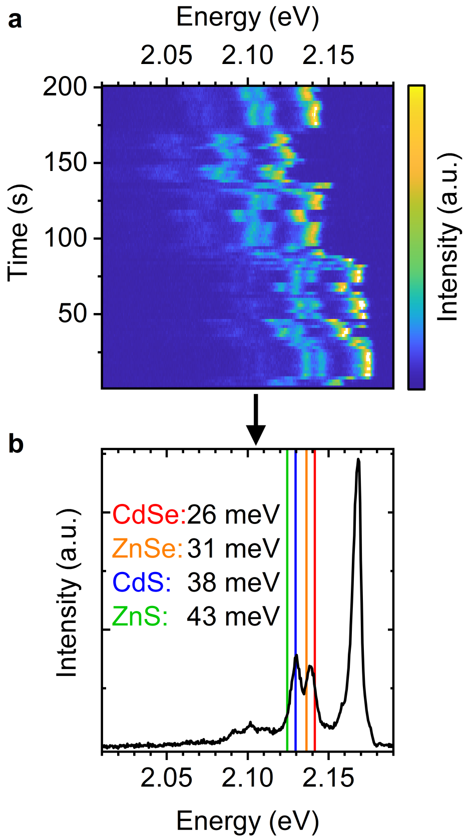

Figure 6.5.: (a) Spectral time trace of the PL from an individual $\mathrm{Zn}_{1-x}\mathrm{Cd}_x\mathrm{Se/CdS}$ DR of sample DR-2 measured at $T = 10$ K. (b) Averaged spectrum of spectra with a similar ZPL energy. The colored horizontal lines indicate the bulk values[130] of the phonon energies from the binary materials. Adapted from Johst et al.[185]

70 meV, the second-order phonon replicas appear, which are less well defined, due to their lower intensity. For the classification of these peaks, the bulk LO-phonon energies[130] of CdSe, ZnSe, CdS, and ZnS are marked by vertical lines. By comparison, the first peak of the first-order phonon lines lies in between the bulk phonon energies of CdSe and ZnSe, and, thus, will be referred to as a Se-type phonon replica in the following. The second peak coincides well with the bulk phonon energy of CdS and will be referred to as an S-type phonon replica.

Figure 6.6 shows one representative averaged spectrum of a single DR from each sample. For a better comparison, the spectra are normalized to their respective ZPL intensity. The total intensity of the LO-phonon coupling decreases with the increasing Cd fraction x and the associated transition from type-II to type-I band alignment. It can be clearly seen that the intensity ratio of the S- to Se-type phonons of first-order decreases continuously along the sample series. In the case of the second-order phonon replica, the individual peaks are less clearly distinguishable from each other due to the lower signal intensity. However, the underlying second-order S- and Se-type phonon replica ratio seems to follow a similar trend as the first-order replicas. In panel b of Figure 6.6, three second-order peaks are visible. If the energies of the first-order LO-phonons are used under the assumption of a harmonic oscillator, the three peaks can be assigned. The dotted vertical lines indicate this assignment, and the outer peaks are the second-order replicas of the Se-type (red) and S-type (blue), while the center peak matches the combined phonon oscillation of the first-order Se- and S-type replicas (violet). The second-order peaks are shifted to lower energies compared to the description of a harmonic oscillator, following expectations. For further discussion, only the individual first-order S- and Se-type phonons are considered

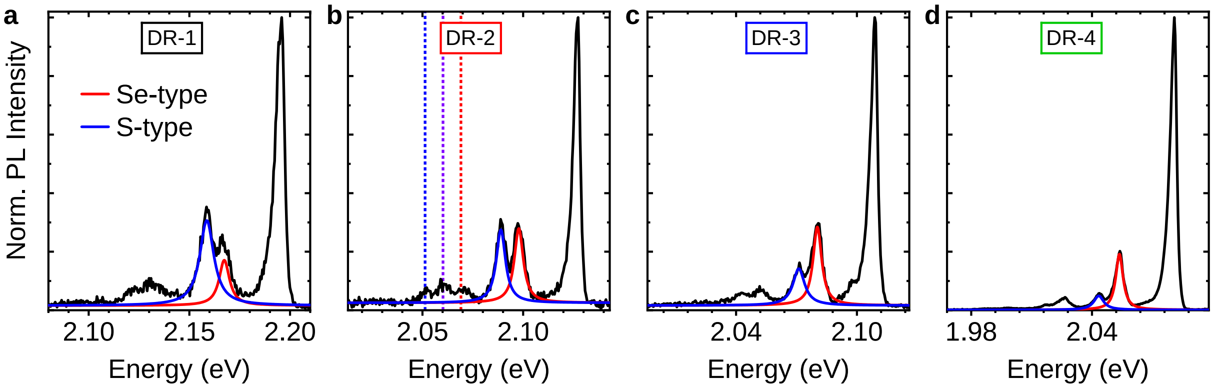

Figure 6.6.: Representative averaged PL spectra from single DRs at $T = 10$ K of each sample (a–d). The spectra are normalized to their respective ZPL intensity. The first-order LO-phonons were fitted by Lorentzian functions. The vertical dotted lines in panel b indicate the theoretical energy positions of the second-order phonon replica of Se(red), S(blue), and combined first-order Se+S(violet), extrapolated from the first-order S- and Se-type phonons. Adapted from Johst et al.[185]

because the higher order and combined oscillation modes have a lower signal-to-noise ratio, include anisotropic effects, and are convoluted due to the energetic proximity of three phonon peaks.

In order to obtain statistical data for the sample series, the averaging process for specific ZPLs described above was repeated on circa 100 individual DRs per sample. These 100 DRs were selected from a greater number of DRs based on their initial photostability and PL intensity. From the resulting spectra, 40–70 % provided a sufficient signal-to-noise ratio needed for accurate fitting of the LO-phonon replica and ZPL with Lorentzian functions. The results of the statistical evaluation of the ZPL energy and LO-phonon energies of the Se- and S-type phonons are listed in Table 6.2. Here, the average ZPL of the individual DRs shifts by around 100 meV across the sample series, which is in good agreement with the ensemble data from Table 6.1. In direct comparison, the average ZPL energies of the individual DRs are all higher than the ensemble PL energies, which is to be expected because the ensemble PL includes phonon coupling. The standard deviations of the average ZPL energies are higher for the samples DR-1–3 than for DR-4, which could arise from the fact that the cation exchange degree among the individual DRs can vary, thereby introducing inhomogeneity. The Se-type phonon energies exhibit no clear trend, albeit the energy of the Se-type phonon is lowest for DR-4, as expected. Overall, the Se-type phonon energies lie in between the bulk values of ZnSe (E_{Se} = 31 meV[130]) and CdSe (E_{Se} = 26 meV[130]), which is consistent for a starting Cd fraction x of 0.5 in sample DR-1. In theory, a continuous shift of the energy would have been expected,[195] which might be too small to be resolvable here.

Table 6.2.: Average values and standard deviations of the ZPL energy E_{ZPL}, first-order Se-type phonon $E_{\mathrm{LO_1(Se)}}$, and S-type phonon $E_{\mathrm{LO_1(S)}}$ evaluated from the statistical data of single-particle PL spectroscopy of the samples DR-1–4 at $T = 10$ K.

	DR-1	DR-2	DR-3	DR-4
E_{ZPL} (eV)	2.180 ± 0.052	2.154 ± 0.051	2.111 ± 0.051	2.082 ± 0.030
$E_{\mathrm{LO_1(Se)}}$ (meV)	28 ± 0.7	28 ± 0.5	28 ± 0.7	27 ± 0.4
$E_{\mathrm{LO_1(S)}}$(meV)	36 ± 0.4	38 ± 0.3	37 ± 0.7	36 ± 0.6

Likewise, the S-type phonon energy also shows no apparent trend, which is in line with expectations, as the CdS lattice should be nearly unchanged in the sample series. Both the S- and Se-type phonon modes can be red-shifted as a result of phonon confinement, although this effect is negligible due to its small magnitude.[102–104] Unlike the phonon energies, the relative intensities of the phonon replica can be linked to the Cd fraction x, as hinted before in Figure 6.6.

An overview of the statistical investigation of the different phonon coupling intensity ratios is given in Figure 6.7 by box plots. The corresponding average values and standard deviations are summarized in Table 6.3. In general, the scattering of the coupling intensities varies and is lowest in sample DR-4. The intensity ratios that were analyzed are: $(I_\mathrm{S}+I_\mathrm{Se})/I_\mathrm{ZPL}$, $I_\mathrm{S}/I_\mathrm{ZPL}$, $I_\mathrm{Se}/I_\mathrm{ZPL}$, and $I_\mathrm{S}/I_\mathrm{Se}$. The total coupling intensity $(I_\mathrm{S}+I_\mathrm{Se})/I_\mathrm{ZPL}$, depicted in Figure 6.3a, decreases across the sample series with the transition from the type-II to type-I band alignment. As shown in Figure 6.7b, the relative intensity of the S-type phonon $I_\mathrm{S}/I_\mathrm{ZPL}$ decreases continuously by a total factor of 5. The relative intensity of the Se-type phonon $I_\mathrm{Se}/I_\mathrm{ZPL}$, shown in Figure 6.7c, increases slightly in the first three samples (DR-1–3) and drops in sample DR-4, demonstrating a nonlinear trend. In order to describe the phonon coupling independently of the ZPL, the relative intensity ratio of the S- to Se-type phonon $I_\mathrm{S}/I_\mathrm{Se}$ was also evaluated, which is depicted in Figure 6.7d. The ratio $I_\mathrm{S}/I_\mathrm{Se}$ gradually decreases from sample DR-1 to DR-4.

To explain the observations in Figure 6.7, let us briefly recap the relevant theoretical background for exciton–phonon coupling in semiconductors. In ionic semiconductors as it is the case here, the exciton–LO-phonon coupling primarily originates from the Fröhlich interaction.[196] The Fröhlich interaction is facilitated by the coupling of the charge distribution from the exciton with the LO phonon via Coulomb interaction.[86,88] When the band alignment changes from type-II to type-I, the wave function overlap increases, which reduces the magnitude of exciton–phonon coupling, leading to the decrease of the total coupling in Figure 6.7a. Similar observations have been made by Groeneveld and de Mello Donegá[19], who investigated type-II bipod-shaped and prolate CdTe/CdSe NCs by ensemble photoluminescence excitation spectroscopy. They also found that the exciton–phonon coupling is stronger in the case of larger electron–hole wave function overlaps, which they attributed to the reduced Fröhlich coupling. In their sample set, the exciton–phonon coupling is less comparable because of the convolution with morphological changes. Furthermore, they could not distinguish the different phonon replicas and were only able to evaluate the total coupling owing to the similar phonon energies of CdTe and CdSe. The morphological changes in this work are minimized because of the applied cation exchange approach. The influence of morphological changes on the exciton–phonon coupling has been investigated by Lin et al.[93] They performed Raman spectroscopy of spherical CdSe/CdS NCs with different shell thicknesses and found that the exciton–phonon coupling was reduced with increasing shell thickness. This reduction was contrary to their expectations, as the overlap is decreasing, and the phonon coupling should have increased. The overall reduction of phonon coupling due to shell growth was later explained by Cui et al.[12] They found that a better surface passivation isolates the exciton from surface charges, which are responsible for an increase in the Fröhlich interaction.

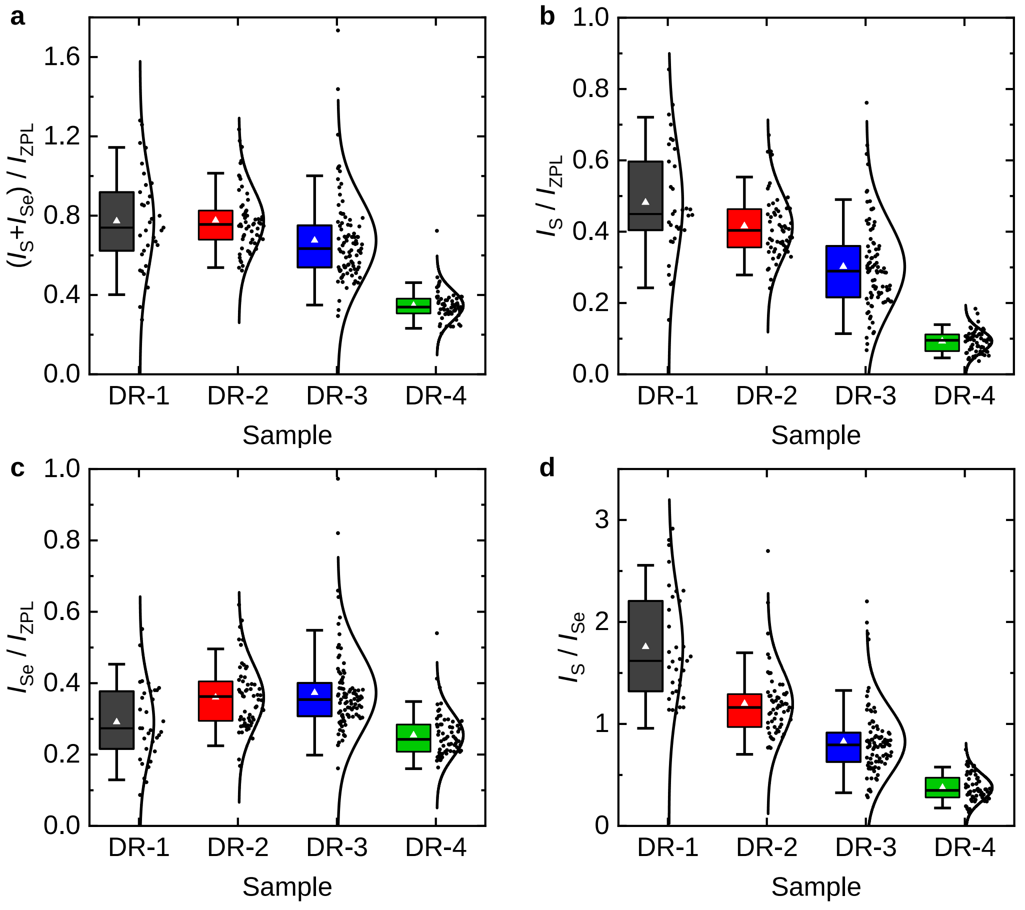

Figure 6.7.: Statistical data for relative phonon coupling intensities of individual Zn$_{1-x}$Cd$_x$Se/CdS DRs evaluated from the samples DR-1–4. (a) Relative total phonon intensity, (b) relative intensity of the S-type phonon, (c) relative intensity of the Se-type phonon, and (d) intensity ratio of the S- to Se-type phonon. The boxes span the interquartile range, the whiskers indicate the 95th percentile, the white triangles mark the average values, and the horizontal black lines inside the boxes show the median values. The statistical data were described by normal distributions. From the samples DR-1–4: 33, 59, 91, and 63, single DRs were analyzed, respectively. Adapted from Johst et al.[185]

Table 6.3.: Evaluation of the different phonon coupling ratios from Figure 6.7: Sum of the S- and Se-type phonon $(I_{(\mathrm{LO_1(Se)}}+I_{\mathrm{LO_1(S))}})$, S-type phonon $I_{\mathrm{LO_1(S)}}/I_{\mathrm{ZPL}}$ and Se-type phonon $I_{\mathrm{LO_1(Se)}}/I_{\mathrm{ZPL}}$ in relation to the ZPL. As well as the intensity ratio of the S- to Se-type phonon $I_{\mathrm{LO_1(S)}}/I_{\mathrm{LO_1(Se)}}$.

	DR-1	DR-2	DR-3	DR-4
$(I_{(\mathrm{LO_1(Se)}}+I_{\mathrm{LO_1(S))}})/I_{\mathrm{ZPL}}$	0.77 ± 0.24	0.78 ± 0.16	0.69 ± 0.24	0.35 ± 0.08
$I_{\mathrm{LO_1(S)}}/I_{\mathrm{ZPL}}$	0.48 ± 0.16	0.42 ± 0.09	0.30 ± 0.13	0.09 ± 0.03
$I_{\mathrm{LO_1(Se)}}/I_{\mathrm{ZPL}}$	0.29 ± 0.11	0.36 ± 0.09	0.37 ± 0.12	0.25 ± 0.06
$I_{\mathrm{LO_1(S)}}/I_{\mathrm{LO_1(Se)}}$	1.76 ± 0.53	1.20 ± 0.33	0.83 ± 0.33	0.38 ± 0.13

The strong decrease of the coupling to the S-type phonon in Figure 6.7b is in agreement with the change of the electron localization. The probability of the electron in the CdS shell decreases while it increases in the $Zn_{1-x}Cd_xSe$ core as a consequence of the transition from a type-II to a type-I band alignment.

For the Se-phonon coupling in Figure 6.7c, the alloy type is of particular importance. As a result of the high temperature during the in situ cation exchange[151,192], a homogeneous alloy is present in the $Zn_{1-x}Cd_xSe$ cores. Gong et al.[197] investigated spherical $Zn_{1-x}Cd_xSe$ NCs with different x in the case of an inhomogeneous alloy formed at 220 °C by performing resonance Raman spectroscopy. They found that the exciton–phonon coupling decreases with rising Cd fraction x due to the localization of the exciton in Cd-rich regions of the NCs. This decrease of the Se-type phonon is not present here, following expectations. Interestingly a nonlinear trend is present here, which could be the result of a more complex underlying behavior. For example, changes in the band-edge exciton fine structure could play a crucial role here, as they exhibit different coupling behaviors.[19]

Upon closer inspection of Figure 6.7, it becomes apparent that the coupling intensities scatter to different degrees, and the distribution width is smallest in sample DR-4. This can result from different particle-size distributions, varying degrees of cation exchange, and different surface-charge situations among the individual NCs. For comparison, Empedocles et al.[74] performed single-particle PL spectroscopy of spherical CdSe and CdSe/ZnS NCs and reported significant variations of the HR factors in the range of 0.06–1.3, with an average value of 0.488. In the same way, Dufaker et al.[198] investigated InGaAs NCs, which were grown in the vapor phase. These InGaAs NCs are nearly identical in their morphologies but still exhibited varying HR factors by a factor of up to 2, even for identical charge states of the exciton.

6.1.4. Calculation of Excitons and their Phonon Coupling

For a better understanding of the exciton–phonon coupling, quantum mechanical calculations are needed. II-VI semiconductor DRs contain around 20,000 heavy atoms, leading to an even larger number of electrons; hence, accurate quantum mechanical calculations for these nanostructures are resource-intensive and difficult to perform. Thus, a simplified approach based on quantum mechanical calculations was adapted from literature.[82,111]

Convergence of the Calculations

In order to calculate the exciton–phonon coupling, the first step is to solve the Schrödinger equations of the electron and hole, including their Coulomb interaction. This is implemented by the iterative calculation of the Schrödinger and Poisson equations. Additionally, the self-polarization can be approximated from the difference of the electric potential of a charge carrier in the case of an inhomogeneous dielectric environment and a hypothetical homogeneous environment.[111] The geometry of the DRs was approximated by a rod with a diameter D and length l. At the end of the (001) facet, a truncated cone with a base diameter C, height $C/2$, and top diameter equal to the rod diameter D was added. Three MLs (3×0.35 nm[199]) away from the (001) facet, inside the cone, a spherical core with diameter d was placed. The geometry parameters were mainly obtained from TEM data except for the average core diameters, which were determined by the absorption maxima in UV/Vis spectroscopy.[200,201] A list of the average geometry parameters and their standard deviations is compiled in Table A.1. The cation distribution of the core was modeled as a homogeneous alloy.[151,191,192,202] Strain effects, due to the lattice mismatch between core and shell, were neglected owing to their weak effect on the band alignment.[141] More details on the calculations are presented in Chapter 4.4.

In the case of a type-II, and to some degree also for a quasi-type-II band alignment, the Coulomb interaction between the electron and hole and the self-polarization of the charge carriers are of similar magnitude. As a consequence, they counteract each other. This, combined with the fact that the Coulomb interaction and self-potential cannot be calculated simultaneously but in separate steps, impacts the convergence of the self-consistent calculation. For a high-symmetry structure, like a sphere, the calculations converge without a problem. However, the calculations do not easily converge in the asymmetric DR system. Thus, three different calculation sequences have been evaluated for the implementation of the Coulomb interaction and self-polarization. A detailed overview of the sequences can be found in Chapter 4.4.

In sequence 1, the Coulomb interaction between electron and hole and the self-polarization are calculated from the respective probability densities. The probability densities used here were derived from the Schrödinger equations, which included both the electron–hole Coulomb interaction and the self-polarization from the previous iteration step. The resulting convergences of the electron and hole energies for a ZnSe/CdS DR, without the band gap energy, are shown in Figure 6.8a/b as black dots. In both cases, the energy changes by 10 % between the 9th and 10th iteration steps. This first sequence was adjusted by including not only the self-polarization from the previous iteration but from the previous two iterations as a superposition. The corresponding self-potentials of the electron and hole used in sequence 2 were

$$\phi_{\mathrm{e,sp},i} = 0.5\phi_{\mathrm{e,sp},i-1} + 0.5\phi_{\mathrm{e,sp},i-2} \tag{6.1.1}$$

and

$$\phi_{\mathrm{h,sp},i} = 0.5\phi_{\mathrm{h,sp},i-1} + 0.5\phi_{\mathrm{h,sp},i-2}, \tag{6.1.2}$$

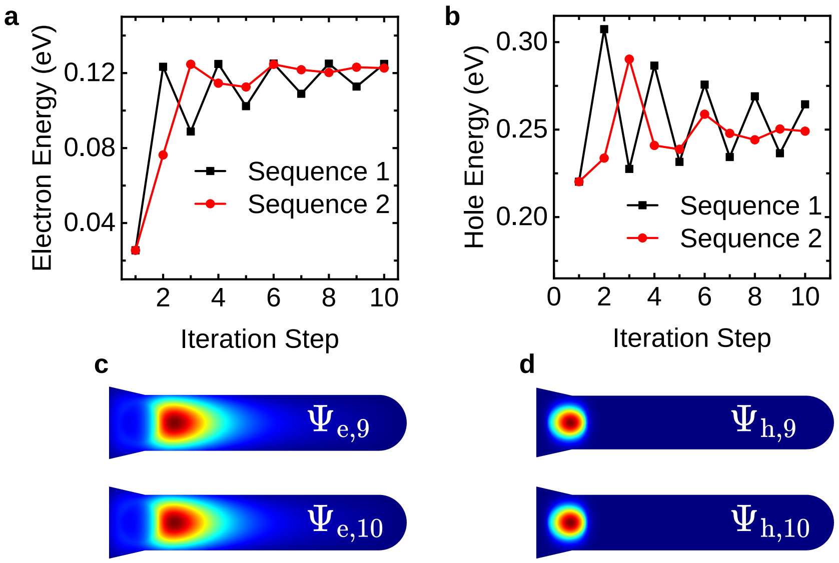

Figure 6.8.: Comparison of the convergence behavior of the self-consistent exciton calculation for the sequences 1 and 2 (see Chapter 4.4) for a ZnSe/CdS DR. Energy convergence of (a) the electron and (b) the hole. Cross sections of the wave functions from the 9th and 10th iteration steps of sequence 2 for (c) the electron and (d) hole, respectively.

respectively. The convergence by application of sequence 2 is shown in Figure 6.8a and b as red dots. The convergence is improved, and the energy of the electron and hole changes by <0.5 % from iteration step 9 to 10. In Figure 6.8c/d, the corresponding wave functions of sequence 2 are visualized as cross sections. It can be seen that the wave functions remain nearly constant between the iteration steps.

At first glance, the convergence behavior of sequence 2 appears to be fine, but if the geometry of the DRs is varied slightly, the convergence behavior worsens. For example, if the core position is changed by two MLs in the $[00\bar{1}]$ direction, the good convergence behavior is lost. Figure 6.9 shows the results for the variation of the core position. The electron energy retains a good convergence, but the hole energy varies by 11 % in the last iterations. Furthermore, the electron wave function changes greatly between the 9th and 10th iteration steps. This behavior repeats itself in the preceding iterations. To a smaller degree, the hole wave function varies between these iteration steps as well.

For sequence 3, the calculation of the self-polarization is decoupled from the convergence of the electron and hole interaction. As a consequence, in Figure 6.10, the energies of electron and hole are already converged after the second iteration. It can also be seen that the wave functions of electron and hole stay constant between the 5th and 6th iteration steps.

In this work, the self-polarization was approximated by calculating the difference between the electric potential of the respective charger carrier in an inhomogeneous and homogeneous dielectric environment (Equation 3.3.7), as proposed by Park et al.[111,180]

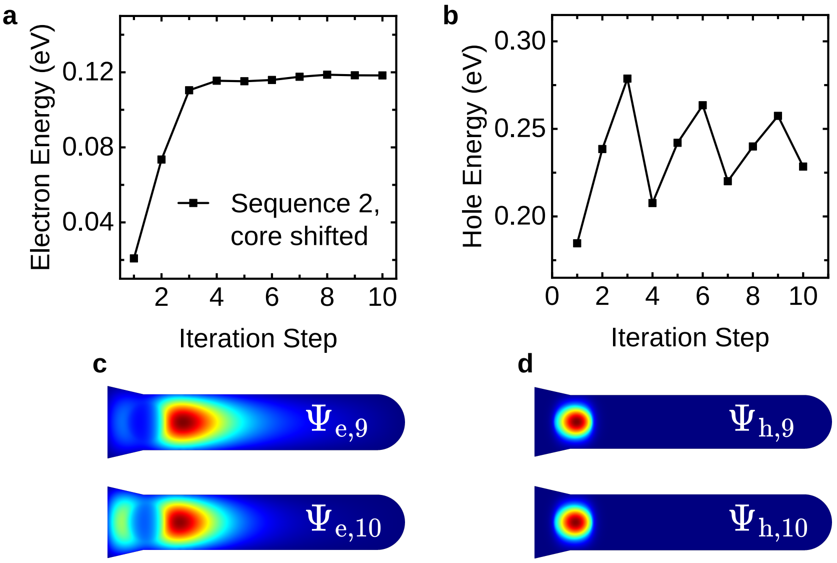

Figure 6.9.: Overview of the convergence behavior of the self-consistent exciton calculation for sequence 2 for a ZnSe/CdS DR, for which the core position was shifted by 3 MLs in the $[00\bar{1}]$ direction (see Chapter 4.4). Energy convergence of (a) the electron and (b) the hole. Cross sections of the wave functions from the 9th and 10th iteration steps for (c) the electron and (d) hole, respectively.

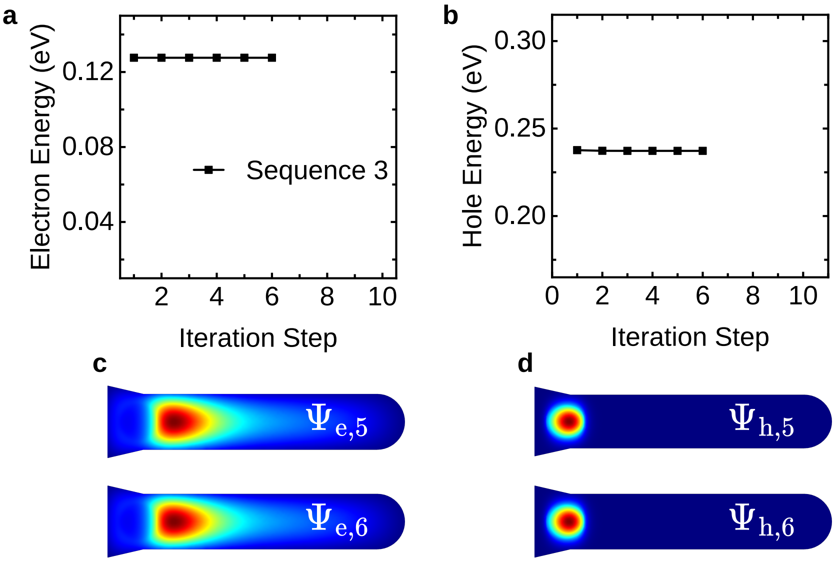

Figure 6.10.: Overview of the convergence behavior of the self-consistent exciton calculation for sequence 3 (see Chapter 4.4) for a ZnSe/CdS DR. Energy convergence of (a) the electron and (b) the hole. Cross sections of the wave functions from the 5th and 6th iteration step for (c) the electron and (d) hole, respectively.

For the calculation of the homogeneous dielectric environment, the dielectric constant of either the core, shell or an average of the two is used. In the case of the DRs, the dielectric constant of the $Zn_{1-x}Cd_xSe$ was chosen. This means that the accuracy of the approximation for the self-polarization changes with the Cd fraction in the core x and overlaps with the analysis of calculated trends. Hence, for further evaluations, the self-polarization is neglected.

Exciton Energy and Overlap

In Figure 6.11a, the calculated exciton energy shift for the four sample geometries DR-1–4 at $T = 10$ K is depicted, with respect to the energy in case of a Cd fraction of $x = 0.5$. Additionally, the experimental values of the samples DR-1–4 are indicated by horizontal lines. The energy decreases continuously as the Cd fraction x increases. This trend is similar regardless of the respective sample geometry, demonstrating that the geometrical influence is kept to a minimum. Compared to the experimentally observed red-shift of the emission energy from sample DR-1 to DR-4 of around 0.1 eV (Table 6.1), the energy shift is overestimated in the calculations, which could originate from the selection of the calculation parameters. In order to prevent overfitting of the data, the calculation parameters were collected from as few literature sources as possible.

The calculated absolute squared overlap of the electron and hole wave functions, depicted in Figure 6.11b, increases in the form of a sigmoid function. This sigmoid function is in agreement with the transition from the type-II to type-I band alignment with increasing Cd fraction and thereby increasing wave function overlap. For comparison, the measured decay rates, normalized to sample DR-4, are marked by horizontal lines.

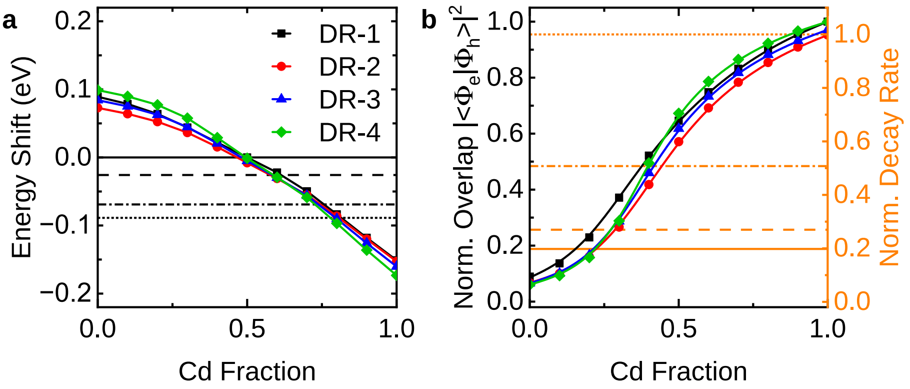

Figure 6.11.: Calculations of (a) the energy shift, in relation to the Cd fraction of $x = 0.5$, and (b) the normalized squared wave function overlap integral of the exciton for the samples DR-1–4 at $T = 10$ K. The horizontal lines mark the experimental data of sample DR-1 (continuous line), DR-2 (dashed line), DR-3 (dotted-dashed line) and DR-4 (dotted line). Both the squared absolute value of the overlap integral and the decay rate were normalized with respect to sample DR-4.

Exciton–Phonon Coupling Derived from the Wave Functions

A deeper understanding of the spectroscopical investigation can be gained by performing calculations of the exciton–phonon coupling. These calculations are challenging as a result of the large number of heavy atoms present in the NCs. Nonetheless, sophisticated atomistic calculations have been reported by different groups.[15,96] Such calculations are beyond the scope of this work, and instead, a simplified approach was developed to model the exciton–phonon coupling.

The magnitude of exciton–phonon coupling is commonly described by the Huang–Rhys factor.[203] In PL measurements, the HR factor is equal to the intensity ratio of the first-order phonon-replica to the ZPL.[19,86,95] The proposed model of this work is built around the fact that the coupling strength is proportional to the absolute difference in probability density of electron and hole.[21,25,94,198] The contributions of the electron and hole to the exciton–phonon coupling are not equal due to their different effective masses[89], which has to be accounted for in the model development. Moreover, the coupling strength depends on the respective material,[89] and is thus different in the core and shell of the DRs. This leads to the simplified model description of relative intensities of the S-type phonon of the shell and the Se-type phonon of the core:

$$\frac{I_{\mathrm{S}}}{I_{\mathrm{ZPL}}} = \left|\beta_{\mathrm{S}}^{\mathrm{e}} \cdot \rho_{\mathrm{shell}}^{\mathrm{e}} - \beta_{\mathrm{S}}^{\mathrm{h}} \cdot \rho_{\mathrm{shell}}^{\mathrm{h}}\right| \tag{6.1.3}$$

and

$$\frac{I_{\mathrm{Se}}}{I_{\mathrm{ZPL}}} = \left|\beta_{\mathrm{Se}}^{\mathrm{e}} \cdot \rho_{\mathrm{core}}^{\mathrm{e}} - \beta_{\mathrm{Se}}^{\mathrm{h}} \cdot \rho_{\mathrm{core}}^{\mathrm{h}}\right| . \tag{6.1.4}$$

Here, the probabilities

$$\rho_{\mathrm{shell,core}}^{\mathrm{e,h}} = \int_{\mathrm{shell,core}} |\Psi_{\mathrm{e,h}}|^2 \mathrm{d}V \tag{6.1.5}$$

are weighted by coupling constants $\beta_{\mathrm{S,Se}}^{\mathrm{e,h}}$, which account for the charge-carrier and material specific coupling differences. From the Equations 6.1.3 and 6.1.4 it becomes apparent that the phonon coupling vanishes in the case of a perfect overlap of the electron and hole wave functions $\Psi_{\mathrm{e,h}}$, which is consistent with the mechanisms behind exciton–phonon coupling.

In order to derive the four unknown coupling constants $\beta_{\mathrm{S,Se}}^{\mathrm{e,h}}$, four equations are needed. For each sample, two equations can be constructed: one for the shell (Equation 6.1.3) and one for the core (Equation 6.1.4). The Cd fraction has to be known for two samples. In the case of the samples DR-2–3, the Cd fractions x have the highest uncertainty. For sample DR-1, the Cd fraction was determined to be around 0.5[191] (Chapter 6.1.2). The

Cd fraction in sample DR-4 is known to be 1.0. Accordingly, sample DR-1 and DR-4 are suitable for building two linear systems of equations for the shell

$$\left|\begin{pmatrix} \rho^{\mathrm{e}}_{\mathrm{S}}(0.5) & -\rho^{\mathrm{h}}_{\mathrm{S}}(0.5) \\ \rho^{\mathrm{e}}_{\mathrm{S}}(1.0) & -\rho^{\mathrm{h}}_{\mathrm{S}}(1.0) \end{pmatrix} \begin{pmatrix} \beta^{\mathrm{e}}_{\mathrm{S}} \\ \beta^{\mathrm{h}}_{\mathrm{S}} \end{pmatrix}\right| = \begin{pmatrix} \frac{I_{\mathrm{S}}}{I_{\mathrm{ZPL}}}(0.5) \\ \frac{I_{\mathrm{S}}}{I_{\mathrm{ZPL}}}(1.0) \end{pmatrix} \tag{6.1.6}$$

and the core

$$\left|\begin{pmatrix} \rho^{\mathrm{e}}_{\mathrm{Se}}(0.5) & -\rho^{\mathrm{h}}_{\mathrm{Se}}(0.5) \\ \rho^{\mathrm{e}}_{\mathrm{Se}}(1.0) & -\rho^{\mathrm{h}}_{\mathrm{Se}}(1.0) \end{pmatrix} \begin{pmatrix} \beta^{\mathrm{e}}_{\mathrm{Se}} \\ \beta^{\mathrm{h}}_{\mathrm{Se}} \end{pmatrix}\right| = \begin{pmatrix} \frac{I_{\mathrm{Se}}}{I_{\mathrm{ZPL}}}(0.5) \\ \frac{I_{\mathrm{Se}}}{I_{\mathrm{ZPL}}}(1.0) \end{pmatrix}. \tag{6.1.7}$$

To solve these equation systems, the corresponding probabilities $\rho^{\mathrm{e,h}}_{\mathrm{shell,core}}(x)$ were calculated within the effective mass approximation based on the Cd fractions of $x = 0.5$ and 1.0. Together with the experimental data of DR-1 and DR-4, from Table 6.3, the equation systems for the shell

$$\left|\begin{pmatrix} 0.68 & -0.13 \\ 0.44 & -0.15 \end{pmatrix} \begin{pmatrix} \beta^{\mathrm{e}}_{\mathrm{Se}} \\ \beta^{\mathrm{h}}_{\mathrm{Se}} \end{pmatrix}\right| = \begin{pmatrix} 0.48 \\ 0.09 \end{pmatrix} \tag{6.1.8}$$

and the core

$$\left|\begin{pmatrix} 0.32 & -0.87 \\ 0.56 & -0.85 \end{pmatrix} \begin{pmatrix} \beta^{\mathrm{e}}_{\mathrm{S}} \\ \beta^{\mathrm{h}}_{\mathrm{S}} \end{pmatrix}\right| = \begin{pmatrix} 0.29 \\ 0.25 \end{pmatrix} \tag{6.1.9}$$

were obtained. By solving these two equation systems, the coupling constants $\beta^{\mathrm{e}}_{\mathrm{S}} = 1.35$, $\beta^{\mathrm{h}}_{\mathrm{S}} = 3.35$, $\beta^{\mathrm{e}}_{\mathrm{Se}} = 0.12$, and $\beta^{\mathrm{h}}_{\mathrm{Se}} = 0.38$ are obtained. Comparing the coupling constants β with the bulk Fröhlich coupling constants α (Table 4.2) makes it clear that they share some similarities. In both cases, the coupling constants for the hole are larger than for the electron. Additionally, the ratio of $\beta^{\mathrm{e}}_{\mathrm{S}}/\beta^{\mathrm{h}}_{\mathrm{S}}$ resembles that of $\alpha^{\mathrm{e}}_{\mathrm{S}}/\alpha^{\mathrm{h}}_{\mathrm{S}}$. This means that the coupling constants β behave like Fröhlich coupling constants for the NC case. These coupling constants β were used together with calculated probabilities to solve Equations 6.1.3 and 6.1.4.

From this procedure, the coupling ratios for different Cd fractions x were calculated, which are summarized in Figure 6.12. Panels a–c depict the relative coupling intensities of the S-type phonon $(I_{\mathrm{S}})/I_{\mathrm{ZPL}}$, the Se-type phonon $(I_{\mathrm{Se}})/I_{\mathrm{ZPL}}$, and their sum in relation to the ZPL. Besides this, panel d shows the intensity ratio of the S- to Se-type phonon. The black curves in all panels represent the calculation results in the case of the averaged sample geometry. For an easier comparison, the average values of the experimental coupling ratios are included as horizontal lines. The calculated total coupling intensity (Figure 6.12a) decreases continuously. Hence, the weak experimental decrease among the

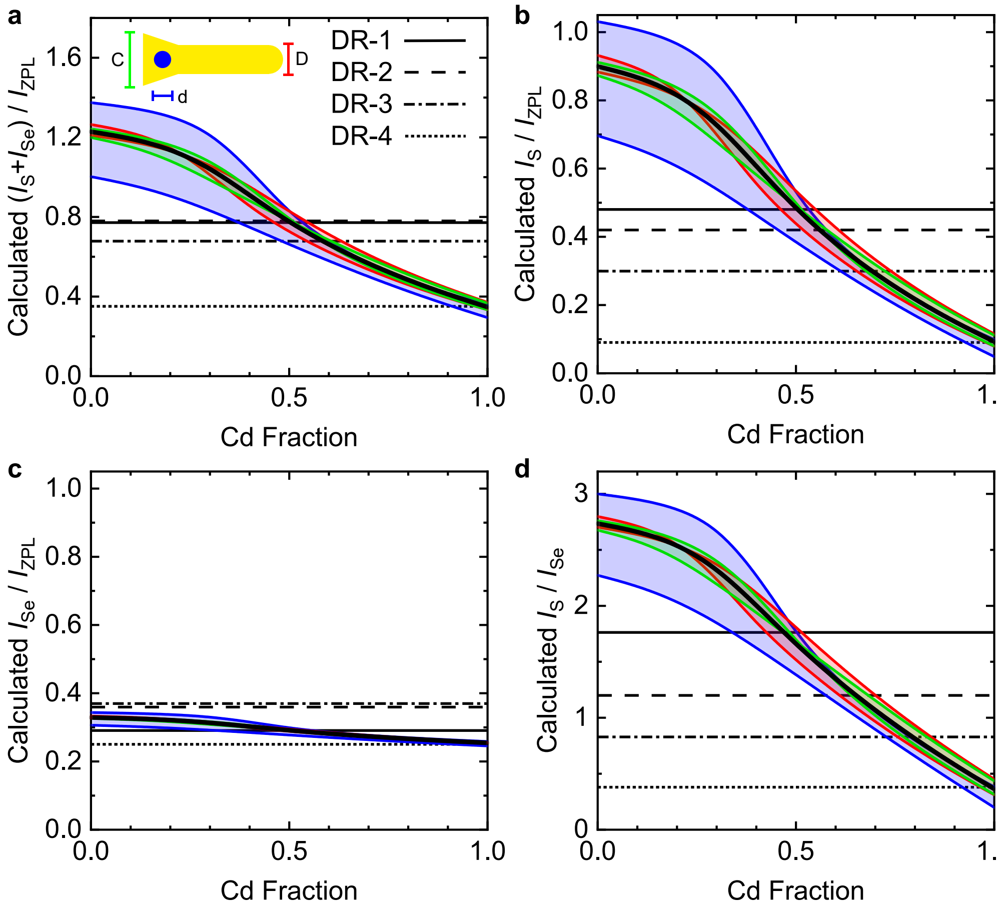

Figure 6.12.: Theoretical modeling of the phonon coupling intensity ratios from Figure 6.7. The different coupling ratios are (a) $(I_\mathrm{S}+I_\mathrm{Se})/I_\mathrm{ZPL}$, (b) $I_\mathrm{S}/I_\mathrm{ZPL}$, (c) $I_\mathrm{Se}/I_\mathrm{ZPL}$ and (d) $I_\mathrm{S}/I_\mathrm{Se}$. The black line corresponds to calculations using the averaged geometry, while the colored lines illustrate the influence of independently changing the core (d = 3.17 ± 0.43 nm), rod (D = 4.78±0.62 nm), and cone (C = 6.21±1.40 nm) diameters, based on standard deviations evaluated from TEM data. The rod length was fixed to the average value of 25.78 nm. Experimental values are included as horizontal lines. A cross-section of the geometry used in the calculation is shown as an inset. Adapted from Johst et al.[185]

first three samples is retained. Coupling to the S-type phonon decreases strongest with increasing Cd fraction x (Figure 6.12b), which is in agreement with the experimental change from 0.5 down to 0.1. Accordingly, the model predicts x of DR-2 and DR-3 to be 0.57 and 0.69. The predicted coupling to the Se-type phonon decreases on a much smaller scale from around 0.35 to 0.25 with increasing x. It can be seen as nearly constant, which concurs with the experimental trend of the Se-type phonon. Consequently, the main contribution towards the total phonon coupling (Figure 6.12) comes from the coupling to the S-type phonon. In order to describe the S- and Se-type phonon coupling independent of the ZPL, their direct coupling ratio is evaluated in Figure 6.12d. From this ratio, the derived Cd fractions x of DR-2 and DR-3 are 0.65 and 0.79, respectively. As a result, the predicted Cd fractions x of DR-2 and DR-3 are comparable to expectations based on the EXAFS spectroscopy data (Chapter 6.1.2).

Within the sample, the individual NCs, each slightly vary in size, resulting in the observation of a distribution of coupling ratios (Figure 6.7). It is, therefore, interesting to perform an analysis of the geometrical influences of each geometry parameter. For this purpose, the core diameter (blue), rod diameter (red), and cone diameter (green) were separately changed according to their standard size deviations, which were derived from their respective TEM data (Table A.1 in Appendix A.1). This parameter variation is indicated in Figure 6.12 by colored lines. The calculations reveal that the strongest dependence of the phonon coupling is related to the core diameter, while the rod and cone diameters are less important. Moreover, the combination of the effects from the different size distributions results in a broader distribution of phonon coupling ratios for lower Cd fractions x. This effect is also visible in the experimental results depicted in Figure 6.7.

Aside from geometrical influences, the modeled coupling ratios also depend on the choice of the parameters used in the calculation of the probabilities $\rho^{\mathrm{e,h}}_{\mathrm{shell,core}}$. Therefore, in order to determine the sensitivity toward changes in the chosen parameters, further calculations were performed. Figure 6.13 shows a comparison of the parameter variation (colored lines) to previous calculations (black). Varying the core position along the $[00\bar{1}]$ crystal direction by 2 MLs (0.7 nm[199]) has a minimal influence. Regarding the values of the band offsets, various values can be found in the literature; for simplicity, only two exemplary values are evaluated here. The first is the larger valence band offset of CdS–CdSe of 0.55 eV[134], which primarily increases the coupling to the S-type phonon over the whole range of Cd fractions x while keeping the overall coupling trends the same. The second is the larger valence band offset of ZnSe–CdSe of 0.11 eV[134], also retains the coupling trends and only shifts them to slightly lower values. Overall, the parameter variations in Figure 6.13 affected the exciton–phonon coupling only to a small degree.

When the standard deviations in Figure 6.7d are evaluated quantitatively, it becomes clear that the standard deviation measured for sample DR-1 is four times larger than for DR-4. When compared to the summation of the calculated standard deviations, based on the geometrical variations, it stands out that the standard deviation for DR-1 is only 1.5 times larger than for DR-4. Pointing towards an additional influence that has not been accounted for thus far. Multiple groups reported that the intrinsic exciton–phonon coupling is increased in the presence of surface charges and point defects.[12,21–25] Hence, the relevance of surface charges was investigated for the DRs. In order to model the influence of surface charges, either a negative or positive single point charge was placed at the transition point between the cone and rod cylinder. Modeling surface charges by using point charges has previously been proven to be a suitable method.[77,79,82]

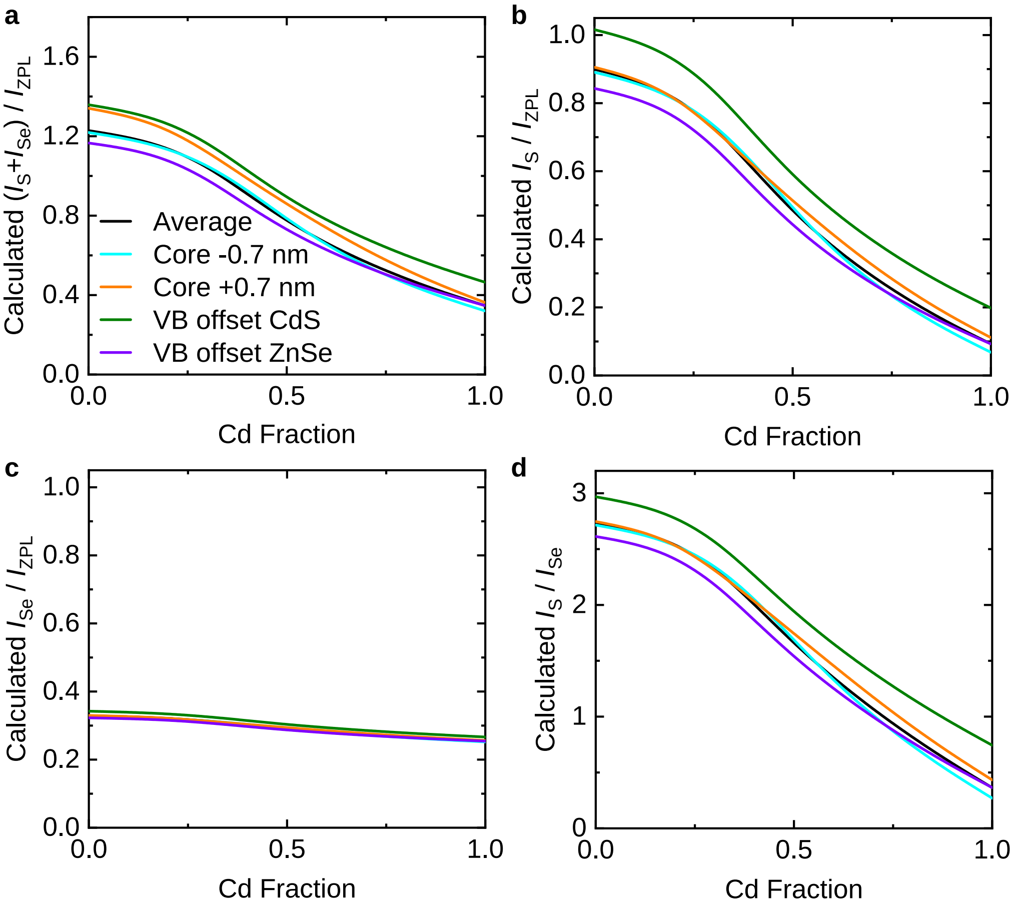

Figure 6.13.: Influence the core position in the $[00\bar{1}]$ crystal direction by ± 2 MLs, and use of different valence band offsets between CdS–CdSe of 0.55 eV[134], and ZnSe–CdSe of 0.11 eV[134] on the different coupling ratios (a) $(I_{\mathrm{S}} + I_{\mathrm{Se}})/I_{\mathrm{ZPL}}$, (b) $I_{\mathrm{S}}/I_{\mathrm{ZPL}}$, (c) $I_{\mathrm{Se}}/I_{\mathrm{ZPL}}$ and (d) $I_{\mathrm{S}}/I_{\mathrm{Se}}$. Adapted from Johst et al.[185]

Figure 6.14 illustrates the influence that a single positive and negative surface charge, respectively, has on the wave function of the electron and hole for different x. In the case of a positive surface charge, the electron and hole both remain localized around the core region. The electron wave function gets pulled toward the surface charge while the hole gets pushed away inside the core. Furthermore, with increasing Cd fraction x, the influence of the surface charge diminishes. In case of a negative surface charge, the electron and hole get dissociated, as the electron is driven out of the core region into the CdS rod, while the hole keeps its localization in the core. This dissociation of electron and hole is present for $x = 0.0$ and 0.5, while for $x = 1.0$, the electron and hole stay bound together. These simulations demonstrate that the influence of surface charges is much higher for lower Cd fractions x and decreases with increasing type-I character of the band alignment. This is also in agreement with the stronger spectral diffusion observed in sample DR-1–3 compared to DR-4, as discussed in Figure 6.4.

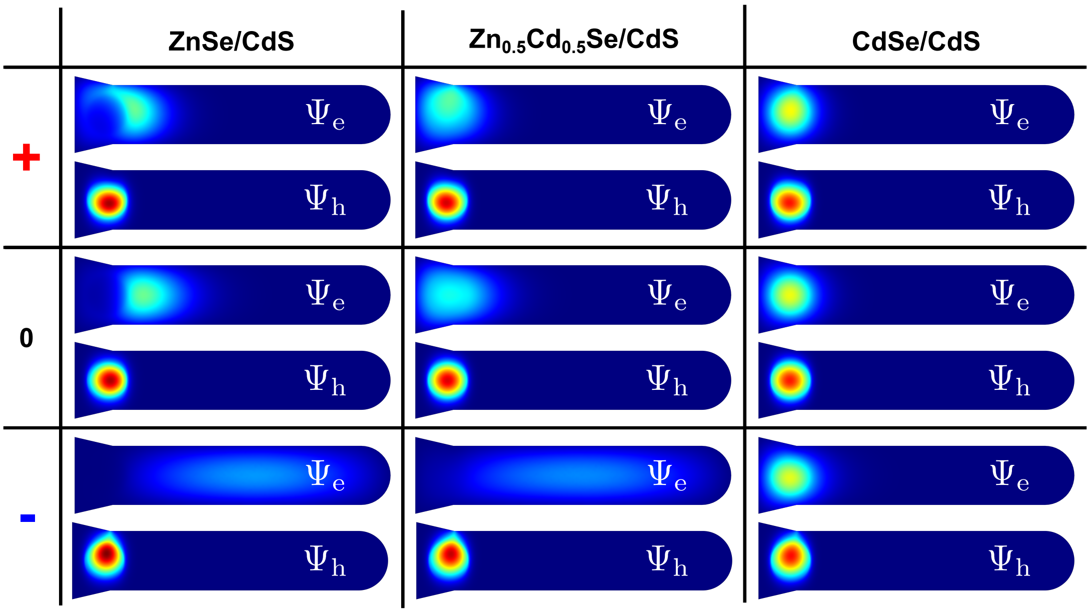

Figure 6.14.: Effect of a single negative or positive surface charge, localized at the transition between the cone and rod cylinder, on the electron and hole wave functions, compared to the neutral state of $Zn_{1-x}Cd_xSe/CdS$ DRs with different Cd fractions.

Figure 6.15 shows the effect of a single negative or positive surface charge, respectively, on the different phonon coupling ratios compared to the neutral case. Depending on the charge state, the total exciton–phonon coupling (Figure 6.15a) can either increase or decrease. For this particular surface charge placement, the predicted effect of the negative surface charge has a much stronger influence than the positive surface charge. It also becomes clear that with increasing Cd fraction, the influence of the surface charge is reduced. In particular, for Cd fractions larger than $x = 0.75$, the phonon coupling is almost unaffected by the surface charges. Furthermore, the calculations reveal a maximum at around $x = 0.5$, corresponding to DR-1. The biggest change becomes apparent for the coupling to the S-type phonon in Figure 6.15b. Here, the negative surface charge almost doubles the coupling to the S-type phonon. In contrast to this, the Se-type phonon is nearly unaffected by the surface charge. Similar to the S-type phonon, the negative surface charge has a larger impact than the positive surface charge, with a maximum around $x = 0.5$.

To conclude, the surface charges are likely the main origin behind the broader distributions of phonon coupling ratios observed for sample DR-1–3, compared to DR-4. Furthermore, the surface charges could be a possible explanation for the observation that the average values of the S-type phonon coupling are always higher than their median values. This could originate from the increased S-type phonon coupling due to the presence of surface charges. Whether the $Zn_{1-x}Cd_xSe/CdS$ DRs contain primarily positive or negative surface charges is unclear, and it is easy to generalize. For example, one

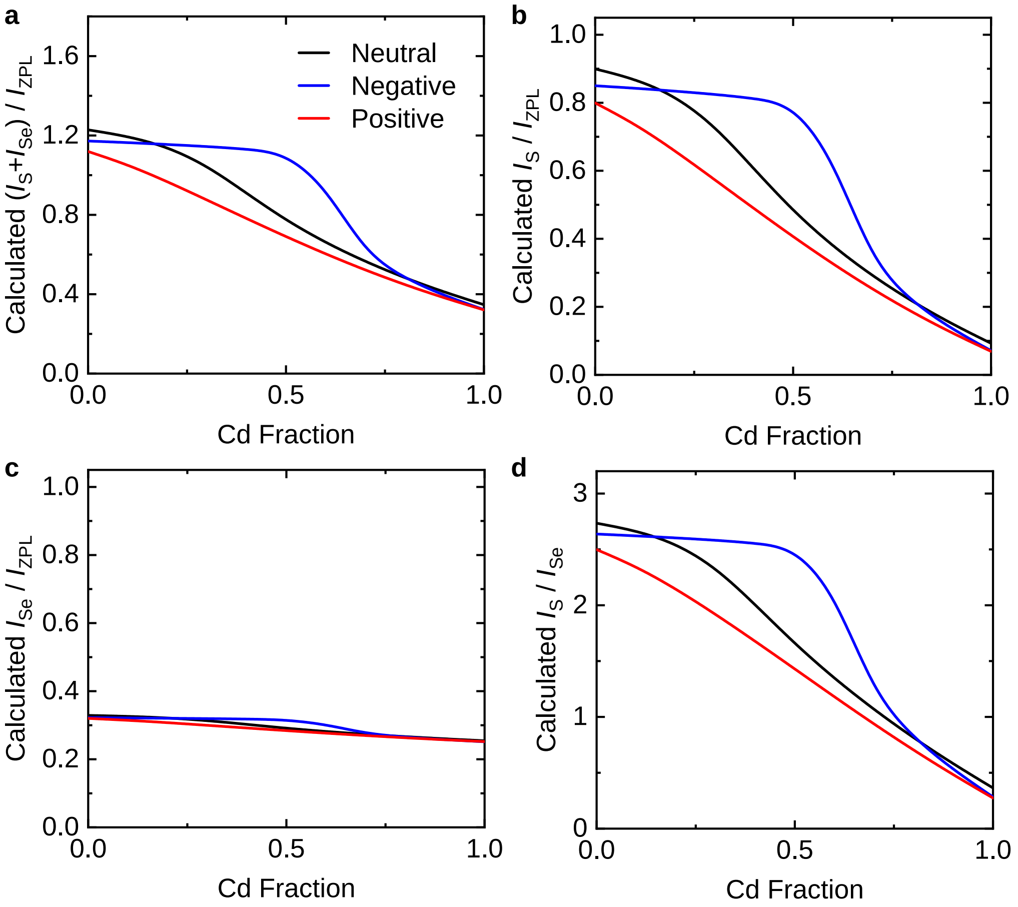

Figure 6.15.: Influence of a single negative or positive surface charge on the different phonon coupling ratios (a) $(I_\mathrm{S} + I_\mathrm{Se})/I_\mathrm{ZPL}$, (b) $I_\mathrm{S}/I_\mathrm{ZPL}$, (c) $I_\mathrm{Se}/I_\mathrm{ZPL}$ and (d) $I_\mathrm{S}/I_\mathrm{Se}$, in comparison to the neutral state. The surface charge was placed at the transition between the cone and the rod cylinder. Adapted from Johst et al.[185]

possibility for the determination of the charge state would be the measurement of the circular polarization of the ensemble PL In the presence of strong magnetic fields at low temperatures.[204] Moreover, it has been proposed and shown that for the same NC system, neither positive nor negative surface charges form exclusively.[79,82] In addition, It has been found that in the presence of oxygen, the QY is increased, which was attributed to the capturing of negative surface charges by oxygen, and the formation of superoxide radicals. This has been assumed to primarily result in negative charging of CdSe/CdS NCs in absence of oxygen.[53,60,205]

Alternative Approaches for the Calculation of Exciton–Phonon Coupling

Further simplified approaches for the modeling of exciton–phonon coupling are also conceivable. Thus, multiple approaches have been tested on the way to the best approach presented in the previous section (based on Equations 6.1.3 and 6.1.4), referred to as approach 1 in the following.

For approach 2, the bulk Fröhlich coupling constants α were used instead of the fitted coupling constants β. Additionally, the difference between the squared wave functions was evaluated and weighted by the respective α before integration and not afterward. It follows for the relative intensity of the S-type phonon

$$\frac{I_{\mathrm{S}}}{I_{\mathrm{ZPL}}} = \int \left| \left|\Psi_{\mathrm{e}}^{\mathrm{S}}\right|^2 \alpha_{\mathrm{S}}^{\mathrm{e}} - \left|\Psi_{\mathrm{h}}^{\mathrm{S}}\right|^2 \alpha_{\mathrm{S}}^{\mathrm{h}} \right| \mathrm{d}V_{\mathrm{shell}}, \tag{6.1.10}$$

and analogous to the Se-type phonon

$$\frac{I_{\mathrm{Se}}}{I_{\mathrm{ZPL}}} = \int \left| \left|\Psi_{\mathrm{e}}^{\mathrm{Se}}\right|^2 \alpha_{\mathrm{Se}}^{\mathrm{e}} - \left|\Psi_{\mathrm{h}}^{\mathrm{Se}}\right|^2 \alpha_{\mathrm{Se}}^{\mathrm{h}} \right| \mathrm{d}V_{\mathrm{core}}. \tag{6.1.11}$$

The strength of exciton–phonon coupling is related to the wave function overlap of electron and hole.[25,75,95] In approach 3, the overlap integral is thus assumed to be proportional to the respective phonon coupling intensities of the S-type phonon

$$\frac{I_{\mathrm{S}}}{I_{\mathrm{ZPL}}} = \int \Psi_{\mathrm{e}}\Psi_{\mathrm{h}} \mathrm{d}V_{\mathrm{shell}} \left|\alpha_{\mathrm{S}}^{\mathrm{e}} - \alpha_{\mathrm{S}}^{\mathrm{h}}\right|, \tag{6.1.12}$$

and Se-type phonon

$$\frac{I_{\mathrm{Se}}}{I_{\mathrm{ZPL}}} = \int \Psi_{\mathrm{e}}\Psi_{\mathrm{h}} \mathrm{d}V_{\mathrm{core}} \left|\alpha_{\mathrm{Se}}^{\mathrm{e}} - \alpha_{\mathrm{Se}}^{\mathrm{h}}\right|, \tag{6.1.13}$$

instead of the difference between the probabilities, as in the case of the other approaches.

In Figure 6.16, the different modeling approaches are compared for the different coupling ratios, like before. Regarding the total phonon coupling intensity (Figure 6.16a), approaches 1 and 3 are similar and in agreement with the experimental data. Approach 2 is unable to reproduce the experimental data because the coupling intensity between $x = 0.5$ and 1.0 is nearly constant. Similarly, the experimental trend of the S-type phonon (Figure 6.16b) is better described by approaches 1 and 2, compared to approach 3. Although the slope between $x = 0.5$ and 1.0 is too low in the case of approach 3. For the calculation of the Se-type phonon intensity (Figure 6.16c), approach 2 predicts a slight increase, which fits samples DR-1–3 but does not reproduce the decrease towards sample DR-4. The calculated S- to Se-type phonon ratio (Figure 6.16d) decreases for all three approaches, but the experimentally observed switch from a coupling ratio of above to below 1 is only reproduced with approach 3. Moreover, the slope in the range of $x = 0.5$ to 1.0, relevant for the samples, is far too low for approaches 2 and 3.

In summary, the calculations using approach 1 provide the best agreement with the different experimentally determined phonon coupling ratios. Approach 2 estimates both

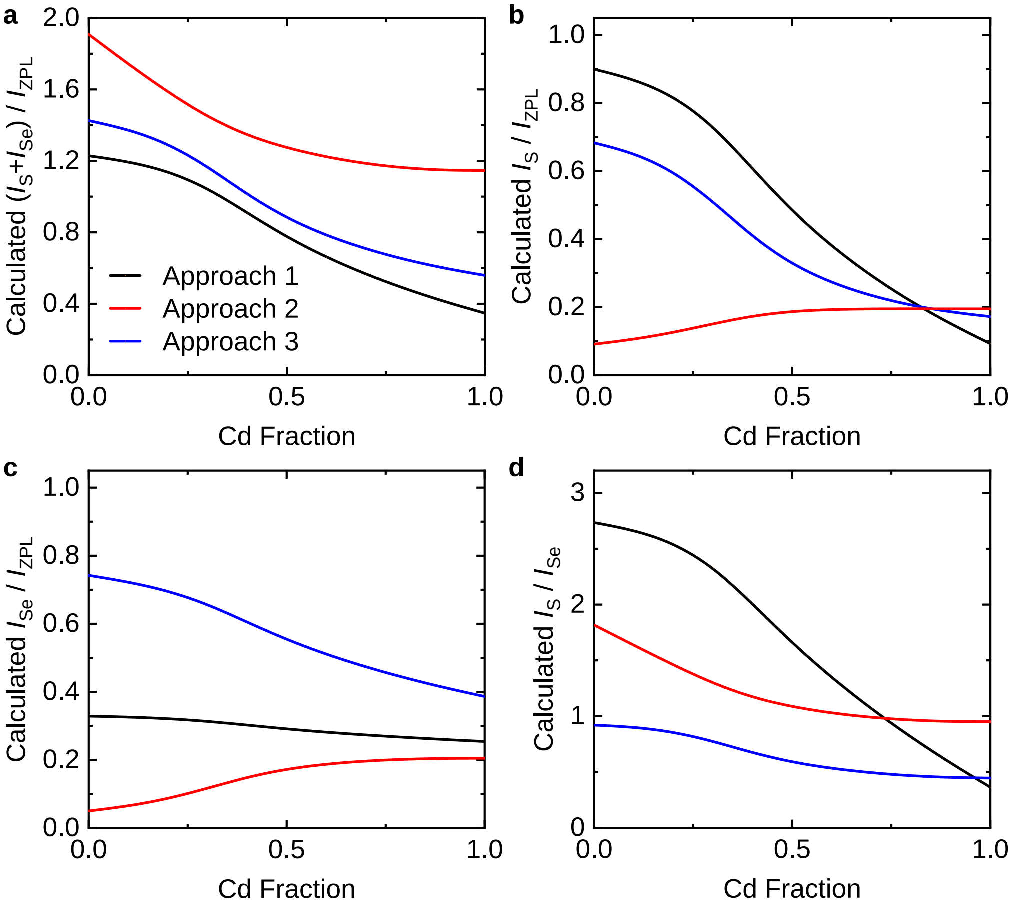

Figure 6.16.: Comparison of the three different model approaches for the different exciton–phonon coupling ratios: (a) $(I_S+I_{Se})/I_{ZPL}$, (b) I_S/I_{ZPL}, (c) I_{Se}/I_{ZPL} and (d) I_S/I_{Se}. Approach 1 was calculated by Equations 6.1.3 and 6.1.4, approach 2 by Equations 6.1.10 and 6.1.11, and approach 3 by Equation 6.1.12 and Equation 6.1.13.

the S- and Se-type phonons to increase similarly and has the lowest agreement with the experimental data. Calculations performed with approach 3 are similar to approach 1 but are unable to match the trend for the S- to Se-type phonon.

For comparison, Lin et al.[15] reported atomistic calculations for the phonon coupling in CdSe/CdS quantum dots with a core diameter of 3 nm and a shell thickness of 3 MLs. Even though their calculations are more sophisticated and used to describe a simpler system, they were unable to accurately model the S- to Se-type phonon ratio. In particular, their calculations strongly underestimated the S-type phonon coupling.

Exciton–Phonon Coupling Derived from the Electric Field

The Fröhlich interaction attributes the coupling of the excitonic charge distribution to the LO phonon via Coulomb interaction.[14,93,206] Hence, the total electric field $|\mathbf{E}|$ generated by the exciton could also be used to derive the magnitude of exciton–phonon coupling. A similar approach has also been used by Lin et al.[93] They performed quantum mechanical calculations for the exciton and its corresponding electric field for force field calculations in order to determine the exciton–phonon coupling.

In order to evaluate the correlation between the electric field of the exciton and the exciton–phonon coupling in this work, its absolute value is integrated over the core and shell domains, respectively. In Figure 6.17, the steps for the calculation of the electric field are illustrated. From the probability densities of electron and hole (Figure 6.17a/b), the corresponding electric potentials were calculated (Figure 6.17c/d) using Poisson's equation. The electric potentials of the electron and hole were then summed up for the electric potential of the exciton ϕ_{exc}. Following this, the absolute electric field

$$|\mathbf{E}| = \sqrt{\left(-\frac{\mathrm{d}\phi_{\mathrm{exc}}}{\mathrm{d}x}\right)^2 + \left(-\frac{\mathrm{d}\phi_{\mathrm{exc}}}{\mathrm{d}y}\right)^2 + \left(-\frac{\mathrm{d}\phi_{\mathrm{exc}}}{\mathrm{d}z}\right)^2} \tag{6.1.14}$$

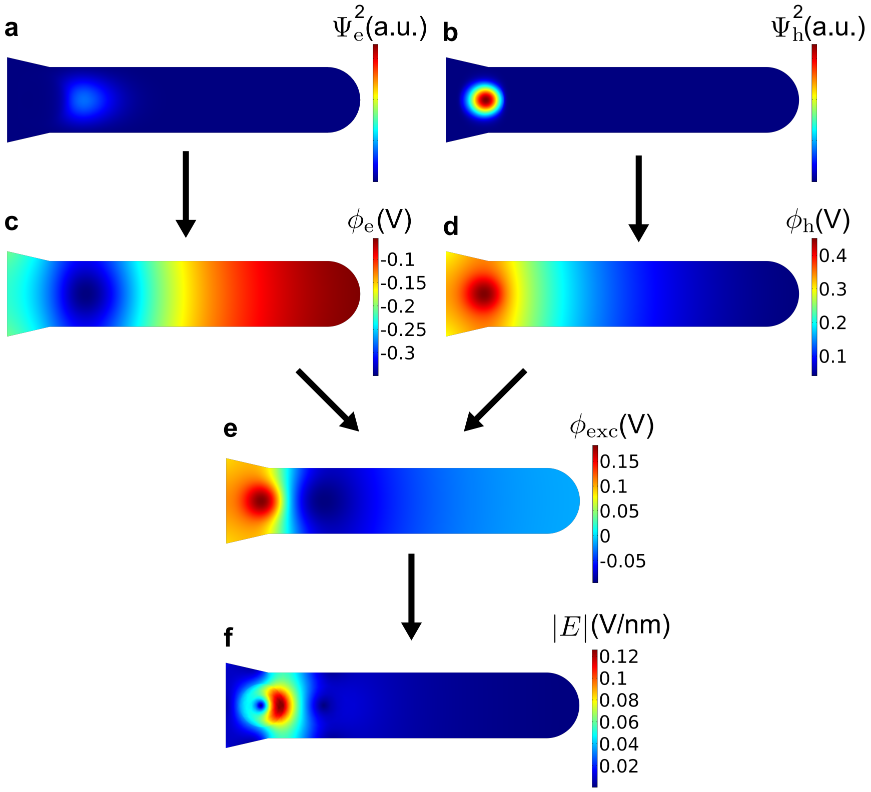

Figure 6.17.: Visualization of the steps in the calculation of the absolute electric field produced by a ground-state exciton in a $Zn_{1-x}Cd_xSe/CdS$ DRs. The calculation starts with (a/b) the probability densities of electron and hole, followed by (c/d) the evaluation of the corresponding electric potentials, which are combined to (e) the electric potential of the exciton. From the electric potential, (f) the electric field is then derived.

was calculated from the first derivate with respect to the x, y, and z components. In this approach, the S-type and Se-type phonon coupling intensities were then assumed to be proportional to the integrated electric field in the shell

$$\frac{I_{\mathrm{S}}}{I_{\mathrm{ZPL}}} \propto \int |\mathbf{E}|\, \mathrm{d}V_{\mathrm{shell}} \tag{6.1.15}$$

and the core

$$\frac{I_{\mathrm{Se}}}{I_{\mathrm{ZPL}}} \propto \int |\mathbf{E}|\, \mathrm{d}V_{\mathrm{core}}. \tag{6.1.16}$$

Figure 6.18 shows the results from the integration of the calculated electric field in the different domains. Analogous to Figure 6.12, the black lines once again represent the calculations for the averaged geometry, and the colored illustrate the variation of the geometry parameters.

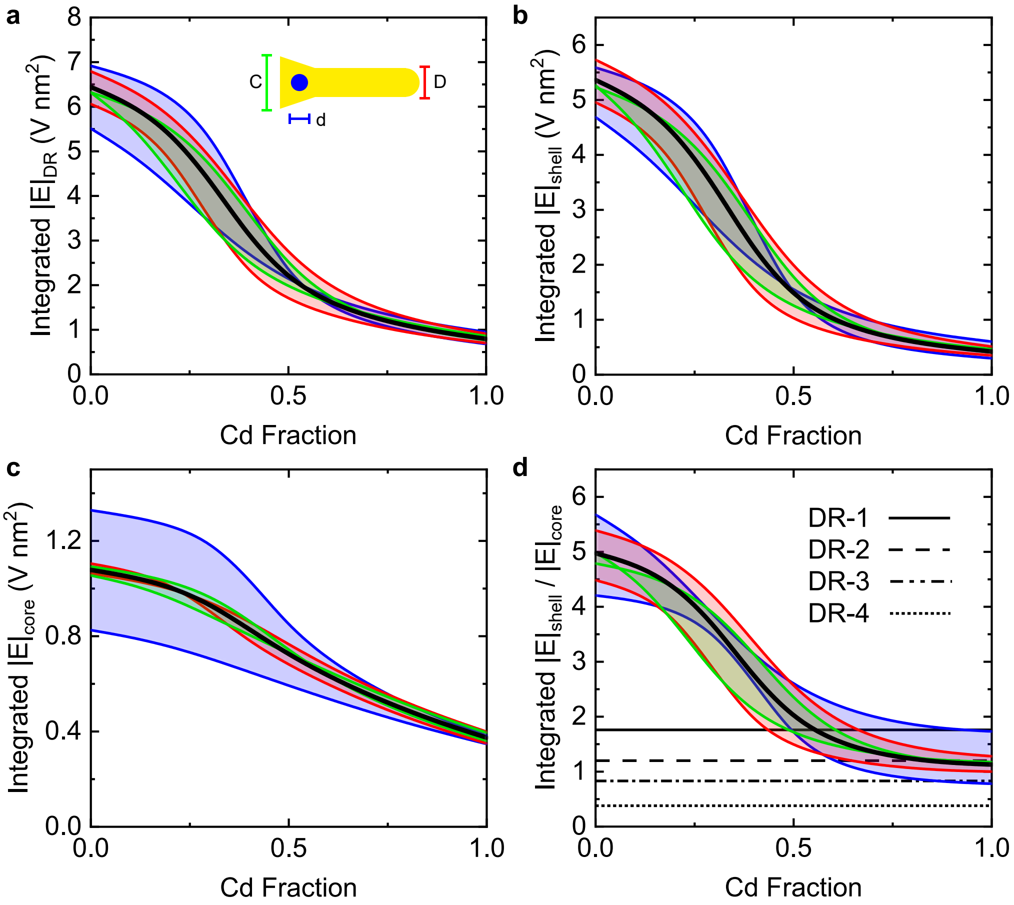

Figure 6.18.: Evaluation of the absolute electric field formed by the exciton integrated in (a) the complete DR, (b) in the shell, (c) in the core, and (d) the ratio of the shell to core domain. The black curves were calculated with the averaged sample geometry, while for the colored curves the core diameter d, shell diameter D and cone diameter C were varied separately, according to their standard deviations. Horizontal lines in panel d indicate the measured values of the S- to Se-type phonon coupling ratios.

In Figure 6.18a, the total electric field of the whole DR is shown, which continuously decreases with rising x. Figure 6.18b depicts the integration for the CdS shell domain, which decreases strongly for low x before its slope becomes less sleep. The electric field integrated over the core domain, in Figure 6.18c, decreases on an overall smaller scale compared to the shell. The dependence of the electric field on the Cd fraction x follows the expected trend. As a result of the transition from a type-II to type-I band alignment, the exciton becomes less polarized, and thus its electric field decreases. A direct comparison to the experimental data is difficult, as the proportionality between the integrated electric field and the HR factor is not clear. Although in direct comparison, the stronger change of the electric field in the shell as opposed to the core resembles the stronger change of the S-type phonon compared to the Se-type phonon. In Figure 6.18d, the ratio of the electric field integrated over the shell and core is evaluated. This ratio is dimensionless and thus should provide a better comparability with experimental data. Indeed, the predicted coupling ratio for the S- to Se-type phonon is on a similar scale as the experimental data. Although the prediction of the ratios of the samples DR-3 and DR-4 seems to fall out of line.

Regarding the geometry dependence, it can be seen that all geometry parameters possess a similar strong influence at different Cd fractions x. In the case of the total electric field in the DR and shell domain, the influence of the core diameter dominates at small x, while at higher x, the influence of the shell diameter increases. Besides the implied overall broadness of the total phonon coupling, S-type and Se-type phonon decreases slightly in the region of $x = 0.5$–1.0.

To sum up briefly, while the electric field correlates with the magnitude of exciton–phonon coupling, a direct comparison to the experimental data is only possible for the S- to Se-type phonon ratio. The ratio of the integrated electric field in the shell to the core is similar to the S- to Se-type phonon ratio, albeit it does not reproduce the data accurately and overestimates the ratio for higher Cd fractions x.

6.2. Spectroscopy of Spherical CdSe/CdS Nanocrystals

Ion exchange and alloy formation play not only a crucial role in the synthesis of ZnSe/CdS DRs but also in the synthesis of CdSe/CdS NCs. In these structures, alloying can lead to the formation of CdSe/CdSe$_y$S$_{1-y}$/CdS NCs, which has the benefit that the QY is increased.[169,170] This way, QY close to unity are obtainable.[167] Additionally, the high QY of the spherical CdSe/CdS makes them suitable as temperature probes, which will be presented afterward.

6.2.1. Exciton–Phonon Coupling in Spherical CdSe/CdS Nanocrystals

Alloy formation in CdSe/CdS NCs affects the localization of the exciton, and thus changes the exciton–phonon coupling. In order to investigate the exciton–phonon coupling in these structures, single-particle PL spectroscopy was performed again at $T = 10$ K. The CdSe/CdS NCs were provided by Sonja Zeller, and synthesized following the approach of Chen et al.[167]. (More details can be found in Chapter 4.2.3.) In addition to the alloying, the influence of the shell thickness on the exciton–phonon coupling was also analyzed.

A set of four samples, GS-1–4, was investigated, which is presented in Table 6.4. The first two samples, GS-1 and 2, were synthesized from CdSe NCs with the same diameter of $d = 3.26$ nm and different shell thicknesses of 2.2 nm and 5.1 nm, respectively. Due to the reduced confinement, the PL energy of GS-2 is slightly red-shifted compared to GS-1. Sample GS-3 and 4 are nearly identical in their geometry; they share a core diameter of ~3.5 nm and a shell thickness of 2.8 nm. What sets them apart is that their synthesis times were 3 h and 18 h, respectively. This increased synthesis time leads to a red-shift of 31 meV of the ensemble PL and suggests that an alloy was formed.[170]

Table 6.4.: Overview of the synthesis time T_{synth}, core diameter d, shell thickness t_{shell}, and ensemble PL energy E_{PL} for the CdSe/CdS quantum dot samples. Ensemble PL energies were measured in solution by Sonja Zeller.

Sample	T_{synth} (h)	d (nm)	t_{shell}(nm)	E_{PL}(eV)
GS-1	4	3.26	2.2	2.016
GS-2	4	3.26	5.1	1.965
GS-3	3	3.53	2.8	1.971
GS-4	18	3.50	2.8	1.940

Single-particle PL measurements and evaluation of the LO-phonon coupling were performed in the same way as described in detail in Figure 6.5, in the previous chapter. An example of an averaged PL spectrum is shown in Figure A.1 in Appendix A.1. Figure 6.19 shows the statistical results from the evaluation of the first-order LO-phonons, measured from samples GS-1–4. The following coupling ratios were analyzed: $(I_\mathrm{S} + I_\mathrm{Se})/I_\mathrm{ZPL}$, $I_\mathrm{S}/I_\mathrm{ZPL}$, $I_\mathrm{Se}/I_\mathrm{ZPL}$, and $I_\mathrm{S}/I_\mathrm{Se}$. Additionally, the average values and standard deviations of the phonon coupling ratios, as well as the energies of the ZPL and first-order phonons, are compiled in Table 6.5. In Figure 6.19a, the total coupling intensity increases, clearly with the shell thickness from 0.37 to 0.48 (GS-1/2). A much smaller increase occurs for the presumed alloy formation from 0.34 to 0.36, which is less unambiguous. Likewise, the S-type phonon in Figure 6.19b, as well as the Se-type phonon in Figure 6.19c, exhibit a stronger and more distinct increase with the shell thickness compared to the alloying. Consequently, the S-to Se-type phonon ratio rises slightly with the shell thickness and

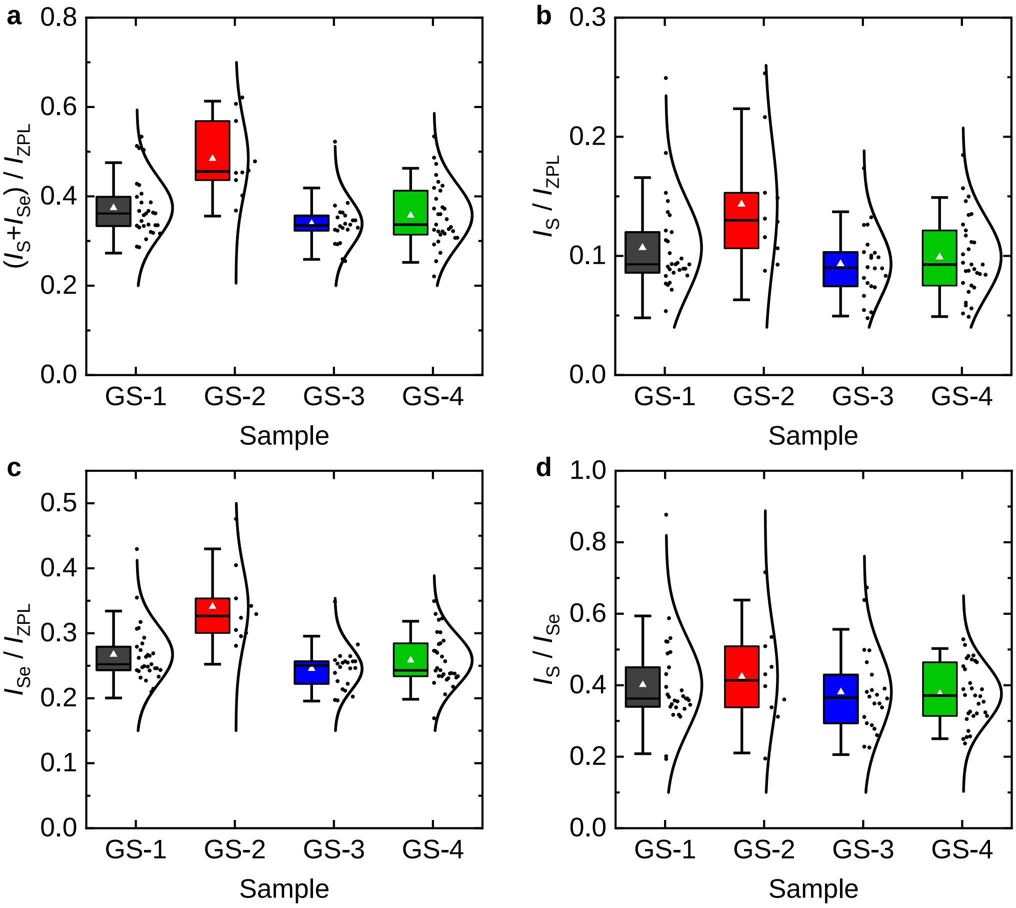

Figure 6.19.: Statistical data of the relative phonon coupling intensities: $(I_\mathrm{S} + I_\mathrm{Se})/I_\mathrm{ZPL}$, $I_\mathrm{S}/I_\mathrm{ZPL}$, $I_\mathrm{Se}/I_\mathrm{ZPL}$ and $I_\mathrm{S}/I_\mathrm{Se}$ measured from individual CdSe/CdS and CdSe/CdSe$_y$S$_{1-y}$/CdS of samples GS-1–4 NCs at $T = 10$ K. The data was quantified from 30, 10, 22, and 31 individual NCs, respectively. In the evaluation, normal distributions were assumed for the data.

Table 6.5.: Average values and standard deviations of the ZPL energy E_{ZPL}, first-order S-type statistical results shown in Figure 6.19 for the phonon coupling ratios: $(I_{\mathrm{S}} + I_{\mathrm{Se}})/I_{\mathrm{ZPL}}$, $I_{\mathrm{S}}/I_{\mathrm{ZPL}}$, $I_{\mathrm{Se}}/I_{\mathrm{ZPL}}$ and $I_{\mathrm{S}}/I_{\mathrm{Se}}$.

	GS-1	GS-2	GS-3	GS-4
E_{ZPL} (eV)	2.102 ± 0.020	2.074 ± 0.019	2.040 ± 0.021	2.031 ± 0.019
$E_{\mathrm{LO_1(Se)}}$ (meV)	27 ± 0.2	27 ± 0.2	27 ± 0.2	27 ± 0.1
$E_{\mathrm{LO_1(S)}}$(meV)	37 ± 0.2	38 ± 0.3	37 ± 0.7	36 ± 0.6
$(I_{\mathrm{(LO_1(Se)}}+I_{\mathrm{LO_1(S))}})/I_{\mathrm{ZPL}}$	0.37 ± 0.07	0.48 ± 0.08	0.34 ± 0.05	0.36 ± 0.07
$I_{\mathrm{LO_1(S)}}/I_{\mathrm{ZPL}}$	0.11 ± 0.04	0.14 ± 0.05	0.09 ± 0.03	0.10 ± 0.03
$I_{\mathrm{LO_1(Se)}}/I_{\mathrm{ZPL}}$	0.27 ± 0.04	0.34 ± 0.08	0.25 ± 0.03	0.26 ± 0.04
$I_{\mathrm{LO_1(S)}}/I_{\mathrm{LO_1(Se)}}$	0.40 ± 0.13	0.42 ± 0.14	0.38 ± 0.11	0.38 ± 0.08

stays constant for the alloy formation. Regarding the average ZPL energies, in both cases, the respective energy shifts from GS-1 to GS-2 and GS-3 to GS-4 are smaller compared to the ensemble measurements in Table A.1. Furthermore, the energies of the S- and Se-type phonons remain nearly constant among the samples.

The increase of the S- and Se-type phonon due to the thicker shell, can be explained by the higher delocalization of the exciton, resulting from the reduced confinement. As a consequence, the wave function overlap of electron and hole is reduced, and thus, the Fröhlich interaction rises. This observation is also consistent with literature reports.[93] In the same way, the alloy formation of a $\mathrm{CdSe}_y\mathrm{S}_{1-y}$ alloy reduces the band offsets, which would also reduce the wave function overlap.[169] Hence, a stronger Fröhlich interaction would be expected. However, the increase in S- and Se-type phonon coupling is minimal and practically nonexistent. It is likely that the observed red-shift from GS-3 to GS-4 primarily results from the lowered band potentials in the alloy and, to a smaller degree, from the reduced confinement. This indicates that the effect of the alloy formation is not strong enough to result in a distinct trend for the S- and Se-type phonon coupling. The small change due to the alloying is also in line with the small change of the average ZPL energy in Table 6.5, which hints at a weak change of the charge-carrier localization, as opposed to the ensemble data in Table A.1. Furthermore, the alloying can only vary the band alignment to a small degree, which primarily affects the localization of bi-excitons and not single excitons.[170] For the S- to Se-type phonon ratio, no distinct change is present for both sample pairs GS-1/2 and GS-3/4.

In summary, exciton–phonon coupling measured from individual NCs is, on one hand, sensitive enough to reflect changes in the shell thickness. On the other hand, alloying in the $\mathrm{CdSe}/\mathrm{CdSe}_y\mathrm{S}_{1-y}/\mathrm{CdS}$ NCs does not noticeably affect the charge-carrier localization, which is likely a consequence of the small energy-shift of the average ZPL energy, in contrast to the larger energy shift in the ensemble of 31 meV.

6.2.2. CdSe/CdS Dots as Temperature Probes

The properties of NCs are sensitive towards the sorption of atoms and molecules on their surface.[53] One possibility to directly measure the sorption events is single nanoparticle mass spectrometry. Howder et al. have shown that ion traps can be used simultaneously for mass spectrometry and PL spectroscopy of single NCs.[207,208] A deciding parameter for sorption processes is the temperature, which is not readily accessible. As described by the Varshni relation, the PL energy depends on the temperature. Hence, the PL energy can be used to draw conclusions for the NC temperature.

In order to capture a NC in an ion trap, it is first charged by electron spray ionization. Inside the ion trap, the particle is kept in a stable orbit by applying an oscillating voltage to the ion trap, which creates a corresponding oscillating potential. For example, argon can be used as a buffer gas to allow cooling of the NC, thereby stabilizing the particle in the trap , as sketched Figure 6.20a. Furthermore, the argon is ionized to allow for changes in the charge state, which can then be used to extract information on the particle mass.[210] As a consequence of the active charging of the NC surface or its ligands, the QY could be reduced due to Auger recombination. In order to isolate the exciton from these surface charges and keep the QY high, the giant-shells CdSe/CdS NCs are ideal. Therefore, CdSe/CdS NCs with a core diameter of 4.2 nm and shell thickness of 5.3 nm were investigated. A representative TEM image of these NCs is depicted in Figure 6.20b.

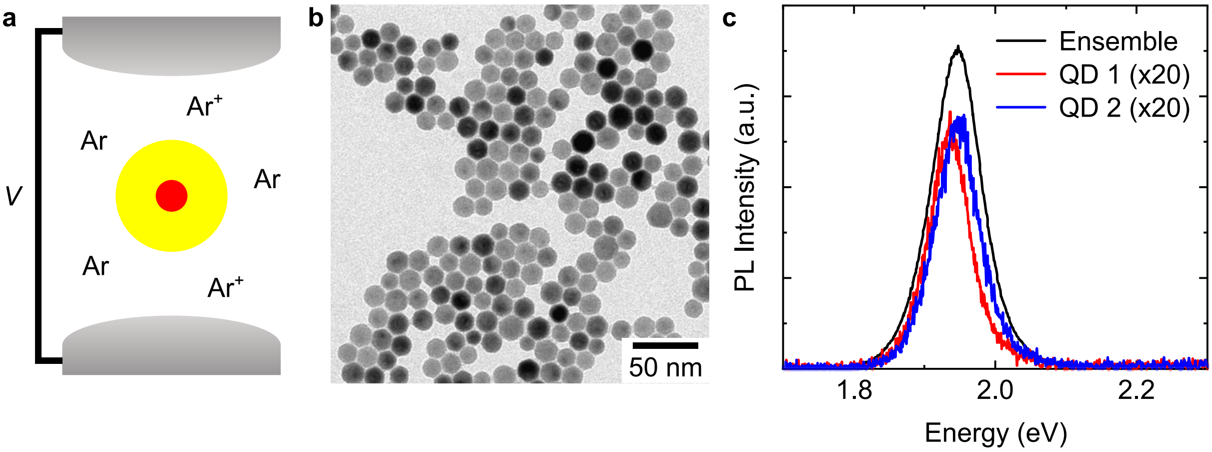

Figure 6.20.: (a) Schematic depiction of a CdSe/CdS NC surrounded by Argon within an ion trap, with an applied voltage V. (b) Representative TEM image of CdSe/CdS NC. (c) Comparison of the ensemble and single-particle PL measured in vacuum at room temperature. Adapted from Leippe et al.[209]

Here, it can be seen that the NCs have a homogeneous size and shape. The small deviations in their sizes are also reflected in the similarity of the single-particle PL spectra to each other and to the ensemble (Figure 6.20c).

For evaluation of the temperature-dependent PL, ensemble spectra were measured from thin films of CdSe/CdS NCs, spin-coated onto a piece of Si/SiO$_2$ wafer. An integration time of 10 s per spectrum was used while the sample was continuously illuminated and heated with 0.7 K/min. Figure 6.21a shows exemplary spectra at different temperatures. As the temperature increases, the emission energy red-shifts and the FWHM broadens. Furthermore, at 25 K, an additional peak with lower energy than the main peak appears. Based on the energy difference, this shoulder could arise from first-order LO-phonon coupling to the CdSe. All spectra were fitted by Gaussian functions in order to evaluate the center of the PL energy and the FWHM of the main peak. Subsequently, the temperature-dependent emission energy, displayed in Figure 6.21b, was fitted by the Varshni relation[59] (Equation 2.1.12). This yields the following fit parameters: $E_0 = (2.02 \pm 9 \cdot 10^{-9})$ eV, $\alpha_\mathrm{T} = (4.82 \pm 0.06) \cdot 10^{-4}$ eV/K, and $\beta_\mathrm{T} = (286 \pm 7)$ K. For comparison Jing et al.[211] reported the following parameters $E_0 = 2.11 \pm 9$ eV, $\alpha_\mathrm{T} = (4.0 \pm 0.2) \cdot 10^{-4}$ eV/K, and $\beta_\mathrm{T} = (173 \pm 19.5)$ K for CdSe/CdS dots with a core diameter of 2.8 nm and shell thickness of 2.1 nm. Based on the work of Jing et al. an increase in β_T is to be expected with increasing shell thickness.[211] Finally, the Varshni fit parameters of this work were successfully used in a cooperation with Leippe et al.[209] for the development of a temperature-dependent sorption model for NCs in the gas phase. Regarding the temperature dependence of the FWHM, shown in Figure 6.21c, a similar trend is present as reported by Al Salman et al.[63] for bare CdSe dots with a diameter of 3 nm.

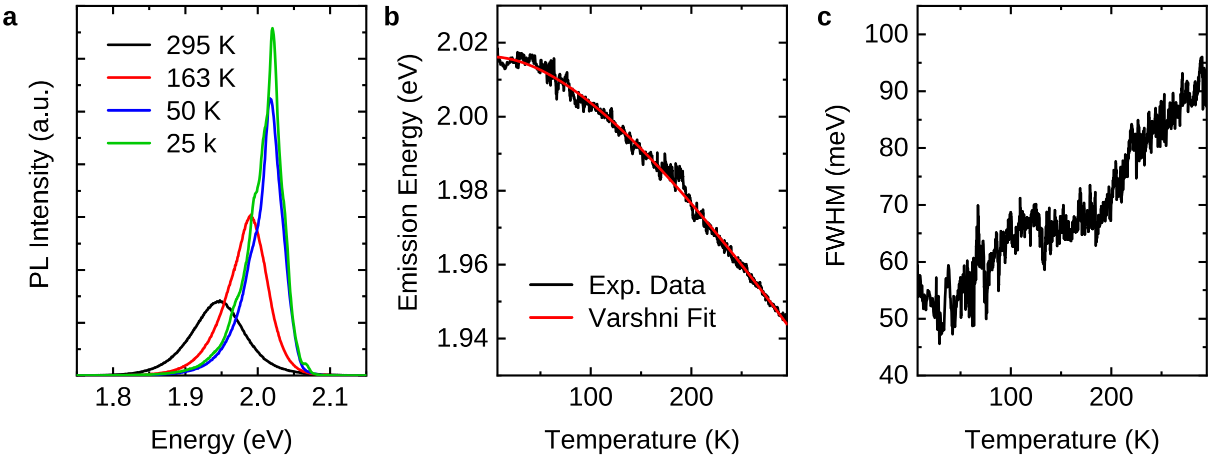

Figure 6.21.: Influence of the temperature on (a) the PL spectra, (b) the emission energy. The emission energy and FWHM were obtained by fitting the spectral data with Gaussian functions. Adapted from Leippe et al.[209]

6.3. Spectroscopy of Dot-in-Rod Nanocrystals in Electric Fields

Dot-in-rod NCs are especially well suited to being switched with external electrical fields because of their anisotropy, which allows the electron and hole to be separated effectively. Moreover, the anisotropic structure is suitable for the investigation of influences of surface charges. In this chapter, the influence of external electric fields on both CdSe/CdS and $Zn_{1-x}Cd_xSe$/CdS DRs will be discussed. Strong electric fields of 100-500 kV/cm are needed for controlling the excitations within the DRs.[31,111,112] Thus, IDEs structures on the micrometer scale are employed, created by optical lithography.

For the spectroscopic investigation, once again, single-particle spectroscopy at $T = 10$ K was applied. This allows us to take a deeper look at the influence of surface charges and exciton–phonon coupling. All PL spectra were fitted by using a self-written MATLAB script. Within the script, the prominent peaks with the highest energy are searched and used as an initial starting point for the ZPL. If no peaks with sufficient prominence are found, the peak with the highest intensity and energy is used instead as a starting point. The ZPL and first-order LO phonon replica are all fitted by Lorentzian functions. All spectra with too low PL intensity were sorted out. In order to account only for physically plausible data, all fits with too small FWHM were excluded, which are the result of measurement artifacts. Additionally, fits with too low coefficients of determination were removed to ensure good fit quality.

6.3.1. Device Development for Spectroscopy in Electric Fields

In an ideal case, the substrates for lithography are completely flat, free of defects, and clean. Si wafers with a 2000 nm thick SiO_2 layer fulfill these requirements to a high degree and thus were used in this work. Another benefit is that Si has a high thermal conductivity, which allows for better cooling of the sample in the cryostat when compared to pure SiO_2.

Inside the cryostat the microscope objective located below the sample radiates heat towards the sample. For this reason, the sample size was kept small to limit the heat transfer. In order to make the handling of small substrates easier during the lithography processing, an array 4 × 4 IDE devices was designed, as shown in Figure 6.22a. The repeating device unit is illustrated in Figure 6.22b, which by itself consists of four independent IDE sub-devices. If any electrical short-circuits or inhomogeneities in the NCs matrix would occur in one of the IDE fields, the other IDE fields would be unaffected. This setup makes the device less prone to errors. Additionally, text fields and arrow markers were included in the lithography mask to improve the spatial orientation during

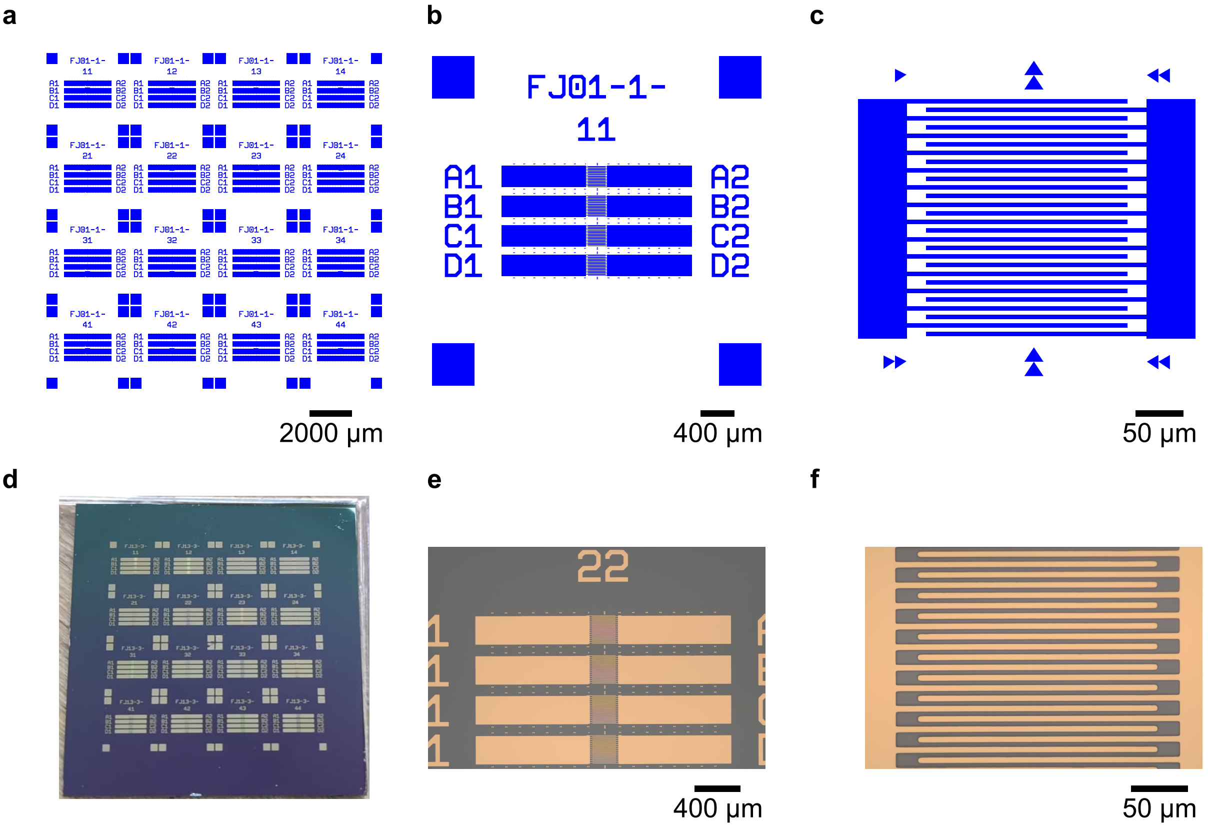

Figure 6.22.: (a–c) Different magnifications of the virtual lithography mask used for the microwriter. (d) Photography and (e,f) light-microscopy images of the finished lithography pattern on the wafer.

confocal microscopy. Figure 6.22c shows a close-up of the IDE structure, where the arrow markers are better visible. A photography of a finished array of IDE devices is shown in Figure 6.22d. This array was cleaved into its squared repeating units, thereby yielding 16 samples that can be further processed. The electrodes consist of a 10 nm Ti layer to provide good adhesion, followed by a 50 nm Au layer. Before further processing, each IDE device was reviewed by light microscopy, as shown in Figure 6.22e and f. Finally, the electrode spacing was determined by AFM to be 4.2 µm for the samples investigated in Chapter A.2 and 6.3.3. Combined with the available voltage source of up to 200 V, electric fields of up to 476 kV/cm can be generated.

Sometimes the IDEs were not flat but showed edges in AFM measurements that were much higher than the deposited film height, as depicted in Figure 6.23a and marked by a red arrow. These lift-off edges originate from the wall coverage of the photoresist during the physical vapor deposition, which is illustrated in Figure 6.23 b. This is, in particular, the case if the evaporation source is not directly located orthogonal to the substrate. The problem with lift-off edges is that they lead to inhomogeneous electric fields and lowered reproducibility because they often break apart. The inhomogeneous sample structure would also causes problems for the spin-coating of the NCs with their polymer matrix. In order to prevent the formation of lift-off edges, two layers of photoresists were used. Due to the faster development rate of the lift-off resist, the lift-off resist is getting dissolved at a higher rate than the photoresist on top. This leads to the development of a so-called undercut. If this undercut is small, as shown in Figure 6.23 b, wall coverage occurs. If the development time of the resists is long enough a large undercut can be formed, as illustrated in Figure 6.23 c, thereby inhibiting the formation of wall coverage in direct connection to the device structure. Additionally, the choice of the evaporation system is important because if its cooling power is too low, the photoresist can soften. Consequently, the photoresist would bend, which facilitates wall coverage. Finally, after tuning the undercut, flat IDEs were obtained, as shown in the AFM scan of Figure 6.23c.

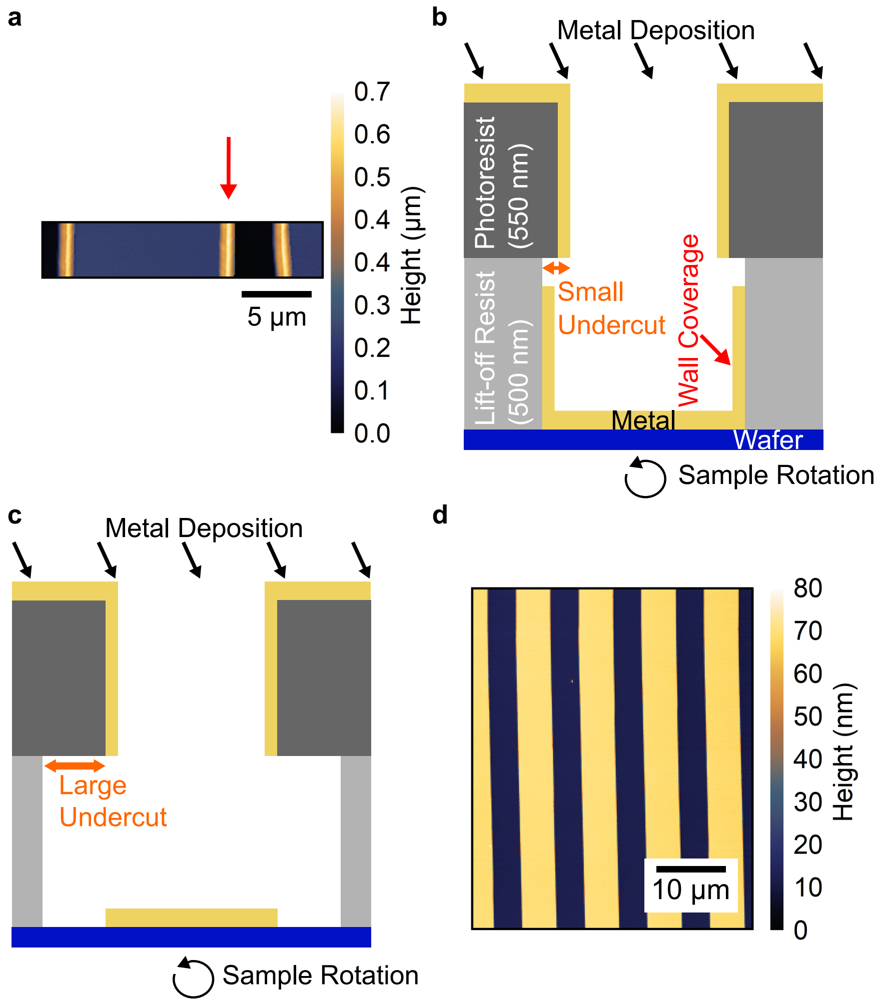
a
5 µm
0.7
0.6
0.5
0.4
0.4
0.3
0.2
0.1
0.0
Height (µm)
b
Metal Deposition
Photoresist (550 nm)
Lift-off Resist (500 nm)
Small Undercut
Wall Coverage
Metal
Wafer
Sample Rotation
c
Metal Deposition
Large Undercut
Sample Rotation
d
10 µm
80
70
60
50
40
30
20
10
0
Height (nm)

Figure 6.23.: (a) AFM scan of a substrate with lift-off edges, Illustration of the formation of lift-off edges in case of (b) an small undercut, and (c) a large undercut and (d) AFM scan of a substrate without lift-off edges.

The DRs were embedded in a PMMA matrix in order to isolate and fixate them in between the IDEs. This prevents the DRs from agglomerating on the electrodes themselves during the spin-coating process. For this, a diluted toluene-PMMA solution was used. When the toluene-PMMA is spin-coated, disjoining forces lead to an equilibrium thickness, which is tunable on a nanometer to micrometer range.[212] Another benefit of embedding the NCs in a polymer matrix is that the dielectric mismatch between the NCs and their surroundings is reduced, and with it also the dielectric screening. This leads to an increased effective electric field within the NCs.[116]

When using PMMA as a matrix, its film height in between the IDEs has to be below that of the electrodes in order to ensure that the DRs in between the IDEs are located below the top of the electrodes. In order to find a suitable PMMA concentration for the spin-coating, electron-beam lithography was applied, which is illustrated in Figure 6.24. After spin-coating of the PMMA film, a section of the IDEs is imaged by scanning electron microscopy (Figure 6.24a). This imaging process degrades the polymer film, which is

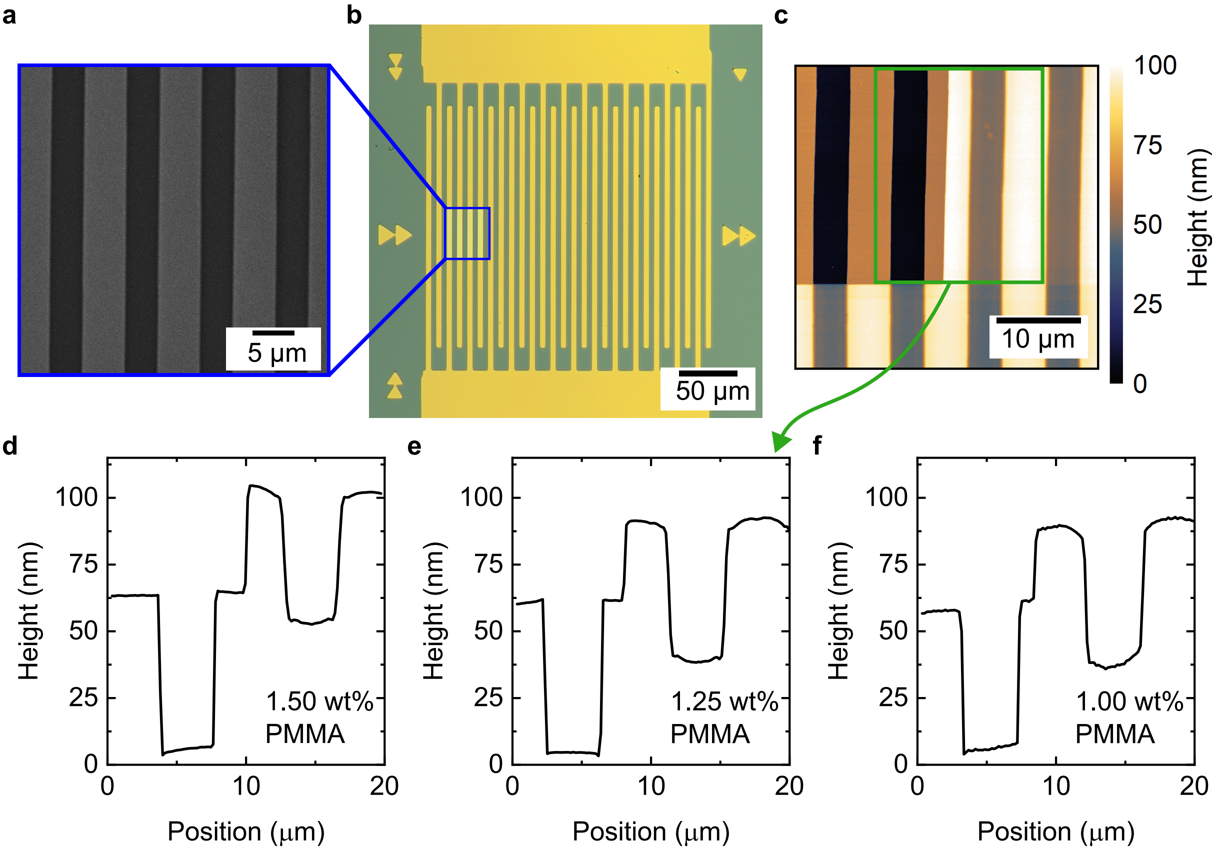

Figure 6.24.: Determination of the PMMA film thickness by electron beam lithography. (a) Scanning electron microscopy image for the illumination of the PMMA film, (b) light microscopy image of the same position after the development step, (c) AFM scan of a developed section, and and (d–f) comparison of averaged AFM line profiles for different PMMA concentrations. The blue and green boxes highlight the measured sample positions.

then processed in a developer solution. Figure 6.24b shows a light microscopy image of the same substrate after development. Here, the effect of electron-beam lithography is apparent by the slightly different light reflection. Following this, in Figure 6.24c, an AFM scan of the same position is displayed, where a clear cut-out of the removed PMMA film is visible. In Figure 6.24d–f, averaged line profiles from AFM measurements of different concentrations are compared. The determined film heights resulting from the respective PMMA concentrations in toluene of 1.50 wt%, 1.25 wt%, and 1.00 wt%, are 45 nm, 34 nm, and 24 nm. For the sample preparations of all further measurements, a PMMA concentration of 1.25 wt% was used.

In order to build an electrical connection, thin gold wires were bonded to the electrode pads of the IDEs. Figure 6.25a shows a light microscopy image of the bonded sample, which is investigated in the following chapter. The dark spots visible on the sample are connections of gold wires, which were bonded to a custom-designed circuit board, depicted in Figure 6.25b. For more efficient cooling, a thin copper plate was embedded into the printed circuit board, on which the sample was glued to by using conductive silver paint. (A sketch of the design from the printed circuit board is shown in Figure 4.2 of Chapter 4.3.2.) Figure 6.25c shows the sample holder after mounting onto the cryostat.

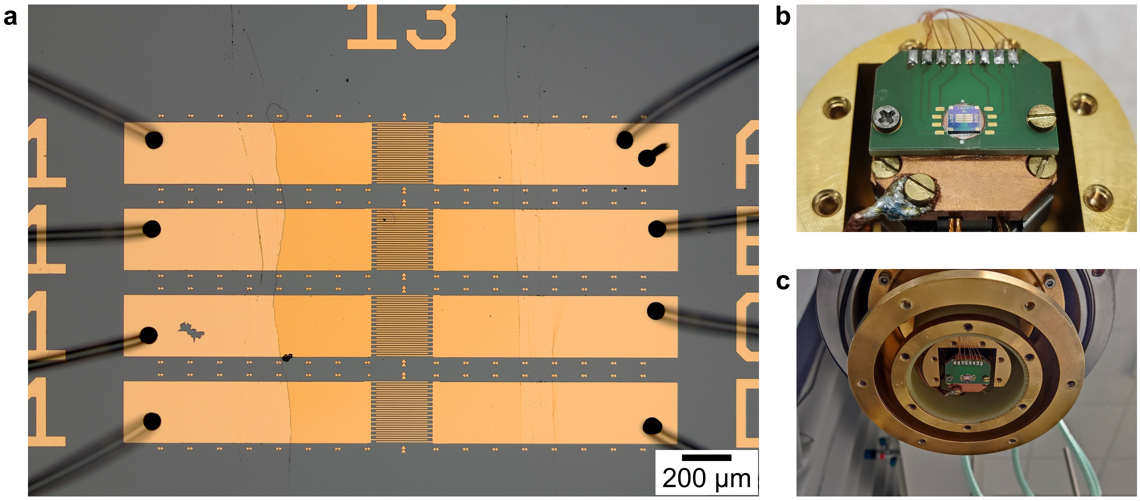

Figure 6.25.: (a) Light microscopy image of a contacted device, with a deposited PMMA film in the middle containing DRs. (b) Device glued onto a copper plate, embedded in a printed circuit board, connected to the sample holder. (c) Sample holder mounted on the cryostat.

Figure 6.26a and b depict confocal laser scanning microscopy images of the reflected laser light from the sample. These scans were used in order to navigate around the sample. Here, the IDEs and the wafer surface in between can be easily distinguished because the gap between the IDEs is smaller than the width of the IDEs. In Figure 6.26c, a PL scan is shown, where the PL of the DRs leads to bright spots. This verifies that the

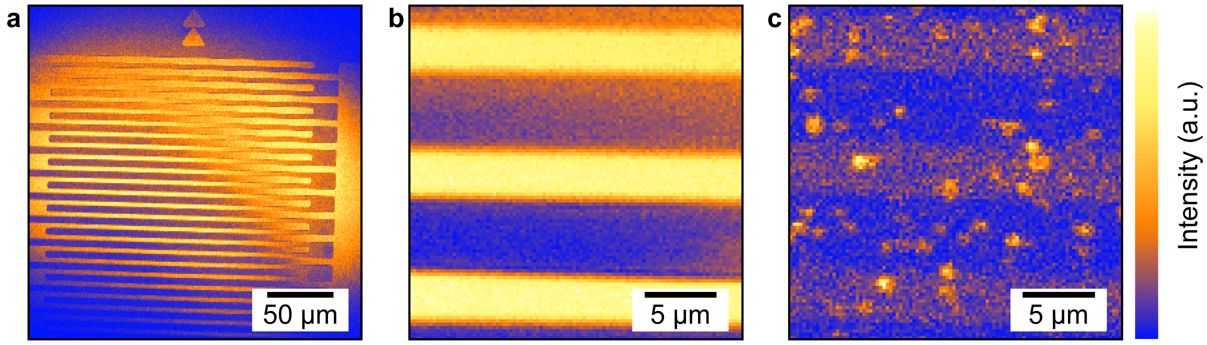

Figure 6.26.: Scans of (a,b) the reflection light and (c) the PL measured by laser scanning microscopy from the sample is discussed Chapter A.2. All images were scaled differently for better visibility.

PMMA matrix successfully fixated the DRs in between the IDEs. It can also be seen that some DRs are fixated above the electrodes, which does not impact the single-particle measurements.

6.3.2. CdSe/CdS Dot-in-Rod NCs in external Electric Fields

In this chapter, the spectroscopic investigation of CdSe/CdS DRs in external electric fields will be discussed. These DRs have a core diameter of 2.3 nm, a rod diameter of 5.0 nm, and a rod length of 30.4 nm. (An exemplary TEM image of the DRs is shown in Figure A.2 in Appendix A.1.) A small CdSe core size was chosen because it results in a quasi-type-II band alignment, which leads to a more pronounced QCSE.[139] All DRs exhibited photodarkening, which combined with overlapping spectral diffusion, complicates the analysis of the influence of electric field on these structures. This makes even the comparison of an individual NC with itself difficult as time passes. By comparing the optical response of many individual DRs, different trends were found. These trends include regular cases that followed expectations and irregular cases that contrasted expectations.

Determination of the Nanocrystal Orientation

After the spin-coating process, the DRs are randomly orientated within the PMMAs matrix. The response of the DRs to the electric fields is strongly affected by their orientation. Therefore, their orientation has to be determined for a better understanding of their spectroscopy measurements. CdSe/CdS and ZnSe/CdS DRs emit light, which is linearly polarized parallel to their long axis.[27,112] As a result, their orientation can be determined by mapping the corresponding polarization direction of their PL light. Figure 6.27 illustrates the setup used to measure the emission polarization. Here, the blue line illustrates the polarized light, and the black arrows indicate the horizontal and vertical polarization

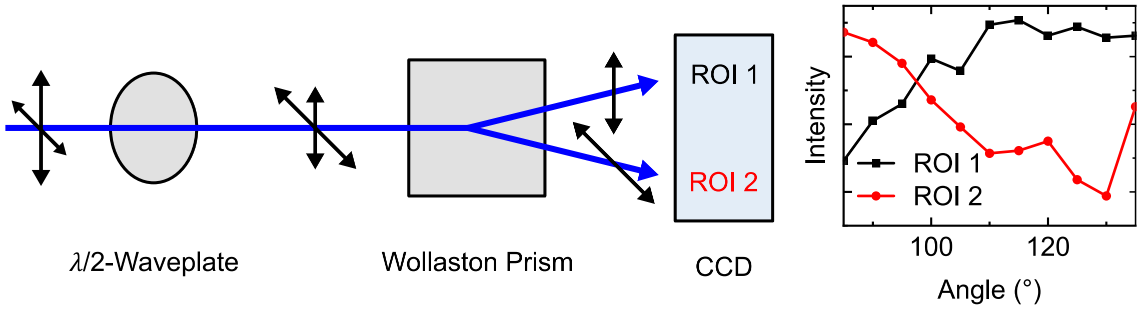

Figure 6.27.: Measurement setup used for the polarization of the DRs. The blue arrows represent PL light, and the black arrows indicate the magnitude of the horizontal and vertical polarization. The $\lambda/2$-waveplate rotates the polarization of incoming light. Afterwards, a Wollaston prism spatially separates the parallel and vertical components of the light, which is then detected on two different region of interests (ROIs) on the CCD detector. By measurement during the rotation of the $\lambda/2$-waveplate, the illustrated graph is obtained.

components. First, the light passes a $\lambda/2$-waveplate, which retards light depending on the orientation of the incident light and the fast axis. This effectively rotates the polarization direction of incoming light. Subsequently, a Wollaston prism separates the horizontal and vertical polarization components in space by a specific angle. The two separated polarized beams are spectrally dispersed by a spectrograph and detected on a CCD array detector. In order to determine the particle orientation, the $\lambda/2$-waveplate was rotated continuously while recording the PL light. The resulting graph for the measurement of an individual DR is shown as a graph in Figure 6.27. Finding the maximum of ROI 2 and the corresponding minimum of ROI 1 allows the determination of the particle orientation projected onto the sample plane.

Figure 6.28 shows multiple examples of spectral time traces measured from different single CdSe/CdS DRs during electric field sweeps. Each vertical line in the 2D image represents a single spectrum. The integration time was adjusted based on the spectral diffusion and PL intensity. Below each spectral time trace, the corresponding electric field sweep that was used during the measurement is displayed. Here, and in the following subsections, different electric field sweep profiles were used, in order to study different spectral dynamics. It can be seen that the emission energy and PL intensity change in response to the electric field. By tendency, this response is stronger when the DR is oriented parallel to the electric field. In Figure 6.28a and b, the emission energy shifts by up to 15 meV and 18 meV, respectively, compared to the absence of the electric field. Furthermore, the PL intensity in Figure 6.28a is nearly turned off once the electric field is above +175.8 kV/cm, while in the opposite field direction, the intensity remains nearly constant. This indicates that for the positive electric field, the electron is pushed away from the core, and in the negative electric field, the electron is pushed towards the core, while the hole remains in the core. The reason for this is that the position of the CdSe

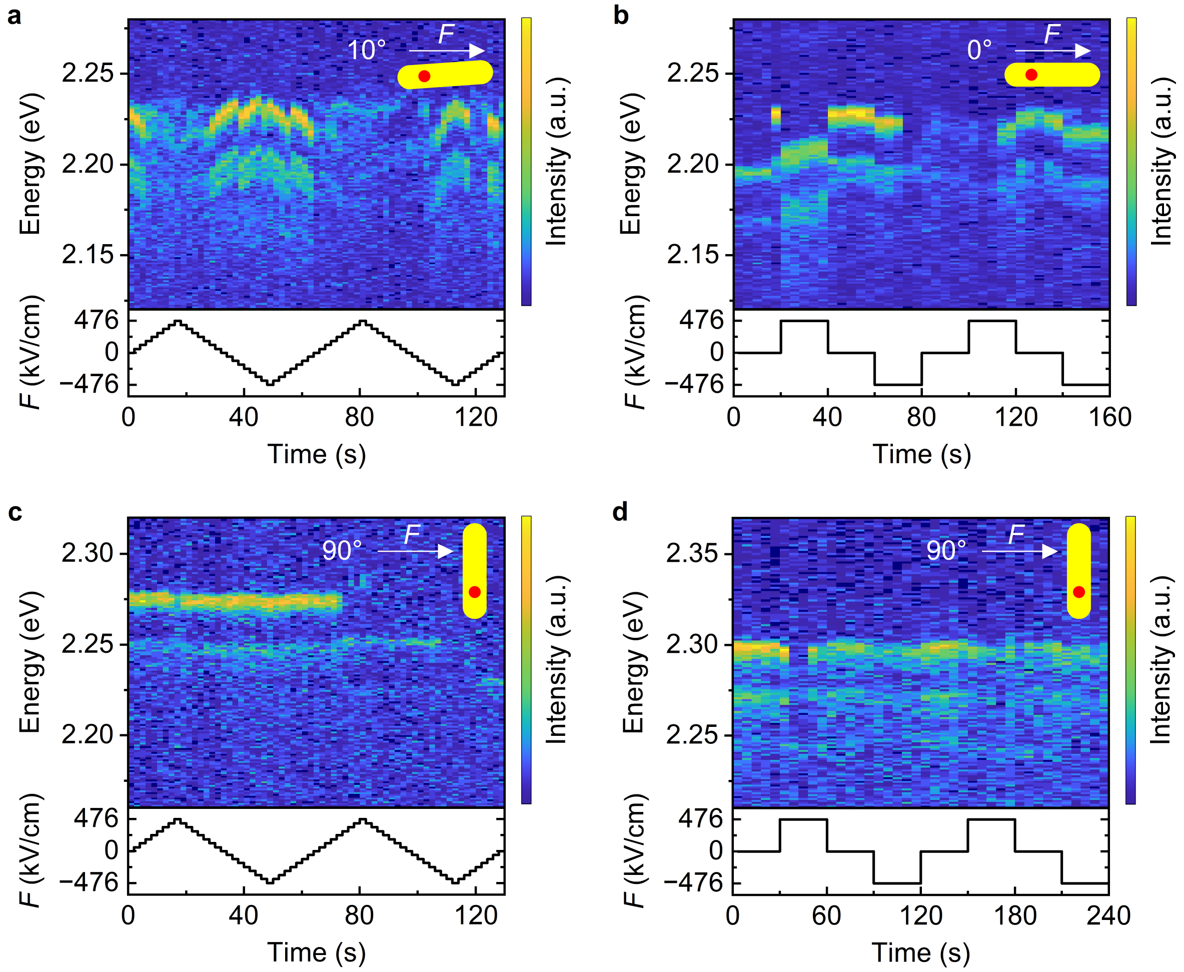

Figure 6.28.: Examples of spectral time traces measured from single CdSe/CdS DRs illustrating the influence of the DR orientation for the response to electric fields. Insets of the DRs indicate the in-plane orientation in relation to the electric field.

core is asymmetric. Based on the mole fraction of the octadecylphosphonic acid used in the synthesis, the CdSe core should be located most commonly at one-third of the DR long axis.[142,213] In Figure 6.28c and d, the DRs are oriented orthogonal to the electric field, and the emission energies remain nearly constant, shifting only up to 2–3 meV. The stronger QCSE for a parallel alignment of the DR to the electric field is expected because the exciton can be more easily polarized parallel to the long axis of the DRs. Additionally, photobleaching is present, and the PL intensity decreases towards the end of the measurements. This could be a result of charging of the DR, due to the inert conditions.[53,60,205]

Multiple interesting observations can be made here for the emission energy under the influence of electric fields. First, it can be seen that in Figure 6.28a, the electric field can both red- and blue-shift the emission energy of a single DR compared to the absence of the electric field. This is unusual for CdSe/CdS DRs, as the quasi-type-II band alignment should only allow for red-shifts of the emission. Second, in Figure 6.28b, spectral diffusion overlaps with the influence of the electric field. Third, in Figure 6.28b, between 20–40 s, spectral diffusion seems to be facilitated by the electric field. Fourth, it stands out that in Figure 6.28a, reproducible spectral jumps occur during the first negative electric field section. These observations will be discussed in detail in the following subsections. In addition, exciton–phonon coupling, influence of the excitation energy, emission polarization, and decay dynamics will also be discussed in detail.

Blue-Shifting the Emission Energy with Electric Fields

In order to use DR as optical switches or in voltage sensing applications, their spectral response needs to be understood. Additionally, their changes in emission energy and PL intensity need to be predictable. CdSe/CdS DRs, depending on their core size, are known to have a type-I or quasi-type-II band alignment.[138] Hence, external electric fields are expected to always produce red-shifts, regardless of the particle orientation.[31,111,125] In contrast to this, multiple CdSe/CdS DRs in this work exhibited both red- and blue-shifts, which are only expected for type-II band alignments. In ZnSe/CdS, the emission energy blue-shifts when the electron is pushed towards the ZnSe core, which has a higher potential energy in the conduction band compared to CdS, while the hole remains in the ZnSe core.[111,114] Figure 6.29 showcases four examples of spectral time traces measured from single DRs during electric field sweeps. In Figures 6.29a and b, both DRs exhibit a very similar behavior, as their emission energy red- and blue-shifts symmetrically by ±3 meV and ±5 meV, respectively. The only difference is that the dependence on the electric-field sign is reversed. Furthermore, for both DRs, the dependence on the electric field is linear. This suggests, based on Equation 2.1.24 in Chapter 2.1.5, that the polarizability of the emitting exciton state is very small for both measurements.[108] The spectral time trace in Figure 6.29c displays a much larger red-shift of 14 meV, induced by the positive electric field, compared to a smaller 5 meV blue-shift, created by the negative electric field. In Figure 6.29d, the measured red- and blue-shifts are 20 meV and 7 meV, respectively. The asymmetric behavior of the emission energy, depicted in Figures 6.29c and d, contains a linear and a quadratic contribution. Hence, the polarization of the emitting state is higher compared to Figures 6.29a and b. The asymmetric behavior could be a result of the CdSe core not being centered in the CdS rod.

A possible explanation for the observation of a blue-shift could be the presence of a static positive or negative surface charge that mimics the presence of a type-II band alignment by sitting between the electron and hole of the exciton. This would also explain the emission energy blue-shifts in only some of the DRs in response to the electric field. To test this theory, the emission energy of a CdSe/CdS DR with a single negative surface

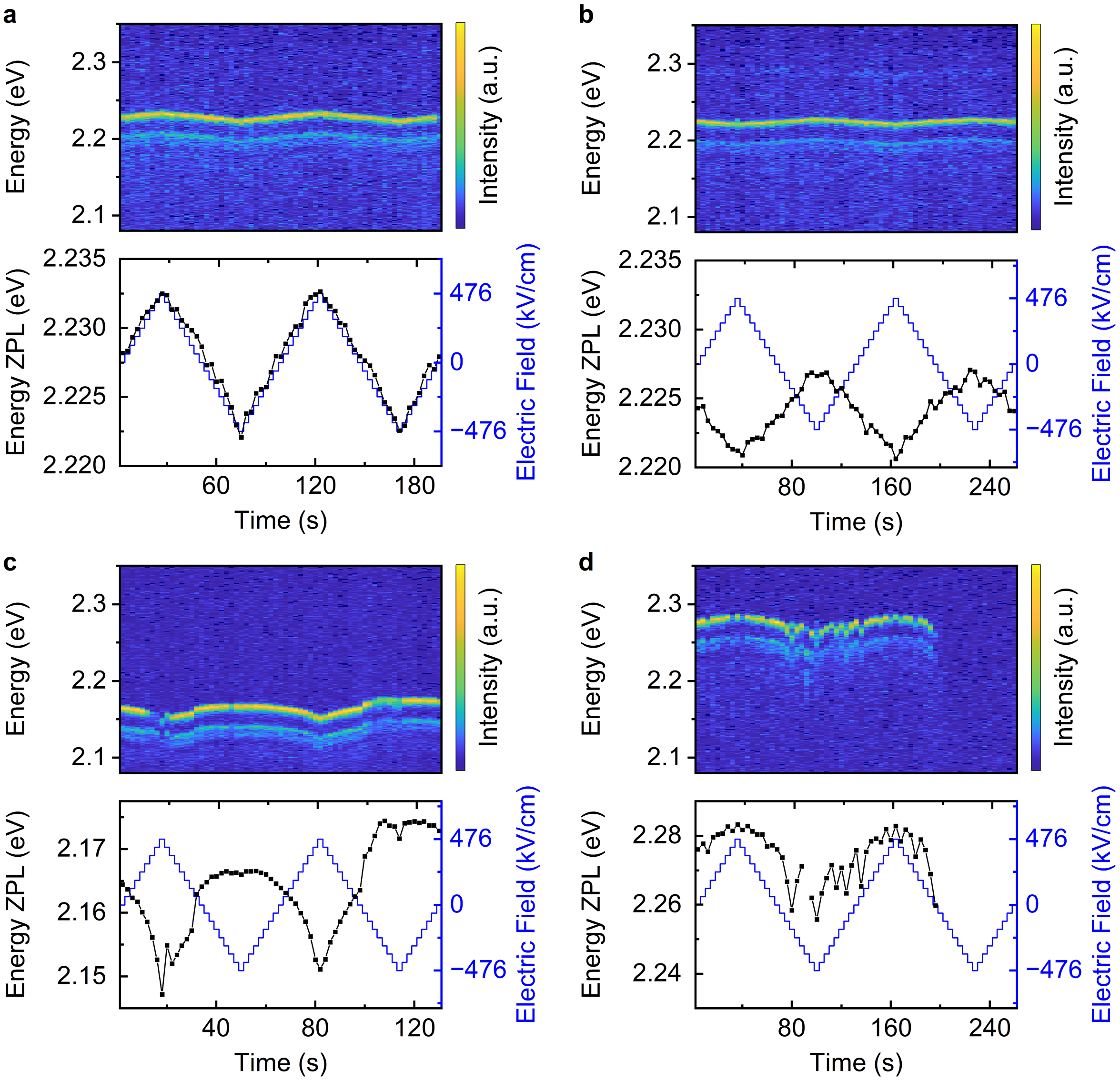

Figure 6.29.: Examples of spectral time traces measured from single CdSe/CdS DRs exhibiting both red- and blue-shifts, during electric field sweeps.

charge above the core was calculated under the influence of an external electric field. In the calculations, the CdSe core was placed at one-third of the rod axis, and the permittivity of the surrounding PMMA matrix was set to 2.4[116]. The calculation results are illustrated in Figure 6.30, where the horizontal lines serves as a guideline for the emission energy at zero electric field $E(0)$. Here, it can be seen that indeed a surface charge can allow the emission energy to blue-shift when an electric field is applied.

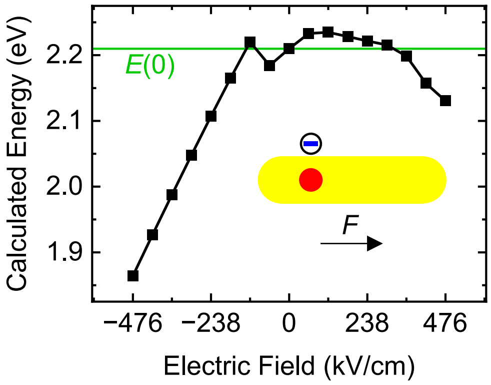

Figure 6.30.: Calculated emission energy of a CdSe/CdS parallel for different electric fields including a single negative surface charge, as indicated by the inset. For the simulation of the surface charge a negative point charge was added on top of the CdS shell. The horizontal green line indicates the emission energy without an electric field $E(0)$.

Memory Effect of Surface Charges

Multiple of the measured single DRs changed their spectral response when applying the same electric field at a different time. Regarding this behavior, Figure 6.31 demonstrates four examples of spectral time traces from single DRs. In Figure 6.31a, initially, the positive electric field induces a red-shift (10 s to 12 s), but after turning the electric field off (20 s to 22 s), an additional red-shift occurs. This is in contrast to the expectation of the emission energy returning to the start value of 2.244 eV for no electric field. When subsequently switching to negative electric field (30 s to 32 s), the emission energy blue-shifts to around 2.243 eV, which is near the zero field value. After the electric field is turned off again (40 s to 42 s), only a subtle blue-shift by 1 meV occurs. However, it is also possible that this small-blue-shift occurred randomly and independently of the electric field. Following this, in the next step, when a positive electric field is created (50–60 s) and turned off again (60 s to 62 s), the emission is red-shifted stepwise again, leading to two red-shifts. Besides the spectral shifts, the positive electric field increases the PL intensity, indicating that the wave function overlap of electron and hole might be increased. In the last step, the emission blue-shifts in the case of the negative electric field (70 s to 72 s), thereby repeating the previous pattern. Obviously, the change of the optical properties does not only depend on the applied field but also on the preceding state of the system.

Hence, four different states can be attributed, as illustrated in Figure 6.32. Here, the change from the preceding step is indicated by an up arrow, or down arrow, except for the initial state that is marked with a "?", while the current step is defined by "0", "+", or "-". The question mark describes the fact that the emission state before the measurement is unknown. For a better overview, the color code from the pattern is applied

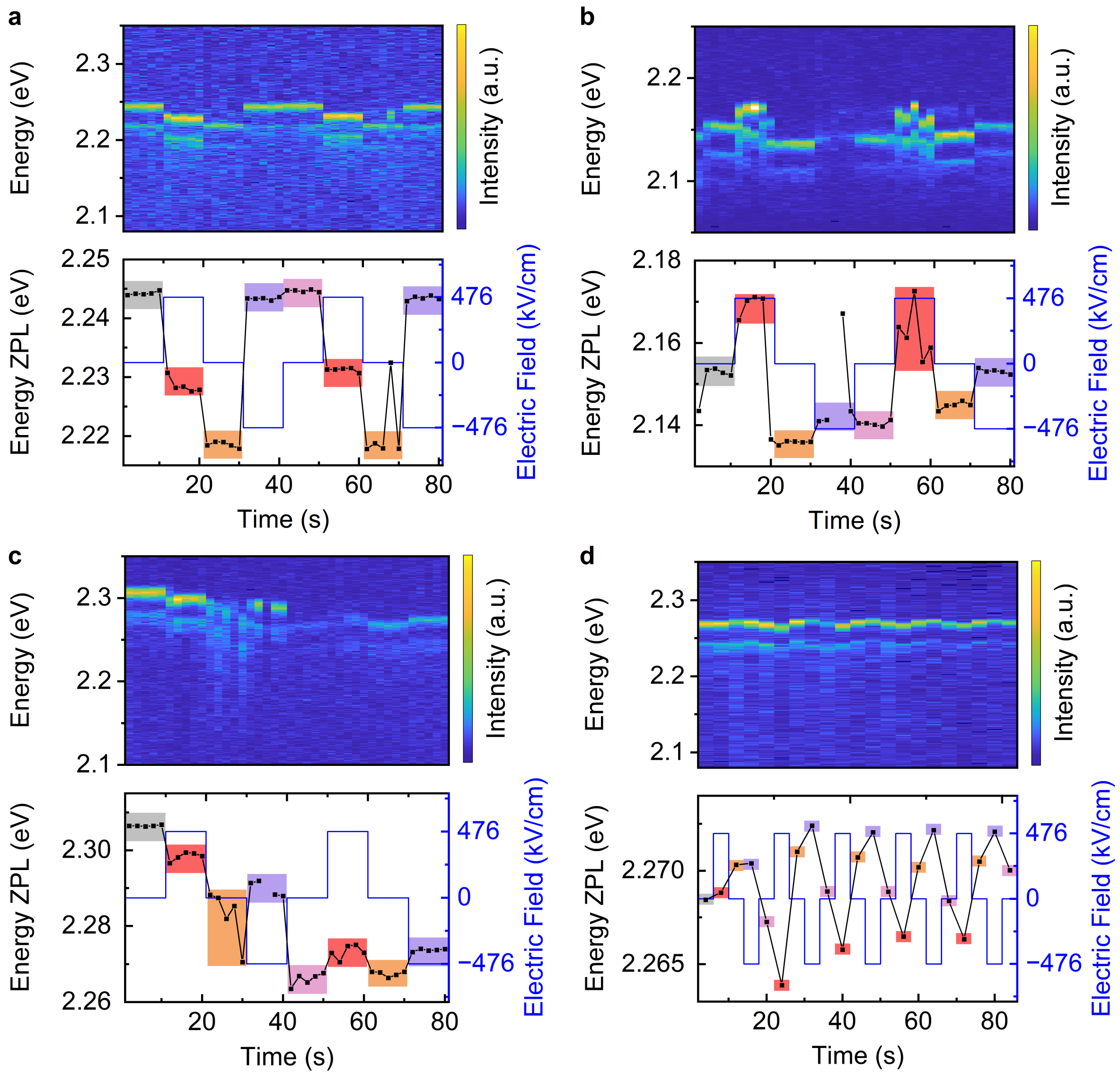

Figure 6.31.: Spectral time traces measured from single CdSe/CdS DRs displaying varying QCSE responses. Colored boxes highlight the directional dependence, explained in Figure 6.32.

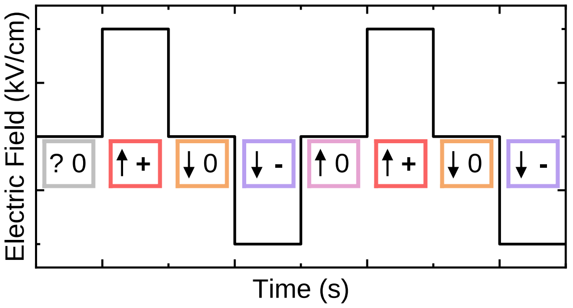

Figure 6.32.: Scheme for the dependence of the spectral time trace on the electric field sequence order.

to Figure 6.31a–d. Similar to Figure 6.31a, the red- and blue-shifts depend on the order of the electric field sweep in Figure 6.31b as well. One difference is that for this DR, both the "↑+" (red) and "↓-" (violet) emission states are blue-shifted compared to their preceding steps. Moreover, the positive electric field seems to promote spectral diffusion for this DR. This promotion of spectral diffusion by external electric fields has also been reported by Conradt et al.[125], although to a much weaker degree. In Figure 6.31c, "↑0" (purple) and "↓0" (orange) again have different emission energies, as before in panels a and b. The emission red-shifts and the PL intensity decreases throughout the measurement, which limits the comparability of the different emission states. In general, by shortening the electric field steps, more cycles can be included, as shown for the next DR in Figure 6.31d. After the first four field states (0–16 s), where the system undergoes a kind of equilibrium, a distinct pattern is formed by the four different emission states.

A possible mechanism for the difference between "↑0" (purple) and "↓0" (orange) is illustrated in Figure 6.33. Here, the former color code of Figure 6.32 is used. Initially, without an electric field, a surface charge is in an energy minimum of a potential energy landscape (grey). If a positive electric field is created, the potential energy landscape is tilted and as a consequence the surface charge moves to a different energy minimum (red). After the electric field is turned off, the surface charge remains in the energy minimum, as the energy barriers surrounding it are too high for spontaneous changes (orange). Thereby memorizing the previous electric field step. Only when an opposing electric field is applied the surface charge is moved out of its position (violet). This memory effect during electric field switching has not been reported yet. Moreover, this memory effect has to be considered in the design of future applications that use switchable NCs.

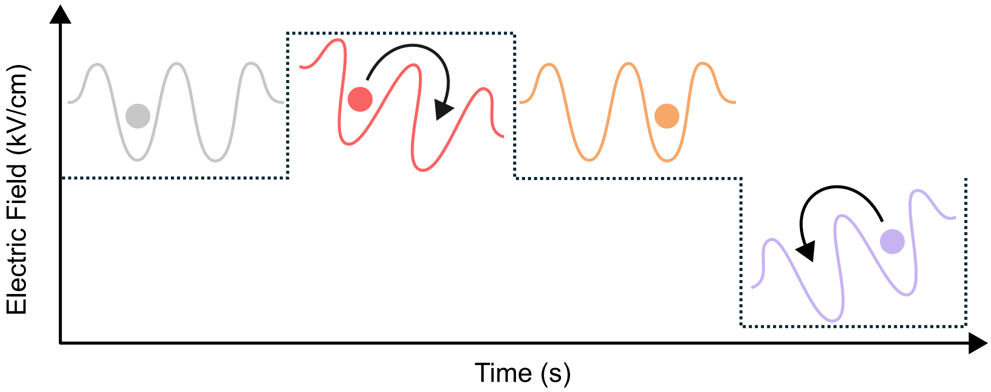

Figure 6.33.: Induced changes of the surface charge state when the electric field is changed. The colors are based on the notation of Figure 6.32.

Directed Spectral Diffusion

Further interaction between the external electric field and surface charges was also observed in the spectral dynamics following a rapid and strong increase of the external electric field. In these measurements, the electric fields seemingly activated and directed spectral diffusion to a specific higher or lower energy. For this behavior, Figure 6.34 displays four examples of spectral time traces from single DRs.

For a detailed discussion of Figure 6.34a, roman numerals are assigned to the different steps. Initially, the emission energy red-shifts in response to the positive electric field from step I to II, while the PL intensity decreases significantly. Therefore, the remaining emission signal in step II could either be from the ZPL or a phonon replica. While the positive electric field is kept active, the emission energy continuously blue-shifts from 12 s to 20 s by a total of 29 meV. Interestingly, this blue-shifting process is strong in the beginning and goes into saturation later on. Once the electric field is switched off in step III, the emission energy stays blue-shifted, even with respect to the initial zero field state. This same pattern returns when the positive electric field step is repeated from step V to VIII. At first, from step V to VI, the emission energy red-shifts by 31 meV from 50 s to 52 s. Afterwards, in step VI, the emission energy blue-shifts between 52–60 s by a total of 24 meV. When the electric field is turned off again from step VI to VII, initially the emission energy blue-shifts strongly by 41 meV. Followed by red-shifting stepwise to 2.210 eV. In both cases, it seems that the continuous diffusion is activated by the electric field and saturates on a time scale of 10 s. Furthermore, during the first negative field step, the emission energy red-shifts initially by 12 meV, followed by red-shifting continuously from 32 s to 40 s by 8 meV.

In Figure 6.34b, again directed spectral diffusion takes place in the beginning between 12–20 s, which goes into saturation at the end. When the electric field is turned off, the emission blue-shifts after a delay of 2 s. Subsequently, the emission energy continues to blue-shift. The second time, the positive electric field is turned on and off again, the emission continues to blue-shift again (62–70 s), also showing a saturation behavior. Interestingly, when the negative electric field is turned on a second time, a strong continuous blue-shift occurs from 72 s to 78 s. Again, this indicates that the external electric field induces directed spectral diffusion. In Figure 6.34c, the first positive electric field step enhances spectral diffusion, this time with a continuous red-shift instead of a blue-shift, as seen in the previous two examples. This red-shift is not repeated between 52–58 s, which could be related to the photodarkening that occurs temporarily. In the last example, Figure 6.34d, directed spectral diffusion seems to occur only once, during the first positive electric field step (12–20 s). When the field is turned off afterwards, the emission blue-shifts back to the previous emission energy measured after 10 s.

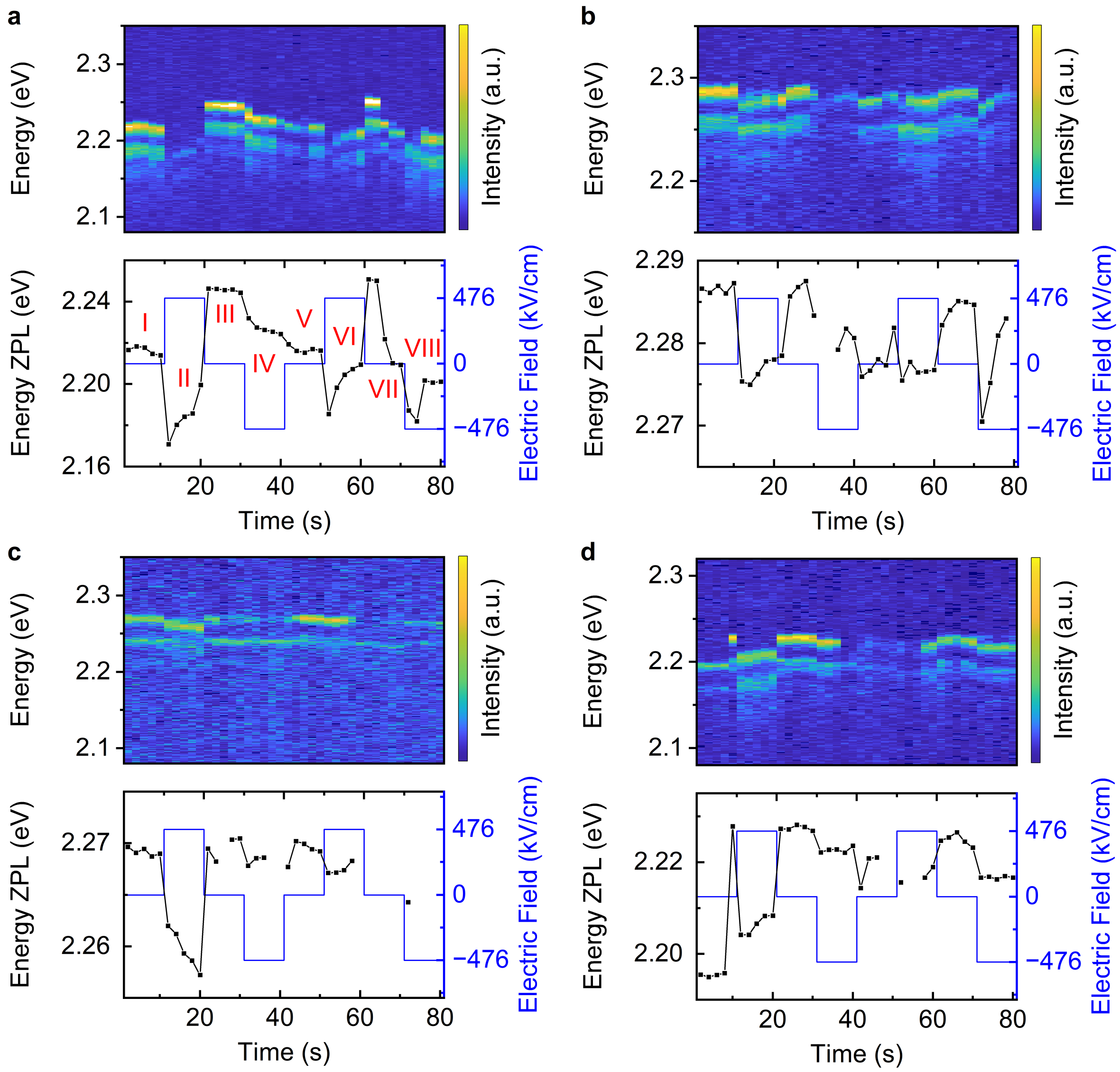

Figure 6.34.: Spectral time traces recorded from single CdSe/CdS DRs showing directed spectral diffusion after changes of the electric field. To make the detailed discussion for panel a clearer, roman numerals were assigned to the individual electric field steps.

This present phenomenon of directed spectral diffusion has not been reported yet. In particular, the long time scale on which the direct spectral diffusion takes place stands out. Future molecular dynamics simulations could, for example, be of use to find corresponding changes of ligand conformations or positions that take place on the same time scale, if an external electric fields is applied. Moreover, the saturation of the directed spectral diffusion could mean that strong static electric fields could be of potential use to bring the NC system into a stable emission state, where surface charge movement becomes impaired.

Induced Repeatable Spectral Jumps

If the electric field is changed in smaller steps of 59.5 kV/cm, repeatable spectral jumps can be found for some of the DRs. In contrast to before, these spectral jumps are not created by strong changes of the electric field, but occur when a threshold of the electric field strength is reached. Four examples of these spectral jumps measured from single DRs are shown in Figure 6.35. During the electric field sweep, in Figure 6.35a, distinct jumps of 7 meV occur repeatedly at 357 kV/cm, which red-shift the emission energy. Analogous jumps that blue-shift the emission by 3 meV take place repeatedly at −357 kV/cm. Additionally, larger spectral jumps of the emission of around 22 meV appear when the electric field transitions from positive to negative. In the next example, Figure 6.35b, spectral jumps are also present in the first positive electric field section. Here, the emission blue-shifts by around 5 meV when the electric field reaches 297 kV/cm. In Figure 6.35c, spectral jumps are visible at 119 kV/cm. Initially, in the first spectral jump (from 12 s to 18 s), a larger blue-shift of 6 meV takes place. For further spectral jumps, from 90 s to 96 s and 204 s to 210 s, the blue-shift decreases by 4 and 2 meV, respectively. The spectral time trace in Figure 6.35d displays a more complex spectral behavior, which includes more spectral jumps than the other examples. Within the first positive loop part, these jumps occur symmetrically at 119 and 357 kV/cm. Interestingly, the spectral jumps appear at nearly the same field strengths in the negative loop section.

Spectral jumps to lower energy have also been reported by Rothenberg et al. for CdSe nanorods. They explained this by the tilting of the energy levels due to the Stark effect, which promotes the trapping of a charge carrier, leading to the emission of a negatively charged exciton.[110] Likewise, the same assisted trapping could also apply to the CdSe/CdS DRs. The observation of both spectral jumps towards lower and higher energy in Figure 6.35a could be a result of either the electron or the hole being trapped, depending on the direction of the electric field. Furthermore, it stands out that the spectral jumps for the negative electric field occur at the same field strength as for the positive case (Figure 6.35a/d). Thus, another explanation could be that the trap states themselves undergo a reversible change, which could, for example, be a conformational or positional change of a ligand.

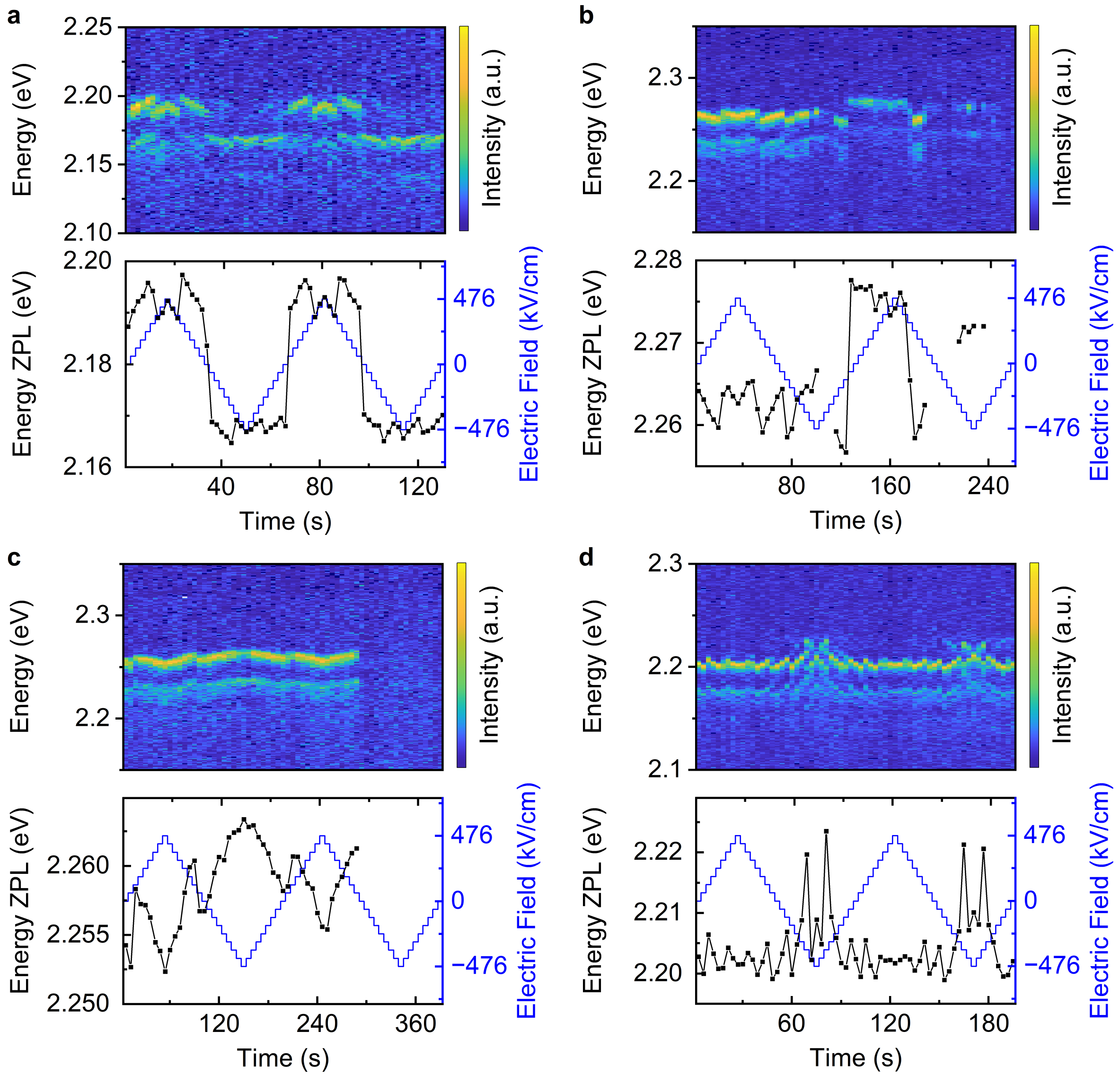

Figure 6.35.: Examples of spectral time traces from single CdSe/CdS DRs exhibiting repeatable spectral jumps.

Exciton–Phonon Coupling

Changes of the electron and hole localization due to the electric field should also be reflected in exciton–phonon phonon coupling, similarly to the results discussed in Chapter 6.1. Figure 6.36 shows four examples of spectral time traces from single DRs for which the intensity of exciton–phonon coupling $(I_\mathrm{S} + I_\mathrm{Se})/I_\mathrm{ZPL}$ was evaluated. It can be clearly observed that the magnitude of exciton–phonon coupling increases when the electric field red-shifts the emission energy. Additionally, the magnitude of exciton–phonon coupling changes over time in response to spectral diffusion.

For a better overview, Figure 6.37 displays the fitting results for the emission energy, total phonon coupling intensity, and S- to Se-type phonon ratio at different electric fields.

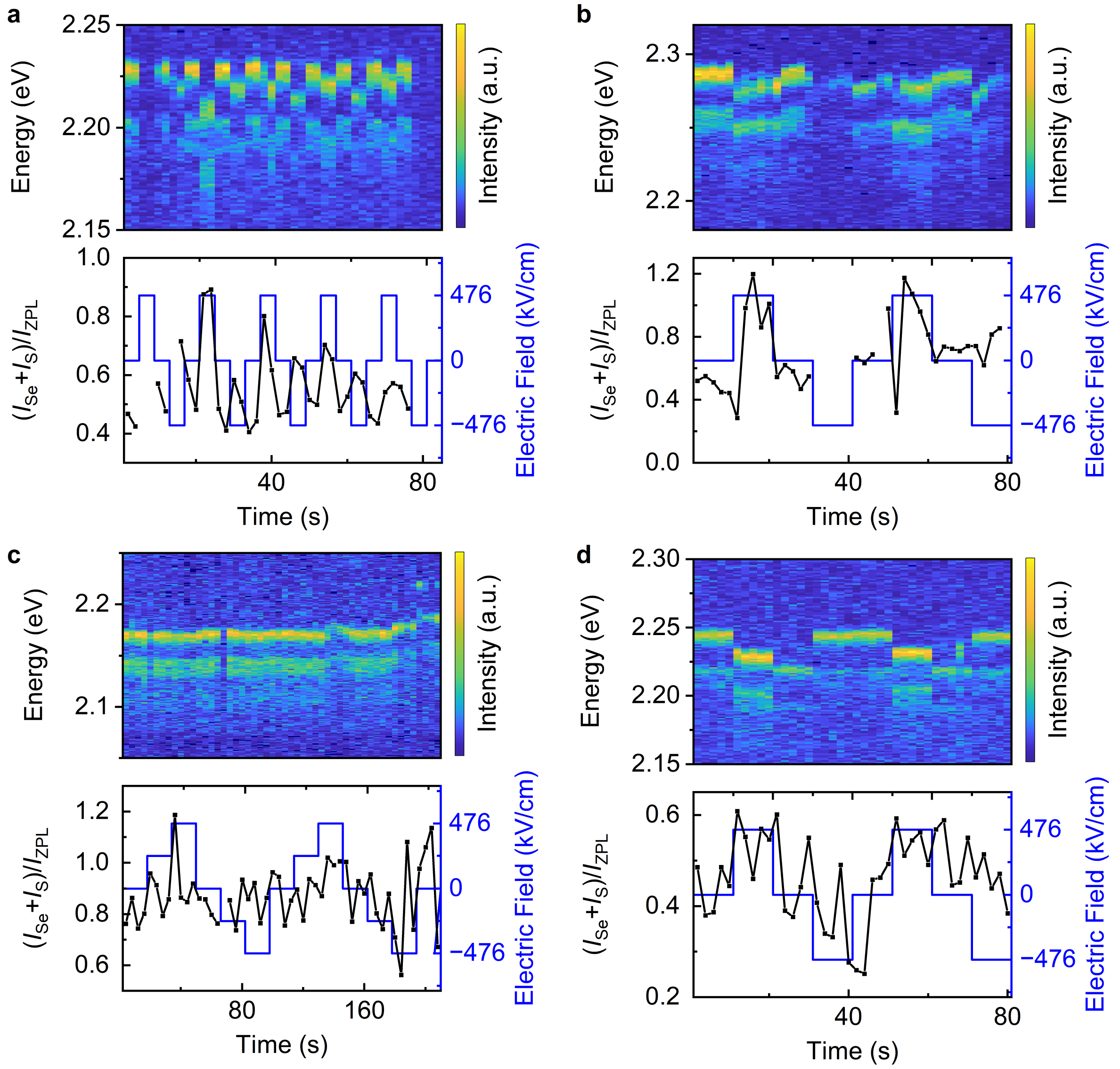

Figure 6.36.: Examples of spectral time traces from single CdSe/CdS DRs for the change of exciton–phonon coupling as a response to the electric field. In addition, the evaluated magnitude of exciton–phonon coupling $(I_\mathrm{S} + I_\mathrm{Se})/I_\mathrm{ZPL}$ is shown.

Here, each column represents the evaluation of a single DR. Fit results of the S- to Se-type phonon ratio should be viewed with caution, as the low PL signal does not allow for unambiguous fits in all spectra. The emission energy of the first particle (Figure 6.37a) red-shifts by around 11 meV for both positive and negative electric fields. This is accompanied by a distinct increase in the magnitude of exciton–phonon coupling (Figure 6.37e) by around 40 %. It can also be seen that the corresponding S-to Se-type phonon ratio decreases for the negative field and increases for the positive electric field. The corresponding S- to Se-type phonon ratio in Figure 6.37i decreases under the influence of the negative electric field, while it increases for the positive electric field. For the second DR, the emission energy shifts to a smaller degree by only 5 meV (Figure 6.37b). This

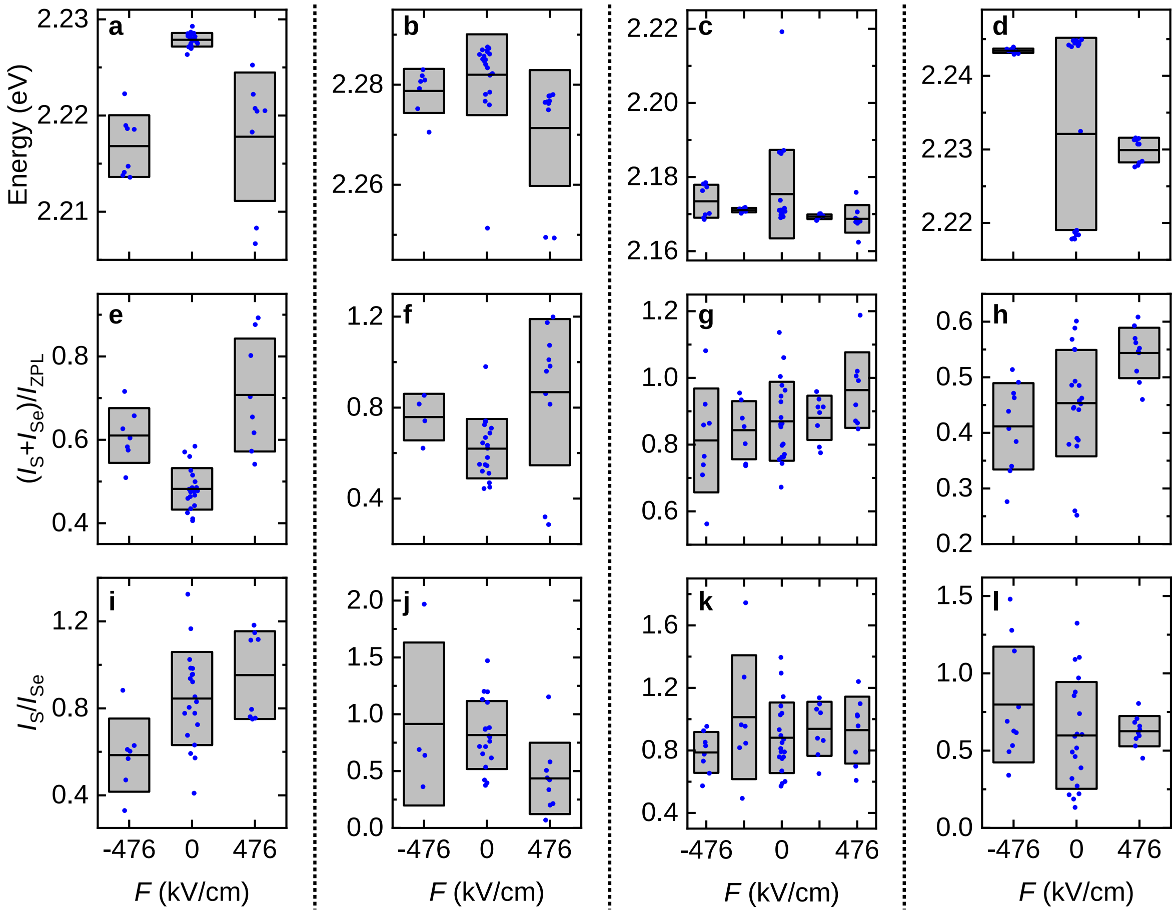

Figure 6.37.: Compilation of the fitting results, of the four DRs of Figure 6.36, for (a–d) the emission energy, (e–h) the relative phonon coupling intensity and (i–l) the S- to Se-type phonon ratio. Each blue dot represents a fitted parameter, while horizontal line inside the box marks the average value. The upper and lower limits of the boxes correspond to the standard deviations.

is again accompanied by an increase in the magnitude in exciton–phonon coupling of around 40 % (Figure 6.37g). The S- to Se-type phonon ratio stays nearly constant in the case of the positive electric field, while its response to the negative electric field is unclear due to the low PL signal (Figure 6.37k). Regarding the third DR, the emission energy blue-shifts and red-shifts in the negative and positive electric fields, respectively. The magnitude of exciton–phonon coupling increases together with the red-shift of the emission energy, while it decreases with the blue-shift. Furthermore, it can be seen that the S- to Se-type phonon ratio slightly decreases in response to the negative electric field, while it increases for the positive electric field. The emission energy of the last DR red-shifts under the influence of the positive electric field, while the emission energy remains nearly constant under the negative electric field (Figure 6.37d). In Figure 6.37h, a distinct increase of exciton–phonon coupling by 20 % is visible for the positive electric field, and a smaller decrease of the exciton–phonon coupling by 10 % is present for the negative electric field. Furthermore, the S- to Se-type phonon ratio stays relatively constant in response to the positive electric field, while it increases in the case of the negative electric field (Figure 6.37l).

In general, when the emission energy is red-shifted by the electric field, the exciton–phonon coupling increases simultaneously, and vice versa; the coupling intensity decreases when the emission energy is blue-shifted. The observed increase in exciton–phonon coupling in response to the electric field can be attributed to the decreased wave function overlap, as the electron and hole are pulled apart.[21,25,94,198] Any influences on the S- to Se-type phonon ratio are less clear, as it can both increase and decrease when the emission energy red-shifts due to the electric field. These asymmetric changes of the S- to Se-type phonon ratio likely reflect the asymmetric position of the CdSe core inside the DRs and could be used to elucidate the position of the CdSe core of the DRs in relation to the direction of the electric field. For example, an increase of the S- to Se-type phonon ratio could mean that the electron is getting pulled towards the $(00\bar{1})$ facet.

Emission Polarization

The usage of a Wollaston prism before the spectrograph allows the online measurement of the emission polarization during the electric field sweeps. An example of the evaluated DOP (see Equation 2.2.2) of a single DR, measured under influence of external electric fields, is depicted in Figure 6.38. (Corresponding spectral data can be found in the appendix in Figure A.3.) If the electric field is turned off, the DOP, determined from the ZPL, already varies for each spectral measurement from 0.03 to 0.36 (Figure 6.38). By tendency, the positive electric field seemingly increases the DOP. Vice versa, the negative electric field decreases the DOP. When the DOP is evaluated for the sum of the ZPL and phonon replica intensities, this previous trend is preserved. Interestingly, the values shift slightly, indicating that phonon replicas have a different polarization DOP. (An additional

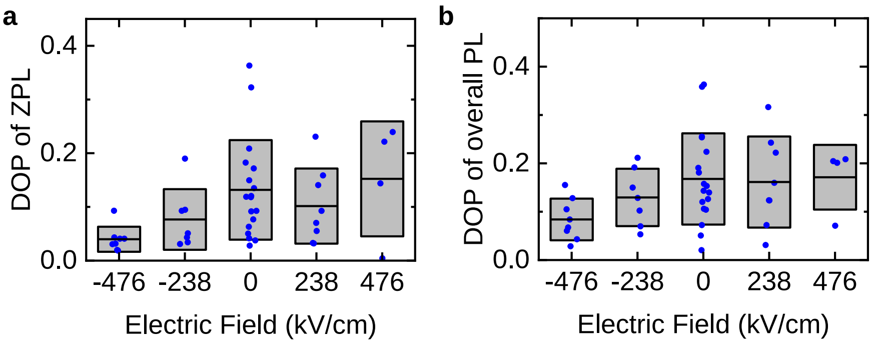

Figure 6.38.: Degree of Polarization evaluated from (a) the ZPL and (b) the summed PL intensity of a single CdSe/CdS DR for different electric fields. Blue dots represents the fitted DOP of single spectra, and the horizontal line inside the box marks the average value. The upper and lower limits of the boxes correspond to the standard deviations.

spectral time trace of the same particle is illustrated in Figure A.4 in Appendix A.1, in which a positive electric field leads to a distinct red-shifts of the emission energy, while a negative electric field results in a blue-shift.)

Temporal variations of the DOP can be attributed to the influence of spectral diffusion. For example, Zhang et al.[155] found that active charging of CdSe/CdS on indium tin oxide broadens the distribution of DOPs. They attributed this to the change of the exciton–fine structure due to the surface charges. Similarly, here the external electric field might reorder the exciton-fine structure states, which intrinsically exhibit different DOPs.[153,154]

Influence of Excitation Energy

So far, all measurements were performed with excitation at 2.78 eV (446 nm). In order to investigate the influence of the excitation energy on the QCSE, the same single DRs were first measured with the regular excitation at 2.78 eV, followed by the repetition of the measurement with excitation at 2.43 eV (510 nm). As a consequence, the higher excitation energy excites primarily states in the CdS shell, while the lower excitation energy selectively excites energy states in the CdSe core.[142] Two examples of single CdSe/CdS DRs, excited with different energies, are displayed in Figure 6.39 (a/b and c/d). For the first DR, the response towards the electric field is similar for both excitation in the shell (Figure 6.39a) and core (Figure 6.39b), as the emission is red- and blue-shifted by around ±5 meV. However, a more pronounced spectral diffusion is present for the core excitation. The second particle in Figure 6.39c/d also exhibits a similar response to the electric field for both core and shell excitation. In both situations, the emission energy gets shifted by around ±8 meV and is overlayed with spectral diffusion to a similar degree.

To allow for a better comparison, the fitted ZPL energy is shown as a function of the electric field in Figure 6.40 for shell excitation (black circles) and core excitation (green squares). The first DR in Figure 6.40a shows both a linear and quadratic contribution. Transparent boxes serve as guidelines and indicate different surface charge situations. For the energetically lower emission state, in the case of the core excitation, the slope is higher than for the shell excitation. Whereas the slope for the higher emission states, during core excitation, is more similar compared to the shell excitation. In Figure 6.40b, the slopes for core and shell excitation are very similar for related surface charge configurations.

Variations of the linear and quadratic contributions originate from changes in the excited-state dipole moment and polarizability, respectively, as described by the Stark effect equation (Equation 2.1.24). The different slopes present in Figure 6.40 likely result from the influence of surface charges. These surface charges, depending on their position, can easily change the dipole moment of the emitting state, as described by the Stark effect equation (Equation 2.1.24). Exciting the DRs closer to their band edge should have led

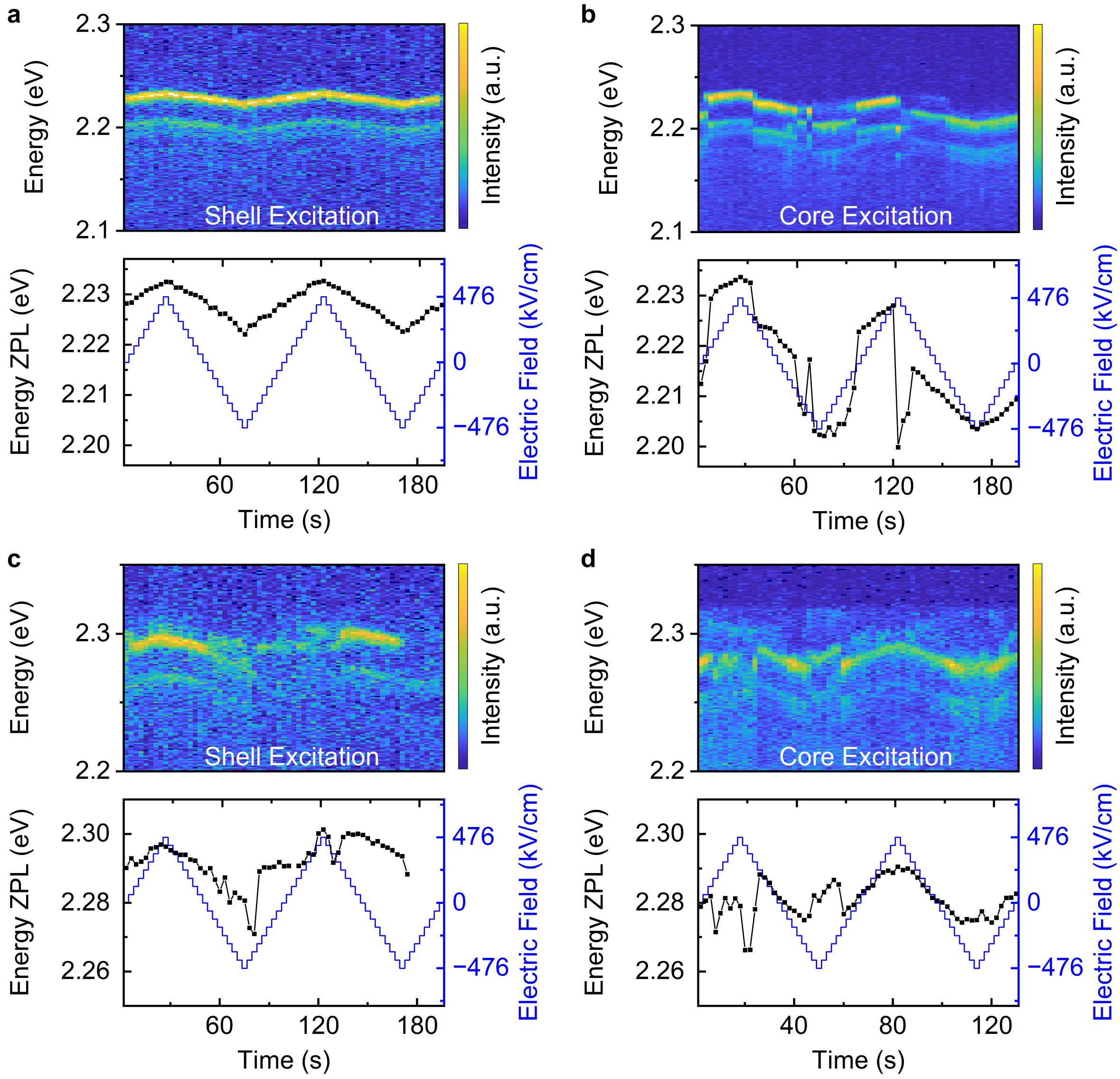

Figure 6.39.: Comparison of spectral time traces of two single CdSe/CdS DRs excited at (a/c) 2.78 eV and (b/d) 2.43 eV.

to a lower spectral diffusion because less excess energy is introduced into the system. A possible explanation for the stronger spectral diffusion, when the sample is excited in the core region at 2.43 eV, could be the higher excitation power that was used because of the low absorption cross-section of the core. This higher excitation power was also absorbed by the substrate, which could have promoted local charge variations in the environment of the DRs. Furthermore, the higher slope in the case of core excitation in Figure 6.40 indicates a higher dipole moment of the emitting state, which is unexpected as the emitting state after relaxation to the band edge should be the same for both core and shell excitation.

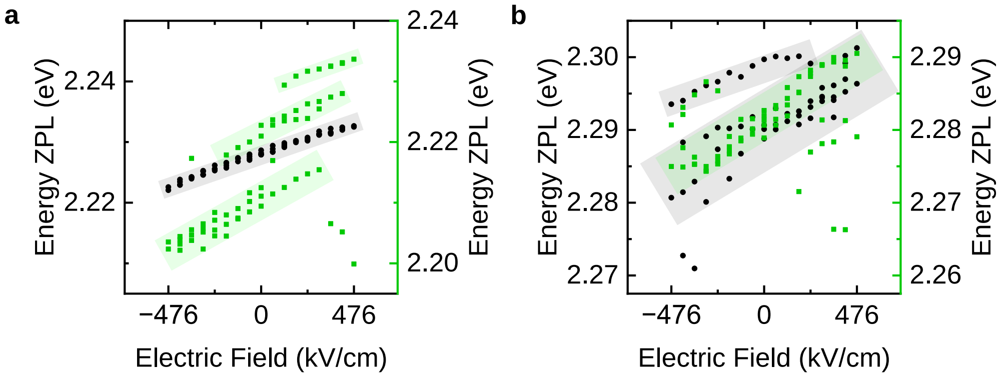

Figure 6.40.: Comparison of the fitted ZPL energies for (a) particle 1 and (b) particle for excitation with 2.78 eV (black circles) and 2.43 eV (green squares). These are the same DR previously shown in Figure 6.39 a/b and c/d, respectively. Transparent boxes indicate different surface charge constellations.

Decay Dynamics

In order to investigate the influence of the electric field on the recombination dynamics of the exciton, PL decay curves were measured during an electric field sweep. Figure 6.41 depicts two examples of PL decay curves of single CdSe/CdS DRs. It can be seen, for both DRs, that with increasing positive electric field, the decay time increases. Whereas the decay time shortens with the rising negative electric field. Measurements of the background signal at different spots, depicted in Figure A.5, show that the background is not static and the corresponding lifetimes vary. Thus, a background removal is not possible. In order to reduce the influence of the background signal in the fitting process, all fits were started with a delay of 1 ns after the intensity maximum.

Table 6.6 gives an overview of the fit results of the two DRs from Figure 6.41. For both particles, the PL intensity increases with the positive electric field, while it decreases for the opposite field direction. Regarding the first particle, the shorter lifetime component τ_1

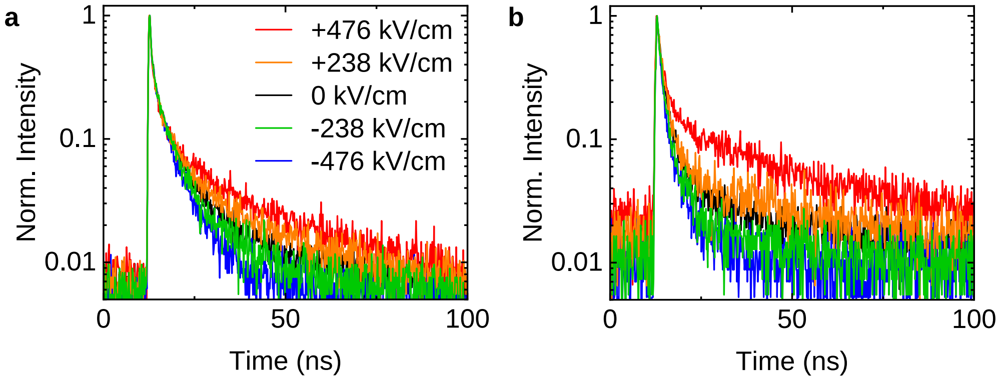

Figure 6.41.: Photoluminescence decay curves of two separate CdSe/CdS DRs measured during an electric field sweep. The corresponding electric field loop in depicted in Figure A.6.

Table 6.6.: Fitting results for the same two particles depicted in Figure 6.41a and b: weight and lifetime of the short A_1 / τ_1 and long component A_2 / τ_2, intensity-averaged lifetime τ_{average} and average PL intensity I_{PL}.

Particle	F(kV/cm)	A_1	τ_1 (ns)	A_2	τ_2 (ns)	τ_{average}(ns)	I_{PL}(a.u.)
1	+476	0.22	1.8	0.10	16.8	14.0	1754
1	+238	0.21	2.1	0.10	13.2	10.3	1594
1	0	0.19	1.5	0.15	8.1	6.8	1470
1	−238	0.18	1.6	0.16	6.9	5.8	1384
1	−476	0.14	0.9	0.22	5.0	4.6	1275
2	+476	0.34	1.9	0.12	27.5	23.3	1006
2	+238	0.46	1.8	0.05	23.6	14.2	660
2	0	0.46	1.6	0.06	12.7	7.3	617
2	−238	0.41	1.0	0.11	5.5	3.7	534
2	−476	0.35	1.1	0.10	5.1	3.4	504

decreases slightly for the negative electric field and increases minimally for the positive electric field. The long component of the lifetime τ_1 shares the same trend but changes on a larger scale from 5 ns to 16.8 ns. Because of the larger contribution of the long component, the average lifetime also shows a clear increase from the negative to the positive electric field. Regarding the second particle, the same trend as for the first one is present. Here, both the short and long components, as well as the average lifetime, change on a larger scale. As a result, the average lifetime decreases by a factor of two in the presence of the negative electric field, while it increases by a factor of three due to the positive electric field. In the corresponding PL time traces in Figure A.7 in Appendix A.1, it can be seen that with increasing positive electric field, the PL intensity increases, while it decreases the stronger the negative electric field gets. (It was also tested how the recombination dynamics of the exciton change when a single DR is excited in shell (at 2.78 eV) or core (at 2.34 eV), which is briefly discussed in Figure A.8 in Appendix A.1.)

From the changes in PL intensity for both particles, it can be concluded that the positive electric field likely pushes the electron towards the CdSe core, while the hole stays in the core. Due to the larger wave function overlap of the electron and the hole, it is expected that the radiative lifetime shortens in the case of the positive electric field. The observed increase in the average fluorescence lifetime means that the QY increases, thereby indicating that the contribution of non-radiative decay decreases, based on Equation 2.1.11. Consequently, the reduction of the non-radiative decay therefore causes the average fluorescence lifetime to increase, outweighing the changes in the radiative lifetime.

The reduced contribution of the non-radiative decay could be a result of the lowered electron mobility and reduced trapping of the electron. In the opposite case, the negative electric field reduces the QY. As a result, the contribution of the non-radiative decay likely increases. This overshadows the expected increase in the radiative decay because of the reduced wave function overlap in the exciton.

6.3.3. ZnCdSe/CdS Dot-in-Rod NCs in external Electric Field

The type-II band alignment of $Zn_{1-x}Cd_xSe/CdS$ DRs makes them good candidates for electric field switching. All measurements of $Zn_{1-x}Cd_xSe/CdS$ DRs in electric fields were performed with DRs that have an average core diameter of 2.91 nm, a rod diameter of 5.88 nm, and a length of 45.9 nm. These samples were synthesized by Mareike Dittmar. (More details can be found in Chapter 4.2.3.) Due to the synthesis conditions, the Cd fraction is likely around $x \approx 0.5$–0.6. (An exemplary TEM image of the DRs is shown in Figure A.10 in Appendix A.1.)

Comparison of Type-I and Type-II

Figure 6.42 displays an exemplary comparison of single $Zn_{1-x}Cd_xSe/CdS$ and CdSe/CdS DRs with a nearly parallel orientation toward the electric field. In the case of the first $Zn_{1-x}Cd_xSe/CdS$ DR (Figure 6.42a), the emission energy exhibits a blue-shift of 12 meV and a strong red-shift of up to 55 meV in response to the electric field. A weaker influence of the electric field is present for the second $Zn_{1-x}Cd_xSe/CdS$ DR (Figure 6.42b), which blue-shifts and red-shifts the emission by up to 15 meV and 13 meV, respectively. The emission energy of the CdSe/CdS example in Figure 6.42c blue-shifts by up to 4 meV and red-shifts by up to 13 meV due to the electric field. In the second CdSe/CdS example (Figure 6.42d), the emission red-shifts by up to 18 meV in the positive electric field, while remaining relatively constant in the negative electric field.

These observations indicate a stronger influence of the electric field on the optical properties of the $Zn_{1-x}Cd_xSe/CdS$ DRs and are consistent with the stronger polarizability of the excitons due to the type-II band alignment ($Zn_{1-x}Cd_xSe/CdS$) compared to the type-I band alignment (CdSe/CdS). The type-II band alignment also explains the stronger blue-shifts that are possible in the $Zn_{1-x}Cd_xSe/CdS$ case, while the larger red-shifts are a result of the slightly longer rod length.

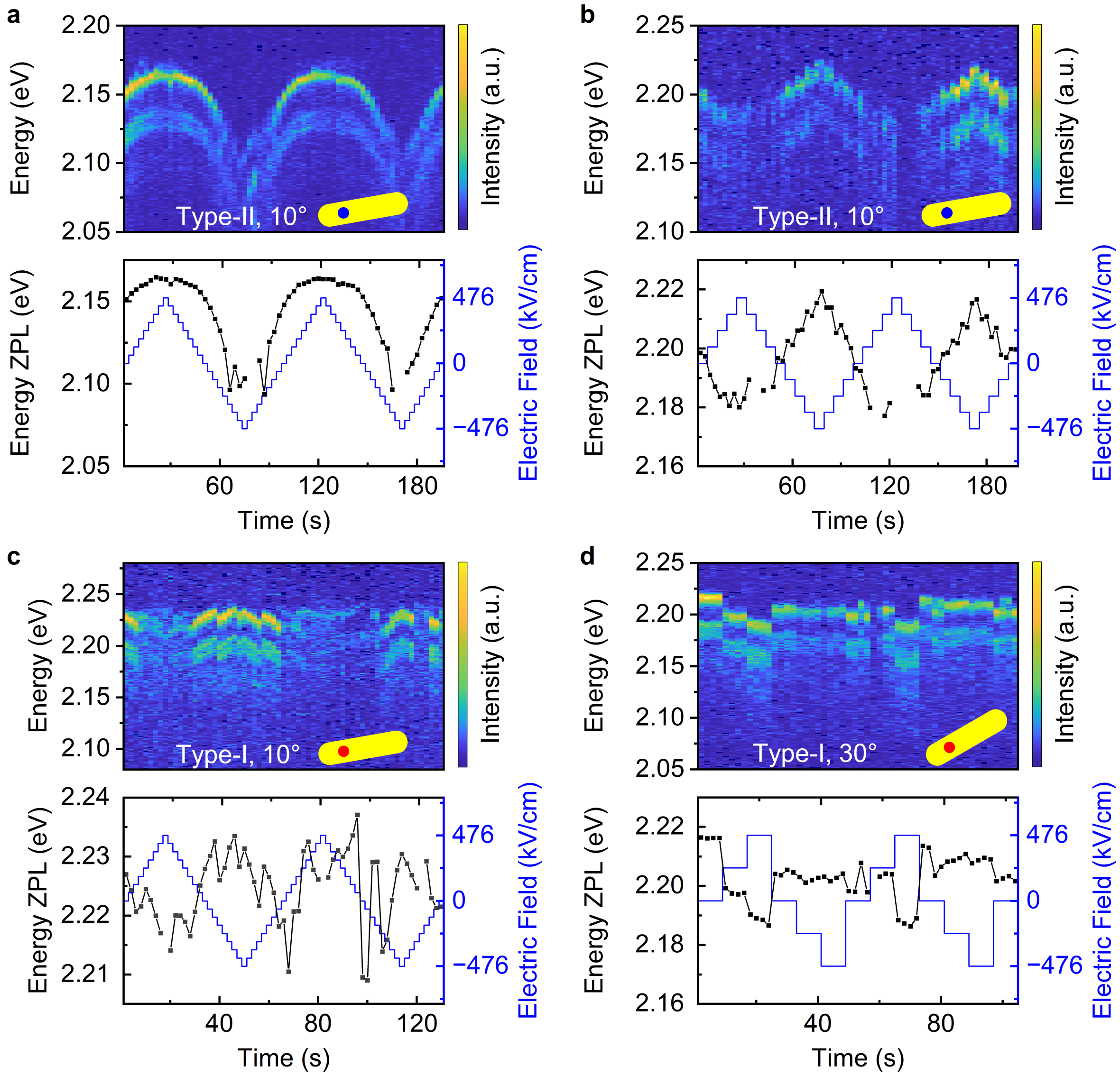

Figure 6.42.: Comparison of spectral time traces measured from single (a/b) $Zn_{1-x}Cd_xSe/CdS$ and (c/d) CdSe/CdS DRs. The insets of DR indicate their orientation in relation to the electric field.

Exciton–Phonon Coupling

Figure 6.43 shows two examples of spectral time traces and fitting results of the corresponding magnitude of exciton–phonon coupling. In Figure 6.43a, when the emission energy red-shifts in response to the negative electric field, the intensity of exciton–phonon coupling increases. In the case of the positive electric field, the emission energy blue-shifts while the exciton–phonon coupling decreases slightly. In the second example, Figure 6.43b, the analogous spectral changes are exhibited, but for the opposite field directions.

Figure 6.44 displays the fittings results of the emission energy, intensity of exciton–phonon coupling, and S- to Se-type phonon ratio. In Figure 6.44a, the emission energy

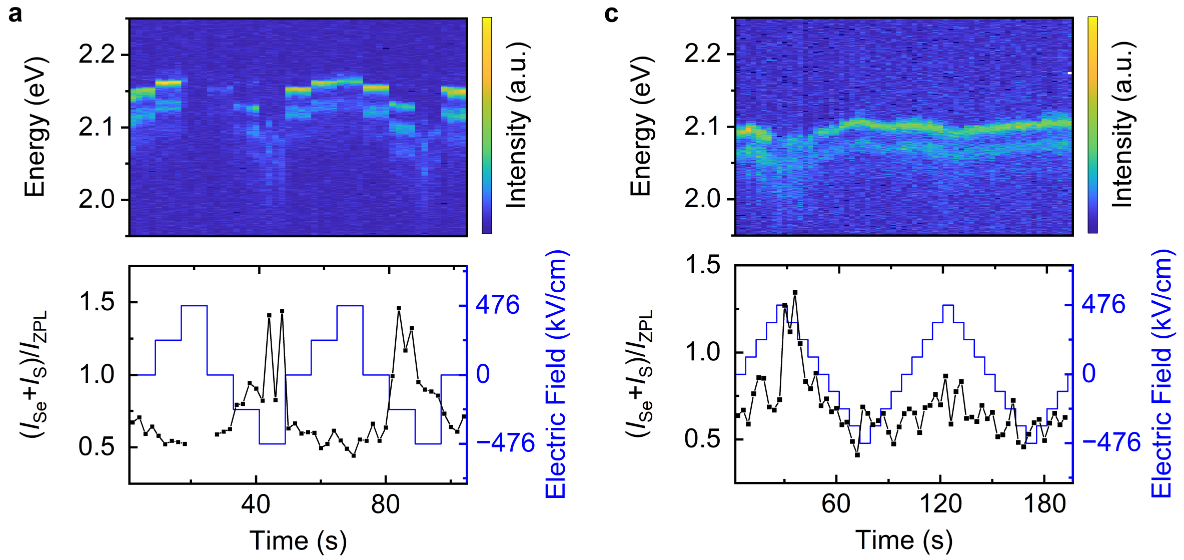

Figure 6.43.: Examples of spectral time traces of single $Zn_{1-x}Cd_xSe/CdS$ DR and their relative intensity of exciton–phonon coupling $(I_S + I_{Se})/I_{ZPL}$.

red-shifts by 63 meV and blue-shifty by 12 meV due to the negative and positive electric fields, respectively. The red-shift is accompanied by an increase in the exciton–phonon coupling intensity of 60 %, whereas the blue-shift occurs together with a reduction of the exciton–phonon coupling by 20 % (Figure 6.44c). In Figure 6.44e, it can be seen that the S- to Se-type phonon ratio decreases with increasing positive electric field. In the case of the negative electric field, the S- to Se- type phonon ratio decreases before it increases. The increase for −476 kV/c is not certain because of the low PL signal that makes the fit error-prone. A similar behavior of the response towards the electric field is found for the second particle. Its emission energy red- and blue-shifts on average by 20 meV and 8 meV, respectively (Figure 6.44b). Again, the red-shift goes hand in hand with an increase in the magnitude of exciton–phonon coupling by around 30 %. In reverse, the intensity of exciton–phonon coupling declines slightly by 10 % as the emission blue-shifts (Figure 6.44d). By tendency, the S- to Se-type phonon ratio in Figure 6.44f goes up slightly for the positive electric field and vice versa; it goes down for the negative electric field.

In brief summary, the exciton–phonon coupling increases clearly in response to the electric field, as the electron and hole are pulled apart from each other, which is also indicated by the associated red-shift. The opposite is observed when the emission blue-shifts in response to the electric field, as the exciton–phonon coupling decreases. Thus, the exciton–phonon coupling can be easily controlled by external electric fields. When the emission energy blue-shifts the S- to Se-type phonon ratio decreases, which can be explained by the increasing localization of the electron in the core region, while the hole

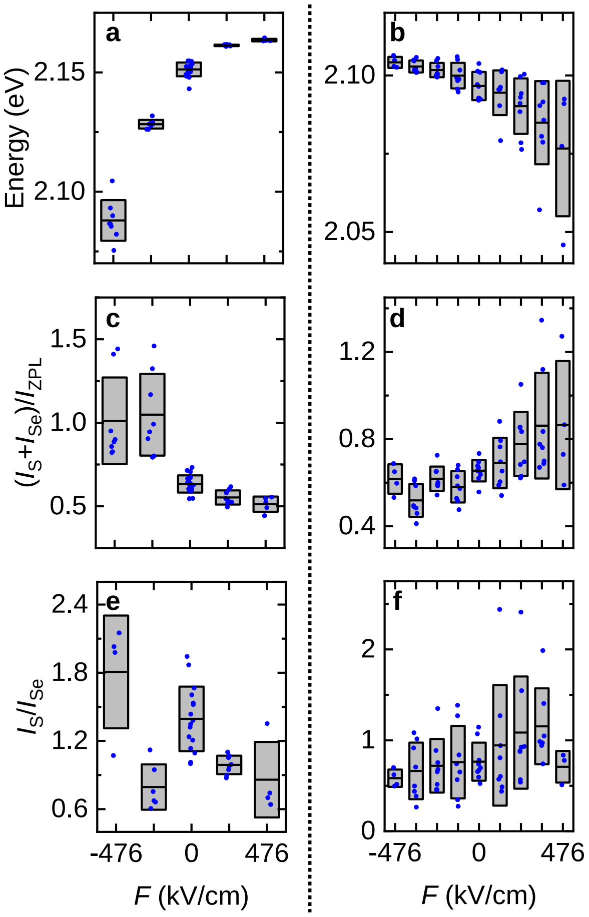

Figure 6.44.: Overview of the fitting results of (a,b) the emission energy, (c,d) magnitude of exciton–phonon coupling $(I_\mathrm{S}+I_\mathrm{Se})/I_\mathrm{ZPL}$, and (e,f) S- to Se-type phonon ratio for the two particles of Figure 6.43. Each blue dot represents a fitted parameter, while horizontal line inside the box marks the average value. The upper and lower limits of the boxes correspond to the standard deviations.

remains in the core. The corresponding increase of the S- to Se-type phonon ratio, when the emission energy red-shifts is primarily clear in Figure 6.44f. Here, the electron and hole are moved away from the core, explaining the increasing S- to Se-type phonon coupling. The analogous behavior is not unambiguous in Figure 6.44e, which could be related to the position of the core and the influence of possible surface charges.

Decay Dynamics

Figure 6.45 displays an exemplary measurement of the fluorescence lifetime of the same DR from Figure 6.42 for different electric fields. A negative electric field results in a faster PL decay rate, whereas a positive electric field prolongs the PL decay rate. The corresponding time trace of the PL is shown in Figure A.11. This time traces indicate that the wave function overlap is highest for an electric field of −238 kV/cm and lowest for +476 kV/cm.

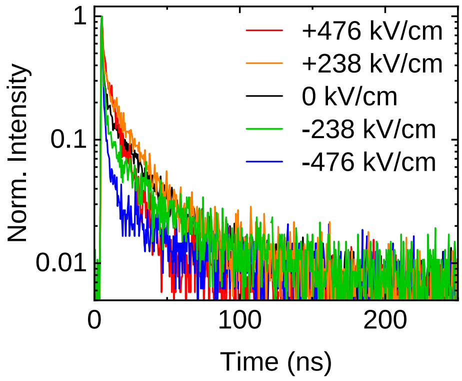

Figure 6.45.: Photoluminescence decay curve of a single $Zn_{1-x}Cd_xSe$/CdS DR measured under different electric field conditions. The corresponding electric field loop in depicted in Figure A.6.

All decay curves were fitted with biexponential functions, and the results are compiled in Table 6.7. Regarding the PL intensity, a maximum is present at +238 kV/cm. The short component of the lifetime increases slightly for a positive electric field, while the long component and average lifetime decrease in response to the negative electric field. Furthermore, a strong decrease of the average lifetime is found from +238 kV/cm to +476 kV/cm.

As a consequence of the type-II band alignment, the fluorescence lifetimes of the ZnSe/CdS DRs are longer than those measured for the CdSe/CdS DRs (Table 6.6). By tendency, the average lifetime and the long component decrease with rising PL intensity, in contrast to results for CdSe/CdS DRs. Here, the decrease in the average lifetime correlates with the increasing wave function overlap, which is consistent with the blue-shift for the DR in Figure 6.42a if a positive electric field is applied. A possible explanation for the strong decrease of the average fluorescence lifetime when the field is changed from +238 kV/cm to +476 kV/cm could be that electron localization is brought closer to a specific trap state. Another possible influence could also arise from changes in the exciton fine structure in response to the electric field that could affect the lifetimes.[214,215]

Table 6.7.: Fitting results for Figure 6.45: weight and lifetime of the short A_1 / τ_1 and long component A_2 / τ_2, intensity-averaged lifetime τ_{average} and I_{PL}.

F(kV/cm)	A_1	τ_1 (ns)	A_2	τ_2 (ns)	τ_{average}(ns)	I_{PL} (a.u.)
+476	0.23	2.3	0.32	11.0	9.9	485
+238	0.21	3.0	0.23	22.8	20.7	630
0	0.21	2.1	0.16	25.5	23.1	547
−238	0.26	1.9	0.09	32.2	27.8	487
−476	0.25	1.6	0.03	42.6	33.5	374

7. Conclusion

In this work, the influence of the charge-carrier localization on the optical properties of semiconductor NC was investigated by single-particle PL spectroscopy. The corresponding interpretation was supported by quantum mechanical calculations. Hereby, a special focus was set on exciton–phonon coupling, as well as on the interaction of excitons with surface charges. For this reason, DRs were chosen as the main sample system because their anisotropy facilitates the polarization of the exciton. Thereby, increasing exciton–phonon coupling and interaction with surface charges. For controlling the charge-carrier localization, the material composition and shape were varied. Further control over the charge-carrier localization was gained by applying external electric fields.

In order to investigate exciton–phonon coupling as a first sample system, a set of four $Zn_{1-x}Cd_xSe/CdS$ DR samples, DR-1–4, with increasing x, was analyzed. This sample set represented a stepwise transition from a type-II to a type-I band alignment, while the geometry was kept constant. The transition of the band alignment was reflected in the red-shift of the emission energy by 100 meV and the reduction of the fluorescence lifetime. Interestingly, the fluorescence lifetime at 10 K was not always longer than at 295 K. Thus, hinting at a more complex exciton–fine structure that the common three-state model can not describe. Statistical single particle spectroscopy at 10 K allowed to directly probe the exciton–phonon coupling of the lowest exciton state. Two first-order phonon replicas were resolved, referred to as S-type and Se-type phonons. In contrast to expectations, the corresponding energies of the S- and Se-type phonons did not show a distinct trend with increasing Cd fraction x and remained at 36–38 meV and 27–28 meV, respectively. It is likely that the trend was too small to be resolved here. However, the relative intensities of the first-order phonon replica exhibited an unambiguous change for the transition from the type-II to type-I band alignment. To be more precise, the total exciton–phonon coupling, defined by the HR factor, decreased continuously from 0.77 to 0.35. The S-type phonon coupling decreased the most, from 0.48 to 0.9, whereas the Se-type phonon remained nearly constant around 0.35. A better understanding of the experimental results was obtained by developing a simple model that evaluates the magnitude of exciton–phonon coupling from the difference in probability of electron and hole, weighted by coupling constants β. The corresponding probability densities of the electron and hole were simulated by quantum mechanical calculations within the effective-mass approximation, including the self-consistent calculation of the Coulomb interaction. The coupling constants were derived from the spectroscopy data of the first and fourth sample, to be $\beta_{\mathrm{S}}^{\mathrm{e}} = 1.35$, $\beta_{\mathrm{S}}^{\mathrm{h}} = 3.35$, $\beta_{\mathrm{Se}}^{\mathrm{e}} = 0.12$. Interestingly, these coupling constants share similarities with the Fröhlich coupling constants α used for bulk systems. Based on the calculations of the S- to Se-type phonon ratio, the Cd fractions x of the second and third sample were estimated to be 0.65 and 0.79, respectively. These values are in agreement with expectations from EXAFS spectroscopy. Moreover, the calculations allowed evaluating the influence of the different geometry parameters, showing that the core diameter is the most important factor for the exciton–phonon coupling. The calculations also revealed that surface charges have a strong impact on exciton–phonon coupling. This also explained the broader distributions of exciton–phonon coupling intensities found in the measurements.

As a second sample set exciton–phonon coupling was investigated in spherical CdSe/CdS and $\mathrm{CdSe}_y\mathrm{S}_{1-y}$/CdS NCs by single-particle spectroscopy at 10 K. Here, an increase in the shell thickness from 2.2 nm to 5.1 nm resulted in an increase of the summed first-order exciton–phonon coupling from 0.37 to 0.48, thereby indicating an increased delocalization of the exciton. Regarding the alloying, the change of the exciton localization did not cause a noticeable change in the exciton–phonon coupling. According to the average ZPL energy, no strong change in the charge-carrier localization and related exciton–phonon coupling would have been expected here.

To enable external control of the exciton localization by strong external electric fields, single DRs were embedded inside a PMMA matrix between IDEs. As a third sample system, CdSe/CdS and $\mathrm{Zn}_{1-x}\mathrm{Cd}_x\mathrm{Se}$/CdS DRs were measured. Within these experiments, several interesting properties were discovered. When the DRs were aligned parallel to the electric field, their optical properties exhibited a strong response, following expectations. Surprisingly, quasi-type-II CdSe/CdS DRs showed both red- and blue-shift, which usually only occurs in the case of a true type-II band alignment. This behavior was attributed to the influence of surface charges, which induced a potential similar to a type-II band alignment. Calculations also verified this assumption. Additionally, these shifts not only depend on the applied electric field but also on the previously applied field. Thereby, creating a memory effect on some of the DRs was found during the electric field sweeps. When the electric field was turned on and off, the emission energy did not return to its former state. A possible origin for this could be changes in the binding or conformation of ligands in response to the electric field. Another effect that was observed was the directed spectral diffusion. Upon change of the electric field, in some cases, spectral diffusion towards lower or higher energy was promoted, which initially shifted the emission energy strongly before saturating over several seconds. Thereby, indicating slow a relaxation effect. By sweeping the electric field in smaller steps, induced repeatable jumps in the emission energy were measured at specific field strengths. These jumps could not be explained by trapping alone, due to the observation of jumps occurring at constant field strengths in both electric field directions. Thus, changes in the ligand sphere are a more likely origin. Measurement of the polarized emission of the DR showed that the DOP is relatively independent of the external electric field and changes only on a small scale. The electric field also influenced the magnitude of exciton–phonon coupling. In general, when the electron and hole were pulled in opposite directions and the emission energy red-shifted, the strength of exciton–phonon coupling was increased. Whereas, when electron and hole were pushed together, the exciton–phonon coupling decreased, following expectations. In case of CdSe/CdS, where red-shifts occurred for both electric field directions, a slight increase or decrease of the S- to Se-type phonon ratio was found, thereby allowing to evaluate the position of the CdSe core inside the CdS rod. By comparison of CdSe/CdS and $Zn_{1-x}Cd_xSe$/CdS DRs, it has been shown that both the emission energy, as well as the exciton–phonon coupling, can be manipulated on a larger scale. Furthermore, electric fields were successfully used to continuously tune the fluorescence lifetime of excitons in both CdSe/CdS and $Zn_{1-x}Cd_xSe$/CdS DRs. Additionally, the comparison of core and shell excitation showed that the core excitation seemingly leads to a slightly higher dipole moment of the emissive state, which could also be a consequence of the influence from surface charges.

8. Outlook

The results of this work establish that exciton–phonon coupling can serve as a new quantity for the charge-carrier localization. Moreover, the strong influence of surface charges demonstrates that in order to reduce exciton–phonon coupling in the application of NCs, the exciton needs to be sufficiently shielded from surface charges. The collected statistical data set also provides an excellent basis for comparison to future atomistic calculations, paving the way for accurately simulating exciton–phonon coupling. As long as more accurate atomistic calculations remain challenging, the developed model of this work for the description of exciton–phonon coupling is a useful tool that can be easily transferred to other systems. It would, for example, also be interesting to combine the model of this work with atomistic calculations of exciton wave functions. Once exciton–phonon coupling is better understood, the emission linewidth, transport properties, and coherence of emitted photons from NCs can be improved for applications. The newly observed effects found in the optical properties of the NCs under the influence of an electric field also advance the fundamental understanding of spectral diffusion. Here, molecular dynamics simulations for the ligands under the influence of external electric fields would be of great interest to find a conclusive origin of spectral diffusion. The saturation of the directed spectral diffusion also suggests that static electric fields could be used to hinder spectral diffusion, thereby stabilizing the emission state of NCs.

9. References

(1) Smith, A. M.; Nie, S. *Acc. Chem. Res.* **2010**, *43*, 190–200.

(2) Panfil, Y. E.; Oded, M.; Banin, U. *Angew. Chem. Int. Ed. Engl.* **2018**, *57*, 4274–4295.

(3) Guo, Y.; Gao, F.; Huang, P.; Wu, R.; Gu, W.; Wei, J.; Liu, F.; Li, H. *Energy Mater. Adv.* **2022**, *2022*, 34540–34547.

(4) Li, H.; Zhu, X.; Zhang, D.; Gao, Y.; Feng, Y.; Ma, Z.; Huang, J.; He, H.; Ye, Z.; Dai, X. *Nat. Commun.* **2024**, *15*, 6561.

(5) Yang, B.; Cang, J.; Li, Z.; Chen, J. *Nanoscale Adv.* **2024**, *6*, 1331–1360.

(6) Moroz, P.; Boddy, A.; Zamkov, M. *Front. Chem.* **2018**, *6*, 353.

(7) Rainò, G.; Stöferle, T.; Moreels, I.; Gomes, R.; Kamal, J. S.; Hens, Z.; Mahrt, R. F. *ACS Nano* **2011**, *5*, 4031–4036.

(8) Morgan, D. P.; Kelley, D. F. *J. Phys. Chem. C* **2019**, *123*, 18665–18675.

(9) Yazdani, N.; Andermatt, S.; Yarema, M.; Farto, V.; Bani-Hashemian, M. H.; Volk, S.; Lin, W. M. M.; Yarema, O.; Luisier, M.; Wood, V. *Nat. Commun.* **2020**, *11*, 2852.

(10) Jo, W.; Kee, J.; Kim, K.; Landahl, E. C.; Longbons, G.; Walko, D. A.; Wen, H.; Lee, D. R.; Lee, S. *Sci. Rep.* **2022**, *12*, 16606.

(11) Stroscio, M. A.; Dutta, M., *Phonons in Nanostructures*; Cambridge University Press: Cambridge, 2001.

(12) Cui, J.; Beyler, A. P.; Coropceanu, I.; Cleary, L.; Avila, T. R.; Chen, Y.; Cordero, J. M.; Heathcote, S. L.; Harris, D. K.; Chen, O.; Cao, J.; Bawendi, M. G. *Nano Lett.* **2016**, *16*, 289–296.

(13) Biadala, L.; Louyer, Y.; Tamarat, P.; Lounis, B. *Phys. Rev. Lett.* **2009**, *103*, 037404.

(14) Kelley, A. M. *J. Chem. Phys.* **2019**, *151*, 140901.

(15) Lin, K.; Jasrasaria, D.; Yoo, J. J.; Bawendi, M.; Utzat, H.; Rabani, E. *J. Phys. Chem. Lett.* **2023**, *14*, 7241–7248.

(16) Lange, H.; Artemyev, M.; Woggon, U.; Niermann, T.; Thomsen, C. *Phys. Rev. B* **2008**, *77*, 193303.

(17) Tschirner, N.; Lange, H.; Schliwa, A.; Biermann, A.; Thomsen, C.; Lambert, K.; Gomes, R.; Hens, Z. *Chem. Mater.* **2012**, *24*, 311–318.

(18) Dzhagan, V.; Mazur, N.; Kapush, O.; Selyshchev, O.; Karnaukhov, A.; Yeshchenko, O. A.; Danylenko, M. I.; Yukhymchuk, V.; Zahn, D. R. T. *Nanomaterials* **2023**, *13*, 921.

(19) Groeneveld, E.; de Mello Donegá, C. *J. Phys. Chem. C* **2012**, *116*, 16240–16250.

(20) Brodu, A.; Ballottin, M. V.; Buhot, J.; Dupont, D.; Tessier, M.; Hens, Z.; Rabouw, F. T.; Christianen, P. C. M.; de Mello Donega, C.; Vanmaekelbergh, D. *Phys. Rev. B* **2020**, *101*, 125413.

(21) Nomura, S.; Kobayashi, T. *Phys. Rev. B* **1992**, *45*, 1305–1316.

(22) Krauss, T. D.; Wise, F. W. *Phys. Rev. B* **1997**, *55*, 9860–9865.

(23) Sagar, D. M.; Cooney, R. R.; Sewall, S. L.; Dias, E. A.; Barsan, M. M.; Butler, I. S.; Kambhampati, P. *Phys. Rev. B* **2008**, *77*, 235321.

(24) Yazdani, N.; Volk, S.; Yarema, O.; Yarema, M.; Wood, V. *ACS Photonics* **2020**, *7*, 1088–1095.

(25) Iaru, C. M.; Brodu, A.; van Hoof, N. J. J.; ter Huurne, S. E. T.; Buhot, J.; Montanarella, F.; Buhbut, S.; Christianen, P. C. M.; Vanmaekelbergh, D.; de Mello Donega, C.; Rivas, J. G.; Koenraad, P. M.; Silov, A. Y. *Nat. Commun.* **2021**, *12*, 5844.

(26) De Mello Donegá, C. *Chem. Soc. Rev.* **2011**, *40*, 1512–1546.

(27) Talapin, D. V.; Koeppe, R.; Götzinger, S.; Kornowski, A.; Lupton, J. M.; Rogach, A. L.; Benson, O.; Feldmann, J.; Weller, H. *Nano Lett.* **2003**, *3*, 1677–1681.

(28) Diroll, B. T.; Koschitzky, A.; Murray, C. B. *J. Phys. Chem. Lett.* **2014**, *5*, 85–91.

(29) Rastogi, P.; Palazon, F.; Prato, M.; Di Stasio, F.; Krahne, R. *ACS Appl. Mater. Interfaces* **2018**, *10*, 5665–5672.

(30) Manfredi, G.; Lova, P.; Di Stasio, F.; Rastogi, P.; Krahne, R.; Comoretto, D. *RSC Adv.* **2018**, *8*, 13026–13033.

(31) Müller, J.; Lupton, J. M.; Lagoudakis, P. G.; Schindler, F.; Koeppe, R.; Rogach, A. L.; Feldmann, J.; Talapin, D. V.; Weller, H. *Nano Lett.* **2005**, *5*, 2044–2049.

(32) *Nanoparticles: Workhorses of nanoscience*; Mello Donegá, C., Ed.; Material science/chemistry; Springer: Berlin et al., 2014.

(33) Gross, R.; Marx, A.; Einzel, D.; Geprägs, S., *Festkörperphysik: Aufgaben und Lösungen*, 2. Auflage; De Gruyter Studium; De Gruyter: Berlin and Boston, 2018.

(34) Klingshirn, C. F., *Semiconductor Optics*; Springer Berlin Heidelberg: Berlin, Heidelberg, 2012.

(35) Kittel, C., *Introduction to solid state physics*, 8. ed., internat. ed.; Wiley: Hoboken, NJ, 2005.

(36) Rogach, A. L., *Semiconductor nanocrystal quantum dots: Synthesis, assembly, spectroscopy, and applications*; Springer: Wien and New York, 2008.

(37) Kalt, H.; Klingshirn, C. F., *Semiconductor Optics 1*; Springer International Publishing: Cham, 2019.

(38) Atkins, P. W.; de Paula, J., *Thermodynamics and kinetics*, 9th ed., 1. print; Physical chemistry / Peter Atkins Julio de Paula, Vol. 1; Freeman: New York, 2010.

(39) Pelant, I.; Valenta, J., *Luminescence Spectroscopy of Semiconductors*; OUP Oxford: Oxford, 2012.

(40) Edvinsson, T. *R. Soc. Open Sci.* **2018**, *5*, 180387.

(41) Rupp, M. *Int. J. Quantum Chem.* **2015**, *115*, 1058–1073.

(42) Brus, L. *J. Phys. Chem.* **1986**, *90*, 2555–2560.

(43) Nirmal, M.; Dabbousi, B. O.; Bawendi, M. G.; Macklin, J. J.; Trautman, J. K.; Harris, T. D.; Brus, L. E. *Nature* **1996**, *383*, 802–804.

(44) Efros, A. L.; Nesbitt, D. J. *Nat. Nanotechnol.* **2016**, *11*, 661–671.

(45) Kuno, M.; Fromm, D. P.; Hamann, H. F.; Gallagher, A.; Nesbitt, D. J. *J. Chem. Phys.* **2000**, *112*, 3117–3120.

(46) Verberk, R.; van Oijen, A. M.; Orrit, M. *Phys. Rev. B* **2002**, *66*, 233202.

(47) Kuno, M.; Fromm, D. P.; Hamann, H. F.; Gallagher, A.; Nesbitt, D. J. *J. Chem. Phys.* **2001**, *115*, 1028–1040.

(48) Frantsuzov, P.; Kuno, M.; Jankó, B.; Marcus, R. A. *Nat. Phys.* **2008**, *4*, 519–522.

(49) Jain, P. K.; Beberwyck, B. J.; Fong, L.-K.; Polking, M. J.; Alivisatos, A. P. *Angew. Chem. Int. Ed. Engl.* **2012**, *51*, 2387–2390.

(50) Cordones, A. A.; Leone, S. R. *Chem. Soc. Rev.* **2013**, *42*, 3209–3221.

(51) Califano, M.; Gómez-Campos, F. M. *Nano Lett.* **2013**, *13*, 2047–2052.

(52) Veamatahau, A.; Jiang, B.; Seifert, T.; Makuta, S.; Latham, K.; Kanehara, M.; Teranishi, T.; Tachibana, Y. *Phys. Chem. Chem. Phys.* **2015**, *17*, 2850–2858.

(53) Müller, J.; Lupton, J. M.; Rogach, A. L.; Feldmann, J.; Talapin, D. V.; Weller, H. *Appl. Phys. Lett.* **2004**, *85*, 381–383.

(54) Galland, C.; Ghosh, Y.; Steinbrück, A.; Sykora, M.; Hollingsworth, J. A.; Klimov, V. I.; Htoon, H. *Nature* **2011**, *479*, 203–207.

(55) Yuan, G.; Gómez, D. E.; Kirkwood, N.; Boldt, K.; Mulvaney, P. *ACS Nano* **2018**, *12*, 3397–3405.

(56) Sillen, A.; Engelborghs, Y. *Photochem. Photobiol.* **1998**, *67*, 475–486.

(57) Acharya, K. P.; Khnayzer, R. S.; O'Connor, T.; Diederich, G.; Kirsanova, M.; Klinkova, A.; Roth, D.; Kinder, E.; Imboden, M.; Zamkov, M. *Nano Lett.* **2011**, *11*, 2919–2926.

(58) O'Connor, T.; Panov, M. S.; Mereshchenko, A.; Tarnovsky, A. N.; Lorek, R.; Perera, D.; Diederich, G.; Lambright, S.; Moroz, P.; Zamkov, M. *ACS Nano* **2012**, *6*, 8156–8165.

(59) Y.P. Varshni *Physica* **1967**, *34*, 149–154.

(60) Liu, S.; Shu, Y.; Zhu, M.; Qin, H.; Peng, X. *Nano Lett.* **2022**, *22*, 3011–3017.

(61) Rudin, S.; Reinecke, T. L.; Segall, B. *Phys. Rev. B* **1990**, *42*, 11218–11231.

(62) Gindele, F.; Hild, K.; Langbein, W.; Woggon, U. *J. Lumin.* **2000**, *87-89*, 381–383.

(63) Al Salman, A.; Tortschanoff, A.; Mohamed, M. B.; Tonti, D.; van Mourik, F.; Chergui, M. *Appl. Phys. Lett.* **2007**, *90*, 093104.

(64) Lee, J.; Koteles, E. S.; Vassell, M. O. *Phys. Rev. B* **1986**, *33*, 5512–5516.

(65) Wen, X.; Sitt, A.; Yu, P.; Toh, Y.-R.; Tang, J. *Phys. Chem. Chem. Phys.* **2012**, *14*, 3505–3512.

(66) Bui, H.; Karpulevich, A.; Bester, G. *Phys. Rev. B* **2020**, *101*, 115414.

(67) Nirmal, M.; Norris, D. J.; Kuno, M.; Bawendi, M. G.; Efros, A. L.; Rosen, M. *Phys. Rev. Lett.* **1995**, *75*, 3728–3731.

(68) Biadala, L.; Siebers, B.; Gomes, R.; Hens, Z.; Yakovlev, D. R.; Bayer, M. *J. Phys. Chem. C* **2014**, *118*, 22309–22316.

(69) Klimov, V. I. *Annu. Rev. Phys. Chem.* **2007**, *58*, 635–673.

(70) Labeau, O.; Tamarat, P.; Lounis, B. *Phys. Rev. Lett.* **2003**, *90*, 257404.

(71) Biadala, L.; Liu, F.; Tessier, M. D.; Yakovlev, D. R.; Dubertret, B.; Bayer, M. *Nano Lett.* **2014**, *14*, 1134–1139.

(72) Shornikova, E. V. et al. *Nanoscale* **2018**, *10*, 646–656.

(73) Blanton, S. A.; Hines, M. A.; Guyot-Sionnest, P. *Appl. Phys. Lett.* **1996**, *69*, 3905–3907.

(74) Empedocles, S. A.; Norris, D. J.; Bawendi, M. G. *Phys. Rev. Lett.* **1996**, *77*, 3873–3876.

(75) Empedocles, S. A.; Neuhauser, R.; Shimizu, K.; Bawendi, M. G. *Adv. Mater.* **1999**, *11*, 1243–1256.

(76) Neuhauser, R. G.; Shimizu, K. T.; Woo, W. K.; Empedocles, S. A.; Bawendi, M. G. *Phys. Rev. Lett.* **2000**, *85*, 3301–3304.

(77) Müller, J.; Lupton, J. M.; Rogach, A. L.; Feldmann, J.; Talapin, D. V.; Weller, H. *Phys. Rev. Lett.* **2004**, *93*, 167402.

(78) Matsuda, K.; Inoue, T.; Murakami, Y.; Maruyama, S.; Kanemitsu, Y. *Phys. Rev. B* **2008**, *77*, 193405.

(79) Lohmann, S.-H.; Strelow, C.; Mews, A.; Kipp, T. *ACS Nano* **2017**, *11*, 12185–12192.

(80) Voznyy, O. *J. Phys. Chem. C* **2011**, *115*, 15927–15932.

(81) Fernée, M. J.; Tamarat, P.; Lounis, B. *Chem. Soc. Rev.* **2014**, *43*, 1311–1337.

(82) Panfil, Y. E.; Cui, J.; Koley, S.; Banin, U. *ACS Nano* **2022**, *16*, 5566–5576.

(83) Fox, M., *Optical properties of solids*, 2. ed.; Oxford master series in physics Condensed matter physics, Vol. 3; Oxford Univ. Press: Oxford, 2010.

(84) Lendvay, G. *J. Mol. Struct.* **2000**, *501-502*, 389–393.

(85) Bawendi, M. G.; Wilson, W. L.; Rothberg, L.; Carroll, P. J.; Jedju, T. M.; Steigerwald, M. L.; Brus, L. E. *Phys. Rev. Lett.* **1990**, *65*, 1623–1626.

(86) Gindele, F.; Hild, K.; Langbein, W.; Woggon, U. *Phys. Rev. B* **1999**, *60*, R2157–R2160.

(87) Lin, M.-L.; Miscuglio, M.; Polovitsyn, A.; Leng, Y.-C.; Martín-García, B.; Moreels, I.; Tan, P.-H.; Krahne, R. *J. Phys. Chem. Lett.* **2019**, *10*, 399–405.

(88) Kalliakos, S.; Lefebvre, P.; Zhang, X. B.; Taliercio, T.; Gil, B.; Grandjean, N.; Damilano, B.; Massies, J. *Phys. Stat. Sol. (a)* **2002**, *190*, 149–154.

(89) J. T. Devreese Fröhlich Polarons. Lecture course including detailed theoretical derivations, Ver. 6, 2015, arXiv 1012.4576, last accessed 15.04.2025, `https://arxiv.org/abs/1012.4576`.

(90) Emin, D., *Polarons*; Cambridge University Press: Cambridge and New York, 2013.

(91) Bardeen, J.; Shockley, W. *Phys. Rev.* **1950**, *80*, 72–80.

(92) Chernikov, A.; Bornwasser, V.; Koch, M.; Chatterjee, S.; Böttge, C. N.; Feldtmann, T.; Kira, M.; Koch, S. W.; Wassner, T.; Lautenschläger, S.; Meyer, B. K.; Eickhoff, M. *Phys. Rev. B* **2012**, *85*, 035201.

(93) Lin, C.; Gong, K.; Kelley, D. F.; Kelley, A. M. *ACS Nano* **2015**, *9*, 8131–8141.

(94) Callsen, G. et al. *Phys. Rev. B* **2015**, *92*, 235439.

(95) Cho, K.; Tahara, H.; Yamada, T.; Suzuura, H.; Tadano, T.; Sato, R.; Saruyama, M.; Hirori, H.; Teranishi, T.; Kanemitsu, Y. *Nano Lett.* **2022**, *22*, 7674–7681.

(96) Han, P.; Bester, G. *Phys. Rev. B* **2022**, *106*, 245404.

(97) Lin, C.; Gong, K.; Kelley, D. F.; Kelley, A. M. *J. Phys. Chem. C* **2015**, *119*, 7491–7498.

(98) Alivisatos, A. P.; Harris, T. D.; Carroll, P. J.; Steigerwald, M. L.; Brus, L. E. *J. Chem. Phys.* **1989**, *90*, 3463–3468.

(99) Krauss, T. D.; Wise, F. W. *Phys. Rev. Lett.* **1997**, *79*, 5102–5105.

(100) Han, P.; Bester, G. *Phys. Rev. B* **2019**, *99*, 100302.

(101) Klein, M. C.; Hache, F.; Ricard, D.; Flytzanis, C. *Phys. Rev. B* **1990**, *42*, 11123–11132.

(102) Rolo, A. G.; Vasilevskiy, M. I. *J. Raman Spectrosc.* **2007**, *38*, 618–633.

(103) Yang, C. C.; Li, S. *J. Phys. Chem. B* **2008**, *112*, 14193–14197.

(104) Pejova, B. *J. Phys. Chem. C* **2013**, *117*, 19689–19700.

(105) Arora, A. K.; Rajalakshmi, M.; Ravindran, T. R.; Sivasubramanian, V. *J. Raman Spectrosc.* **2007**, *38*, 604–617.

(106) Peng, K.; Rabani, E. *Nano Lett.* **2023**, *23*, 10587–10593.

(107) Achtstein, A. W.; Scott, R.; Kickhöfel, S.; Jagsch, S. T.; Christodoulou, S.; Bertrand, G. H. V.; Prudnikau, A. V.; Antanovich, A.; Artemyev, M.; Moreels, I.; Schliwa, A.; Woggon, U. *Phys. Rev. Lett.* **2016**, *116*, 116802.

(108) Empedocles; Bawendi *Science* **1997**, *278*, 2114–2117.

(109) Scavuzzo, A.; Mangel, S.; Park, J.-H.; Lee, S.; Loc Duong, D.; Strelow, C.; Mews, A.; Burghard, M.; Kern, K. *Appl. Phys. Lett.* **2019**, *114*, 062104.

(110) Rothenberg, E.; Kazes, M.; Shaviv, E.; Banin, U. *Nano Lett.* **2005**, *5*, 1581–1586.

(111) Park, K.; Deutsch, Z.; Li, J. J.; Oron, D.; Weiss, S. *ACS Nano* **2012**, *6*, 10013–10023.

(112) Bar-Elli, O.; Steinitz, D.; Yang, G.; Tenne, R.; Ludwig, A.; Kuo, Y.; Triller, A.; Weiss, S.; Oron, D. *ACS Photonics* **2018**, *5*, 2860–2867.

(113) Miller, D. A. B.; Chemla, D. S.; Damen, T. C.; Gossard, A. C.; Wiegmann, W.; Wood, T. H.; Burrus, C. A. *Phys. Rev. Lett.* **1984**, *53*, 2173–2176.

(114) Kuo, Y.; Li, J.; Michalet, X.; Chizhik, A.; Meir, N.; Bar-Elli, O.; Chan, E.; Oron, D.; Enderlein, J.; Weiss, S. *ACS Photonics* **2018**, *5*, 4788–4800.

(115) Wang, C.; Fu, J.; Wei, Q.; Ren, H.; Liu, Q.; Zhou, L.; Wang, P.; Li, M. *Nano Lett.* **2023**, *23*, 5705–5712.

(116) Ossia, Y.; Levi, A.; Panfil, Y. E.; Koley, S.; Scharf, E.; Chefetz, N.; Remennik, S.; Vakahi, A.; Banin, U. *Nat. Mater.* **2023**, *22*, pages 1210–1217.

(117) Marshall, J. D.; Schnitzer, M. J. *ACS Nano* **2013**, *7*, 4601–4609.

(118) Rowland, C. E.; Susumu, K.; Stewart, M. H.; Oh, E.; Mäkinen, A. J.; O'Shaughnessy, T. J.; Kushto, G.; Wolak, M. A.; Erickson, J. S.; Efros, A. L.; Huston, A. L.; Delehanty, J. B. *Nano Lett.* **2015**, *15*, 6848–6854.

(119) Park, K.; Weiss, S. *Biophys. J.* **2017**, *112*, 703–713.

(120) Caglar, M.; Pandya, R.; Xiao, J.; Foster, S. K.; Divitini, G.; Chen, R. Y. S.; Greenham, N. C.; Franze, K.; Rao, A.; Keyser, U. F. *Nano Lett.* **2019**, *19*, 8539–8549.

(121) Roy, D.; Shapira, Z.; Weiss, S. *J. Chem. Phys.* **2022**, *156*, 084201.

(122) Park, K.; Kuo, Y.; Shvadchak, V.; Ingargiola, A.; Dai, X.; Hsiung, L.; Kim, W.; Zhou, H.; Zou, P.; Levine, A. J.; Li, J.; Weiss, S. *Sci. Adv.* **2018**, *4*, e1601453.

(123) Ludwig, A.; Serna, P.; Morgenstein, L.; Yang, G.; Bar-Elli, O.; Ortiz, G.; Miller, E.; Oron, D.; Grupi, A.; Weiss, S.; Triller, A. *ACS Photonics* **2020**, *7*, 1141–1152.

(124) Huang, Z. et al. *Nat. Commun.* **2024**, *15*, 4586.

(125) Conradt, F.; Bezold, V.; Wiechert, V.; Huber, S.; Mecking, S.; Leitenstorfer, A.; Tenne, R. *Nano Lett.* **2023**, *23*, 9753–9759.

(126) Peng, X.; Schlamp, M. C.; Kadavanich, A. V.; Alivisatos, A. P. *J. Am. Chem. Soc.* **1997**, *119*, 7019–7029.

(127) Carbone, L. et al. *Nano Lett.* **2007**, *7*, 2942–2950.

(128) Wei, S.-H.; Zunger, A. *Appl. Phys. Lett.* **1998**, *72*, 2011–2013.

(129) Cui, J.; Panfil, Y. E.; Koley, S.; Shamalia, D.; Waiskopf, N.; Remennik, S.; Popov, I.; Oded, M.; Banin, U. *Nat. Commun.* **2019**, *10*, 5401.

(130) Madelung, O., *Semiconductors: Data Handbook*; Springer Berlin Heidelberg: Berlin, Heidelberg, 2004.

(131) C Trager-Cowan; P J Parbrook; B Henderson; K P O'Donnell *Semicond. Sci. Technol.* **1992**, *7*, 536.

(132) Nethercot, A. H. *Phys. Rev. Lett.* **1974**, *33*, 1088–1091.

(133) Wei, S.-H.; Zhang, S. B.; Zunger, A. *J. Appl. Phys.* **2000**, *87*, 1304–1311.

(134) Hinuma, Y.; Grüneis, A.; Kresse, G.; Oba, F. *Phys. Rev. B* **2014**, *90*, 155405.

(135) Brovelli, S.; Schaller, R. D.; Crooker, S. A.; García-Santamaría, F.; Chen, Y.; Viswanatha, R.; Hollingsworth, J. A.; Htoon, H.; Klimov, V. I. *Nat. Commun.* **2011**, *2*, 280.

(136) Christodoulou, S.; Rajadell, F.; Casu, A.; Vaccaro, G.; Grim, J. Q.; Genovese, A.; Manna, L.; Climente, J. I.; Meinardi, F.; Rainò, G.; Stöferle, T.; Mahrt, R. F.; Planelles, J.; Brovelli, S.; Moreels, I. *Nat. Commun.* **2015**, *6*, 7905.

(137) Segarra, C.; Climente, J. I.; Polovitsyn, A.; Rajadell, F.; Moreels, I.; Planelles, J. *J. Phys. Chem. Lett.* **2016**, *7*, 2182–2188.

(138) Steiner, D.; Dorfs, D.; Banin, U.; Della Sala, F.; Manna, L.; Millo, O. *Nano Lett.* **2008**, *8*, 2954–2958.

(139) Sitt, A.; Della Sala, F.; Menagen, G.; Banin, U. *Nano Lett.* **2009**, *9*, 3470–3476.

(140) Eshet, H.; Grünwald, M.; Rabani, E. *Nano Lett.* **2013**, *13*, 5880–5885.

(141) Lohmann, S.-H.; Harder, P.; Bourier, F.; Strelow, C.; Mews, A.; Kipp, T. *J. Phys. Chem. C* **2019**, *123*, 5099–5109.

(142) Hinsch, A.; Lohmann, S.-H.; Strelow, C.; Kipp, T.; Würth, C.; Geißler, D.; Kornowski, A.; Wolter, C.; Weller, H.; Resch-Genger, U.; Mews, A. *J. Phys. Chem. C* **2019**, *123*, 24338–24346.

(143) Dorfs, D.; Salant, A.; Popov, I.; Banin, U. *Small* **2008**, *4*, 1319–1323.

(144) Jain, P. K.; Amirav, L.; Aloni, S.; Alivisatos, A. P. *J. Am. Chem. Soc.* **2010**, *132*, 9997–9999.

(145) Son, D. H.; Hughes, S. M.; Yin, Y.; Paul Alivisatos, A. *Science* **2004**, *306*, 1009–1012.

(146) Routzahn, A. L.; Jain, P. K. *Nano Lett.* **2015**, *15*, 2504–2509.

(147) Rivest, J. B.; Jain, P. K. *Chem. Soc. Rev.* **2013**, *42*, 89–96.

(148) Parr, R. G.; Pearson, R. G. *J. Am. Chem. Soc.* **1983**, *105*, 7512–7516.

(149) Beberwyck, B. J.; Surendranath, Y.; Alivisatos, A. P. *J. Phys. Chem. C* **2013**, *117*, 19759–19770.

(150) Lange, N. A., *Lange's handbook of chemistry*, 15. ed.; McGraw-Hill handbooks; McGraw-Hill: New York, NY, 1999.

(151) Groeneveld, E.; Witteman, L.; Lefferts, M.; Ke, X.; Bals, S.; van Tendeloo, G.; Donega, C. d. M. *ACS Nano* **2013**, *7*, 7913–7930.

(152) Sitt, A.; Salant, A.; Menagen, G.; Banin, U. *Nano Lett.* **2011**, *11*, 2054–2060.

(153) Vezzoli, S.; Manceau, M.; Leménager, G.; Glorieux, Q.; Giacobino, E.; Carbone, L.; de Vittorio, M.; Bramati, A. *ACS Nano* **2015**, *9*, 7992–8003.

(154) Planelles, J.; Rajadell, F.; Climente, J. I. *J. Phys. Chem. C* **2016**, *120*, 27724–27730.

(155) Zhang, G.-F.; Yang, C.-G.; Ge, Y.; Peng, Y.-G.; Chen, R.-Y.; Qin, C.-B.; Gao, Y.; Zhang, L.; Zhong, H.-Z.; Zheng, Y.-J.; Xiao, L.-T.; Jia, S.-T. *Front. Phys.* **2019**, *14*, 63601.

(156) Hewa-Kasakarage, N. N.; Kirsanova, M.; Nemchinov, A.; Schmall, N.; El-Khoury, P. Z.; Tarnovsky, A. N.; Zamkov, M. *J. Am. Chem. Soc.* **2009**, *131*, 1328–1334.

(157) Wu, K.; Chen, Z.; Lv, H.; Zhu, H.; Hill, C. L.; Lian, T. *J. Am. Chem. Soc.* **2014**, *136*, 7708–7716.

(158) Kalisman, P.; Houben, L.; Aronovitch, E.; Kauffmann, Y.; Bar-Sadan, M.; Amirav, L. *J. Mater. Chem. A* **2015**, *3*, 19679–19682.

(159) Nakibli, Y.; Mazal, Y.; Dubi, Y.; Wächtler, M.; Amirav, L. *Nano Lett.* **2018**, *18*, 357–364.

(160) Hentschel, S.; Dittmar, M.; Strelow, C.; Ruhmlieb, C.; Hackl, T.; Mews, A. *Adv. Sustain. Syst.* **2025**, *9*, 2400782.

(161) Saba, M.; Minniberger, S.; Quochi, F.; Roither, J.; Marceddu, M.; Gocalinska, A.; Kovalenko, M. V.; Talapin, D. V.; Heiss, W.; Mura, A.; Bongiovanni, G. *Adv. Mater.* **2009**, *21*, 4942–4946.

(162) Zavelani-Rossi, M.; Krahne, R.; Della Valle, G.; Longhi, S.; Franchini, I. R.; Girardo, S.; Scotognella, F.; Pisignano, D.; Manna, L.; Lanzani, G.; Tassone, F. *Laser Photonics Rev.* **2012**, *6*, 678–683.

(163) Grivas, C.; Li, C.; Andreakou, P.; Wang, P.; Ding, M.; Brambilla, G.; Manna, L.; Lagoudakis, P. *Nat. Commun.* **2013**, *4*, 2376.

(164) Sonnichsen, C. D.; Kipp, T.; Tang, X.; Kambhampati, P. *ACS Photonics* **2019**, *6*, 382–388.

(165) Onal, A.; Eren, G. O.; Melikov, R.; Kaya, L.; Nizamoglu, S. *Adv Materials Technologies* **2023**, *8*, 2201799.

(166) Malko, A. V.; Park, Y.-S.; Sampat, S.; Galland, C.; Vela, J.; Chen, Y.; Hollingsworth, J. A.; Klimov, V. I.; Htoon, H. *Nano Lett.* **2011**, *11*, 5213–5218.

(167) Chen, Y.; Vela, J.; Htoon, H.; Casson, J. L.; Werder, D. J.; Bussian, D. A.; Klimov, V. I.; Hollingsworth, J. A. *J. Am. Chem. Soc.* **2008**, *130*, 5026–5027.

(168) Christodoulou, S.; Vaccaro, G.; Pinchetti, V.; de Donato, F.; Grim, J. Q.; Casu, A.; Genovese, A.; Vicidomini, G.; Diaspro, A.; Brovelli, S.; Manna, L.; Moreels, I. *J. Mater. Chem. C* **2014**, *2*, 3439.

(169) Bae, W. K.; Padilha, L. A.; Park, Y.-S.; McDaniel, H.; Robel, I.; Pietryga, J. M.; Klimov, V. I. *ACS Nano* **2013**, *7*, 3411–3419.

(170) Park, Y.-S.; Bae, W. K.; Padilha, L. A.; Pietryga, J. M.; Klimov, V. I. *Nano Lett.* **2014**, *14*, 396–402.

(171) Altintas, Y.; Gungor, K.; Gao, Y.; Sak, M.; Quliyeva, U.; Bappi, G.; Mutlugun, E.; Sargent, E. H.; Demir, H. V. *ACS Nano* **2019**, *13*, 10662–10670.

(172) Cragg, G. E.; Efros, A. L. *Nano Lett.* **2010**, *10*, 313–317.

(173) *A Laboratory Guide to the Tight Junction*; Jianghui Hou, Ed.; Academic Press: 2020.

(174) Jonkman, J.; Brown, C. M. *J. Biomol. Tech.* **2015**, *26*, 54–65.

(175) Elliott, A. D. *Curr. Protoc. Cytom.* **2020**, *92*, e68.

(176) Voigtländer, B., *Scanning Probe Microscopy*; Springer Berlin Heidelberg: Berlin, Heidelberg, 2015.

(177) Meyer, E., *Scanning Probe Microscopy: The Lab on a Tip*; Advanced Texts in Physics; Springer: Berlin and Heidelberg, 2004.

(178) Larson, M. G.; Bengzon, F., *The Finite Element Method: Theory, Implementation, and Applications*; Springer Berlin Heidelberg: Berlin, Heidelberg, 2013; Vol. 10.

(179) Langtangen, H. P.; Mardal, K.-A., *Introduction to Numerical Methods for Variational Problems*, 1st ed. 2019; Texts in Computational Science and Engineering; Springer International Publishing and Imprint: Springer: Cham, 2019.

(180) Panfil, Y. E.; Shamalia, D.; Cui, J.; Koley, S.; Banin, U. *J. Chem. Phys.* **2019**, *151*, 224501.

(181) BenDaniel, D. J.; Duke, C. B. *Phys. Rev.* **1966**, *152*, 683–692.

(182) Adachi, S., *Properties of semiconductor alloys: Group-IV, III-V and II-VI semiconductors*; Wiley series in materials for electronic & optoelectronic applications; Wiley: Chichester U.K., 2009.

(183) Koch, C.; Rinke, T. J., *Fotolithografie: Grundlagen der Mikrostrukturierung*, 1. Auflage; MicroChemicals GmbH: Ulm, 2017.

(184) Chen, Y. *Microelectron. Eng.* **2015**, *135*, 57–72.

(185) Johst, F.; Rebmann, J.; Werners, H.; Klemeyer, L.; Kopula Kesavan, J.; Koziej, D.; Strelow, C.; Bester, G.; Mews, A.; Kipp, T. *ACS Photonics* **2024**, *11*, 3741–3749.

(186) Cozzoli, P. D.; Manna, L.; Curri, M. L.; Kudera, S.; Giannini, C.; Striccoli, M.; Agostiano, A. *Chem. Mater.* **2005**, *17*, 1296–1306.

(187) Huang, J.; Kovalenko, M. V.; Talapin, D. V. *J. Am. Chem. Soc.* **2010**, *132*, 15866–15868.

(188) Adachi, S., *Properties of group-IV, III-V and II-VI semiconductors*; Wiley series in materials for electronic and optoelectronic applications; Wiley: Chichester, 2005.

(189) Zhu, H.; Chen, Z.; Wu, K.; Lian, T. *Chem. Sci.* **2014**, *5*, 3905–3914.

(190) Thibert, A.; Frame, F. A.; Busby, E.; Holmes, M. A.; Osterloh, F. E.; Larsen, D. S. *J. Phys. Chem. Lett.* **2011**, *2*, 2688–2694.

(191) Rebmann, J.; Werners, H.; Johst, F.; Dohrmann, M.; Staechelin, Y. U.; Strelow, C.; Mews, A.; Kipp, T. *Chem. Mater.* **2023**, *35*, 1238–1248.

(192) Boldt, K.; Bartlett, S.; Kirkwood, N.; Johannessen, B. *Nano Lett.* **2020**, *20*, 1009–1017.

(193) Fernée, M. J.; Littleton, B.; Plakhotnik, T.; Rubinsztein-Dunlop, H.; Gómez, D. E.; Mulvaney, P. *Phys. Rev. B* **2010**, *81*, 155307.

(194) Mangnus, M. J. J.; de Wit, J. W.; Vonk, S. J. W.; Geuchies, J. J.; Albrecht, W.; Bals, S.; Houtepen, A. J.; Rabouw, F. T. *ACS Photonics* **2023**, *10*, 2688–2698.

(195) Azhniuk, Y. M.; Milekhin, A. G.; Gomonnai, A. V.; Hutych, Y. I.; Lopushansky, V. V.; Zahn, D. R. T. *Phys. Stat. Sol. (c)* **2009**, *6*, 2068–2071.

(196) Fröhlich, H. *Adv. Phys.* **1954**, *3*, 325–361.

(197) Gong, K.; Kelley, D. F.; Kelley, A. M. *J. Phys. Chem.* **2017**, *8*, 626–630.

(198) Dufåker, D.; Karlsson, K. F.; Dimastrodonato, V.; Mereni, L. O.; Sernelius, B. E.; Holtz, P. O.; Pelucchi, E. *Phys. Rev. B* **2010**, *82*, 205421.

(199) Xie, R.; Kolb, U.; Li, J.; Basché, T.; Mews, A. *J. Am. Chem. Soc.* **2005**, *127*, 7480–7488.

(200) Toufanian, R.; Zhong, X.; Kays, J. C.; Saeboe, A. M.; Dennis, A. M. *Chem. Mater.* **2021**, *33*, 7527–7536.

(201) Manthiram, K.; Beberwyck, B. J.; Talapin, D. V.; Alivisatos, A. P. *J. Vis. Exp.* **2013**, e50731.

(202) Zhong, X.; Feng, Y.; Zhang, Y.; Gu, Z.; Zou, L. *Nanotechnology* **2007**, *18*, 385606.

(203) Huang, K.; Rhys, A. *Proc. R. Soc. Lond. A* **1950**, *204*, 406–423.

(204) Shornikova, E. V.; Yakovlev, D. R.; Biadala, L.; Crooker, S. A.; Belykh, V. V.; Kochiev, M. V.; Kuntzmann, A.; Nasilowski, M.; Dubertret, B.; Bayer, M. *Nano Lett.* **2020**, *20*, 1370–1377.

(205) Hu, Z.; Liu, S.; Qin, H.; Zhou, J.; Peng, X. *J. Am. Chem. Soc.* **2020**, *142*, 4254–4264.

(206) Empedocles, S. A.; Bawendi, M. G. *J. Phys. Chem. B* **1999**, *103*, 1826–1830.

(207) Howder, C. R.; Bell, D. M.; Anderson, S. L. *Rev. Sci. Instrum.* **2014**, *85*, 014104.

(208) Howder, C. R.; Long, B. A.; Bell, D. M.; Furakawa, K. H.; Johnson, R. C.; Fang, Z.; Anderson, S. L. *ACS Nano* **2014**, *8*, 12534–12548.

(209) Leippe, S. C.; Johst, F.; Hoffmann, B.; Krohn, S.; Papagrigoriou, K.; Asmis, K. R.; Mews, A.; Bastian, B. *J. Phys. Chem. C* **2024**, *128*, 21472–21478.

(210) Hoffmann, B.; Esser, T. K.; Abel, B.; Asmis, K. R. *J. Phys. Chem. Lett.* **2020**, *11*, 6051–6056.

(211) Jing, P.; Zheng, J.; Ikezawa, M.; Liu, X.; Lv, S.; Kong, X.; Zhao, J.; Masumoto, Y. *J. Phys. Chem. C* **2009**, *113*, 13545–13550.

(212) Hall, D. B.; Underhill, P.; Torkelson, J. M. *Polym. Eng. Sci.* **1998**, *38*, 2039–2045.

(213) Jang, H.; Jung, D.; Bae, W. K.; Park, Y.-S.; Lee, D. C. *J. Chem. Phys.* **2023**, *158*, 134712.

(214) Bennett, A. J.; Pooley, M. A.; Stevenson, R. M.; Ward, M. B.; Patel, R. B.; de La Giroday, A. B.; Sköld, N.; Farrer, I.; Nicoll, C. A.; Ritchie, D. A.; Shields, A. J. *Nat. Phys.* **2010**, *6*, 947–950.

(215) Lv, B.; Zhu, T.; Tang, Y.; Lv, Y.; Zhang, C.; Wang, X.; Shu, D.; Xiao, M. *Phys. Rev. Lett.* **2021**, *126*, 197403.

(216) Sigma-Aldrich Material Safety Data Sheets, last accessed 18.03.2025, `https://www.sigmaaldrich.com/DE/de`.

(217) Institut für Arbeitsschutz der Deutschen Gesetzlichen Unfallversicherung GESTIS substance database, last accessed 18.03.2025, `https://gestis.dguv.de/`.

(218) Allresist Material Safety Data Sheet, last accessed 18.03.2025, `https://www.allresist.com/wp-content/uploads/sites/2/2021/12/AR600-56_SDB_GB_11.1_1415.pdf`.

(219) Kayaku Advanced Materials Material Safety Data Sheet, last accessed 18.03.2025, `https://kayakuam.com/wp-content/uploads/2019/12/SDS_LOR_A_Series_Resists_-_EU.pdf`.

(220) DuPont Material Safety Data Sheet, last accessed 18.03.2025, `https://www.conro.com/downloads/Manuals/Dupont-Microposit-MF-319-Developer-5-Litre-Can-SDS.pdf`.

(221) Dow Chemical Material Safety Data Sheet, last accessed 18.03.2025, `https://www.uni-muenster.de/imperia/md/content/mnf/s1813_photoresist_sds.pdf`.

A. Appendix

A.1. Supplementary Information

Table A.1.: Compilation of the DRs sample geometries for Chapter 6.1. Listed are the average rod diameter D, base cone diameter C and length L and their standard deviations.

Sample	$\boldsymbol{D}$**(nm)**	$\boldsymbol{C}$**(nm)**	$\boldsymbol{L}$**(nm)**
DR-1	4.8 ± 0.7	7.2 ± 1.7	27.4 ± 2.9
DR-2	5.2 ± 0.7	6.2 ± 1.0	28.8 ± 3.0
DR-3	4.8 ± 0.6	6.0 ± 1.3	25.2 ± 3.6
DR-4	4.8 ± 0.6	5.4 ± 1.5	21.7 ± 11.6
Average	4.8 ± 0.6	6.2 ± 1.4	25.8 ± 6.4

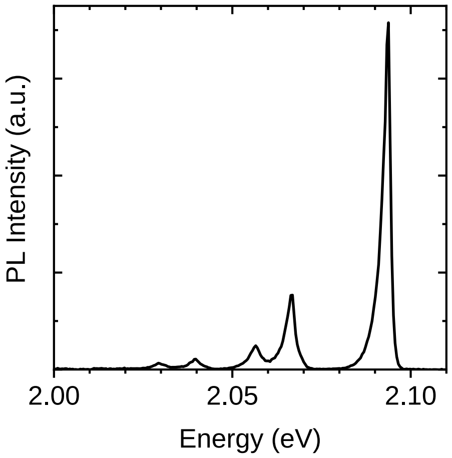

Figure A.1.: Averaged PL spectrum of an individual NC from sample GS-1 at $T = 10$ K.

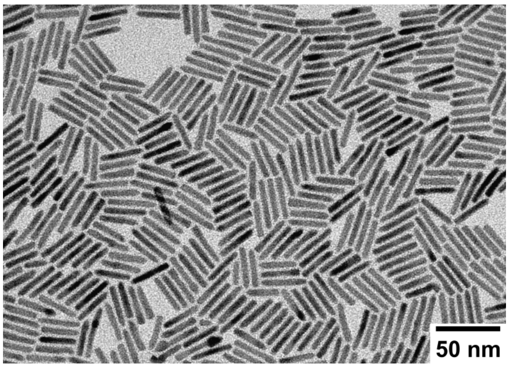

Figure A.2.: TEM image of the CdSe/CdS DRs discussed in Chapter , synthesized by Mareike Dittmar.

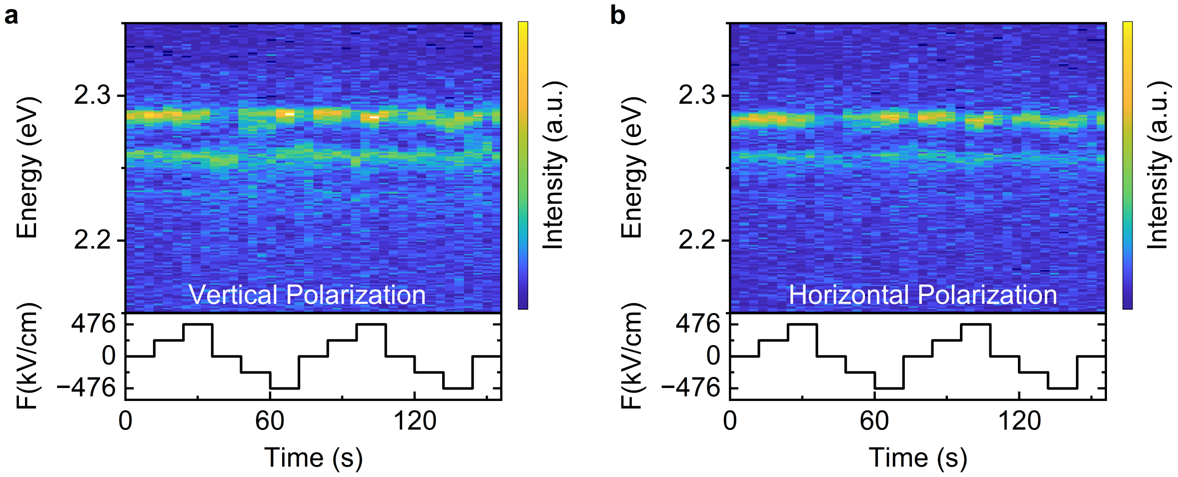

Figure A.3.: Spectral time traces of a single DR recorded simultaneously from two different ROIs, using the measurement setup shown in Figure 6.27.

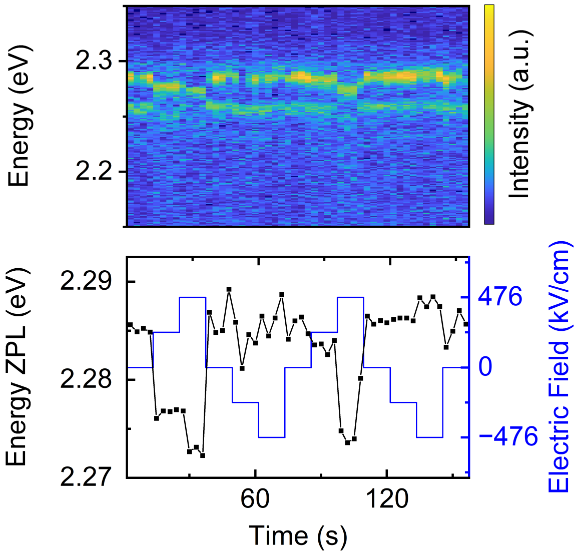

Figure A.4.: Initial spectral time trace of the single DR from Figure A.3.

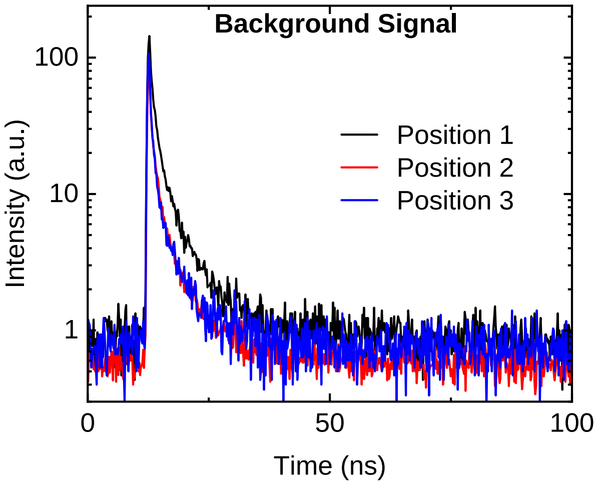

Figure A.5.: Photoluminescence decay curves of different background obtained from different positions on the substrates for electric field measurements at $T = 10$ K.

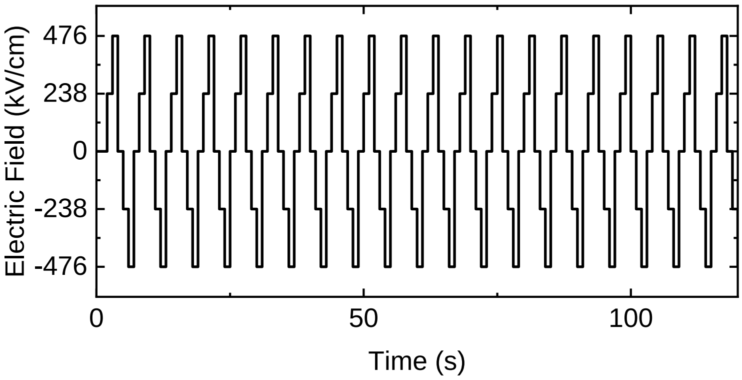

Figure A.6.: Electric field sweep used for the measurement of decay curves in Chapter 6.3.2 and 6.3.3.

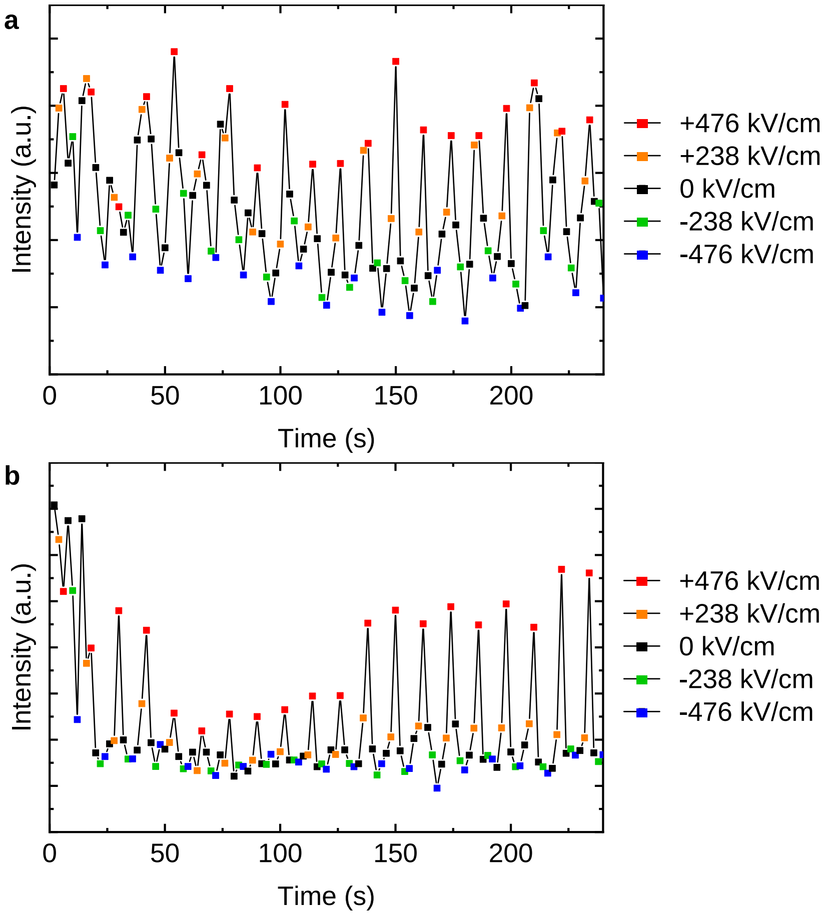

Figure A.7.: Time trace of the PL intensity corresponding to the CdSe/CdS DRs of Figure 6.41a and b respectively.

Figure A.8 compares PL decay curves of a single CdSe/CdS DRs for shell and core excitation during different electric fields. Corresponding fitting results are compiled in Table A.2, and the electric sweep that was performed during the measurement is illustrated in Figure A.9. When the PL intensity increases in response to the negative electric field, the average PL lifetime increases. Complementary, the positive electric field decreases the PL intensity and average PL lifetime. This is the case for both excitation energies. The difference between average PL lifetimes in the case of shell excitation and core excitation is that the PL lifetime is overall longer for shell excitation and shorter for core excitation. These observations can be explained by the larger overlap of the exciton in the case of core excitation, which leads to a reduced PL lifetime, compared to the larger delocalization in the case of shell excitation.[142] Interestingly, even if the band potentials are tilted by the external electric field, the lower PL lifetime in the case of core excitation is retained. Although it should be noted that the background signal had a high contribution during the measurement in the case of core excitation. Therefore, the results should be viewed with caution.

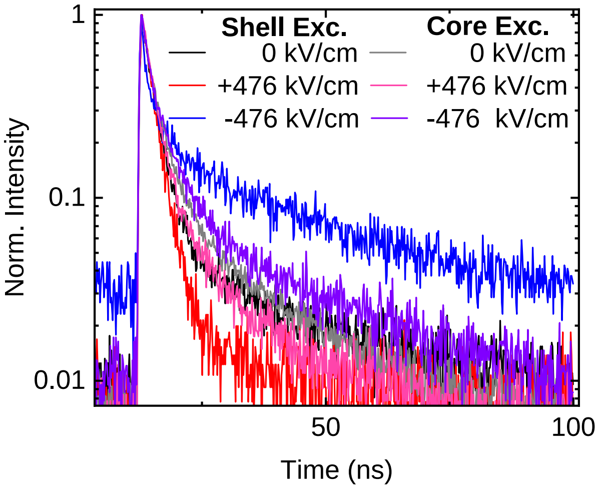

Figure A.8.: Photoluminescence decay curves of a single CdSe/CdS DR excited at shell excitation (2.78 eV) and core excitation (2.43 eV) during exposure to different electric field conditions.

Table A.2.: Fitting results for the PL decay curves the CdSe/CdS DR of Figure A.8: weight and lifetime of the short A_1 / τ_1 and long component A_2 / τ_2, intensity-averaged lifetime τ_{average} and I_{PL}.

Excitation	F(kV/cm)	A_1	τ_1 (ns)	A_2	τ_2 (ns)	τ_{average}(ns)	I_{PL} (a.u.)
Shell	+476	0.67	2.1	0.03	12.6	4.0	998
Shell	0	0.59	2.4	0.05	21.3	10.8	1300
Shell	−476	0.27	2.4	0.17	26.5	23.4	2049
Core	+476	0.61	2.3	0.09	13.2	7.2	2846
Core	0	0.56	2.6	0.11	18.8	9.6	2929
Core	−476	0.48	2.5	0.15	14.6	10.2	2828

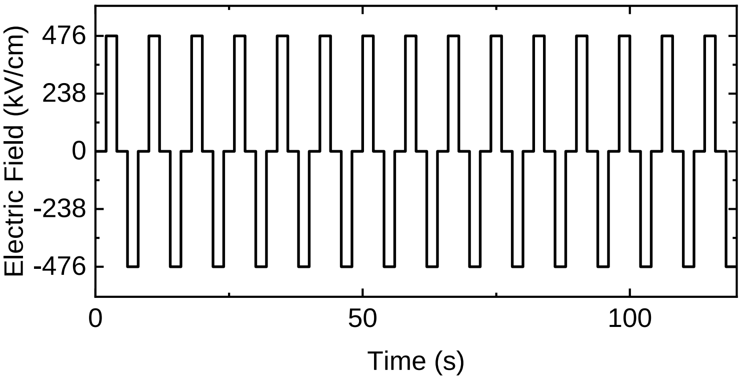

Figure A.9.: Electric field sweep used for the measurement of decay curves of Figure A.8.

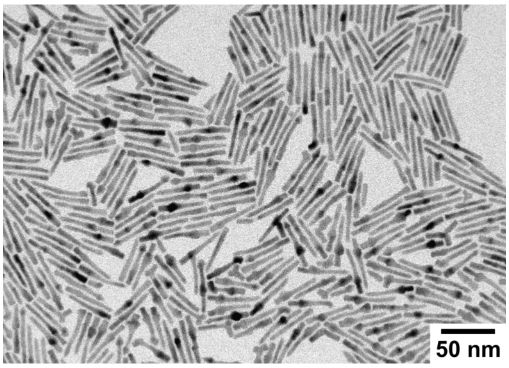

Figure A.10.: TEM image of the ZnSe/CdS DRs discussed in Chapter 6.3.3, synthesized by Mareike Dittmar.

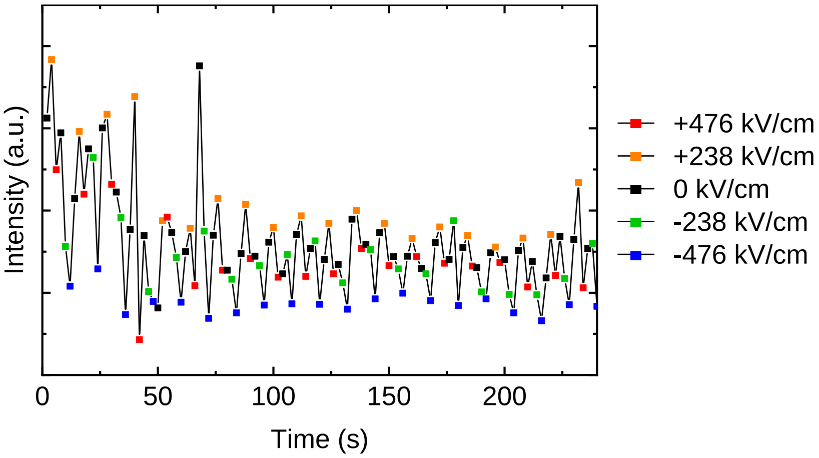

Figure A.11.: Time trace of the PL intensity corresponding to the ZnSe/CdS DR of Figure 6.45.

A.2. Hazard and Safety

Table A.3.: Safety and disposal information of the chemicals used in this work.[216,217]

Chemical	**GHS Symbol**	**P-Sentences**	**H-Sentences**	**Disposal**
Acetone	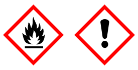	H225-H319-H336	P210-P233-P261-P280-P303 + P361 + P353-P370 + P378	(a)
AR 600-56[218] developer	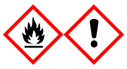	H225-H319-H335-H336	P101-P102-P103-P210-P241-P280-P303+P361+P353-P304+P340-P305+P351+P338-P405-P501	(a)
Cadmium selenide	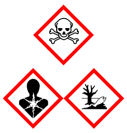	H301+H331-H312-H373-H410	P273-P280-P301+P310-P302+P352+P312-P304+P340+P311-P314	(b)
Cadmium sulfide	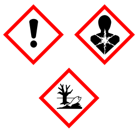	H302-H341-H350-H361fd-H372-H410	P201-P273-P301 + P312 + P330-P308 + P313	(b)
Gold	Not a hazardous according to (EG) no. 1272/2008			(b)
n-Hexane	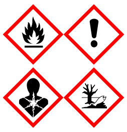	H225-H304-H315-H336-H361f-H373-H411	P202-P210-P273-P301+P310-P303+P361+P353-P331	(c)

Table A.3.: Safety and disposal information of the chemicals used in this work.[216,217]

Chemical	GHS Symbol	P-Sentences	H-Sentences	Disposal
LOR-5A Lift-Off Resist[219]	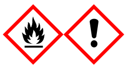	H226-H315-H319	P210-P260-P280-P301+P310-P305+P351+P338-P333+P313-P337+P313-P370+P378-P403+P235-P501	(a)
MICROPOSIT MF-319 developer[220]	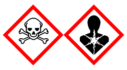	H311-H315-H319-H371-H373	P260-P264-P280-P302+P352+P312-P308+P311-P337+P313	(d)
MICROPOSIT Remover 1165	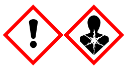	H315-H319-H335-H360D	P202-P261-P264-P302+P352-P305+P351+P338-P308+P313	(c)
MICROPOSIT S1805 positive photo resist[221]	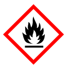	H226	P210-P233-P240-P241-P242-P243-P280	(a)
Poly(methyl methacrylate), MW=35 k	Not a hazardous according to (EG) no. 1272/2008			(b)
2-Propanol	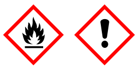	H225-H319-H336	P210-P305 + P351 + P338-P370 + P378-P403 + P235	(a)
Titanium	Not a hazardous according to (EG) no. 1272/2008			(b)

Table A.3.: Safety and disposal information of the chemicals used in this work.[216,217]

Chemical	**GHS Symbol**	**P-Sentences**	**H-Sentences**	**Disposal**
Toluene	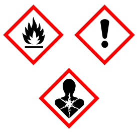	H225-H304-H315-H336-H361d-H373	P210-P260-P280-P301 + P310-P370 + P378-P403 + P235	(c)
Zinc selenide	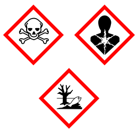	H301+H331-H373-H410	P273-P301 + P310 + P330-P304 + P340 + P311-P314	(b)
Zinc sulfide	Not a hazardous according to (EG) no. 1272/2008			(b)

Disposal information:

(a) Container for halogen free solvents.

(b) Container for contaminated equipment.

(c) Container for halogenated, carcinogenic and toxic solvents.

(d) Container for inorganic bases.

Table A.4.: List of used CMR chemicals, with their respective applications, amounts and categorization.[217]

CAS Number	**Compound Name (IUPAC)**	**Usage and Amount**	**CMR Category(GHS)**
1306-24-7	Cadmium selenide	Spincoating of nanocrystals for analysis, µg scale	C: 1B
1306-23-6	Cadmium sulfide	Nanocrystals solution spin coated for analysis, µg scale	C: 1B
872-50-4	*N*-Methyl-2-pyrrolidone	Remover solution for lithography	R: 1B

A.3. Acknowledgement

Abschließend möchte mich noch bei allen bedanken, ohne die ich nie so weit gekommen wäre:

Ganz herzlich möchte ich mich bei PD Dr. Tobias Kipp bedanken, für die allerbeste Betreuung, die es für eine Doktoranden nur geben kann. Ich danke ihm für die Unterstützung, unendlich vielen Meetings, blitzschnellen Antworten auf Teams, sowie seine Begeisterung für neue Exprimente und Comsol Rechnungen.

Ebenso möchte ich mich bei Prof. Dr. Alf Mews bedanken für die willkommene Aufnahme in seinen Arbeitskreis, die zahlreichen Meetings, Denkanstöße und Motivation neues auszuprobieren.

Bei Prof. Dr. Tobias Beck möchte ich für die Betreuung im Graduiertenkolleg und das Feedback zu meinen Vorträgen bedanken.

Prof. Dr. Gabriel Bester möchte danken für seine Begeisterung an meinem Thema und sein wertvolles Feedback zu meiner Forschung, sowie der Übernahme des 2. Gutachtens dieser Arbeit.

Prof. Dr. Dorota Koziej und PD Dr. Christoph Wutz möchte ich danken für die Teilnahme an meiner Disputation als Prüfungsmitglieder.

Dr. Corinna Flügge und Andreas Kolditz möchte ich Danken für die engagierte Organisation des Graduiertenkollegs Nanohybrid, die gelungenen Workshops, Bearbeitung zahlreicher Bestellungen und Anträge, sowie alles weitere hinter den Kulissen.

Ebenfalls möchte ich der Deutschen Forschungsgesellschaft für die Finanzierung meiner Promotion im Rahmen des Graduiertenkollegs danken.

Bei Dr. Christian Strewlow möchte ich mich bedanken für die Hilfe bei der Umsetzung neuer Experimente und allgemein für die Beantwortung zahlreicher Fragen.

Dipl-Ing. Jan Flügge möchte ich danken für die allseits schnelle Hilfe bei der Lösung von Problemen jeglicher Art, sei es die Kommunikation mit der Werkstatt, das Löten von Kabeln, Bestellungen und Design von Leiterplatten, der Transport von Gasflaschen und vieles mehr.

Dr. Jannik Rebmann, Mareike Dittmar, Dr. Sonja Zeller und Dr. Vincent Mittag möchte ich für die Synthese verschiedenster Nanokristalle und Zusammenarbeit danken.

Für die Zusammenarbeit in unseren Kooperationen möchte ich mich bei Dr. Jannik Rebmann, Prof. Dr. Gabriel Bester, Dr. Lars Klemeyer, Dr. Jagadesh Kopula Kesavan, Prof. Dr. Dorota Koziej, Dr. Sonja Zeller, Dr. Björn Bastian, Sophia Leippe und Dr. Benjamin Hoffmann bedanken.

Bei Hans Werners möchte ich mich bedanken für die großartige Unterstützung in meiner Anfangszeit, die Einarbeitung ins BlueLab und die Spektroskopie allgemein.

Bei Dr. Daniel Lengle möchte ich mich bedanken für die Einarbeitung in die Lithografie und AFM, sowie die Hilfe bei Problemen, wenn mal etwas nicht ganz nach Plan verlief.

Nicklas Giese möchte ich danken für die Hilfe bei der Einarbeitung in den Wire Bonder und die E-Beam Lithografie.

Meinen Praktikanten Julius Fraedrich, Adrian Vaghar und Yannick Gruber-Roet möchte ich danken für euren Beitrag in den Forschungspraktika. Insbesondere bei Adrian Vaghar für die Spektroskopie von Sonjas Quantum Dots.

Julia Funk, Sascha Busler und Dr. Christian Strelow möchte ich danken für das Korrekturlesen und Feedback zur Dissertation.

Sascha Busler und Nicklas Giese möchte ich für die schöne Zeit in unserem Büro 144 danken. Dank euch war die Büroarbeit immer unterhaltsam und nie langweilig.

Dem gesamten Arbeitskreis möchte ich danken für die tolle Arbeitsatmosphäre, Hilfsbereitschaft und Zusammenarbeit und allgemein schöne Zeit mit euch.

Mein ganz besonderer Dank geht an meine Freunde, Familie und unsere Katzen für die Unterstützung während meiner gesamten Studienzeit und darüber hinaus. Danke: Mama, Jonathan, Josie, Wolfgang, Annie, Winni, Asa, Oma, Opa, Mario, Luigi, Arthur und Merlin. Insbesondere möchte ich mich von ganzem Herzen bei meiner Frau Julia bedanken. Danke, dass du immer für mich da bist.

A.4. Eidesstattliche Erklärung

Hiermit versichere ich an Eides statt, die vorliegende Dissertationsschrift selbst verfasst und keine anderen als die angegebenen Quellen und Hilfsmittel benutzt zu haben. Sofern im Zuge der Erstellung der vorliegenden Dissertationsschrift generative Künstliche Intelligenz (gKI) basierte elektronische Hilfsmittel verwendet wurden, versichere ich, dass meine eigene Leistung im Vordergrund stand und dass eine vollständige Dokumentation aller verwendeten Hilfsmittel gemäß der Guten wissenschaftlichen Praxis vorliegt. Ich trage die Verantwortung für eventuell durch die gKI generierte fehlerhafte oder verzerrte Inhalte, fehlerhafte Referenzen, Verstöße gegen das Datenschutz- und Urheberrecht oder Plagiate.

Hamburg, den 19.08.2025

Florian Funk